UC San Diego

UC San Diego Electronic Theses and Dissertations

Title

Friction-based Structural Components for Earthquake-Resistant Buildings

Permalink

https://escholarship.org/uc/item/1963997s

ISBN

9798190938906

Author

Chen, Kaixin

Publication Date

2026-09-15

Peer reviewed|Thesis/dissertation

eScholarship.org Powered by the California Digital Library
University of California

UNIVERSITY OF CALIFORNIA SAN DIEGO

Friction-based Structural Components for Earthquake-Resistant Buildings

A dissertation submitted in partial satisfaction of the
requirements for the degree Doctor of Philosophy

in

Structural Engineering

by

Kaixin Chen

Committee in charge:

Professor Georgios Tsampras, Chair
Professor Constantin Christopoulos
Professor Joel Conte
Professor Yuri Fialko
Professor Gilberto Mosqueda
Professor Chia-Ming Uang

2026

Copyright

Kaixin Chen, 2026

All rights reserved.

The Dissertation of Kaixin Chen is approved, and it is acceptable in quality and form for publication on microfilm and electronically.

University of California San Diego

2026

DEDICATION

This dissertation is dedicated to my parents and grandparents, with my deepest love and gratitude.

Your love, support, and sacrifices have made this journey possible. Thank you for always believing in me and for giving me the strength to keep moving forward.

EPIGRAPH

Among any three people, there must be one who has something to teach me.

Confucius, *The Analects*

If I have seen further, it is by standing on the shoulders of giants.

Isaac Newton, *Letter to Robert Hooke*

为天下人谋永福

Juemin Lin, *Farewell Letter to His Wife*

TABLE OF CONTENTS

Dissertation Approval Page iii

Dedication iv

Epigraph v

Table of Contents vi

List of Figures ix

List of Tables xvii

Acknowledgements xviii

Vita xxiii

Abstract of the Dissertation xxiv

Chapter 1 Introduction 1
1.1 Earthquake Impacts and Seismic Protection Systems 1
1.2 Friction-Based Structural Components for Earthquake-Resistant Structures 3
1.2.1 Applications of Friction-Based Structural Components 4
1.2.2 Design Considerations of Friction-Based Structural Components 5
1.2.3 Research Gaps in Friction-Based Structural Components 24
1.3 Research Objectives and Dissertation Organization 27

Chapter 2 Experimental Characterization of Mechanical and Tribological Properties of Composite Materials for Friction-based Structural Components 29
2.1 Overview and Scope of Study 29
2.2 Composite Friction Materials 30
2.2.1 Constituents 30
2.2.2 Manufacturing 31
2.2.3 Testing 32
2.3 Experimental Testing: Background and Setup 33
2.3.1 Material Overview 33
2.3.2 Specimen Preparation 34
2.3.3 Experimental Testing Set-up 35
2.3.4 Digital Image Correlation Technique 52
2.4 Results 53
2.4.1 Coupon Tensile Test 53
2.4.2 Plate Bearing Test 57
2.4.3 Bolt Relaxation Test 58
2.4.4 Friction Test 62

2.5 Conclusions 83

Chapter 3 Low-Cost Friction-Based Structural Components With Reduced Sensitivity to Machining Tolerances and Accelerated Repairability 87
3.1 Overview and Scope of Study 87
3.2 Design Concept 88
3.2.1 Connection Configuration 88
3.2.2 Preliminary Numerical Assessment of the Design Concept 92
3.3 Experimental Program 94
3.3.1 Summary of Testing Phases 94
3.3.2 Test Phase 1: Component-level Connection Test 94
3.3.3 Test Phase 2: Shaking Table Test 108
3.4 Conclusions 118

Chapter 4 Friction-Based Structural Components with Predetermined Discrete Variable Friction Forces at Target Design Displacement Levels 123
4.1 Overview 123
4.2 Background 123
4.2.1 Practical Force-Limiting Connections 123
4.2.2 Friction-based Force-limiting Connections in Core Wall Buildings 124
4.2.3 Structural Connections Capable of Developing Multiple Discrete Variable Force Levels at Target Displacement Levels 126
4.3 Scope of Study 129
4.4 Modified FD 130
4.4.1 Components and Assembly 130
4.4.2 Expected Kinematics and Force-displacement Response 132
4.5 Numerical Simulations of the Modified FD 136
4.5.1 Description of the Solid Model 136
4.5.2 Solid Model Analysis Results 139
4.5.3 Description of the Truss Model 140
4.5.4 Truss Model Analysis Results 144
4.6 Seismic Demands in Modified FDs from Numerical Earthquake Simulation of Core Wall Building 147
4.6.1 Numerical Model of Example Building 148
4.6.2 Seismic Response of the Modified FD in the Example Building Model . 150
4.7 Conclusions 153

Chapter 5 Experimental Characterization of Friction-Based Structural Components with Predetermined Discrete Variable Friction Forces at Target Design Displacement Levels 155
5.1 Scope of Study 155
5.2 Experimental Testing 156
5.2.1 Preliminary Studies 157
5.2.2 Full-scale Connection Testing 178

5.3 Conclusions 196

Chapter 6 Summary and Conclusions 199
6.1 Summary 199
6.1.1 Research Goal 199
6.1.2 Research Objectives 200
6.1.3 Research Scope 200
6.1.4 Research Findings of Chapter 2 202
6.1.5 Research Findings of Chapter 3 204
6.1.6 Research Findings of Chapter 4 207
6.1.7 Research Findings of Chapter 5 207
6.2 Conclusions 209
6.3 Original Contributions 211
6.4 Future Research 212
6.4.1 Material-level 212
6.4.2 Component-level 213
6.4.3 System-level 213

Bibliography 215

LIST OF FIGURES

Figure 1.1. Historical earthquake impact data from the NCEI/WDS Global Significant Earthquake Database [1]: (a) earthquake-related fatalities data and (b) reported earthquake damage data 2

Figure 1.2. Schematic representation of an example slotted-bolted friction-based structural component: (a) Exploded view (b) Assembly 6

Figure 1.3. (a) High axial stiffness with two significantly different sliding force levels using the same friction-based structural component (b) Geometric tolerances used to machine the friction-based structural component may contribute to an uncontrolled variation of the sliding friction force. 14

Figure 1.4. (a) Schematic representation of the force-displacement response of a friction-based component. (b) Friction-based force-limiting connections (friction-based components + rubber bearings) in a building with planar rocking walls [2, 3] 16

Figure 1.5. Photos of RF42 friction shims from [4]: (a) friction shims before the test, (b) damaged friction shim with elongated bolt holes, and (c) damaged friction shim with elongated bolt holes associated with net section tensile failure 17

Figure 1.6. (a) Ideal load path of the example slotted-bolted friction-based structural component in Figure 1.2 (b) A schematic representation of the break-in effect reported in [2] (c) Load path of the example slotted-bolted friction-based structural component considering the break-in effect 18

Figure 1.7. (a) Fractured RF42 friction shim (b) The force-displacement response of the friction-based component in the test when the fracture of the friction shim first occurred (c) The force-displacement response of the component in the tenth test following the fracture of the friction shim 20

Figure 1.8. Schematic demonstration of the effect of non-parallel plates on applying the normal load. (a) Initial state of the bolted assembly with a non-flat plate. (b) Final state of the bolted assembly with an applied bolt load $N = N_b$ given an applied tightening torque T ($N_b \propto T$) 21

Figure 1.9. Schematic demonstration of long-term bolt relaxation in a bolted assembly. (a) The initial state of a simplified model of a bolted assembly (b) The state of the bolted assembly instantly after the pretensioning of the bolt (c) The state of the bolted assembly in long-term operation 22

Figure 2.1. Specimen preparation process 34

Figure 2.2. Nominal dimensions of test specimens: (a) Tensile coupons (b) Bearing plates and (c) Square plates (Units: in mm) 34

Figure 2.3. Coupon tensile test setup 36

Figure 2.4. Plate bearing test setup 37

Figure 2.5. Bolt relaxation test: (a) schematic representation of the test setup and (b) photo of the actual test setup 40

Figure 2.6. Schematic representation of the friction test setup: (a) Exploded view (b) Assembly 41

Figure 2.7. Photos of the friction test setup: (a) Components (b) Assembly on the testing machine 41

Figure 2.8. Friction test loading protocol. From top to bottom: imposed displacement history; cumulative displacement history of each test; and absolute sliding velocity history 46

Figure 2.9. Engineering parameters of interest for the coupon tensile test 54

Figure 2.10. (a) Coupon tensile test results: engineering stress-strain curves upon failure (example photos of two Gatke 112 specimens with different failure modes are shown with Gatke 112 results) 54

Figure 2.11. Plate bearing test results: bearing force versus the recorded displacement . 57

Figure 2.12. Bolt relaxation test results: normalized bolt load (N/N_{ini}) time history . . . 59

Figure 2.13. (a) Bolt load loss of all test specimens upon reaching the steady state of the bolt load; one of the results of Gatke 112 specimens with the largest bolt load loss of 37.12% is highlighted (b) Microscopy images of the Gatke 112 specimen with 37.12% bolt load loss 60

Figure 2.14. Images of pressure recording films of two Gatke 112 specimens from the bolt relaxation test 61

Figure 2.15. Friction shims conditions before (left) and after (right) the friction test . . . 62

Figure 2.16. Friction shims with (a) no damage (example friction shim from Test Group Gatke 398 (L)) (b) minor damage (example friction shim from Test Group Gatke 81 (L)) (c) severe damage (example friction shim from Test Group Gatke 113 (H)) 63

Figure 2.17. (a) Unworn sliding plates before the friction test (b) Representative example of sliding plates conditions after completing one test group (Gatke 112 (L)) and before cleaning (c) Representative example of sliding plates conditions after cleaning using aerosol brake parts cleaner and heavy-duty shop towels 64

Figure 2.18. Assessment of the break-in effect 66

Figure 2.19. Assessment of effect of sliding velocity (Test IDs 5∼10) 69

Figure 2.20. Relative difference between $\overline{\mu_i}$ and $\overline{\mu_5}$ in Test IDs 5∼10 71

Figure 2.21. Schematic explanation of Bowden and Tabor's adhesive friction theory: (a) Two plates are clamped together under a certain normal pressure (b) Top view of the contact interface (c) Zoomed-in top view of the contact interface, with real contact areas being exaggerated 74

Figure 2.22. Schematic representation of the state of the friction interface (a) at the beginning of Test ID 5 (b) during Test IDs 7∼8 and (c) during Test IDs 9∼10 74

Figure 2.23. (a) Absolute sliding velocity history and recorded friction force history of one selected representative sliding travel from Test ID 6 in Test Groups Gatke 398 (H) and Gatke 112 (H) (b) Absolute sliding velocity history and recorded friction force history of one selected representative sliding travel 76

Figure 2.24. Force-displacement responses of the tested friction interfaces under earthquake-type input excitation (Test IDs 4, 11, and 14) 77

Figure 2.25. Evolution of μ of the friction interfaces under earthquake-type input excitation (Test IDs 4, 11, and 14) 78

Figure 2.26. Assessment of the effect of dwell time (Test IDs 15∼20) 79

Figure 2.27. (a) Normalized bolt load time history of all test groups and (b) Normalized bolt load time history of Test IDs 7 and 8 in Test Group Gatke 398 (H); the color of the marker is defined based on the instantaneous absolute sliding velocity 81

Figure 2.28. Recorded force response time history of Test IDs 5 and 7 from Test Group Gatke 112 (H) 82

Figure 3.1. Schematic representation of the proposed friction-based force-limiting connection: (a) Exploded view (b) Assembly 89

Figure 3.2. Load path of the friction-based connection: (a) The connection generates a tensile force of $f = 2\mu N$. (b) Schematic free body diagram of the steel channel when in contact with the friction shim in the opening (c) Schematic free body diagram of the friction shim 90

Figure 3.3. Numerical simulation of the proposed friction-based connection 93

Figure 3.4. Connection assembly demonstration 98

Figure 3.5. Representative connection test setup 99

Figure 3.6. (a) Selected force-displacement responses of the connection in Test Phase 1 Test Group 1 (b) Selected DIC analysis results of Test Group 1 101

Figure 3.7. Representative surface and edge appearance of Gatke 398 friction shims (a) before a test and (b) after a test 102

Figure 3.8. Selected results of Test Phase 1 Test Group 2: force-displacement responses of the connection under earthquake-type input excitation (Tests 1, 2, 3, 13, 14, and 15) 104

Figure 3.9. Results of Test Phase 1 Test Group 2: evolution of the connection force with respect to the cumulative displacement and the variation of the bolt load in each test (tests are separated using dashed lines) 104

Figure 3.10. Proposed break-in loading protocol for the friction-based connection in this study. From top to bottom: imposed displacement time history; cumulative displacement time history; absolute sliding velocity time history 106

Figure 3.11. Results of Test Phase 1 Test Group 3: (a) Force-displacement responses of the connection in Test Group 3 (b) Time history results of Test Group 3 (tests are separated by dashed blue lines). 108

Figure 3.12. Test Phase 2 shaking table test (a) overview of the steel frame specimen and (b) instrumentation related to the friction-based connection 110

Figure 3.13. Demonstration of the connection installation process 111

Figure 3.14. Selected results of Test Phase 2 Test Group 1 of one representative connection. From top to bottom: imposed displacement time history; connection sliding force time history; and friction bolt load time history 112

Figure 3.15. Selected results of the shaking table test: displacement time history, cumulative displacement time history, and absolute sliding velocity time history of RFL-W (in black) and RFL-E (in red) friction-based connections 114

Figure 3.16. Friction bolt load time history of all the friction-based connections in this frame specimen throughout the shaking table test. From top to bottom: friction bolts for RFL connections, for 3FL connections, and for 2FL connections. 116

Figure 3.17. Friction shim replacement demonstration after the completion of the shaking table tests while the friction-based connection remained installed on the frame specimen 116

Figure 3.18. Force-displacement responses of the connection in Test Phase 2 Test Group 3 117

Figure 3.19. Force-displacement responses of the connection in Test Phase 2 Test Group 4 118

Figure 4.1. In contrast with the planar wall system, the relative movement between the floors and the core wall system is constrained by the rubber bearings. The planar wall system is shown in (a) and the core wall system is shown in (b). 126

Figure 4.2. Schematics of the Modified FD (a) components, (b) exploded view, (c) assembly, and (d) front view with initial gap dimensions D_1 and D_2 between the bearing plates and the slots in the external plates. 131

Figure 4.3. Expected kinematics and expected force-displacement response in the Modified FD. 133

Figure 4.4. Finite element model developed to assess the expected kinematics and the expected force-displacement response of the Modified FD. 137

Figure 4.5. Static structural analysis of the Solid Model shows that it is possible to develop predetermined friction forces at target design displacements with the proposed Modified FD. 140

Figure 4.6. Schematic representation of the Modified FD Truss Model and the associated material definitions. 142

Figure 4.7. Schematic representation of the geometric terms used to estimate the stiffness of the components of the Modified FD simulated with the Truss Model. 142

Figure 4.8. Comparison of the force-displacement response computed using the Solid Model and the Truss Model assuming standard oversized pin holes and zero oversized pin holes. 145

Figure 4.9. The force-displacement responses from six analysis cases of the Truss Model show that the expected performance of the Modified FD is possible to be controlled by selecting the design parameters that lead to predefined discrete variable forces at target displacement levels. 147

Figure 4.10. (a) Typical floor plan and (b) section A of the eighteen-story building (all dimensions are in meters). 148

Figure 4.11. Schematic representation of (a) the eighteen-story core wall building with the Modified FDs, (b) the numerical model of the eighteen-story core wall building and (c) a typical floor simulated in the numerical model of the building. 150

Figure 4.12. Scaled ground acceleration of the two horizontal components (a) SHI000 (H1) and (b) SHI090 (H2), and (c) pseudo acceleration response spectra of scaled ground motions and design spectrum with a 5% damping ratio. 150

Figure 4.13. Peak force and peak displacement responses in the Modified FD along the global X- and Y-directions, and (b) the force-displacement response of the Modified FD at floor levels 5, 14, and 18. 152

Figure 4.14. Peak floor total acceleration, peak connection displacement, and peak connection force in global X- and Y-directions. 152

Figure 5.1. Schematic representation of the Modified Friction Device (Modified FD) introduced in Chapter 4: (a) components, (b) exploded view, (c) assembly, showing design parameters D_1 and D_2, and (d) force-displacement response with design parameters D_1, D_2, F_1, F_2, and F_3 156

Figure 5.2. Schematic representation of the PS-C1 specimen: (a) assembly, and (b) exploded view. 158

Figure 5.3. Photos of (a) parts of the PS-C1 specimen, (b) front view of the PS-C1 specimen assembly, (c) top view of the PS-C1 specimen assembly, and (d) shorter and longer bearing plates for adjusting D_1 and D_2. 159

Figure 5.4. (a) Schematic representation of the PS-C1R specimen assembly and, (b) changes on the PS-C1R configuration compared with PS-C1. 160

Figure 5.5. Schematic representation of the PS-C2 specimen: (a) assembly, and (b) exploded view. 162

Figure 5.6. Photos of (a) parts of the PS-C2 specimen (bolts and associated assemblies are not shown), (b) PS-C2 specimen assembly, and (c) shorter and longer friction shims to adjust design parameters D_1 and D_2. 162

Figure 5.7. (a) Overview of the experimental testing setup for the preliminary studies, (b) photos of PS-C1, PS-C1R, and PS-C2 specimens on the testing machine, and (c) through-hole bolt load cell for monitoring the bolt load. 163

Figure 5.8. Loading protocol for the preliminary studies. From top to bottom: imposed displacement time history; cumulative displacement time history; absolute sliding velocity time history. 169

Figure 5.9. Selected force-displacement responses of the PS-C1 specimen (with the case of design parameters DP5) 170

Figure 5.10. Demonstration of the design parameters adjustability of PS-C1 using Test 7 170

Figure 5.11. PS-C1 bolt load cells numbering plan and PS-C1 BL testing bolt load variation results 172

Figure 5.12. Observations from PS-C1 testing: (a) bearing plates getting tilted during the testing, (b) off-centered contact due to tilted bearing plate, (c) gouging between the side of the bearing plate and the external plate due to tilted bearing plate 173

Figure 5.13. Force-displacement responses of the PS-C1R specimen 174

Figure 5.14. Selected DIC analysis results from the PS-C1R testing 176

Figure 5.15. Force-displacement responses of the PS-C2 specimen (with design parameters PS-C2 BL) 176

Figure 5.16. Demonstration of adjusting design parameters for PS-C2: (a) shorter friction shims for larger D_1 in PS-C2 BL, (b) longer friction shims for smaller D_1 in PS-C2 DP1, and (c) comparison of the force-displacement response of PS-C2 BL and PS-C2 DP2 in Test 7 177

Figure 5.17. Schematic representation of the full-scale Modified FD specimen (a) assembly and (b) exploded view 179

Figure 5.18. (a) Photo of the channel component and (b)(c) speckled channel component for DIC data collection 179

Figure 5.19. (a) Photo of the W-section component, (b) as-received condition of the W-section surface, and (c) W-section surface after cleaning 180

Figure 5.20. Photo of the parts of the full-scale Modified FD: (a) longer washer plates, (b) shorter washer plates, (c) longer friction shims (for F_1), (d) shorter friction shims (for F_2 and F_3), (e) friction shims of different lengths for adjusting D_1 and D_2, and (f) 3.2 mm ($\frac{1}{8}$ inch) thickness PTFE shims 181

Figure 5.21. (a) Schematic representation of the test setup, and (b) photo of the actual test setup 183

Figure 5.22. Photo of the full-scale Modified FD specimen in the test setup 184

Figure 5.23. (a) Schematic representation of the full-scale Modified FD test instrumentation plan, (b) photos of displacement transducers, (c) photo of one through-hole bolt load cell, (d) photo of through-hole bolt load cells on the specimen and their numbering indices 185

Figure 5.24. (a) The imposed displacement time history used for Tests 1-1, 1-2, 2.1∼2.5, and 2.6-5∼6, and (b) the imposed displacement time history for Tests 2.6-1 to 2.6-8 190

Figure 5.25. Force-displacement response of the full-scale Modified FD (FS BL case) . 191

Figure 5.26. Comparison of full-scale Modified FD design cases 192

Figure 5.27. Bolt load results from Test 2.6-6: (a) imposed displacement time history of Test 2.6-6, (b) time history of LC1 to LC6, (c) time history of the sum of LC1 to LC3 and LC4 to LC6, (d) time history of LC7 and LC8, and (e) time history of LC9 and LC10 194

Figure 5.28. Evolution of the Modified FD connection stiffness during the wind load test 195

LIST OF TABLES

Table 1.1. Seismic protection systems summarized by Christopoulos and Filiatrault [5] 3

Table 2.1. Summary of Test Groups for the Friction Test 44

Table 2.2. Friction Test Loading Protocol: Imposed Displacement Histories 47

Table 2.3. Summary of Mean Material Tensile Properties from the Coupon Tensile Test 55

Table 2.4. Summary of Mean Ultimate Bearing Strengths and Specimen Failure Modes from the Plate Bearing Test 58

Table 2.5. Summary of Break-in Effect Assessment Results 67

Table 2.6. Summary of Mean COF ($\overline{\mu_i}$) and Relative Difference between $\overline{\mu_i}$ and $\overline{\mu_5}$ ($\delta_{i\text{-}5}$) for Test IDs 5$\sim$10 70

Table 3.1. Test phases of the proposed friction-based connection 95

Table 3.2. Information about the machining of the parts of the connection specimen used in Test Phase 1 97

Table 3.3. Loading protocol of Test Phase 1 Test Group 2 103

Table 3.4. Loading protocol of Test Group 3 107

Table 3.5. Testing sequence of the shaking table test 113

Table 4.1. Summary of previous studies on structural connections capable of developing multiple discrete force levels at target displacement levels 128

Table 4.2. Design parameters considered in six variations of the Truss Model 146

Table 5.1. Cases of design parameters considered in PS-C1 testing 160

Table 5.2. Loading protocol for the preliminary studies 166

Table 5.3. Cases of design parameters considered in full-scale Modified FD testing . . 182

Table 5.4. Loading protocol for full-scale Modified FD testing 187

ACKNOWLEDGEMENTS

The research presented in this dissertation was conducted under the supervision of Professor Georgios Tsampras. I would like to express my deepest gratitude to him for his guidance, support, and mentorship throughout my Ph.D. study at the University of California San Diego. I am truly grateful for the opportunity to work with Professor Tsampras. He trusted me with this research, gave me the freedom to explore my own ideas, and guided me with patience and care. His advice helped me through both the exciting moments and the difficult parts of my Ph.D. journey. More importantly, the way he approaches research, engineering, and people has set an example that I will continue to learn from. I sincerely thank Professor Tsampras for his time, encouragement, and support over the past five years. His high standards and thoughtful guidance have shaped this dissertation and helped me grow as an engineer, a researcher, and a person.

I would also like to sincerely thank my dissertation committee members, Professors Constantin Christopoulos, Joel Conte, Yuri Fialko, Gilberto Mosqueda, and Chia-Ming Uang, for their time, support, and valuable feedback throughout my Ph.D. study. Their thoughtful comments, questions, and suggestions helped improve this dissertation and guided me to think more carefully about my research from different perspectives. In particular, I would like to thank Professor Chia-Ming Uang for kindly allowing us to use his existing damper test setup, which made the full-scale component testing presented in Chapter 5 of this dissertation possible.

A special thanks is reserved for Dr. Shivaglal Cheruvalath and Dr. Mary Thundathil. Their collaboration, contributions, and guidance were essential to the work presented in Chapter 2 of this dissertation. I am very grateful for their time, patience, and generous support throughout the material-level experimental study. Their knowledge and insight helped shape the direction of this work, and their thoughtful discussions greatly improved my understanding of composite friction materials. I sincerely appreciate the opportunity to work with and learn from them. I would also like to thank Scan-Pac Manufacturing Inc. for generously donating the composite friction materials used in my experimental study.

My sincere thanks go to Professors Chung-Che Chou, Shih-Ho Chao, Chia-Ming Uang, and Georgios Tsampras for giving me the opportunity to participate in the NTU-UTA-UCSD joint research project and for their support in completing the work presented in Chapter 4 of this dissertation. I am also grateful to Chi-Jeng Wu and Huang-Zuo Lin from NCREE for their important contributions, input, and assistance throughout this collaborative work.

I am also grateful to Jim Malley and Dr. Insung Kim from Degenkolb Engineers for their valuable suggestions on the full-scale test specimen presented in Chapter 5 of this dissertation. Their practical insights and engineering experience helped improve the design and detailing of the specimen and made the test more closely connected to structural engineering practice. I sincerely appreciate their time, support, and willingness to share their expertise.

I would like to acknowledge the financial support provided through the Daniel P. Jenny Fellowship from the Precast/Prestressed Concrete Institute (PCI) and the Structural Engineering Distinguished Fellowship from the Structural Engineering Department at the University of California San Diego. This support made an important part of my Ph.D. research possible.

I am also grateful to Michael Dyson, Joel Fullerton, Zackary Kamibayashiyama, and Michael Sanders from Powell Lab for their technical support and assistance with the experimental work presented in this dissertation. I appreciate their time, expertise, and patience in helping with specimen preparation, test setup, instrumentation, and laboratory operations. Their support made the full-scale component testing presented in Chapter 5 of this dissertation possible.

I would also like to thank the current and past members of the Tsampras Research Group, including Drew Davey, James Dayanghirang, Chaoran Liu, Matthilde Monastiridou, Dr. Asad Naeem, Dr. Priyana Rajbhandari, and Dr. Xianjue Deng. I am grateful for the many discussions, feedback, and support they shared with me throughout my Ph.D. study. Their perspectives and suggestions helped me think more carefully about my research and made my graduate school experience more meaningful. In particular, I would like to thank Dr. Asad Naeem for helping me with the experimental testing presented in Chapter 5 of this dissertation.

My deepest appreciation goes to Kyoungyeon Lee and Carlos Franco Mayorga Gallegos,

who have been not only my research groupmates, but also like family to me. I am truly grateful for the time we spent together in the office and outside of work, sharing ideas, solving problems, and supporting each other through the ups and downs of graduate school. Their kindness and friendship made many difficult days much easier and many good moments even more meaningful. I feel very lucky to have gone through this journey with them, and I will always cherish their support and friendship.

I am thankful to the undergraduate students whom I had the opportunity to mentor during my Ph.D. study. I am grateful for their hard work, curiosity, and contributions. I would also like to thank all the undergraduate students in our group who visited my experiments and showed their support.

I am deeply grateful to Professor Bin Wang and Professor Songye Zhu, who played an important role in the early stage of my academic journey at The Hong Kong Polytechnic University. They were among the first people who guided me into earthquake engineering research and helped me build a solid foundation in this field. Their mentorship, encouragement, and example had a lasting influence on my decision to pursue graduate study and continue working in earthquake engineering.

I am also grateful to my friends in the Department of Structural Engineering for their friendship, support, and encouragement throughout my time at UC San Diego. In particular, I would like to thank Dr. Axel Yarahuaman, Charlie Zhang, Keijiro Tsurukawa, Dr. Guofeng Qian, Louis Lin, Haiwei Lin, Dr. Yangzi He, Dr. Simone Reale, Erick Zavala, Dr. Chao-Hsien Li, Daniel Lee, Dr. Ernesto Hernández, Dr. Claudio Sepulveda, Dr. Sergio Godinez, Dr. Ricardo Bustamante, and Shokrullah Sorosh, along with many others, for the conversations, help, and shared moments that made this journey more enjoyable and memorable. I would also like to thank the SE soccer team for the fun games, teamwork, and much-needed breaks from research.

I also want to recognize my friends in California for their kind support and companionship outside of research. In particular, I thank Junjie Lin, Wubing Shen, Ziwen Wang, and Rouyu Xie for their kindness, care, and help in my daily life. Their friendship made my time in California

warmer and more enjoyable.

I am fortunate to have received support from many friends, including, among many others, Dr. Ke Chen, Jingyue Huang, Haomin Lin, Dr. Zhengkun Chen, Bolong Yao, Xi Chu, and Dr. Shiyao Bao. I am grateful for their friendship, encouragement, and support over the years. Their presence, even from different places and at different stages of my life, has meant a great deal to me. A special thank you is given to Dr. Yuyang Xue, who graduated a few months before me, for his support and friendship since 2002.

Last but not least, I would like to thank my parents and grandparents for their unconditional love, encouragement, and support over the years. Their care has given me strength through many difficult moments and made this journey possible. I dedicate this dissertation to them.

Chapter 2, in full, is a reprint of the material as it appears in: Chen, K., Tsampras, G., Cheruvalath, S., & Thundathil, M. (2025). Experimental characterization of mechanical and tribological properties of composite materials for friction-based force-limiting structural components. *Composites Part B: Engineering*, 302, 112472. Credits are distributed as follows: Kaixin Chen: Writing – original draft, Visualization, Validation, Software, Methodology, Investigation, Formal analysis, Data curation, Conceptualization. Georgios Tsampras: Writing – review & editing, Supervision, Resources, Project administration, Methodology, Investigation, Funding acquisition, Data curation, Conceptualization. Shivaglal Cheruvalath: Writing – review & editing, Resources, Investigation. Mary Thundathil: Writing – review & editing, Resources, Investigation.

Chapter 3, in full, is a reprint of the material as it appears in: Chen, K., Tsampras, G., Chou, C. C., Lin, H. Z., Wu, C. J., Córdova, A., Uang, C. M., & Chao, S. H. (2026). Low-Cost Friction-Based Force-Limiting Connection With Reduced Sensitivity to Machining Tolerances and Accelerated Repairability. *Earthquake Engineering & Structural Dynamics*. Credits are distributed as follows: Kaixin Chen: writing – original draft and editing, Visualization, Experiments, Data curation and analysis, Methodology, Investigation. Georgios Tsampras: writing – original draft and editing, Research need and scope conceptualization, Friction-based

connection design concept, manufacturing and experiments, Resources, Funding acquisition and project administration (UC San Diego), Methodology, Investigation, Data curation and analysis. Chung-Che Chou: writing – review and editing, Resources, Experiments, Resources, Funding acquisition and project administration (NCREE), Methodology, Investigation, Sliding floor shake table testing lead, Shake table testing data curation. Huang-Zuo Lin: writing – review, Experiments, Data curation, Methodology, Investigation. Chi-Jeng Wu: writing – review, Experiments, Data curation, Methodology, Investigation. Alvaro Córdova: writing – review, Experiments, Data curation, Methodology, Investigation. Chia-Ming Uang: writing – review and editing, Sliding floor design conceptualization, Methodology, Investigation. Shih-Ho Chao: writing – review and editing, Sliding floor design conceptualization, Methodology, Investigation.

Chapter 4, in full, is a reprint of the material as it appears in: Chen, K., Tsampras, G., & Lee, K. (2023). Structural connection with predetermined discrete variable friction forces. *Resilient Cities and Structures*, 2(1), 1–17. Credits are distributed as follows: Kaixin Chen: Writing – original draft, Visualization, Validation, Software, Methodology, Investigation, Truss model analysis, Conceptualization. Georgios Tsampras: Writing – original draft, Supervision, Resources, Project administration, Methodology, Solid model analysis, Conceptualization. Kyoungyeon Lee: Writing – original draft, Visualization, Software, Methodology, Investigation, Numerical simulation of the core wall structure.

VITA

2015-2019 Bachelor of Engineering (Honours) in Civil Engineering (Structural Engineering), The Hong Kong Polytechnic University

2019-2021 Master of Science in Civil Engineering, Georgia Institute of Technology

2021-2026 Doctor of Philosophy in Structural Engineering, University of California San Diego

PUBLICATIONS

Chen, K., Tsampras, G., Chou, C., Lin, H., Wu, C., Córdova, A., Uang, C., & Chao, S. (2026). Low-cost friction-based force-limiting connection with reduced sensitivity to machining tolerances and accelerated repairability. *Earthquake Engineering & Structural Dynamics*, 55(6): 1270–1291.

Chen, K., Tsampras, G. (2025). Development and preliminary experimental characterization of a novel friction-based structural connection with predetermined discrete variable friction forces for high-performance earthquake- resistant buildings. In *19th World Conference on Seismic Isolation, Energy Dissipation and Active Vibration Control of Structures (19WCSI)*, Berkeley, CA, USA.

Chen, K., Tsampras, G., Cheruvalath, S., & Thundathil, M. (2025). Experimental characterization of mechanical and tribological properties of composite materials for friction-based force-limiting structural components. *Composites Part B: Engineering*, 112472.

Tsampras, G., Zabel, R., & Chen, K. (2025). Experimental investigation of edge distance effects on uplift response in OSB sheathing-to-framing nailed connections using digital image correlation. *Journal of Building Engineering*, 113348.

Chen, K., Tsampras, G., & Lee, K. (2023). Structural connection with predetermined discrete variable friction forces. *Resilient Cities and Structures*, 2(1), 1–17.

Chen, K., Tsampras, G., Lee, K., & Mayorga, C. F. (2022). Reusable force-limiting connection with variable friction force for high-performance buildings. In *8th Asia Conference on Earthquake Engineering (8ACEE)*, Taipei, Taiwan.

Lee, K., Chen, K., & Tsampras, G. (2022). Seismic response of core wall building with friction-based force-limiting connections. In *3rd European Conference on Earthquake Engineering & Seismology (3ECEES)*, Bucharest, Romania.

FIELDS OF STUDY

Major Field: Structural Engineering (Specialized in Earthquake Engineering)

ABSTRACT OF THE DISSERTATION

Friction-based Structural Components for Earthquake-Resistant Buildings

by

Kaixin Chen

Doctor of Philosophy in Structural Engineering

University of California San Diego, 2026

Professor Georgios Tsampras, Chair

Friction-based structural components have been developed and used in earthquake-resistant buildings for seismic response modification purposes. They can provide high initial stiffness, decoupled strength and stiffness, and energy dissipation, through relatively simple designs. If properly designed, they can be damage-free after earthquakes. However, their broader application requires further understanding at multiple levels. At the material level, the mechanical and tribological properties of composite friction materials remain insufficiently understood for earthquake structural engineering applications. At the component level, conventional friction-based components can be sensitive to machining tolerances, and friction shim inspection and replacement may require removal of external clamping parts, which can be time-consuming. In

addition, friction-based components typically have near-zero post-elastic stiffness, which may lead to excessive connection displacement demands in specific applications.

This dissertation investigates friction-based structural components through material-level experimental characterization and component-level development, testing, and assessment. At the material level, composite friction materials were characterized through tensile tests, bearing tests, bolt relaxation tests, and friction tests. The effects of material constituents, normal load, sliding velocity, displacement history, cumulative displacement, and dwell time were investigated. At the component level, two design concepts were studied. The first used initially loose steel washer plates in slotted-bolted friction-based components to reduce sensitivity to machining tolerances and to achieve accelerated repairability. The connection was evaluated through component-level tests and its implementation in a full-scale shaking table test of a three-story steel braced frame with sliding slabs. The second, termed the Modified Friction Device, was developed to generate predetermined discrete variable forces at target displacement levels. Its response was evaluated through reduced-scale and full-scale experimental testing.

The material-level results of this dissertation provide information for selecting composite friction materials for use in friction-based components for structural engineering applications. Friction-based components with loose-washer-plates design concept generated stable Coulomb-type force-displacement responses without enforcing tight machining tolerances and allowed rapid friction shim replacement. The Modified Friction Device developed the intended discrete variable friction force at predetermined displacement levels, and tests validated its kinematics and design parameters adjustability. Overall, this dissertation improves the understanding, design, and performance of friction-based components for use in earthquake-resistant structures.

Chapter 1

Introduction

1.1 Earthquake Impacts and Seismic Protection Systems

Earthquakes remain one of the most consequential natural hazards affecting the built environment. Strong ground shaking and associated hazards, such as earthquake-induced tsunamis, can damage buildings, bridges, transportation networks, lifeline infrastructure, and other systems that support the normal function of communities. The consequences of earthquakes are therefore not limited to physical damage to structures, but also include casualties, population displacement, interruption of essential services, loss of business operation, and long-term economic impacts. These impacts depend on the characteristics of the earthquake ground motion, the vulnerability of the built environment, the level of exposure, and the capacity of affected communities to respond and recover. Figure 1.1 summarizes historical earthquake impact data from 1900 to 2026 based on the NCEI/WDS Global Significant Earthquake Database [1]. Figure 1.1 (a) presents the annual and cumulative earthquake-related fatalities over this period. Among the 126 years considered, five years recorded annual fatalities greater than 100,000, and the major earthquakes associated with these peaks are also identified in the figure. Figure 1.1 (b) presents the annual and cumulative reported earthquake damage over the same period. Among the 126 years considered, three years recorded annual reported damage greater than 80,000 million US dollars, and the major earthquakes associated with these peaks are also identified in the figure. Overall, Figure 1.1 shows that major earthquakes have repeatedly produced severe social and

economic consequences. Mitigating earthquake-induced impacts therefore remains a central motivation for the structural engineering community.

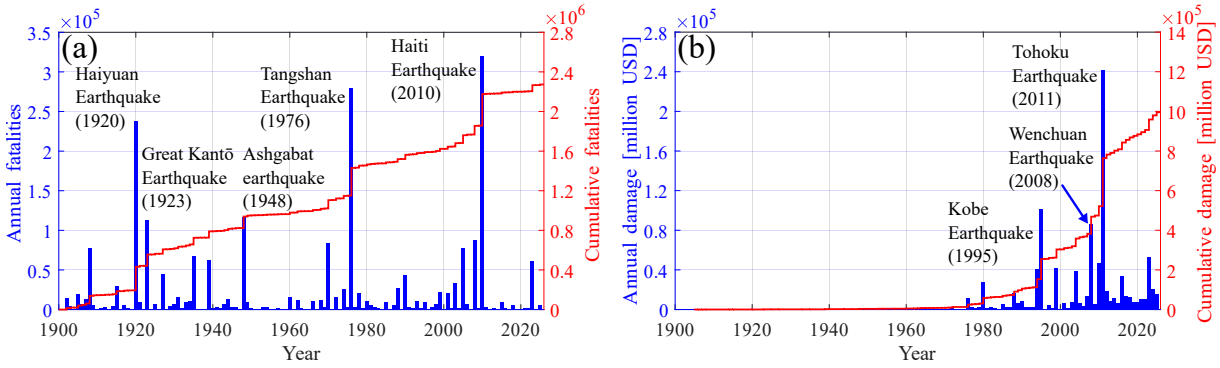

Figure 1.1. Historical earthquake impact data from the NCEI/WDS Global Significant Earthquake Database [1]: (a) earthquake-related fatalities data and (b) reported earthquake damage data

To mitigate earthquake-induced impacts, the structural engineering community has advanced seismic safety through multiple, complementary efforts. One important direction has been the improved characterization of seismic hazards and earthquake ground motions, which provides the basis for seismic hazard maps, design spectra, and site-specific seismic demands. In parallel, seismic design provisions have continued to evolve as new knowledge has been gained from earthquake reconnaissance, laboratory testing, analytical and numerical studies, and field observations. These provisions have supported the development of structural systems with improved seismic response. Design methodologies have also advanced from primarily force-based approaches toward frameworks that more explicitly consider structural performance. For example, capacity design principles are used to promote desirable inelastic mechanisms and to protect primary structural members, while performance-based design and assessment methods provide a more direct connection between earthquake demands, structural responses, damage, and potential consequences. In addition to new design, seismic evaluation and retrofit methods have been developed to reduce the vulnerability of existing buildings and infrastructure that were not designed according to current seismic provisions.

Another important direction in earthquake structural engineering has been the develop-

ment of seismic protection systems that are intended to improve the seismic response of structures during earthquake excitation. Rather than relying solely on the strength and ductility of primary structural members, these systems introduce additional mechanisms into the structural system to achieve improved response characteristics. As summarized by Christopoulos and Filiatrault [5] in Table 1.1, seismic protection systems can be broadly classified into supplemental damping systems and isolation systems. Supplemental damping systems can be further divided into passive structural control systems and semi-active or active structural control systems. Passive seismic response modification components include metallic-based components, viscous- and viscoelastic-based components, tuned-mass dampers, and friction-based components. Depending on the intended response, some of these components can also be combined with restoring mechanisms to achieve self-centering behavior. Within this broader family of passive seismic response modification components, this dissertation focuses on friction-based structural components as one specific type of seismic response modification component for earthquake-resistant structures.

Table 1.1. Seismic protection systems summarized by Christopoulos and Filiatrault [5]

Conventional Systems	**Supplemental Damping Systems**		**Isolation Systems**
	Passive Dampers	**Semi-Active/ Active Dampers**	
Flexural Plastic Hinges	Metallic	Braces	Elastomeric
Shear Plastic Hinges	Friction	Tuned-Mass	Lead-Rubber
Yielding Braces	Viscoelastic	Variable Stiffness	High-Damping Rubber
	Viscous	Variable Damping	Metallic
	Tuned-Mass	Piezoelectric	Lead-Extrusion
	Self-centering	Rheological	Friction Pendulum

1.2 Friction-Based Structural Components for Earthquake-Resistant Structures

Over the past five decades, friction-based structural components have been extensively developed by structural engineers and have been used in various structural applications for seismic

response modification purposes. The use of friction-based structural components in structural applications is commonly considered to be of two types: (1) between the superstructure and the foundation, friction pendulums have been used as base isolators, and (2) for superstructures, friction-based structural components have been designed as primary structural connections, for example, force-limiting connections between floors and walls [2], or as supplemental energy dissipation devices [6]. In both applications, they are strategically placed along the seismic load path and transfer seismic-induced forces through contact interfaces designed to slide at a predetermined friction force. The contact interface is referred to as the friction interface. When the seismic-induced force demand reaches the sliding friction force of the friction interface, the parts associated with the friction interface are expected to move relative to each other. As a result, the force transferred through the component is limited based on the sliding friction force generated at the friction interface. Energy dissipation is typically associated with the resulting cyclic force-displacement response. This dissertation focuses specifically on friction-based structural components for superstructure applications. Friction pendulums are mentioned for comparison purposes only and the detailed investigation of this system is beyond the scope of this dissertation.

1.2.1 Applications of Friction-Based Structural Components

Friction-based components have been used in various structural applications. Clark et al. [7] presented test results for a static load control friction device intended to limit the effect of differential settlement that occurs at foundations. Researchers also used friction devices for energy dissipation in various types of earthquake-resistant structures, such as bridge structures [8], precast concrete structures [9, 10, 11, 12, 13, 14, 15, 16, 17, 18, 19, 20, 21, 22, 23], wall pier coupling beams [24, 25], steel braced frames [26, 27, 28, 29, 30, 31, 32, 33, 34], steel moment resisting frames [35, 36, 37, 38, 39, 40, 41], self-centering moment resisting frames [42, 43, 44, 45, 46, 47], and rocking timber shear walls [48, 49, 50]. Friction dampers [51, 52, 53, 54, 55, 56, 57], negative stiffness friction dampers [58, 59], and self-centering braces

with friction-based energy dissipation [60, 61, 62, 63, 64] have been developed and tested, as well.

Proprietary friction-based structural components that have been used in both new building designs and retrofitting projects include: Pall Friction Dampers [65] and Quaketek [66] from Canada, Damptech from Denmark [67], Oiles [68] Wall-type Friction Damper from Japan, and Tectonus [69] from New Zealand.

1.2.2 Design Considerations of Friction-Based Structural Components

The short- and long-term force-displacement response of friction-based structural components depends on three considerations: (1) the materials used to establish the friction interfaces, (2) the design and manufacturing of the parts that form the friction-based structural component, and (3) the assembly of the parts into the friction-based structural component. Moreover, in long-term operation, the repairability of the friction-based structural component should be considered. This section discusses these design considerations and focuses specifically on the slotted-bolted configuration, which is one of the most commonly used configurations for friction-based structural components [57]. Figure 1.2 presents the schematic representation of an example slotted-bolted friction-based structural component. The example slotted-bolted friction-based structural component consists of two external clamping plates, two friction shims, one internal sliding plate, and six structural bolts and bolt assemblies (nuts and washers). Structural bolts and bolt assemblies clamp the clamping plates, friction shims, and the sliding plate together and provide the normal load acting on the friction interface between friction shims and the sliding plate. In a seismic event, the friction shims are expected to slide against the sliding plate and remain relatively static to the clamping plates. The component shown in Figure 1.2 was intended to be used as the floor-to-wall force-limiting connection in earthquake-resistant structures [70, 2, 3].

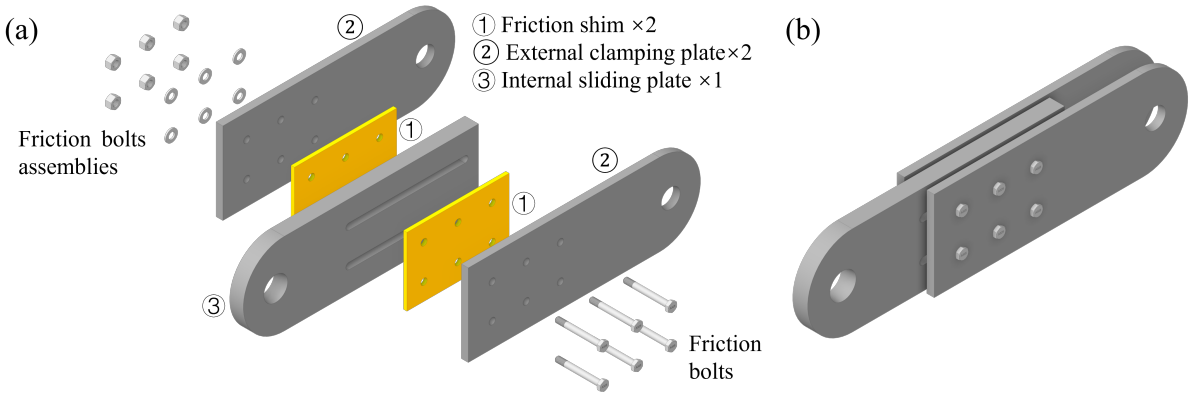

Figure 1.2. Schematic representation of an example slotted-bolted friction-based structural component: (a) Exploded view (b) Assembly

Friction Interface Materials

The response of a friction-based structural component depends on the friction force generated at the friction interface. Hence, the characterization and selection of materials that form the friction interface are important to ensure a desired response of the friction-based structural component. For friction pendulums, the source of the normal load acting on the friction interface comes from the self-weight of the superstructure. Therefore, a desired response of friction pendulums can be achieved by using material pairs with low coefficients of friction, for example, Teflon in contact with polished stainless steel [71], which provides a coefficient of friction of less than 0.2. For friction-based structural components in superstructures, the source of the normal load acting on the friction interface usually comes from prestressed components such as pretensioned structural bolts. The efficient design of friction-based structural components for superstructure applications requires material pairs that result in sliding interfaces with higher coefficients of friction. Otherwise, the number of prestressed components required to provide the normal load could be excessive and impractical to design.

Research has been conducted to characterize material pairs for friction interfaces of friction-based structural components for earthquake structural engineering applications. Bimetallic friction interfaces have been widely studied. FitzGerald et al. [31] applied steel-steel faying

surfaces in slotted-bolted connections for concentrically braced frames. Tremblay [33] tested faying surfaces of five types of materials and their combinations, including four types of steel-based alloys and one type of cobalt-based alloys. Grigorian et al. [34] tested low-carbon structural steel to low-carbon structural steel and low-carbon structural steel to brass friction interfaces. The experimental results [34] showed that low-carbon structural steel to brass friction interfaces generated relatively constant friction forces and thus were considered more suitable for earthquake structural engineering applications. Low-carbon structural steel to brass friction interfaces were also tested in [2] [43] [56] [72] [73] [74] for various earthquake structural engineering applications. Although in [75] it was shown that low-carbon structural steel to low-carbon structural steel friction interfaces generated friction forces having fairly large variations, solutions have been proposed, including treating the low-carbon structural steel plate surface with thermally sprayed aluminum [73] or using hardened abrasion-resistant steel such as Bisalloy [72] [76], to improve the response of steel-steel friction interfaces. Other bimetallic friction interfaces that have been characterized for earthquake structural engineering applications include: low-carbon steel to titanium [56]; low-carbon steel to brown copper [77]; stainless steel and alloy cast steel to leaded bronze [78]; and low-carbon steel to aluminum [72] [74].

The main challenge of using bimetallic friction interfaces is galvanic corrosion induced at the friction interface from the contact between dissimilar metals. For bimetallic friction interfaces, galvanic corrosion generates rust in long-term operation and alters the properties of the friction interface. Chan and Tang's experiment [79] showed that compared with a rust-free polished condition, the coefficient of friction of a bimetallic friction interface with rust can be reduced by 50%. Another challenge associated with bimetallic friction interfaces, as discussed in ASCE/SEI 7-22 Commentary C18.2.4.1 [80], is that the coefficient of friction may increase substantially over time due to cold welding at the friction interface. Because of galvanic corrosion and cold welding at the friction interface, ASCE/SEI 7-22 Commentary C18.2.4.1 made the following statement: "*all bimetallic interfaces result in significant changes in friction force over time that are not possible to predict, and therefore, these types of interfaces should not be used.*".

Hence, if bi-metallic friction interfaces are used, their long-term performance should be further evaluated.

Composite-metallic friction interfaces are considered alternatives to bimetallic friction interfaces because they are less vulnerable to galvanic corrosion problems. The characterization of composite-metallic friction interfaces has been conducted for various earthquake structural engineering applications. Lie [81] used composite-metallic friction interfaces in earthquake energy absorbers. Three types of composites (Ferrobestos: DM1, DM6, and AS10) were tested, and the metallic surface was made of stainless steel. All the tested composite materials were manufactured by Hardie-Ferodo Pty. Limited. According to Lie [81]: DM1 was "*a rigid molded non-metallic material with a random fiber asbestos base*"; DM6 was "*a rigid molded friction material with a random fiber asbestos base and having a metallic inclusion in the form of brass chippings*"; AS10 was "*a semi-rigid, solid woven, asbestos-based friction material with a brass wire content*". Testing parameters in this study included the normal load level, loading frequencies, and the working temperature of the energy absorber (room temperature vs. freezing temperature). Lie [81] reported that the composite-metallic friction interfaces had satisfactory and consistent responses within the range of normal load levels and loading frequencies that were tested, at both room and freezing temperatures.

Tyler [51] tested a friction damper with the composite to bright-drawn mild steel friction interface and the composite material was supplied by Don Agencies in New Zealand and was a type of brake lining. The constituents of this material were not reported. Testing parameters in this study included the normal load level, sliding velocities, and number of loading cycles. Tyler [51] concluded that the composite-metallic friction interface tested in this study had a fairly large difference between the static and dynamic coefficients of friction, and hence it required further investigation. In addition, a loss of friction force of 20% was observed after 20 cycles of loading, and the loss was attributed to the wear of the brake lining material.

Chi and Uang [56] tested the composite (AFT200) to low-carbon structural steel friction interface for a slotted-bolted connection. The composite material AFT200 was manufactured by

Champion Friction Technologies. It was phenolic-treated and consisted of brass wire-inserted cloth. Eight test runs were completed. Chi and Uang [56] concluded that the composite-metallic friction interface tested in this study exhibited satisfactory and repeatable performance and outperformed other bimetallic friction interfaces tested in the same study.

Kim and Christopoulos [45] [82] tested six composite-metallic friction interfaces for use in friction-damped posttensioned self-centering steel moment-resisting frames. The combinations of three types of composites (NF-916, NF-780, and NF-336) and two types of metallic materials (mild steel and stainless steel) were considered. The three types of composite materials were manufactured by Carlisle Brake & Friction. Those materials were reported to be non-asbestos organic (NAO) materials while the constituents of the materials were not reported. Testing parameters in this study included the normal load level, loading frequencies, sliding histories, and the configuration of the tested connection (one bolt vs. two bolts). The experimental testing results showed that the friction interfaces with the composite material NF-916 exhibited a stable and repeatable frictional behavior, and therefore Kim and Christopoulos [45] [82] suggested using the NF-916 to stainless steel friction interface for the beam-column connection proposed in their study.

Golondrino et al. [39] tested the composite (D3923) to low-carbon structural steel friction interface for asymmetrical friction connections. The composite material D3923 was manufactured by Ferotec Friction. The constituents of this material were not reported. Testing parameters were loading frequencies, and moreover, three configurations of the composite material pad were considered. Experimental results showed that the friction interface between the composite (D3923) and the low-carbon structural steel led to effectively constant friction force during sliding. The connection tested exhibited degradations in the sliding friction force of more than 5% and the degradation was attributed to loss of bolt tension due to wear of the composite material (D3923).

Latour et al. [73] tested three composite-metallic friction interfaces for supplemental damping devices. The composite materials were three types of rubber materials (named M0,

M1, and M2 in the study) and the metallic surface was made of low-carbon structural steel. According to Latour et al. [73]: the material M0 was "*a non-asbestos friction material used for standard braking application*" and was "*a blend of mineral and organic fibers aggregated by means of phenolic resin*"; the material M1 was "*a black flexible material with metallic particles*" and it consisted of "*blending mineral, steel and synthetic fiber, nitrilic rubbers and phenolic resin*"; the material M2 was "*a black hard and stiff material composed by a blending mineral and synthetic fiber, nitrilic rubbers and phenolic resin*". Testing parameters in this study included the normal load level and the number of loading cycles. In addition, this study tested two types of bolt washers, i.e., circular flat steel washers and packets of steel disc springs. Out of the three composite materials tested, Latour et al. [73] concluded that Material M0 exhibited a very stable behavior even under a high level of normal load; Material M1 exhibited pinching behavior, a low friction coefficient and rapid degradations; and Material M2 exhibited a very stable behavior but the coefficient of friction was quite low. Latour et al. [73] considered Material M0 suitable for their applications.

Tsampras et al. [2] [4] characterized three composite-metallic friction interfaces for use in force-limiting connections between floors and seismic force resisting building systems. The composite materials tested were AFT200, RF42, and Gatke 398, and the metallic surface was made of low-carbon structural steel. The composite material AFT200 was the same as what was tested in Chi and Uang [56]. RF42 was manufactured by Scan-Pac Manufacturing Inc. and was reported to be a "*rigid molded non-asbestos, non-metallic friction material*". The constituents of RF42 were not reported. Gatke 398 was manufactured by Scan-Pac Manufacturing Inc. It consisted of glass reinforcing fibers, lubricants including graphite, Teflon and molybdenum disulfide MoS_2, and phenolic resin as the binder. Testing parameters in this study included the normal load level, loading frequencies, sliding velocities, velocity profiles (earthquake vs. sinusoidal), and sliding histories. The responses of friction devices manufactured with different machining tolerances were also compared. Tsampras et al. [2] observed that due to the break-in effect, the coefficient of friction of the composite-metallic friction interface at the beginning of

sliding increased when the cumulative displacement increased. In the test of the composite (Gatke 398) to low-carbon structural steel friction interface, the sliding force exhibited an increase in tests with fairly low sliding velocities and a decrease in dynamic tests. Tsampras et al. [2] used Bowden and Tabor's adhesive friction theory [83] to explain the observed velocity-dependent sliding force variation. Although dwell time was not listed as a testing parameter, Tsampras et al. [2] observed that dwell time between tests permitted rejuvenation of the friction interface, characterized by an increase in the sliding force. Tsampras et al. [2] [4] also reported that there was no correlation between the temperature variation and the sliding force variation. The tested composite (Gatke 398) to low-carbon structural steel friction interface was considered suitable for applications in floor-to-wall force-limiting connections [2].

Li et al. [84] tested four composite-metallic friction interfaces. The combinations of two types of composites (non-asbestos organic (NAO) NAO780, and Polytetrafluoroethylene (PTFE)) and two types of metallic materials (mill steel and stainless steel) were considered. The composite material NAO780 appeared to be the same as the NF-780 material tested in [45] [82]. The PTFE material was manufactured by Chemours, and according to Li et al. [84], it was *a fluorocarbon solid with a high-molecular-weight compound consisting wholly of carbon and fluorine*. Testing parameters in this study included the normal load level, loading frequencies, and sliding velocities. Experimental results showed that NAO-steel friction interfaces exhibited higher coefficients of friction, while PTFE-steel friction interfaces exhibited more stable frictional behavior.

Paronesso and Lignos [85] characterized five composite-metallic friction interfaces for sliding friction dampers using the design of the friction-based force-limiting connections proposed by Tsampras et al. [2]. The composite materials were named M1, M2, M3, M4, and M5 in the study and the metallic surface was made of low-carbon structural steel. The materials were reported to be "composed of fibers and organic and inorganic fillers bonded together by phenolic resins". Testing parameters in this study included the normal load level, loading frequencies, sliding velocities, velocity profiles, and sliding histories. Paronesso and Lignos [85] suggested

that materials M1 and M4 were more suitable for use in friction dampers because they exhibited fairly invariant coefficients of friction under different levels of normal pressure and at different sliding velocities. Materials M2 and M3 induced a significant loss of bolt pretension, and the loss was attributed to the processing of these two materials. The material M3 also exhibited a normal pressure-dependent coefficient of friction. The material M5 was not recommended due to its high wear rate and the observed failure of the friction shim during the test. Paronesso and Lignos [85] also reported that for earthquake structural engineering applications, the coefficients of friction of materials M1 and M4 can be practically assumed to be temperature independent.

Similar to Li et al. [84], Gao et al. [86] tested two composite-metallic friction interfaces, considering two types of composite materials, NAO and PTFE, and the metallic surface was made of low-carbon structural steel. The constituents of the tested materials were not reported. Testing parameters in this study included the normal load level, loading frequencies, sliding velocities, and sliding histories. Gao et al. [86] considered four configurations of the test setup for improved connection performance. Gao et al. [86] observed that both NAO-steel and PTFE-steel friction interfaces exhibited velocity-dependent frictional behavior and that the coefficients of friction for both friction interfaces under high-speed loading were reported to be ”significantly greater” than those under low-speed loading. Similar to Tyler [51] a difference between static and dynamic coefficients of friction was observed in this study [86] and the difference was reported to be less than 10% with the increase of loading frequencies. The reusability of the friction interfaces was also assessed in this study.

In summary, the following parameters are typically considered in characterizing the response of composite-metallic friction interfaces for earthquake structural engineering applications: the normal load level, loading frequencies, sliding velocities, sliding histories, velocity profiles, and parameters related to the friction-based component itself, including configurations and machining parameters. Although temperature has been considered an important parameter for other tribological applications such as automotive applications [87], it is not considered as important for composite to low-carbon structural steel friction interfaces used in friction-based

structural components for earthquake structural engineering applications [2] [85].

Force and Displacement Capacities

An advantage of friction-based structural components is that their force and displacement capacities can be adjusted easily according to design targets. In practice, Coulomb's friction equation [88] is typically used to calculate the force generated by a friction-based structural component. From Coulomb's friction equation $f = \mu N$, where f is the friction force, μ is the coefficient of friction, and N is the normal load acting on the friction interface, it can be observed that the force capacity of friction-based structural components can be adjusted by selecting the material pair used for the friction interface (i.e., adjusting μ) or adjusting the normal load acting on the friction interface (i.e., adjusting N). For friction-based components for superstructural applications such as the example shown in Figure 1.2, the normal load acting on the friction interface is typically applied through the pretension of the structural bolts and could be adjusted by changing the number of the structural bolts or the pretension level of the structural bolts.

The displacement capacity of friction-based structural components can be adjusted by modifying the design of their parts. For example, for the slotted-bolted friction-based structural component in Figure 1.2, its displacement capacity can be increased simply by increasing the length of slots on the internal sliding plate. This eliminates the strain limitation of materials which is typically a design constraint for metallic-based seismic response modification structural components such as buckling-restrained braces (BRBs) [89] and shape memory alloy (SMA) based components [90].

Decoupled Elastic Axial Stiffness and Sliding Friction Force

Ideally, friction-based structural components have an elastic-perfectly plastic force-displacement response. The elastic stiffness is effectively independent of the friction force during sliding. Figure 1.3 (a) shows the force-displacement response of an example slotted-bolted friction-based structural component [2]. The component developed two significantly

different force levels while the difference between the elastic axial stiffness was effectively small (for the low normal load and the high normal load cases, the experimentally computed elastic stiffness were 1809 kN/mm and 2245 kN/mm, respectively). The sliding friction force was increased simply by increasing the normal load acting on the friction interface by the bolts. The decoupled elastic axial stiffness and sliding friction force provide structural engineers with enhanced flexibility in practical design.

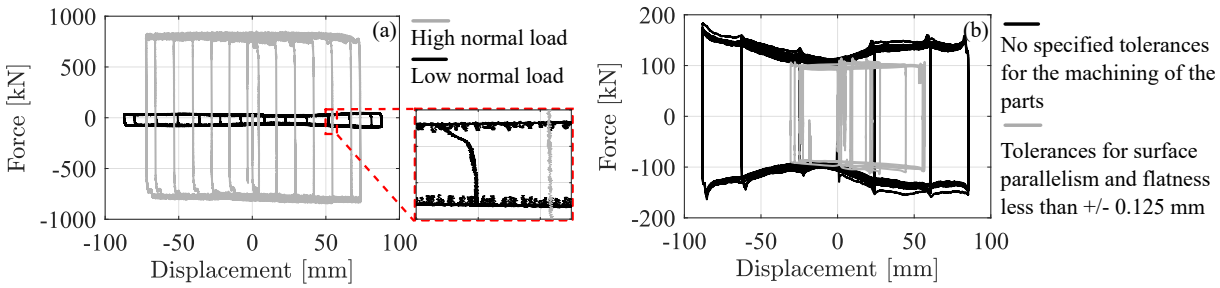

Figure 1.3. (a) High axial stiffness with two significantly different sliding force levels using the same friction-based structural component (b) Geometric tolerances used to machine the friction-based structural component may contribute to an uncontrolled variation of the sliding friction force.

Geometric Tolerances

The geometric tolerances associated with the machining of the parts that form the friction-based structural component can contribute to the variation of the sliding friction force beyond the designed sliding friction force. Figure 1.3 (b) shows the force-displacement response of two friction-based structural components designed to develop a sliding friction force of 100 kN. The friction-based structural component designed with enforced geometric tolerances less than +/-0.125 mm was able to develop a relatively constant friction force during sliding. The low geometric tolerances ensured the flatness and parallelism of the surfaces associated with the friction interfaces and the slots. In contrast, the friction-based structural component designed without specified geometric tolerances developed an uncontrolled displacement-dependent variable friction force during sliding. The reason is the following. When the slots are not parallel within a tolerance, as the displacement increases, the shanks of the bolts that pass through

the slots come into contact with the internal surface of the slots. Additional friction force is developed due to the contact force between the bolt shanks and the internal surface of the slot [2]. In addition, the contact force could result in bending of the bolt. Due to bolt bending, the axial strain in the bolt increases, which as a result increases the axial load of the bolt. The increased bolt load increases the friction force during sliding compared to the designed sliding friction force. Note that although the uncontrolled variable friction force could be mitigated through enforced geometric tolerances, extra time and cost might be required during the machining process of the parts.

Post-elastic Stiffness

The schematic representation of the force-displacement response of a friction-based component is presented in Figure 1.4 (a). If not specially engineered, friction-based structural components typically have a very low, or near zero post-elastic stiffness. This is due to the characteristics of the sliding friction mechanism. A low post-elastic stiffness may lead to increased connection displacement demands. When using friction-based structural components as supplemental energy dissipation devices, this is typically not a concern. However, when designing friction-based structural components as primary structural connections such as force-limiting connections between structural systems, an excessive connection displacement may lead to pounding between structural systems and this may result in uncontrolled transfer of forces. Rubber bearings have been used in previously developed practical friction-based force-limiting connections for planar seismic force-resisting systems [2, 3, 91], as presented in Figure 1.4 (b), for dual purposes: (1) to stabilize the planar seismic force-resisting systems in the out-of-plane direction and (2) to increase the post-elastic stiffness of the connection so that excessive connection deformation demands can be prevented. The schematic representation of the force-displacement response of the friction-based force-limiting connection presented in Figure 1.4 (b), combining friction-based components and rubber bearings, is presented in Figure 1.4 (c).

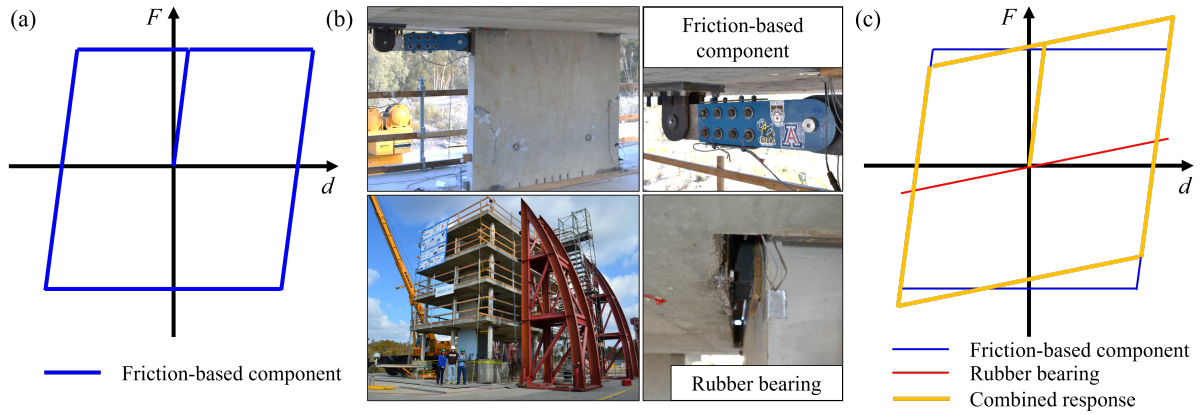

Figure 1.4. (a) Schematic representation of the force-displacement response of a friction-based component. (b) Friction-based force-limiting connections (friction-based components + rubber bearings) in a building with planar rocking walls [2, 3] (c) Schematic representation of the force-displacement response of the friction-based force-limiting connection in (b)

Although force-limiting connections with friction-based components plus rubber bearings have been proved feasible and practical for planar seismic force-resisting systems, this design concept may not be adopted in other structural systems where rubber bearings may not be used due to different three-dimensional kinematic constraints (details to be discussed in Chapter 4). This limitation reveals a need for a friction-based component that can develop predetermined friction forces at target design displacement levels, which resembles a step-like force-displacement response, with the goal of limiting the force and acceleration responses without inducing excessive displacement demand in the connections.

Potential Damage Limit States of Friction-Based Structural Components with Composite Friction Materials

Friction-based structural components can be essentially damage-free and immediately reusable after earthquakes; however, this requires the parts of the friction-based structural component to be designed against limit states that could potentially lead to mechanical failure. For a friction-based structural component having composite-metallic friction interfaces, the limit states of the metallic parts, which are typically made of structural steel, can be identified through structural analysis and can be designed against using the AISC Steel Construction Manual [92]

as a reference. The limit states of friction shims made of composite friction materials should also be considered.

Past studies listed in Section 1.2.2 focused primarily on the tribological properties of the composite-metallic friction interface. Although discussions about the mechanical properties of composite materials were limited in those studies, damages of composite material friction shims were observed in previous experimental tests of friction-based structural components with composite-metallic friction interfaces [2, 4, 85, 93]. Figure 1.5 shows photos of example damaged friction shims made of the composite material RF42 from previous experimental tests [4].

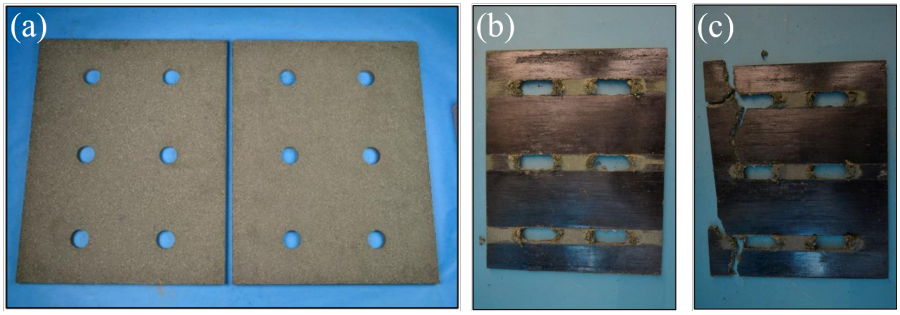

Figure 1.5. Photos of RF42 friction shims from [4]: (a) friction shims before the test, (b) damaged friction shim with elongated bolt holes, and (c) damaged friction shim with elongated bolt holes associated with net section tensile failure

In [2, 4, 85, 93], damages of composite material friction shims were due to the bearing action between friction shims and pretensioned structural bolts. Figures 1.6 explains the mechanics of this bearing action, using the friction-based component in Figure 1.2 as an example. Figure 1.6 (a) shows the ideal load path of the example slotted-bolted friction-based structural component in Figure 1.2. For this component, the total normal load provided by six structural bolts and bolt assemblies is termed N. The coefficient of friction between the friction shims and the clamping plates is termed μ_1. The coefficient of friction between the friction shims and the sliding plate is termed μ_2. According to the Coulomb's friction equation [88], a friction force $f = 2\mu_2 N$ is generated by this component. In an ideal situation, assuming that the clamping

plates and the sliding plate are made of the same material, and without considering the break-in effect, μ_1 is equal to μ_2. For the friction shim, the friction force generated between the surface in contact with the clamping plate is equal to the friction force generated between the surface in contact with the sliding plate. The friction shim is thus under pure in-plane shear in the direction of sliding.

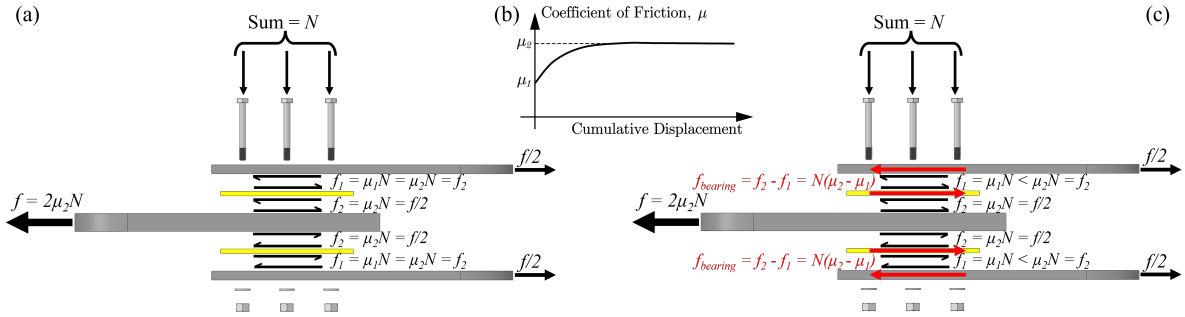

Figure 1.6. (a) Ideal load path of the example slotted-bolted friction-based structural component in Figure 1.2 (b) A schematic representation of the break-in effect reported in [2] (c) Load path of the example slotted-bolted friction-based structural component considering the break-in effect

In practice, the break-in effect of the friction interface will affect the load path of the slotted-bolted friction-based structural component. Figure 1.6 (b) shows a schematic pattern of the break-in effect that has been observed in past experimental tests [2], represented by an increase in the coefficient of friction from μ_1 to μ_2 given an increase in the cumulative displacement of the friction interface. As aforementioned, for the example slotted-bolted friction-based structural component in a seismic event, the friction shims are expected to slide against the sliding plate and remain relatively static to the clamping plates. Therefore, the cumulative displacement of the friction interface between the friction shim and the sliding plate is larger than the cumulative displacement of the friction interface between the friction shim and the clamping plate. Because of the break-in effect as illustrated in Figure 1.6 (b), as the cumulative displacement increases, the coefficient of friction between the friction shims and the sliding plate μ_2 will become larger than the coefficient of friction between the friction shims and the clamping plates μ_1. Figure 1.6 (c) shows the load path of the example slotted-bolted friction-

based structural component considering the break-in effect. The difference between the friction forces on top and bottom surfaces of the friction shim is balanced by the bearing action between the structural bolts and the friction shim. The magnitude of the bearing force can be computed as:

$$f_{bearing} = \mu_2 N - \mu_1 N = N(\mu_2 - \mu_1) \tag{1.1}$$

If the friction shims were not designed against the bearing action, the bearing action could result in elongation of the bolt hole or net section tensile failure of the friction shims as observed in [2] [4] [85] [93]. Even though the damage due to the bearing action could be prevented by using thicker friction shims [2] or by modifying the configuration of the friction-based component [82] [84] [86], it is still important to characterize the tensile and bearing strengths of the composite materials so that the bearing action could be designed against.

Note that although designing against limit states associated with the mechanical failure of friction shims is important, friction-based structural components can be designed to be damage tolerant in case that damage to the friction shims occurs. Figure 1.7 presents the experimental testing result of a slotted-bolted friction-based structural component, in which the friction shim was made of the composite material RF42 [4, 94], same as shown in Figure 1.5. In this test, net section tensile failure of the friction shim was observed, as shown in Figure 1.7 (a). Despite the occurrence of net section tensile failure of the friction shim, the friction-based structural component maintained a relatively stable force-displacement response, as presented in Figure 1.7 (b). Following the net section tensile failure of the friction shim, no significant reduction in the force resistance was observed. The testing series continued after the net section tensile failure of the friction shim. Figure 1.7 (c) presents the force-displacement response in the tenth test following the net section tensile failure of the friction shim. It can be observed that the force-displacement response remained overall stable. High-frequency oscillations observed in the force response were mainly attributed to an issue associated with the actuators' hydraulic power supply [4].

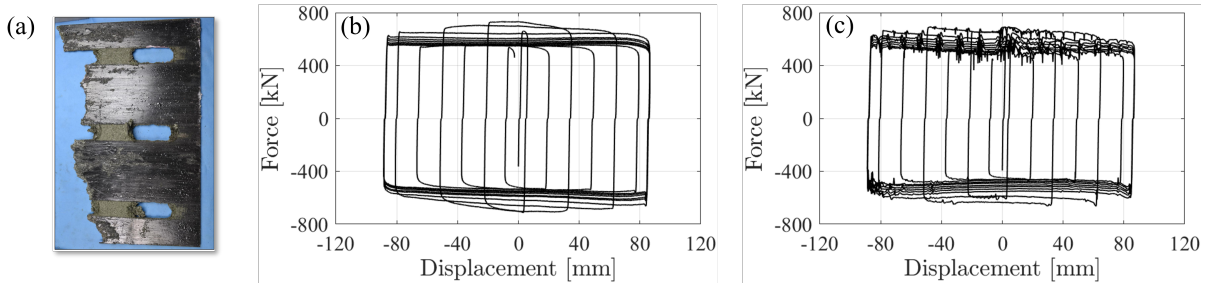

Figure 1.7. (a) Fractured RF42 friction shim (b) The force-displacement response of the friction-based component in the test when the fracture of the friction shim first occurred (c) The force-displacement response of the component in the tenth test following the fracture of the friction shim

Reliability of Normal Load

As previously discussed, the sliding friction force of a friction-based structural component depends on the normal load acting on the friction interface. Therefore, the reliability of the normal load acting on the friction interface should be considered both at the instant when the normal load is applied and during long-term operation.

In laboratory testing of friction-based structural components, the normal load provided by pretensioned structural bolts can be monitored using through-hole bolt load cells, bolts instrumented with inserted strain gauges, or ultrasonic bolt tension monitors; therefore, the applied normal load can be well monitored and controlled. In practice, the calibrated wrench method [95] can be used for a relatively accurate normal load estimate. Note that when using the calibrated wrench method, the relative parallelism between the parts associated with the friction interface should be considered. Figure 1.8 presents a schematic demonstration of the effect of non-parallel plates on applying the normal load. Figure 1.8 (a) represents the initial state of a schematic bolted assembly fixed at both ends, where the parts are not perfectly parallel due to a non-flat plate. Figure 1.8 (b) represents the final state of this bolted assembly. A tightening torque of T is applied to the bolt, resulting in a bolt load of $N = N_b$. In practice, the required tightening torque T for an anticipated bolt pretension N_b is typically calibrated on site [95]. The state of Figure 1.8 (b) can be considered as the superposition of the states of Figure 1.8 (c) and

(d). The total bolt load $N = N_b$ consists of two components: the normal load $N = N_f$ required to flatten the non-parallel plate and the normal load $N = N_a$ effectively acting on the friction interface. It can be observed that, when applying a tightening torque of T to the bolt, if the parts associated with the friction interface are not parallel, the actual normal load effectively acting on the friction interface, i.e., N_a, could be lower than the anticipated normal load, i.e., N_b. The difference between N_a and N_b may be significant in the case of thick and short plates with relatively high out-of-plane flexural stiffness.

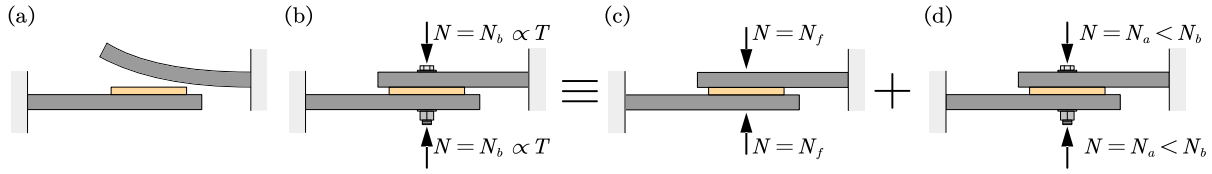

Figure 1.8. Schematic demonstration of the effect of non-parallel plates on applying the normal load. (a) Initial state of the bolted assembly with a non-flat plate. (b) Final state of the bolted assembly with an applied bolt load $N = N_b$ given an applied tightening torque T ($N_b \propto T$); (b) can be considered as the superposition of (c) and (d). (c) A normal load $N = N_f$ is required to flatten the non-parallel plate. (d) The actual normal load $N = N_a$ acting on the friction interface is effectively smaller than N_b.

In long-term operation and considering that a friction-based structural component is primarily at rest, the loss of normal load is mainly attributed to the creep-induced through-thickness deformation of clamped parts. The loss of normal load could induce a reduction in the friction force that a friction-based structural component could generate and therefore should be assessed. Figure 1.9 presents a schematic demonstration of the variation of the bolt load in a bolted assembly in long-term operation. Figure 1.9 (a)–(c) presents a simplified model of a bolted assembly. The bolt is idealized as a spring, and the clamped parts are idealized as a spring and a dashpot connected in series [96]. Figure 1.9 (a) represents the initial state of the bolted assembly when the bolt is not pretensioned. From Figure 1.9 (a) to Figure 1.9 (b), the bolt is pretensioned to a bolt load of P_i. The pretensioning of the bolt results in an elongation of δ_b^i in the bolt and a through-thickness compressive deformation of δ_p^i in the clamped parts. In this state, the kinematic compatibility between the bolt and the clamped parts in the through-thickness

direction can be assumed to be satisfied. Figure 1.9 (c) represents the state of the bolted assembly in long-term operation, where a through-thickness deformation of ΔD_c is further induced, which results in the shortening of the bolt and an increased through-thickness compressive deformation of the clamped parts. Figure 1.9 (d) presents the force-deformation diagram [96] of the bolted assembly. In Figure 1.9 (d), K_b represents the axial stiffness of the bolt-washer assembly. K_p^i and K_p^o represent the through-thickness compressive stiffness of the clamped parts before and after the long-term through-thickness deformation ΔD_c occurs. It can be observed that with the long-term through-thickness deformation ΔD_c, the bolt load drops from P_i to P_o. The bolt load loss can be written as $\Delta P = P_i - P_o = K_b \Delta D_c$. In friction-based structural components, this mechanism is related to the loss of the normal load acting on the friction interface in long-term operation.

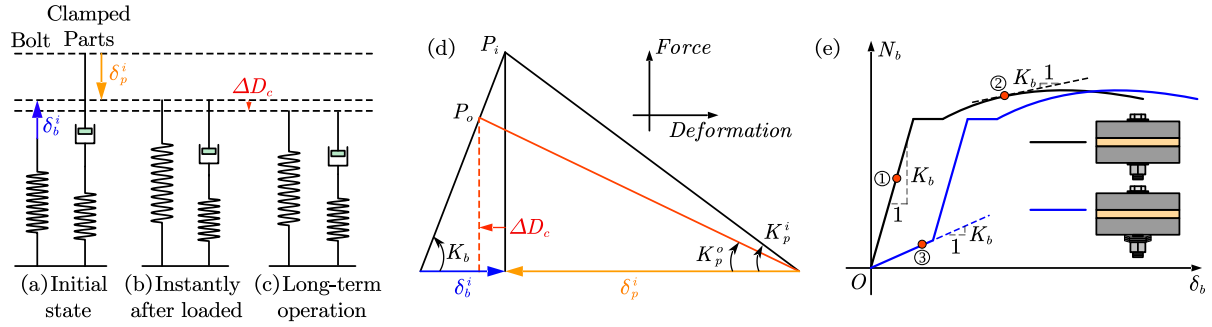

Figure 1.9. Schematic demonstration of long-term bolt relaxation in a bolted assembly. (a) The initial state of a simplified model of a bolted assembly (b) The state of the bolted assembly instantly after the pretensioning of the bolt (c) The state of the bolted assembly in long-term operation (d) Schematic force-deformation diagram of the bolted assembly (e) Schematic force (N_b)-deformation(δ_b) response of the bolt-washer assembly

As described earlier, the long-term through-thickness deformation ΔD_c primarily depends on the through-thickness creep behavior of the clamped parts. ΔD_c can be assessed and predicted but cannot be fully avoided [97, 98, 99, 100]. Past relaxation tests of bolted joints [98, 99] showed that compared with metallic bolted joints, such as steel or aluminum bolted joints, composite bolted joints exhibited an increased percentage of bolt load loss over time. This was attributed to the fact that the viscoelastic characteristics of composite materials exacerbated

the creep behavior of the material in the through-thickness direction and resulted in increased through-thickness deformation. Although the loss of preload due to material creep is an important phenomenon for friction-based structural components with composite-metallic friction interfaces, it has barely been investigated in past studies listed in Section 1.2.2. Tsampras et al. [2] put the friction-based structural component used in their study with the composite (Gatke 398) to low-carbon structural steel friction interface at rest for 11 months and retested the component. A 15% loss of the sliding force was observed, and the loss of the sliding force was attributed to loss of bolt pretension due to the creep-induced through-thickness deformation of clamped parts. Tsampras et al. [2] also retightened the bolts that provided the normal load to the original target normal load level, and the sliding force of the component after bolt retightening was similar to the original target sliding force. For characterization and selection of composite materials for composite-metallic friction interfaces for friction-based structural components, relaxation tests are required to assess the through-thickness creep behavior of the composite material. Composite materials that would induce excessive loss of preload due to their through-thickness creep behavior should not be recommended for use in composite-metallic friction interfaces for friction-based structural components.

From the expression of ΔP and considering the same amount of ΔD_c, it can also be observed that one way to mitigate the bolt load loss, i.e., to reduce ΔP, due to ΔD_c is to increase the axial flexibility, i.e., to reduce K_b, of the bolt-washer assembly. Bolted assemblies with Belleville washers or disc springs, as represented by marker ③ in Figure 1.9 (e), have been used in friction-based structural components to mitigate the bolt load loss due to ΔD_c in past research [101, 41, 73, 102, 103]. One shortcoming of using Belleville washers is that since the flat load of Belleville washers is relatively low, when having an application where a relatively large sliding friction force capacity is required, the designer will have to increase the number of bolts or stack the Belleville washers to meet the normal load demand. This could increase the cost of the friction-based structural component and sometimes make the design impractical. Another alternative is to use bolt-washer assemblies with flat washers and pretension the bolt

to a bolt load larger than its yield strength [2]. From Figure 1.9 (e), it can be observed that by pretensioning the bolt to a bolt load above its yield strength, i.e., from marker ① to ②, the stiffness of the bolt-washer assembly K_b can be effectively reduced. This method is considered more suitable for applications where a relatively large normal load demand is to be met.

Inspection and Repairing in Long-term Operation

As discussed in Section 1.2.2, when properly designed, friction-based structural components can be essentially damage-free and immediately reusable after earthquakes. However, in long-term operation particularly after seismic events, the friction shims of the friction-based structural component might require inspection and replacement if mechanical failure occurs or if excessive surface wear is observed. For the slotted-bolted friction-based structural component in Figure 1.2, the inspection and replacement of the friction shims require the external clamping plate of the component to be removed, which can be practically challenging if the friction-based component has been installed in the structure. Therefore, it is beneficial to have a configuration of the friction-based structural component that allows a quicker inspection and repairing process. A quick inspection and repairing of the friction-based structural component potentially enhances the practicality of the connection in real applications and supports the long-term functionality of earthquake-resistant buildings equipped with it.

1.2.3 Research Gaps in Friction-Based Structural Components

Based on the state-of-the-art and state-of-the-practice reviewed in the previous sections, the research gaps associated with friction-based structural components can be identified and grouped into material-level and component-level research gaps. The material-level research gaps are mainly associated with the characterization and selection of friction interface materials, especially composite friction materials used in composite-metallic friction interfaces. The component-level research gaps are mainly associated with the practical implementation and design considerations of friction-based structural components.

At the material level, although composite-metallic friction interfaces have been characterized in previous studies, most studies focused primarily on the tribological properties of the friction interface. Discussions about the mechanical properties of composite friction materials were limited, even though damage of composite material friction shims was observed in previous experimental tests of friction-based structural components. As previously demonstrated, these damages were mainly associated with bearing action between friction shims and pretensioned structural bolts, which could result in elongation of bolt holes, bearing failure, or net section tensile failure if the friction shims were not designed against it. Therefore, the tensile and bearing strengths of composite friction materials should be characterized so that the relevant limit states can be considered during the practical design.

The long-term behavior of composite friction materials also remains insufficiently understood for friction-based structural components. Since the sliding friction force depends on the normal load acting on the friction interface, loss of preload due to creep-induced through-thickness deformation of clamped composite materials can reduce the sliding friction force that the component can generate. Past relaxation tests of bolted joints showed that composite bolted joints could exhibit an increased percentage of bolt load loss compared with metallic bolted joints. However, the loss of preload due to material creep has barely been investigated for composite friction materials used in friction-based structural components. Therefore, relaxation tests are needed to assess the through-thickness creep behavior of composite friction materials and to support the selection of materials for composite-metallic friction interfaces. In addition, the constituents and manufacturing process of composite friction materials should be considered when interpreting their mechanical and tribological properties.

At the component level, the response and practicality of friction-based structural components can be affected by the design, manufacturing, assembly, and repairability of the parts that form the component. For slotted-bolted friction-based structural components, geometric tolerances associated with the machined parts can contribute to variations of the sliding friction force beyond the designed sliding friction force. Although this issue can be mitigated through

enforced geometric tolerances, extra time and cost may be required during the machining process. In addition, conventional slotted-bolted configurations may require partial disassembly for inspection and replacement of friction shims, which can be practically challenging after the component has been installed in a structure. These issues indicate the need for component configurations that reduce sensitivity to machining tolerances and allow quicker inspection and repair in long-term operation.

Another component-level research gap is associated with the post-elastic stiffness of friction-based structural components. If not specially engineered, friction-based structural components typically have very low, or near-zero, post-elastic stiffness because of the characteristics of the sliding friction mechanism. This may lead to excessive connection displacement demands when friction-based structural components are used as primary structural connections, such as force-limiting connections between structural systems. Rubber bearings have been used in previously developed force-limiting connections for planar seismic force-resisting systems to provide post-elastic stiffness. However, this design concept may not be adopted in other structural systems where rubber bearings may not be used due to different three-dimensional kinematic constraints. This limitation reveals a need for friction-based components that can develop predetermined friction forces at target design displacement levels, with the goal of limiting the force and acceleration responses without inducing excessive displacement demand in the connections.

These research gaps motivate the material-level and component-level studies presented in this dissertation. At the material level, this dissertation characterizes the mechanical properties, tribological properties, and through-thickness creep behavior of selected composite friction materials for composite-metallic friction interfaces. At the component level, this dissertation develops and experimentally characterizes friction-based structural components that are intended to reduce sensitivity to machining tolerances, improve inspection and repair procedures, and achieve intended force-displacement responses under cyclic loading.

1.3 Research Objectives and Dissertation Organization

The overarching objective of this dissertation is to improve the understanding, design, and performance of friction-based structural components in both short- and long-term operation, and ultimately to democratize and advance their applications in earthquake-resistant buildings. This objective is addressed through material-level and component-level experimental studies. At the material level, this dissertation characterizes selected composite friction materials and composite-metallic friction interfaces for use in friction-based structural components. The material-level study evaluates the mechanical properties of composite friction materials, including tensile and bearing strengths, their through-thickness creep behavior through bolt relaxation tests, and the tribological response of composite to low-carbon structural steel friction interfaces under testing parameters relevant to earthquake structural engineering applications. The influence of material constituents and manufacturing process on the observed mechanical and tribological properties is also discussed.

At the component level, this dissertation develops and evaluates friction-based structural components that address practical design considerations. One component-level study focuses on the development and experimental characterization of a friction-based component (termed *Modified Friction Device*, or *Modified FD*) capable of developing predetermined discrete variable friction forces at target design displacement levels. This component is able to limit the force transferred without inducing excessive connection deformation demands, and in the meantime, provides the potential of a multi-level earthquake protection mechanism. Another component-level study focuses on the development and experimental characterization of a low-cost friction-based components design concept with reduced sensitivity to machining tolerances and accelerated repairability. Friction-based components designed with the proposed concept are able to generate relatively constant sliding forces without the need for small geometric tolerances in the machined parts, and also allow quick inspection and replacement of friction shims if needed. Together, the material-level and component-level studies provide experimental evidence

and design considerations to support the future implementation of friction-based structural components in earthquake-resistant structures.

The remainder of this dissertation is organized as follows. Chapter 2 presents the experimental characterization of mechanical and tribological properties of composite materials for friction-based structural components. Chapter 3 presents the development and experimental characterization of the low-cost friction-based component design concept with reduced sensitivity to machining tolerances and accelerated repairability. Chapter 4 presents the development and numerical characterization of the Modified FD. Chapter 5 presents the experimental characterization of the Modified FD and validates the expected kinematics, force-displacement response, and practical adjustability of the design parameters. Chapter 6 summarizes the main findings of this dissertation and provides recommendations for future research.

Acknowledgments

Chapter 1, in part, is a reprint of the material as it appears in the introduction sections of: Chen, K., Tsampras, G., Cheruvalath, S., & Thundathil, M. (2025). Experimental characterization of mechanical and tribological properties of composite materials for friction-based force-limiting structural components. *Composites Part B: Engineering*, 302, 112472, and Chen, K., Tsampras, G., Chou, C. C., Lin, H. Z., Wu, C. J., Córdova, A., Uang, C. M., & Chao, S. H. (2026). Low-Cost Friction-Based Force-Limiting Connection With Reduced Sensitivity to Machining Tolerances and Accelerated Repairability. *Earthquake Engineering & Structural Dynamics*. The author of the dissertation was the author of these sections.

Chapter 2

Experimental Characterization of Mechanical and Tribological Properties of Composite Materials for Friction-based Structural Components

2.1 Overview and Scope of Study

The objective of the study presented in this chapter is to provide practical recommendations on what composite to low-carbon structural steel friction interfaces are appropriate for earthquake structural engineering applications. Six types of phenolic-resin-based fiber-reinforced composite materials were selected for this study. A systematic testing program was proposed. Compared with past studies listed in Section 1.2.2, the testing program proposed in this study not only assessed the tribological properties of the composite-metallic friction interface through a strategically designed loading protocol, but also assessed the mechanical properties and long-term creep behavior of the composite materials, of which the discussions were limited in past studies. The proposed testing program is as follows:

- Coupon tensile tests and plate bearing tests were conducted to characterize the tensile and bearing strengths of the materials, so that the bearing action from pretensioned structural bolts as discussed in Section 1.2.2 could be designed against.
- Bolt relaxation tests were conducted to assess the through-thickness creep behavior of

the composite materials so that the loss of preload due to material creep as discussed in Section 1.2.2 could be predicted.

- Friction tests of the composite-metallic friction interface were conducted. The friction test included the following testing parameters that were considered important for earthquake structural engineering applications: the normal load level, loading frequencies, sliding velocities, velocity profiles (earthquake vs. sinusoidal vs. linear), and sliding histories (the cumulative displacement, the dwell time, and previous sliding events). The ranges of testing parameters were strategically designed to reflect the working condition of a friction-based structural component in a seismic event.

2.2 Composite Friction Materials

Composite friction materials are composite materials developed for use in friction interfaces, designed to provide controlled friction forces in tribological applications. A brief discussion on the constituents, the manufacturing process, and the testing of composite friction materials is provided in this section to facilitate discussions in follow-up sections.

2.2.1 Constituents

According to Cox [104], the constituents of composite friction materials can be characterized into four categories:

- **Binder** is the matrix of the composite friction material. It helps to hold the constituents of the composite materials together. Commonly used binders for composite friction materials include phenolic resin and modified phenolic resin.

- **Fibers** are used in composite friction materials for enhancing mechanical strengths of the material. Besides working as structural reinforcement, fibers also significantly influence the tribological properties of composite friction materials [104]. Commonly used types of fibers for composite friction materials include organic fibers (such as cotton fibers or

aramid fibers), inorganic fibers (such as glass fibers), and metallic fibers (such as brass fibers).

- **Friction modifiers** are added to adjust the coefficient of friction and wear rates of composite friction materials. They can be sub-characterized into two categories: abrasives and lubricants. Abrasives increase the coefficient of friction and the wear rate. Typically, hard materials such as metal oxides and silicates (for example, yellow iron oxide Fe_2O_3, green chromium oxide Cr_2O_3, or aluminum oxide Al_2O_3) are used as abrasives. In contrast, lubricants are used to reduce the coefficient of friction, maintain the coefficient of friction at different working temperatures, and control the wear rate. Commonly used lubricants include graphites, Teflon, and metal sulfides such as molybdenum disulfide MoS_2.

- **Filler** materials are low-cost materials added to occupy the space, lower the material cost, and sometimes modify certain material properties [105]. Fillers can be organic, inorganic, or metallic. Commonly used fillers include wollastonite, vermiculite, mica, and barite.

2.2.2 Manufacturing

Compression molding was used to manufacture the materials used in this study. Typically, compression molding manufacturing techniques involve three main steps: mixing, molding, and post-curing [105]. These steps can be adapted by manufacturers based on the specific raw material constituents and production requirements. This section provides an introduction of the molding process as essential background information for follow-up sections. A more detailed discussion about the manufacturing of composite friction materials is included in [104] [105] [106].

During the molding step, the mix of constituents is put into a mold closure in which it will be compressed under a certain pressure, at a certain temperature, and for a certain period. The molding pressure, temperature, and period are defined by the manufacturer. There are three types of molding closure: flash mold, semi-positive mold, and fully-positive mold. The flash

mold is the simplest and least expensive to use. In the flash molding process, resin is overcharged into the mold and during molding, the overcharged resin will flow out of the mold from the edge. The product of flash molding could have inconsistent density due to overflow of overcharged resin [104] [107]. The semi-positive mold allows for a smaller amount of overcharged resin, but the cost of the mold is higher than the flash mold. The fully-positive mold utilizes an exact metering of the mix of material constituents and provides the best density control, but the tooling cost is the highest among the three methods [104] [107]. The materials tested in this study were manufactured using a flash mold. The detailed manufacturing process for the materials tested in this study is described in Section 2.3.1.

2.2.3 Testing

Standards for testing composite friction materials have been developed primarily for automotive and other industrial applications. These tests typically assess physical properties (e.g., hardness), mechanical properties (e.g., compressibility), chemical properties (e.g., working pH range), and tribological properties, reflecting the working conditions of composite friction materials in automotive applications. The tribological properties of composite friction materials for automotive applications are characterized using testing methods and equipment (e.g., Chase machines [108], FAST machines, Krauss machines, and dynamometers) that simulate braking conditions through controlled rotational motion and contact between the composite friction material and a back plate (typically cast iron). However, the existing testing methods and equipment might not be suitable for characterizing composite friction material properties for earthquake structural engineering applications, due to fundamental differences in simulated loading conditions and failure mechanisms. These differences further emphasize the need for a systematic testing program specifically designed for characterizing composite friction materials for earthquake structural engineering applications. This study addresses this need and proposes a testing program that includes coupon tensile tests, plate bearing tests, bolt relaxation tests, and friction tests, to characterize composite friction materials for use in friction-based structural

components for earthquake structural engineering applications.

2.3 Experimental Testing: Background and Setup

2.3.1 Material Overview

Six types of composite friction materials from the Gatke Series [109] manufactured and supplied by ScanPac Mfg., Inc. were tested in this study. Their names and constituents are shown below. In the material constituents, reinforcing fibers and the binder are listed for all the materials. Friction modifiers are listed only if they are used. Fillers are not listed.

- **Gatke 81** consists of aramid fibers, glass fibers, brass fibers, and acrylic fibers as the reinforcing fibers; yellow iron oxide, green chromium (III) oxide, and aluminum oxide as the friction modifier; and phenolic resin as the binder.
- **Gatke 82** consists of E-glass cloth as the reinforcing fibers; yellow iron oxide, green chromium (III) oxide, and aluminum oxide as the friction modifier; and phenolic resin as the binder.
- **Gatke 112** consists of cotton cloth as the reinforcing fibers; and phenolic resin as the binder.
- **Gatke 113** consists of cotton cloth as the reinforcing fibers; graphite, Teflon, and molybdenum disulfide (MoS_2) as the friction modifier; and phenolic resin as the binder.
- **Gatke 397** consists of E-glass cloth as the reinforcing fibers; and phenolic resin as the binder.
- **Gatke 398** consists of E-glass cloth as the reinforcing fibers; graphite, Teflon, and molybdenum disulfide (MoS_2) as the friction modifier; and phenolic resin as the binder.

The manufacturing process of the Gatke series materials used in this study is as follows: First, single-ply fiber cloths were impregnated with the phenolic resin mixture. After drying, the

impregnated fiber cloths were cut to the required size and were compression molded using the flash mold at a temperature of 148.9°C (300°F) and under a pressure of 3.45 MPa (500 psi). The desired thickness of the molded plate was achieved by stacking the required number of single layers of impregnated fiber cloths and molding.

2.3.2 Specimen Preparation

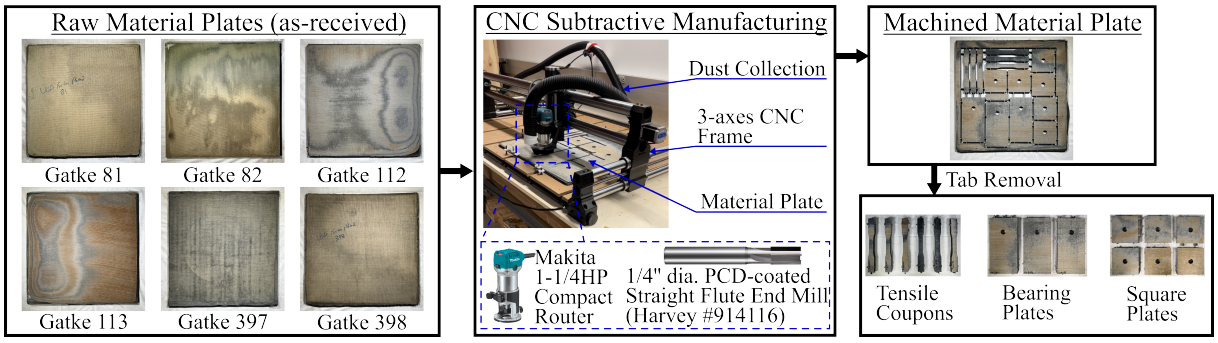

Figure 2.1. Specimen preparation process

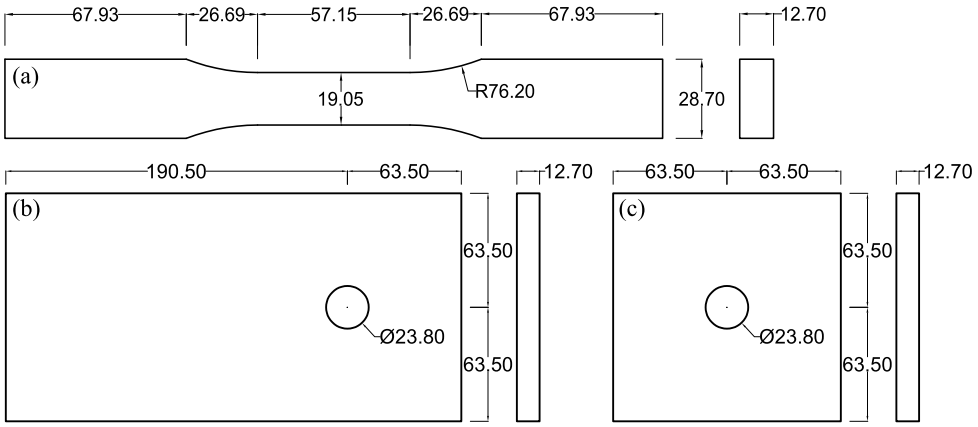

Figure 2.2. Nominal dimensions of test specimens: (a) Tensile coupons (b) Bearing plates and (c) Square plates (Units: in mm)

Figure 2.1 shows the preparation process of the test specimens. The materials were received from the manufacturer in square plates with a nominal area of 0.61 $\times$ 0.61 m^2 (2 $\times$ 2 ft^2) and a nominal thickness of 12.7 mm (0.5 inch). A dry Computer Numerical Controlled (CNC) subtractive manufacturing approach was used in this study for machining the test specimens.

A 6.35 mm ($\frac{1}{4}$ inch) diameter Polycrystalline Diamond (PCD) coated straight flute end mill (Tool #914116, Harvey Tool [110], USA) was used as the cutting tool and was installed on an 1-$\frac{1}{4}$ horsepower compact router (Makita [111], USA) for machining purposes. The cutting parameters used were: spindle speed = 10,000 RPM, resulting in a surface speed of 3.325 m/s (654.5 ft/min); cutting feed rate = 1,524 mm/min (60 inch/min), resulting in a chip load of 0.0381 mm per tooth (0.0015 inch per tooth); the cutting depth was 1.27 mm (0.05 inch) per pass. No delamination or damage of the specimens was observed during machining. Tabs were used to keep the specimens in place throughout the machining process and were removed after the machining was completed. Nominal dimensions of test specimens are shown in Figure 2.2.

2.3.3 Experimental Testing Set-up

Coupon Tensile Test

Figure 2.3 shows the experimental testing setup of the coupon tensile test. The coupon tensile test followed ASTM D638-22 (*Test Method for Tensile Properties of Plastics*) [112]. As shown in Figure 2.1, tensile coupon specimens were sampled in two orthogonal directions, i.e., 0° and 90°. These two directions were selected because they corresponded to the warp and weft directions [113] of the fiber cloth constituents. For each material, three coupons were sampled in each direction. The dimension of the tensile coupon specimen followed the Type III specimen as defined in Figure 1 of ASTM D638-22, which is suitable for materials having a thickness from 7 to 14 mm (0.28 to 0.55 inch). Figure 2.2 (a) shows the nominal dimensions of the tensile coupon specimens. The total length of the specimen was 246.4 mm (9.7 inch). The total width of the specimen was 28.7 mm (1.13 inch). A narrowed section with a width of 19.05 mm (0.75 inch) was created in the middle of the specimen and the length of the narrowed part was 57.15 mm (2.25 inch). A gage length of 50.8 mm (2 inches) at the center of the narrowed part was used for computing the engineering strain. The testing machine was an MTS 810 Material Test System (MTS Systems [114], USA). The Digital Image Correlation (DIC) technique was used in the coupon tensile test to collect full-field displacement and strain data on the tensile

coupon specimen throughout the test. To facilitate DIC data collection, white paint was sprayed over the specimen and a black speckle pattern was applied. The tensile test was monotonic and displacement-controlled. The speed of testing was 5.08 mm/min (0.2 inch/min), resulting in a nominal strain rate of 0.1 (mm/mm)/min at the start of the test.

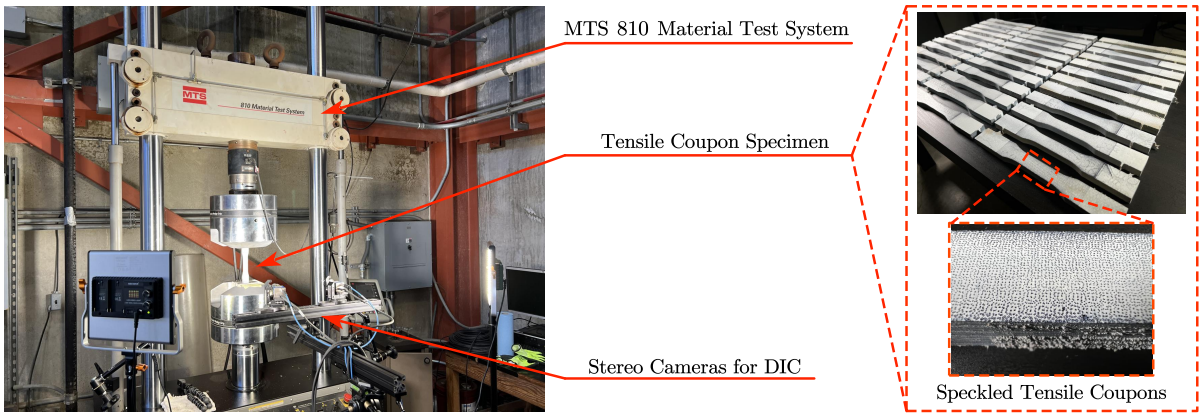

Figure 2.3. Coupon tensile test setup

Plate Bearing Test

Figure 2.4 shows the experimental testing setup of the plate bearing test. The plate bearing test used ASTM D5961-23 (*Standard Test Method for Bearing Response of Polymer Matrix Composite Laminates*) [115] Procedure A (Double Shear, Tension) as a reference, and adjustment was made to make the test setup reflect the dimension of a sub-assembly of a full-scale slotted-bolted friction-based structural component. For each material, three specimens were tested. The plate bearing test specimen was a rectangular plate. The nominal dimension of the specimen was 254 mm $\times$ 127 mm $\times$ 12.7 mm (length(l) $\times$ width(w) $\times$ thickness(h), 10 inch $\times$ 5 inch $\times$ 0.5 inch), as shown in Figure 2.2 (b). A bolt hole of diameter D = 23.8 mm (15/16 inch) was created along the center line perpendicular to the width of the plate in the through-thickness direction. The diameter of the bolt hole was defined per AISC Steel Construction Manual [116] for a 22.2 mm (7/8 inch) diameter bolt with standard tolerance. The bearing fastener in this test was a 22.2 mm (7/8 inch) diameter ASTM A325 medium-strength steel heavy hex head bolt for structural applications. The nominal tensile strength of the bearing fastener was 827.4

MPa (120 ksi). The bearing load was applied through the bearing action between the bearing fastener and the plate specimen and acted perpendicular to the width of the plate. The nominal distance between the center of the bolt hole to the specimen end was e = 63.5 mm (2.5 inch), resulting in a nominal edge distance ratio (e/D) = 2.67. The nominal width to diameter ratio (w/D) was 5.33 and the nominal diameter to thickness ratio (D/h) was 1.875. In this test, a set of testing fixtures made of AISI 1018 cold-rolled steel was fabricated. The configuration of the fixture resembled a double-shear clevis. The dimensions of the fixture were designed to fulfill the strength and stiffness requirements of the test. Speckle patterns were applied on the testing fixtures and the DIC technique was used to collect full-field displacement and strain data on the bearing test fixture so that the fixture deformation throughout the test could be computed. In addition to aforementioned components, a 12.7 mm (1/2 inch) diameter ASTM A325 structural bolt was used as the supplemental fastener to assist in the assembly of the test setup.

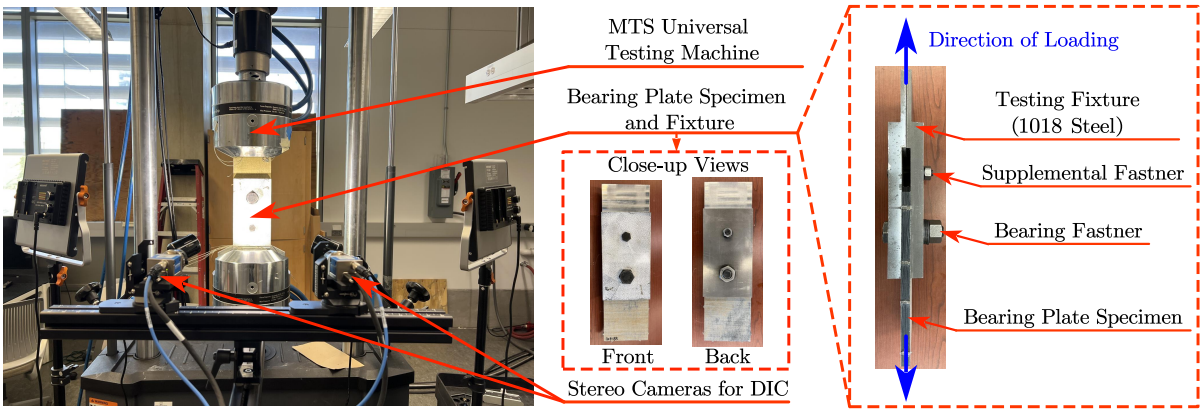

Figure 2.4. Plate bearing test setup

In this test, a minimal clamping torque, just enough to stabilize the test assembly, was applied to the bearing fastener. As summarized in [117], an increase in the clamping torque will overall increase the ultimate bearing strength of the composite material because the onset of delamination is suppressed by the initial clamping pressure, and this makes the failure mode more progressive. As aforementioned, in this test, a minimal clamping torque was applied to the bearing fastener. Therefore, the experimental ultimate bearing strength computed from this test

could be regarded as a lower-bound ultimate bearing strength of the material and can be used as a conservative value for practical design purposes. The plate bearing test was conducted on an MTS 370.25 servo-hydraulic load frame (MTS Systems [114], USA). Same as the coupon tensile test, the plate bearing test was also monotonic and displacement-controlled. As suggested in [115], the speed of testing was 1.27 mm/min (0.05 inch/min). The specimen was loaded until the load was equal to 70 % of the maximum load recorded during the test.

Bolt Relaxation Test

Figure 2.5 (a) and (b) show the schematic representation and the actual test setup of the bolt relaxation test, respectively. The specimens of the bolt relaxation test were square plates having a nominal dimension of 127 mm $\times$ 127 mm $\times$ 12.7 mm (length(l) $\times$ width(w) $\times$ thickness(h), 5 inch $\times$ 5 inch $\times$ 0.5 inch), as shown in Figure 2.2 (c). A bolt hole of diameter D = 23.8 mm (15/16 inch) was created at the center of the plate specimen in the through-thickness direction. The diameter of the bolt hole was defined per AISC Steel Construction Manual [116] for a 22.2 mm (7/8 inch) diameter bolt with standard tolerance. The dimensions of the plate specimen and the bolt hole reflected the dimension of a sub-assembly of a friction shim for a full-scale slotted-bolted friction-based structural component. The plate specimen was clamped between two clamping plates made of A36 steel. The clamping plates had a nominal dimension of 127 mm $\times$ 127 mm $\times$ 25.4 mm (5 inch $\times$ 5 inch $\times$ 1 inch). A bolt hole of diameter equal to 25.4 mm (1 inch) was drilled at the center of each clamping plate in the through-thickness direction. A 22.2 mm (7/8 inch) diameter ASTM A325 structural bolt was used to clamp the plates together, with a structural nut and a set of Hytorc washers (Hytorc [118], USA) including one backup washer and one reaction washer. The use of Hytorc washers eliminated the use of reaction arms or backup wrenches and hence assisted in the bolt tightening process. The Hytorc washers were manufactured in accordance with the requirements in the ASTM F3394/F3394M standard [119] and could be considered as equivalent to flat washers for structural applications. Two levels of clamping loads, i.e., high and low bolt loads, were considered in this test. The

target high bolt load was 173.5 kN (39 kips), representing the minimum pretension of a 22.2 mm (7/8 inch) diameter ASTM A325 structural bolt as defined by the AISC Steel Construction Manual [116]; the target low bolt load was 57.8 kN (13 kips), representing one-third of the target high bolt load. Target high and low bolt loads resulted in target nominal normal pressure of 11 MPa (1.6 ksi) and 3.7 MPa (0.53 ksi) acting on the clamped plate specimen in the through-thickness direction, respectively. In all the tests, the threaded part of the structural bolt was lubricated using bolt anti-seize lubricants (Bostik Never-Seez regular-grade lubricants, Bostik [120], USA). The bolt loads were applied by an electric torque wrench (LST-1200, Hytorc [118], USA). The actual applied bolt load varied from the target bolt load and a variation of $\pm 10\%$ was considered acceptable to account for imperfection in assembly and torquing. A through-hole load cell (THD-50K-Y, Transducer Technique Inc. [121], USA) was used to monitor the bolt load throughout the testing period. The data collection frequency was set to be one data point per every 30 seconds. Data recording was stopped when a steady state of the bolt load, defined as when the bolt load loss rate was lower than or equal to -5×10^{-6} kN/sec, was observed. For each material under each bolt load level, three specimens were tested. In addition to the composite plates, three A36 steel plate specimens were tested under the high bolt load to establish the baseline test cases. For selected cases as shown in Section 2.4.3, the pressure measurement film (Prescale® pressure measurement film, Fujifilm [122], Japan) was put between the clamped plate specimen and the clamping plates to examine the normal pressure distribution pattern around the bolt hole. The bolt relaxation test was conducted in a controlled laboratory environment. Humidity and temperature levels were measured by a humidity and temperature meter and were continuously monitored. The humidity level was about $45\% \sim 50\%$ and the temperature was about 22.5 °C $\sim$ 23.5 °C throughout the test.

Friction Test

Figure 2.6 (a) and (b) show schematic representations of the exploded view and the assembly of the friction test setup, respectively. Figure 2.7 (a) shows the photo of components

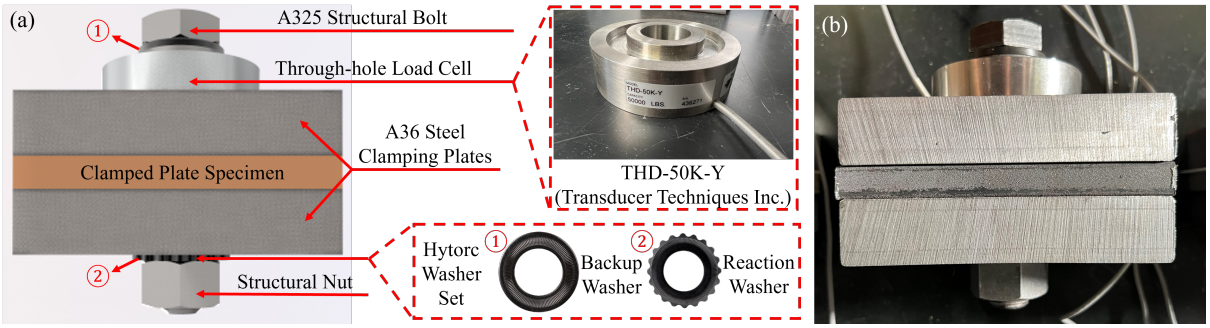

Figure 2.5. Bolt relaxation test: (a) schematic representation of the test setup and (b) photo of the actual test setup

of the friction test setup assembly. Figure 2.7 (b) shows the friction test setup assembly on the testing machine. The testing machine was an MTS 370.25 servo-hydraulic load frame, same as the bearing test. The friction test setup resembled a slotted-bolted friction-based structural component. Two ends of the friction test setup assembly were termed the fixed end and the sliding end. On the fixed end, six 22.2 mm (7/8 inch) diameter ASTM A325 structural bolts were used to clamp two steel channels and three connection plates together. Washers and nuts for structural applications were used associated with the bolts. Bolt holes with standard tolerance per AISC Steel Construction Manual were created on the steel channels and connection plates to allow the bolts to pass through. The connection plates and steel channels were made of A36 steel. The channels were commercially available C10×15.3 hot-rolled steel channels, of which the dimensions followed AISC Steel Construction Manual. The length of each channel was 685.8 mm (27 inch). For each bolt on the fixed end, a torque of 556 Newton·meter (410 pound·foot) was applied to tighten the bolt. The bolts on the fixed end were retightened every day before the test started to make sure that relative movement did not occur between the components on the fixed end.

Friction shims used in the friction test had the same configuration and dimensions as the clamped plate specimens in the bolt relaxation test. The nominal dimensions of the friction shims are shown in Figure 2.2 (c). For each steel channel, a rectangular-shaped opening was created on the channel, in which the friction shim was hosted. Sliding occurred on the end where

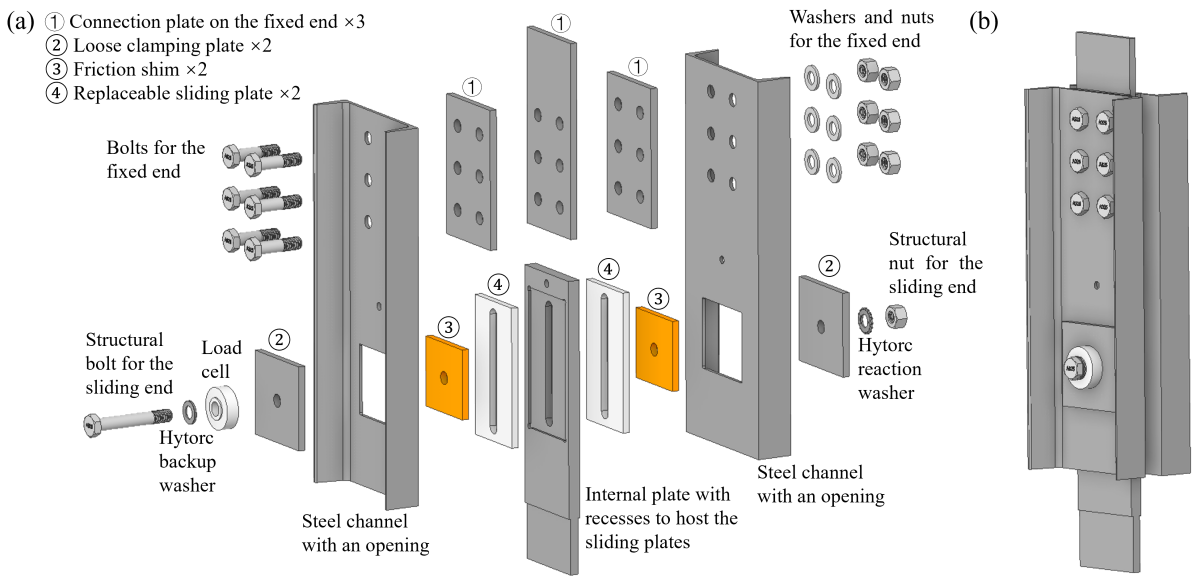

Figure 2.6. Schematic representation of the friction test setup: (a) Exploded view (b) Assembly



Figure 2.7. Photos of the friction test setup: (a) Components (b) Assembly on the testing machine

friction shims were hosted, termed the sliding end. On the sliding end, an internal plate made of A36 steel was fabricated for testing purposes. A slot was created on the internal plate to allow for the movement of the bolt. Two recesses were created on the internal plate, in which the sliding plates were hosted. The design with recesses on the internal plate allowed for the replacement of sliding plates if needed. In this test, the sliding plates were made of low-carbon structural steel (A36 steel) and had a nominal dimension of 254 mm $\times$ 127 mm $\times$ 12.7 mm (10 inch $\times$ 5 inch $\times$ 0.5 inch). The surfaces of the A36 steel sliding plates were not specially treated. For each sliding plate, a slot was created on the plate to allow for the movement of the bolt. The friction shims made of composite friction materials were in contact with the A36 steel sliding plates and formed the friction interfaces. Loose clamping plates made of A36 steel were used to clamp the friction shims, sliding plates, and the internal plate together. A 22.2 mm (7/8 inch) diameter ASTM A325 structural bolt was used for clamping and applying the normal load to the friction interface, associated with the Hytorc washer set including one Hytorc backup washer and one Hytorc reaction washer. A through-hole load cell (THD-50K-Y from Transducer Technique Inc.) was used to monitor the bolt load throughout the friction test. During the test, the components on the fixed end, i.e., steel connection plates, bolts, washers, nuts, and two steel channels, were expected to remain static relative to each other. As the friction shim was hosted inside the rectangular-shaped opening of the steel channel, when the steel channels started moving relative to the internal plate, the steel channels made contact with the edge of the friction shims and pushed the friction shims to move relative to the sliding plates and to activate the sliding friction mechanism.

Similar to the bolt relaxation test, two levels of target normal loads (termed N_{target}), i.e., target high and low bolt loads, were considered in the friction test. The target high bolt load was 173.5 kN (39 kips), representing the minimum pretension of a 22.2 mm (7/8 inch) diameter ASTM A325 structural bolt as defined by the AISC Steel Construction Manual [116]; the target low bolt load was 57.8 kN (13 kips), representing one-third of the high bolt load, which considered the application of a friction-based structural component for a representative lower

force demand. Target high and low bolt loads resulted in target nominal normal pressure of 13.2 MPa (1.92 ksi) and 4.4 MPa (0.64 ksi) acting on the friction interface, respectively. An exception was applied to the testing of Gatke 397, in which to prevent exceeding the testing machine's force capacity, the target high bolt load was reduced from 173.5 kN (39 kips) to 138 kN (31 kips), resulting in a nominal normal pressure of 10.5 MPa (1.53 ksi). In the friction test, the combination of one composite friction material mating with A36 steel sliding plates under one normal load level was termed one test group. The test groups were named based on the friction material used and the target normal load level (Low (L) or High (H)). For example, Test Group Gatke 81 (L) represents the test group using the composite friction material Gatke 81 and under low normal load. Six types of composite friction materials combined with two normal load levels resulted in twelve test groups. A summary of test groups of the friction test is presented in Table 2.1. For each test group, a pair of unworn friction shim surfaces was used to establish the friction interfaces with A36 steel sliding plates. For each material, tests for the low normal load test group were conducted first; after the tests for the low normal load test group were completed, the pair of friction shims were flipped so that the unworn surfaces on the other side of the friction shims could be used for the tests for the high normal load test group. The structural bolt on the sliding end was reused after the tests for the low normal load test group and was replaced with a new bolt after the tests for the high normal load test group, since the structural bolt yielded under a bolt load of the minimum pretension of the bolt. After completing one test group, sliding plates were removed from the test setup for inspection and cleaning. Aerosol brake parts cleaner was used with heavy-duty shop towels to clean the sliding plates to make sure that the sliding plates were free of friction dust before the start of the next test group.

A loading protocol was designed for the friction test. For each test group, twenty displacement-controlled tests (Test IDs 1$\sim$20) were conducted. Table 2.2 summarizes the characteristics of each test, including the type of input excitation, maximum sliding amplitude, peak sliding velocity, loading frequency, cumulative displacement, duration, dwell time, and the descriptions of each test. For Test ID i, dwell time is defined as the idle time between Test IDs

Table 2.1. Summary of Test Groups for the Friction Test

Test Group ID	Friction Material	Target bolt load [kN]	Target nominal normal pressure [MPa]
Gatke 81 (L)	Gatke 81	57.8	4.4
Gatke 81 (H)		173.5	13.2
Gatke 82 (L)	Gatke 82	57.8	4.4
Gatke 82 (H)		173.5	13.2
Gatke 112 (L)	Gatke 112	57.8	4.4
Gatke 112 (H)		173.5	13.2
Gatke 113 (L)	Gatke 113	57.8	4.4
Gatke 113 (H)		173.5	13.2
Gatke 397 (L)	Gatke 397	57.8	4.4
Gatke 397 (H)		138	10.5
Gatke 398 (L)	Gatke 398	57.8	4.4
Gatke 398 (H)		173.5	13.2

i and i+1. Figure 2.8 shows the displacement histories of the input excitation, the cumulative displacement history of each test, and the history of absolute sliding velocities of each test. For the loading protocol, Test IDs 1∼3 were three break-in tests, termed Brk1∼3 as shown in Figure 2.8. The break-in tests were designed to establish and assess the break-in effect of the friction interface. The break-in tests had ramped sinusoidal waves as the displacement histories of the input excitation. A maximum displacement amplitude of 50.8 mm (2 inches) and a peak sliding velocity of 12.7 mm/sec (0.5 inch/sec) were imposed. After each break-in test, the bolt on the sliding end that provided normal load to the friction interface was retightened to the target bolt load level as at the beginning of the test, if bolt load loss was observed. The dwell time of Test IDs 1∼3 depended on the retightening practice and thus was varying. Test ID 4 assessed the response of the friction interface given an earthquake-type input excitation. The displacement history of the earthquake-type input excitation was a representative response of a friction-based structural component from numerical earthquake simulations. The sliding velocity imposed by the representative displacement response was scaled down by elongating the testing period so that it could be limited below the testing machine's capacity. A detailed discussion of the numerical earthquake simulation is beyond the scope of this study and thus not included. Test

IDs 5∼10 were six tests having ramped sinusoidal waves as the displacement histories of the input excitation, with different peak sliding velocities to assess how sliding velocities would affect the response of the friction interface. Three levels of peak sliding velocities were assessed in Test IDs 5∼10. Test IDs 5 and 10 had a peak sliding velocity of 12.7 mm/sec (0.5 inch/sec); Test IDs 6 and 9 had a peak sliding velocity of 25.4 mm/sec (1.0 inch/sec); Test IDs 7 and 8 had a peak sliding velocity of 63.5 mm/sec (2.5 inch/sec). The peak sliding velocities were determined based on the testing machine's capacity, and were justified using the numerical analysis results reported in [123]. Test IDs 5∼10 each had a cumulative displacement of 514 mm (20.2 inches) and the value of the cumulative displacement was also justified using the numerical analysis results reported in [123]. Test ID 11 had the same imposed displacement history as Test ID 4 and was designed to assess the repeatability of the response of the friction interface given an earthquake-type input excitation. Test IDs 12∼13 were two tests having ramped linear waves as the displacement histories of the input excitation with a peak sliding velocity of 25.4 mm/sec (1.0 inch/sec), equal to that of Test IDs 6 and 9. The difference between ramped sinusoidal waves and ramped linear waves was that for ramped linear waves, the anticipated absolute sliding velocity remained constant throughout the test while for ramped sinusoidal waves, the anticipated absolute sliding velocity varied. In addition, compared with Test IDs 6 and 9, Test IDs 12∼13 had a larger loading frequency. Following Test IDs 12∼13 and similar to Test ID 11, Test ID 14 had the same imposed displacement history as Test ID 4 and was designed to assess the repeatability of the response of the friction interface given an earthquake-type input excitation. For Test IDs 4∼14, the dwell time between two consecutive tests was ten seconds. Test IDs 15∼20 assessed the effect of dwell time on the response of the friction interface. The assessment method was that a ramped sinusoidal wave with a peak sliding velocity of 63.5 mm/sec (2.5 inch/sec) was firstly run. This test was termed the prior test of the dwell time effect assessment. After the prior test, the test setup was held idle for a predefined amount of dwell time. Afterward, an earthquake-type input excitation was run to evaluate how the coefficient of friction changed after this certain amount of dwell time. This step was termed the posterior test of the dwell time

effect assessment. Test IDs 15, 17, and 19 were three prior tests and Test IDs 16, 18, and 20 were three corresponding posterior tests. Three different dwell times were assessed. Between Test IDs 15 and 16, the dwell time was 10 seconds; between Test IDs 17 and 18, the dwell time was 10 minutes; between Test IDs 19 and 20, the dwell time was 30 minutes. In Figure 2.8, they are marked as DT10s, DT10m, and DT30m respectively. Twenty tests resulted in a total cumulative displacement of 14.407 meters which is effectively equal to the cumulative sliding of the friction interface.

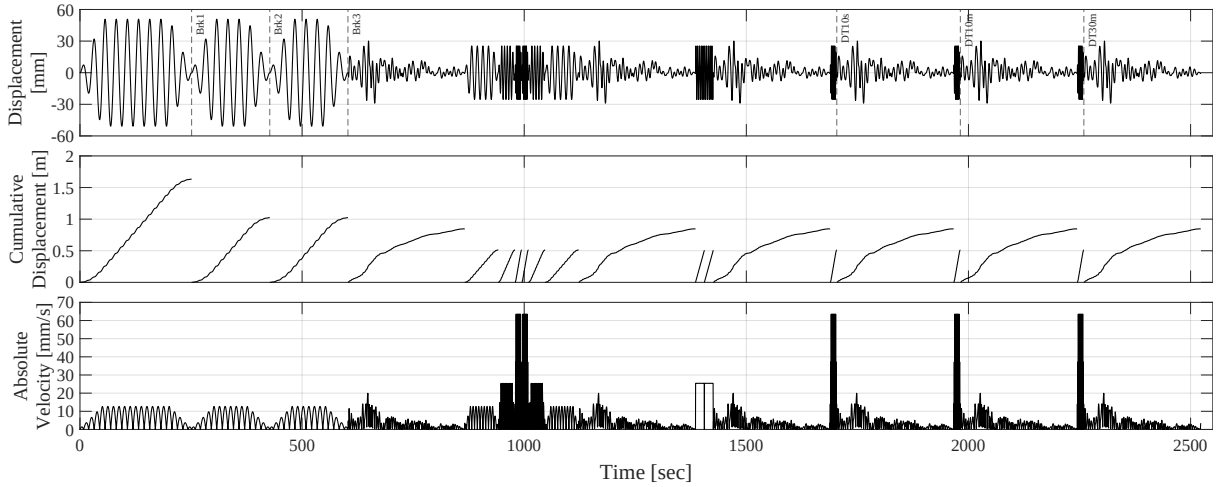

Figure 2.8. Friction test loading protocol. From top to bottom: imposed displacement history; cumulative displacement history of each test; and absolute sliding velocity history

Table 2.2. Friction Test Loading Protocol: Imposed Displacement Histories

Test ID	Input Type	Maximum Amplitude [mm]	Peak Velocity [mm/s]	Loading Frequency [Hz]	Cumulative Displacement [mm]	Duration [s]	Dwell Time [s]	Descriptions
1	Ramped sine	50.8	12.7	0.0398	1633	251.3	Varying	Break-in test one (Brk1) to establish and assess the break-in effect
2	Ramped sine	50.8	12.7	0.0398	1023.4	175.9	Varying	Break-in test two (Brk2) to establish and assess the break-in effect
3	Ramped sine	50.8	12.7	0.0398	1023.4	175.9	Varying	Break-in test three (Brk3) to establish and assess the break-in effect
4	Earthquake	30.1	20.0	N/A	847.6	263	10	Assess the friction interface response after the establishment of the break-in effect under earthquake-type input excitation
5	Ramped sine	25.4	12.7	0.0796	514	75.4	10	Assess the friction interface response under ramped sinusoidal motion with a peak sliding velocity of 12.7 mm/s (0.5 inch/s)

Continued on next page

Table 2.2. Friction Test Loading Protocol: Imposed Displacement Histories (continued)

Test ID	Input Type	Maximum Amplitude [mm]	Peak Velocity [mm/s]	Loading Frequency [Hz]	Cumulative Displacement [mm]	Duration [s]	Dwell Time [s]	Descriptions
6	Ramped sine	25.4	25.4	0.1592	514	37.7	10	Assess the friction interface response under ramped sinusoidal motion with a peak sliding velocity of 25.4 mm/s (1.0 inch/s)
7	Ramped sine	25.4	63.5	0.3979	514	15.1	10	Assess the friction interface response under ramped sinusoidal motion with a peak sliding velocity of 63.5 mm/s (2.5 inch/s)
8	Ramped sine	25.4	63.5	0.3979	514	15.1	10	Assess repeatability of the friction interface response under ramped sinusoidal motion with a peak sliding velocity of 63.5 mm/s (2.5 inch/s), compared with Test ID 7

Continued on next page

Table 2.2. Friction Test Loading Protocol: Imposed Displacement Histories (continued)

Test ID	Input Type	Maximum Amplitude [mm]	Peak Velocity [mm/s]	Loading Frequency [Hz]	Cumulative Displacement [mm]	Duration [s]	Dwell Time [s]	Descriptions
9	Ramped sine	25.4	25.4	0.1592	514	37.7	10	Assess repeatability of the friction interface response under ramped sinusoidal motion with a peak sliding velocity of 25.4 mm/s (1.0 inch/s), compared with Test ID 6
10	Ramped sine	25.4	12.7	0.0796	514	75.4	10	Assess repeatability of the friction interface response under ramped sinusoidal motion with a peak sliding velocity of 12.7 mm/s (0.5 inch/s), compared with Test ID 5
11	Earthquake	30.1	20.0	N/A	847.6	263	10	Assess repeatability of friction interface response under earthquake-type input excitation, compared with Test ID 4

Continued on next page

Table 2.2. Friction Test Loading Protocol: Imposed Displacement Histories (continued)

Test ID	Input Type	Maximum Amplitude [mm]	Peak Velocity [mm/s]	Loading Frequency [Hz]	Cumulative Displacement [mm]	Duration [s]	Dwell Time [s]	Descriptions
12	Ramped linear	25.4	25.4	0.25	508	20	10	Assess the friction interface response under ramped linear motion with the same peak sliding velocity as Test IDs 6 and 7
13	Ramped linear	25.4	25.4	0.25	508	20	10	Assess repeatability of the friction interface response under ramped linear motion, compared with Test ID 12
14	Earthquake	30.1	20.0	N/A	847.6	263	10	Assess repeatability of friction interface response under earthquake-type input excitation, compared with Test IDs 4 and 11
15	Ramped sine	25.4	63.5	0.3979	514	15.1	10	Prior test of dwell time effect assessment with 10 seconds dwell time
16	Earthquake	30.1	20.0	N/A	847.6	263	10	Posterior test of dwell time effect assessment with 10 seconds dwell time

Continued on next page

Table 2.2. Friction Test Loading Protocol: Imposed Displacement Histories (continued)

Test ID	Input Type	Maximum Amplitude [mm]	Peak Velocity [mm/s]	Loading Frequency [Hz]	Cumulative Displacement [mm]	Duration [s]	Dwell Time [s]	Descriptions
17	Ramped sine	25.4	63.5	0.3979	514	15.1	600	Prior test of dwell time effect assessment with 10 minutes dwell time
18	Earthquake	30.1	20.0	N/A	847.6	263	10	Posterior test of dwell time effect assessment with 10 minutes dwell time
19	Ramped sine	25.4	63.5	0.3979	514	15.1	1800	Prior test of dwell time effect assessment with 30 minutes dwell time
20	Earthquake	30.1	20.0	N/A	847.6	263	N/A	Posterior test of dwell time effect assessment with 30 minutes dwell time

In the friction test, recorded data included the connection force, the connection displacement, and the bolt load of the structural bolt on the sliding end. Data collection of three quantities was synchronized.

2.3.4 Digital Image Correlation Technique

A Digital Image Correlation (DIC) technique was used in the testing series to quantify full-field displacement and strain on (1) tensile coupon specimens and (2) bearing test fixtures. Utilizing the DIC technique typically consists of the following steps: (1) Specimen preparation, including spray painting the specimen and applying the speckle pattern of appropriate size over the region of interest on the specimen; (2) System assembly and camera positioning; (3) Camera focusing; (4) System calibration, in which the intrinsic parameters (e.g., focal lengths of the lenses) and extrinsic parameters (e.g., relative positioning between cameras) of the camera lenses will be determined; (5) Image collection throughout the testing; and finally, (6) Data analysis. An important characteristic of the DIC technique is the full-field nature of the measurement data, which provides the possibility to look into highly localized material behavior, for example, strain localization during the testing process [124]. Additionally, in the tensile test, the full-field measurement data enabled an accurate assessment of the engineering strain over the gauge length of the tensile coupon specimens, without using additional instruments like strain gauges or extensometers [124]. The full-field measurement data also enabled the collection of displacement-related data in the transverse direction of the tensile coupon specimens and therefore, enabled the assessment of the Poisson's ratio of the materials [124].

In the setup for this series of experimental testing, two Basler ace acA4112-30um cameras were used. The cameras used a Sony IMX253 monochrome sensor, having a resolution of 12 megapixels (4096 pixels $\times$ 3000 pixels) and a maximum frame rate of 30 frames per second (FPS). The lenses were Schneider-Kreuznach JADE 2.8/25 C lenses, which had a focal length of 25 mm and a range of f-number (the ratio of a lens's focal length to its aperture diameter) from 2.8 to 16. The commercial software, Vic-Snap (Correlated Solutions [125], USA), was used

to facilitate the image collection process. In the data analysis stage, the commercial software, Vic-3D (Correlated Solutions [125], USA), was used to compute full-field displacement-related data by tracking the motions of the speckle patterns through the sequence of the test images.

2.4 Results

2.4.1 Coupon Tensile Test

Figure 2.9 shows a schematic representation of the expected engineering stress-strain curve of the coupon tensile test and is used to define engineering parameters of interest. Figure 2.10 (a) shows the results of the coupon tensile test. Engineering stress versus engineering strain curves upon failure of all tensile coupons are plotted. Results shown in black lines and red lines correspond to tensile coupons sampled in the warp and weft directions, respectively. According to ASTM D638, the modulus of elasticity (E) is defined as "*the ratio of stress to corresponding strain below the proportional limit of a material*". The yield strength (σ_y) is defined as "*the stress at which a material exhibits a specified limiting deviation from the proportionality of stress to strain*". In this test for all the specimens, since the stress-strain curve in the yield range was of gradual curvature change and a distinct yield point was not well-defined, 0.2% offset yield strength (the stress at which the strain exceeded 0.2% an extension of the initial proportional portion of the stress-strain curve) was considered as the yield strength of the material. The yield strain (ε_y) is defined as the strain at the intersection point between the 0.2% extension line and the stress-strain curve. The tensile strength (σ_u) is defined as "*the maximum tensile stress sustained by the specimen during the test*". The tensile strain at break (ε_b) is defined as the maximum strain that the tensile coupon specimen sustained during the test before breaking. The ductility μ_d is defined as the ratio between ε_b and ε_y. The Poisson's ratio (ν) is defined as "*the absolute value of the ratio of transverse strain to the corresponding axial strain resulting from uniformly distributed axial stress below the proportional limit of the material*". The mean material tensile properties of six materials that were tested are summarized in Table 2.3.

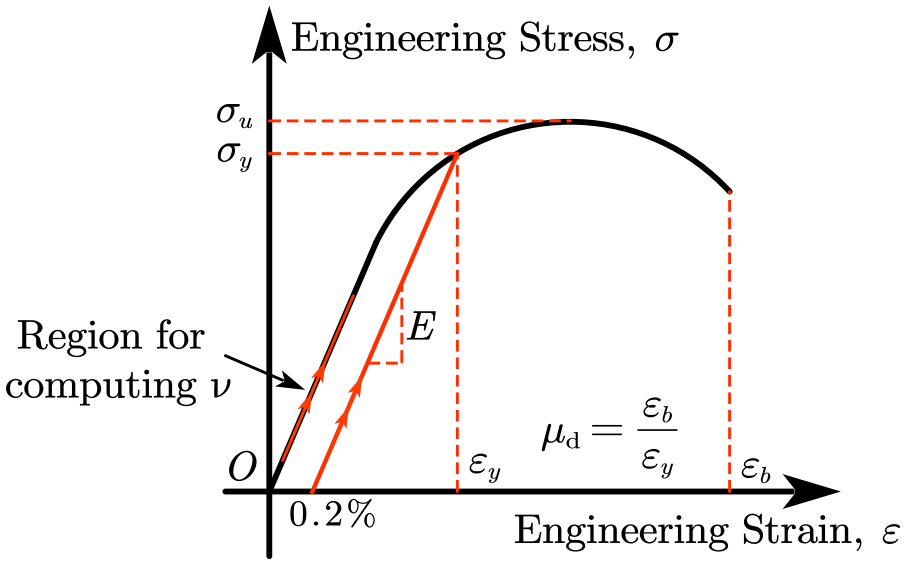

Figure 2.9. Engineering parameters of interest for the coupon tensile test

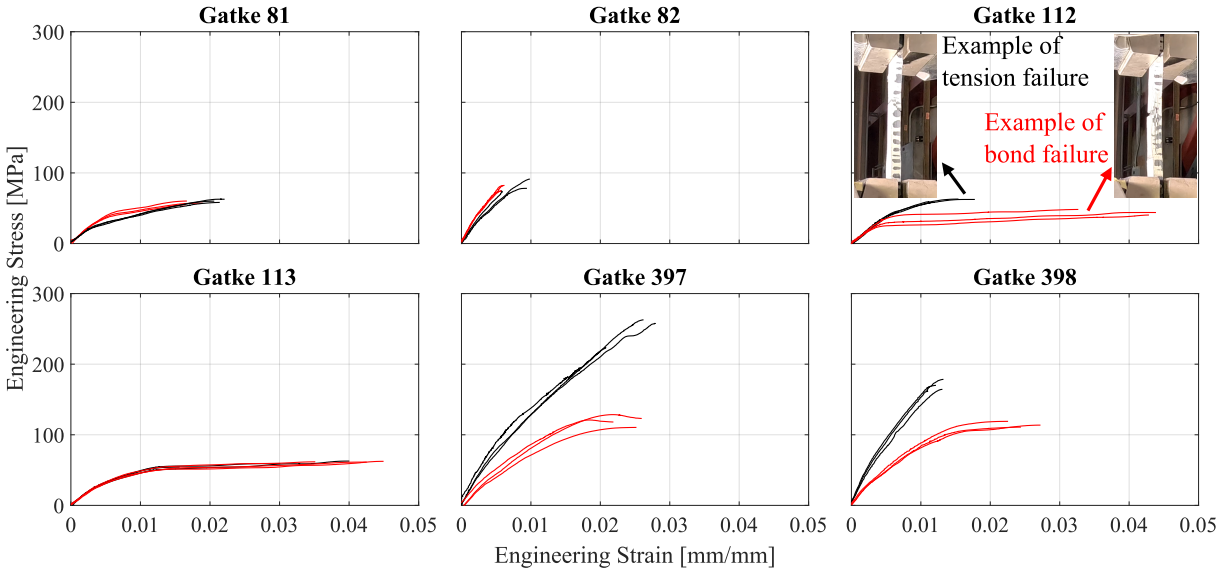

Figure 2.10. (a) Coupon tensile test results: engineering stress-strain curves upon failure (example photos of two Gatke 112 specimens with different failure modes are shown with Gatke 112 results)

Table 2.3. Summary of Mean Material Tensile Properties from the Coupon Tensile Test

Materials	**Direction**	**Yield Strength**[ab] σ_y **[MPa]**	**Tensile Strength** σ_u **[MPa]**	**Modulus of Elasticity** E **[GPa]**	**Poisson's Ratio** ν **[-]**	**Yield Strain** ε_y **[mm/mm]**	**Tensile Strain at Break** ε_b **[mm/mm]**	**Ductility** μ_d **[-]**	**Primary Failure Mode**
Gatke 81	Warp	32.71	60.34	7.26	0.20∼0.25	0.0065	0.0214	3.294	Tension
	Weft	42.69	57.38	9.20	0.25∼0.30	0.0068	0.0174	2.548	Tension
Gatke 82	Warp	-	81.42	14.13	0.10∼0.20	-	0.0080	-	Tension
	Weft	-	79.69	18.52	0.15∼0.20	-	0.0057	-	Tension
Gatke 112	Warp	47.80	61.49	8.80	0.25∼0.30	0.0075	0.0148	1.978	Tension
	Weft	31.95	44.20	7.38	0.20∼0.30	0.0064	0.0398	6.200	Bond
Gatke 113	N/A	38.97	61.50	7.96	0.25∼0.30	0.0070	0.0386	5.506	Tension
Gatke 397	Warp	120.56	248.06	17.38	0.20∼0.30	0.0090	0.0250	2.787	Tension
	Weft	64.22	119.96	11.39	0.10∼0.15	0.0076	0.0244	3.192	Bond + Tension
Gatke 398	Warp	133.24	170.97	20.71	0.05∼0.20	0.0085	0.0128	1.511	Tension
	Weft	68.57	114.52	12.52	0.05∼0.20	0.0075	0.0247	3.302	Bond + Tension

[a] 0.2% offset yield strength was considered as the materials' yield strength.

[b] In the case of Gatke 82, the ultimate tensile strain was too small that the 0.2% offset line did not have intersection with the stress-strain curve.

As shown in Figure 2.10 and Table 2.3, the directionality with respect to warp and weft directions was observed in all materials except for Gatke 113. Fiber-reinforced composite laminated materials exhibit directionality because of the directionality of their constituents. Specifically, fiber cloth has a higher tensile strength in the warp direction than in the weft direction, resulting in the directionality of laminated composites with respect to strength. From Table 2.3, it is observed that in addition to strength, other engineering parameters, including modulus of elasticity (E), Poisson's ratio (ν), yield strain (ε_y), tensile strain at break (ε_b), and ductility (μ_d), also exhibited directionality with respect to warp and weft directions. In the case of Gatke 113, hypothetically during the manufacturing process, the orientation of the fiber cloth was not tightly controlled during the stacking process; as a result, the warp and weft directions were potentially interchanged, resulting in the loss of directionality for Gatke 113. Hypothetically, a more consistent result with respect to tensile strength could be obtained if tighter quality control were imposed on the stacking of fiber cloths during the manufacturing process.

For Gatke 112, 397, and 398, two different failure modes (i.e., tension failure and bond failure) were observed. Example photos of two Gatke 112 specimens with different failure modes are shown in Figure 2.10. The different failure modes were attributed to the inhomogeneous distribution of raw material constituents from manufacturing. As discussed in Section 2.2.2, the flash compression molding process can produce composite material plates having inconsistent density due to overflow of overcharged resin. The seepage of overcharged resin results in regions with a lower concentration of resin than anticipated. From Gatke 112 results, it is observed that tensile coupon specimens that exhibited bond failure during the tensile test appeared to be sampled from regions with a lower concentration of resin. A lower concentration of resin led to weaker bonding between the laminates and exacerbated the delamination of the composite material. This effect consequently resulted in bond failure of the tensile coupon specimen.

2.4.2 Plate Bearing Test

Figure 2.11 shows the bearing force versus the recorded displacement plots of all bearing plate specimens. In the bearing test, the bearing force started increasing once the bearing fastener was in contact with the bolt hole edge of the bearing plate specimen. The recorded displacement response consisted of three parts: bearing fastener deformation, fixture deformation, and bearing plate specimen deformation. The bearing fastener was assumed to deform elastically and the elastic deformation was considered negligible compared with the recorded displacement response. The fixture deformation was computed using the DIC technique and measured to be in the order of 0.03 mm. It was less than one percent of the recorded displacement response and therefore, the fixture deformation was also considered negligible. The recorded displacement response was considered representative of the bearing plate specimen deformation. Note that for Gatke 81, there was one test in which an excessive clamping torque was applied, resulting in a tensile failure outside the bolt hole region. This test was considered invalid and marked in gray in Figure 2.11.

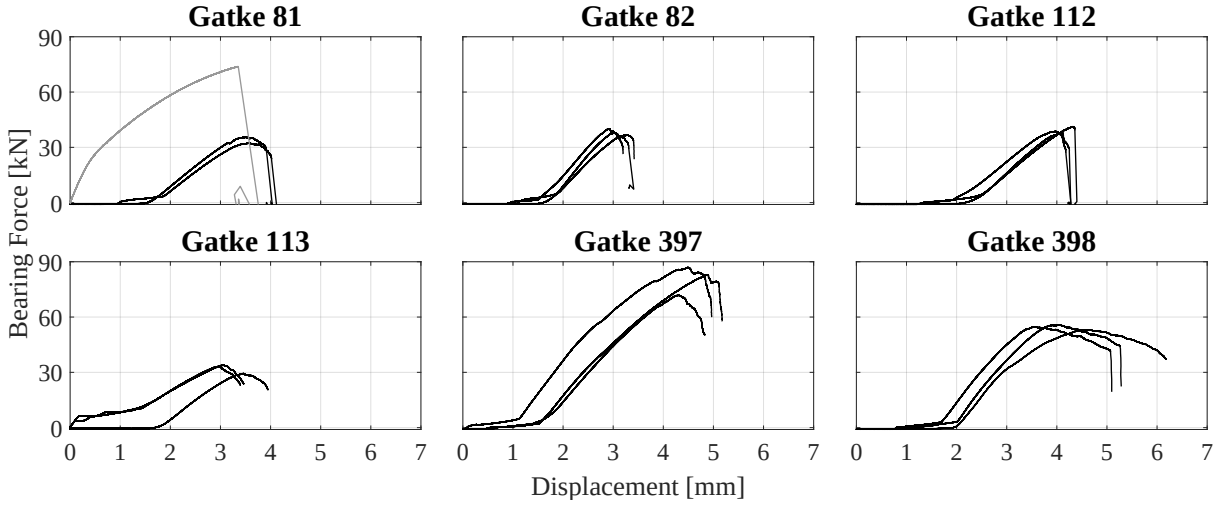

Figure 2.11. Plate bearing test results: bearing force versus the recorded displacement

Table 2.4 summarizes the mean material bearing properties, including the mean ultimate

bearing strength F^{bru} and failure modes of the specimens. Per ASTM D5961, F^{bru} is equal to:

$$F^{bru} = \frac{P_u}{kDh} \tag{2.1}$$

Where P_u is the maximum bearing load that the specimen sustained prior to failure; k is the load-per-hole factor and is equal to one for assembly with one bearing fastener; D is the bolt hole diameter and h is the thickness of the bearing plate specimen. The formula provided by ASTM D5961 computes the material ultimate bearing strength in an average sense and does not take stress concentration into consideration. As summarized in Table 2.4, two failure modes, i.e., net tension and cleavage [115], were observed in the test. Pure bearing failure characterized by significant elongation of bolt holes was not observed in this test because the clamping torque applied was considered minimal and therefore, the confinement from the adjacent assembly to the bearing plate specimen was minimal, which inhibited the formation of the pure bearing failure mode.

Table 2.4. Summary of Mean Ultimate Bearing Strengths and Specimen Failure Modes from the Plate Bearing Test

Materials	**Mean Ultimate Bearing Strength F^{bru} [MPa]**	**Failure Mode**
Gatke 81	112.03	All specimens failed due to net tension
Gatke 82	126.58	All specimens failed due to cleavage
Gatke 112	129.72	All specimens failed due to net tension
Gatke 113	106.36	All specimens failed due to net tension
Gatke 397	266.53	All specimens failed due to cleavage
Gatke 398	180.06	One specimen failed due to net tension; two specimens failed due to cleavage

2.4.3 Bolt Relaxation Test

Figure 2.12 shows the bolt relaxation test results, in which the time history of the normalized bolt load, i.e., recorded bolt load normalized by the initial bolt load (N/N_{ini}), is plotted. Figure 2.13 (a) further summarizes the percentage of bolt load loss of each specimen

upon reaching the steady state. As observed in Figure 2.13 (a), the specimens with A36 steel plates being clamped, as expected, exhibited the least percentage of bolt load loss. Except for three specimens, the specimens with composite friction material plates being clamped, regardless of the material type, exhibited a percentage of bolt load loss ranging approximately from 4.5% to 15%. In one specimen with a Gatke 81 plate being clamped under high bolt load, a 18.55% bolt load loss was observed. In one specimen with a Gatke 113 plate being clamped under low bolt load, a 26.04% bolt load loss was observed. It is noteworthy that in one specimen with a Gatke 112 plate being clamped under high bolt load as highlighted in Figure 2.13 (a), a 37.12% bolt load loss was observed. This outlier case of the Gatke 112 specimen was further investigated and explained in follow-up paragraphs. For Gatke 81, 112, and 398, test specimens under high bolt load overall exhibited an increased percentage of bolt load loss compared with test specimens under low bolt load. In contrast, for Gatke 82, 113, and 397, test specimens under high bolt load overall exhibited a similar or decreased percentage of bolt load loss compared with test specimens with low bolt load. For the materials that were tested, the correlation between material constituents and the percentage of bolt load loss was insignificant.

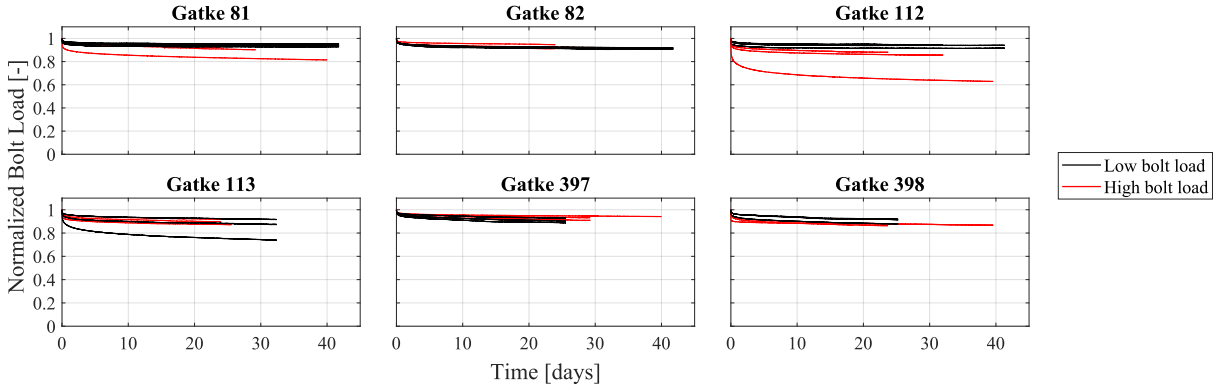

Figure 2.12. Bolt relaxation test results: normalized bolt load (N/N_{ini}) time history

The outlier case of the Gatke 112 specimen with a bolt load loss of 37.12% was further investigated. An optical microscope (VHX-1000, Keyence [126], USA) was adopted to examine the cross section of the specimen. Microscopy images are shown in Figure 2.13 (b). Compared with another rectangular specimen sampled near the center of the machined plate of which the

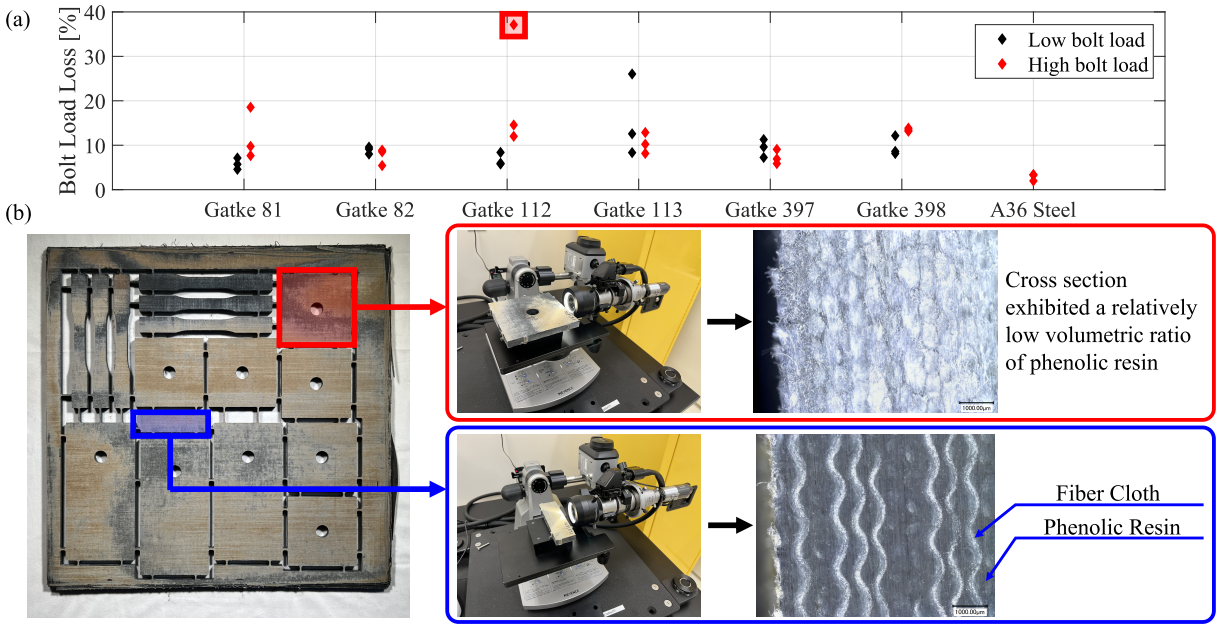

Figure 2.13. (a) Bolt load loss of all test specimens upon reaching the steady state of the bolt load; one of the results of Gatke 112 specimens with the largest bolt load loss of 37.12% is highlighted (b) Microscopy images of the Gatke 112 specimen with 37.12% bolt load loss and another specimen sampled in the region with appropriate volumetric ratio of phenolic resin

cross sectional view exhibited a clear and well-defined laminated structure, the cross sectional view of the Gatke 112 specimen with a bolt load loss of 37.12% exhibited a relatively low volumetric ratio of phenolic resin. Although the images of the outlier Gatke 113 specimen (with a bolt load loss of 26.04% under a low bolt load) were not presented, the examination of the specimen confirmed that it had the same issue as the outlier Gatke 112 specimen, that the cross section of the outlier Gatke 113 specimen also exhibited a relatively low volumetric ratio of phenolic resin. The observed relatively low volumetric ratio of phenolic resin in the outlier specimens was attributed to the manufacturing defect. As discussed in Section 2.2.2, the flash molding technique could result in products having inconsistent density due to overflow of overcharged resin. From Figure 2.13 (b), it can be observed that the Gatke 112 specimen with a bolt load loss of 37.12% was sampled close to the edge of the material plate, where the seepage of overcharged phenolic resin happened. The overflow of overcharged phenolic resin left the region close to the edge of the material plate lack of phenolic resin and resulted

in an excessive percentage of bolt load loss of the specimen. Figure 2.14 shows the images of the pressure recording films of two Gatke 112 specimens from the bolt relaxation test. On the pressure recording films, pink areas represent areas that carried the normal load. Two patterns of normal pressure distribution can be observed. For the case with a bolt load loss of 37.12%, the normal pressure was concentrated around the bolt hole while for the case with a bolt load loss of 11.16%, the distribution of the normal pressure was more uniform. From the result of Gatke 112 specimens, it can be observed that the specimen with a concentrated normal pressure distribution pattern had a higher percentage of bolt load loss compared with the specimen with a more uniformly distributed normal pressure pattern. The normal pressure distribution pattern reflected the compressive stiffness of the specimen in the through-thickness direction, which was affected by the micro-structure of the composite laminates. The relatively low volumetric ratio of phenolic resin resulted in a reduced compressive stiffness of the specimen in the through-thickness direction, causing the normal pressure in the through-thickness direction to be more concentrated around the bolt hole, and consequently resulted in an excessive percentage of bolt load loss. The results of the bolt relaxation test highlighted the importance of quality control in the manufacturing process of composite friction materials for friction-based structural components.

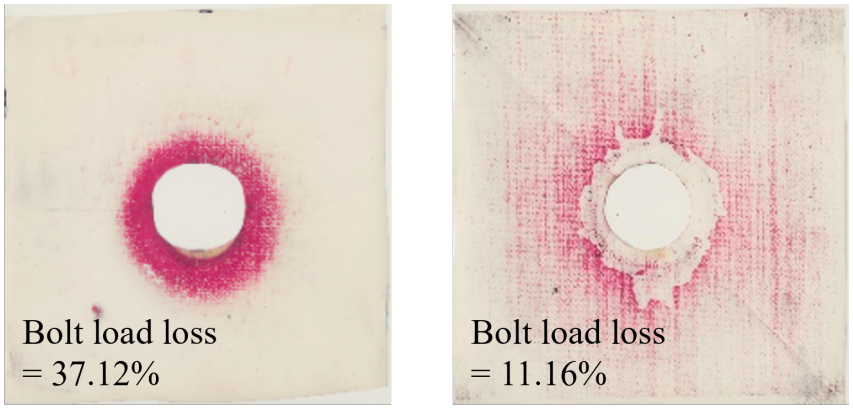

Figure 2.14. Images of pressure recording films of two Gatke 112 specimens from the bolt relaxation test

2.4.4 Friction Test

This section presents the results of the friction test. In this section, the conditions of friction shims and sliding plates are first shown. Within each test group, test data from different test IDs was grouped, processed, and analyzed, with an emphasis on different testing parameters and sliding mechanisms. Test IDs 1∼3 were grouped to assess the break-in effect of the friction interface; Test IDs 5∼10 were grouped to assess the effect of sliding velocities on the response of the friction interface; Test IDs 6, 9, 12, and 13 were grouped to assess the oscillation in friction force responses due to low-velocity stick-slip behavior; Test IDs 4, 11, and 14 were grouped to assess the response and the repeatability of the response of the friction interface under earthquake-type input excitation; Test IDs 15∼20 were grouped to assess the effect of dwell time on the response of the friction interface.

Friction Shim Conditions

Figure 2.15 shows the friction shim conditions before and after the friction test. For each test group, the photo on the left hand side shows the friction shim condition before the friction test, and the photo on the right hand side shows the friction shim condition after the friction test. For all of the friction shims, the surfaces that formed the friction interfaces turned black after the friction test. The black layer was a carbon-rich char structure as the product of the thermo-oxidative degradation process of the phenolic resin matrix [104].

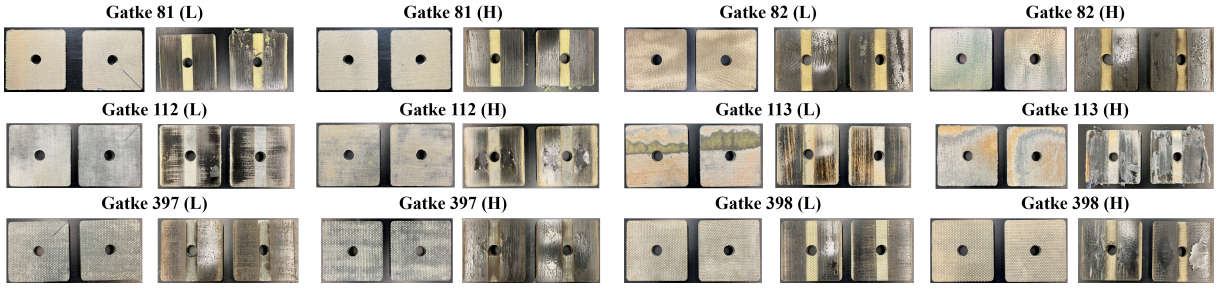

Figure 2.15. Friction shims conditions before (left) and after (right) the friction test

Out of twelve test groups, friction shims from ten test groups had no damage after the

friction test. One representative example is shown in Figure 2.16 (a). In one test group (Gatke 81 (L)), friction shims exhibited minor damage, characterized by composite materials migrating in the sliding direction under the friction force but not getting scraped off, as shown in Figure 2.16 (b). In this case, the friction test could still be continued toward the end of the loading protocol. In one test group (Gatke 113 (H)), friction shims exhibited severe damage during Test ID 1, characterized by a significant amount of material being scraped off and removed from the surface of the friction shim, as shown in Figure 2.16 (c) and (d). In this case, the friction shims were significantly thinned, inducing a drop of the bolt load by 70%. This test group was stopped prematurely after the completion of Test ID 1.

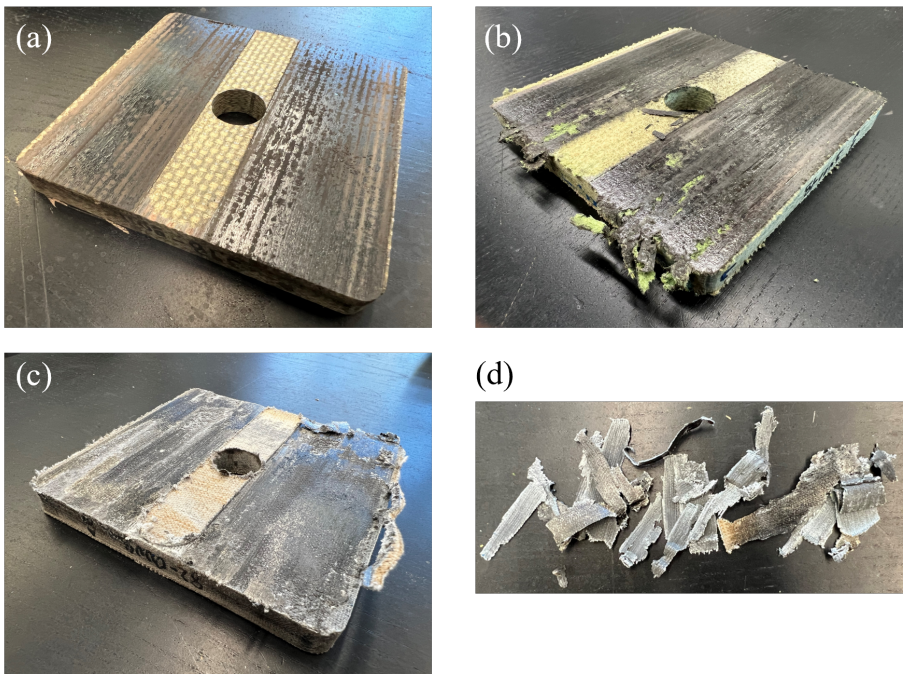

Figure 2.16. Friction shims with (a) no damage (example friction shim from Test Group Gatke 398 (L)) (b) minor damage (example friction shim from Test Group Gatke 81 (L)) (c) severe damage (example friction shim from Test Group Gatke 113 (H)) and (d) materials scraped off from the friction shim surface in (c)

Sliding Plates Conditions

As described in Section 2.3.3, after the completion of one test group, the pair of A36 steel sliding plates was removed from the test setup for inspection and cleaning purposes. Figure

2.17 (a) shows the unworn state of the A36 steel sliding plates used in this study. Figure 2.17 (b) shows one representative example of sliding plate conditions after the completion of one test group and before cleaning, from Gatke 112 (L). Friction dust was observed to spread over the surfaces of the sliding plates. Aerosol brake parts cleaner and shop towels were used to clean the sliding plates. Figure 2.17 (c) shows a representative example of the sliding plate condition after cleaning. Visual inspection of the sliding plates indicated that except for some removal of the mill scale on the sliding plate surfaces, the surface topography of the sliding plates was overall unchanged; hence, the A36 steel sliding plates were reused for all test groups in this study.

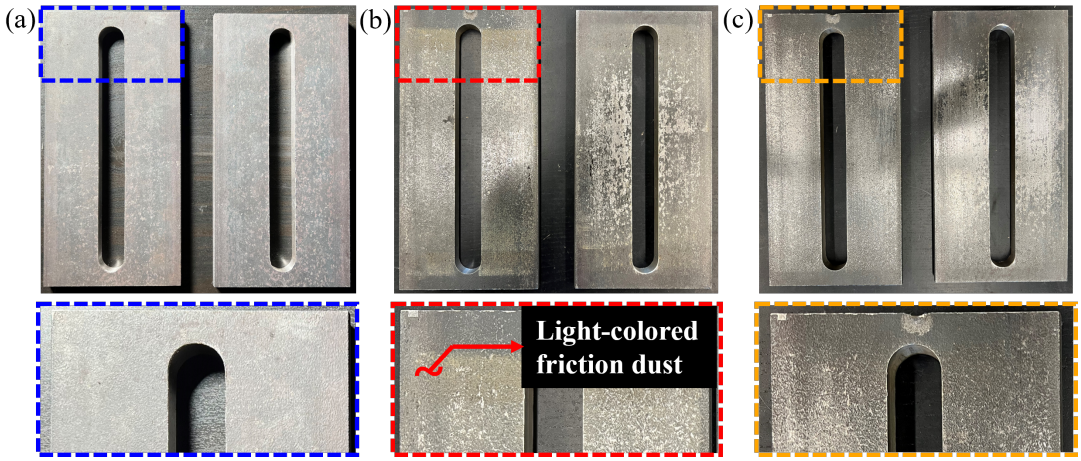

Figure 2.17. (a) Unworn sliding plates before the friction test (b) Representative example of sliding plates conditions after completing one test group (Gatke 112 (L)) and before cleaning (c) Representative example of sliding plates conditions after cleaning using aerosol brake parts cleaner and heavy-duty shop towels

Break-in Effect Assessment

According to Blau [87], the break-in process is defined as the initial sliding process when two surfaces are first brought into contact under the normal load and start sliding relative to each other, in which changes in the surface conditions occur. During the break-in process, changes in the coefficient of friction and the wear rate of a friction interface usually happened. After the break-in process, the coefficient of friction and the wear rate of a friction interface would reach a relatively constant level, and Blau [87] defined this state as the ”steady state”. The break-in

effect is defined as the effect of the break-in process on the response of the friction interface.

Figure 2.18 shows the assessment results of the break-in effect. The computed coefficient of friction (COF) $\mu_{computed}$ is defined as $\mu_{\text{computed}} = \left|\frac{f}{n_b n_s N}\right|$, where f is the recorded connection force, n_b = 1 is the number of bolts that provided normal force onto the friction interface, n_s = 2 is the number of friction interfaces that contributed to the friction force, and N is the recorded bolt load. The absolute operator is to account for the fact that the coefficient of friction μ has to be positive. In Figure 2.18, each purple circular marker represents the mean $\mu_{computed}$ within one sliding travel, where the sliding travel is defined as the sliding between two consecutive points of zero sliding velocity (i.e., the sliding direction is monotonic within one sliding travel), and its corresponding mean cumulative displacement within this sliding travel. To analyze the break-in effect quantitatively, regression analysis with a Logistic function was performed for purple circular markers. The Logistic function is defined as:

$$\mu = \frac{L}{1 + e^{-k(x - x_0)}} \tag{2.2}$$

Where μ is the coefficient of friction and x is the cumulative displacement. L, k, and x_0 are three parameters of the Logistic function to be obtained from the regression analysis. L is mathematically the maximum value of the Logistic function and physically represents the steady-state coefficient of friction of the friction interface given the Logistic function model; k and x_0 define the steepness of the function and x-value of the inflection point of the function, respectively. They don't have physical meanings in this context but assist in obtaining quantities of interest. As a standard practice, the fitness of the obtained Logistic function model from the regression analysis for the data points was quantified by the coefficient of determination, R^2 (R-squared). R^2 values of each test group are summarized in Table 2.5. Overall, the Logistic function had a good fit with the data points, indicated by an R^2 value larger than 0.8. One exception was Test Group Gatke 112 (H), in which an R^2 value equal to 0.32 was obtained from the regression analysis. From Figure 2.18, it is observed that for Test Group Gatke 112 (H), as the cumulative

displacement increased, the coefficient of friction increased, reached a peak, and then decreased. The Logistic function could not capture the declining trend and therefore, could not fit well with the data points for Test Group Gatke 112 (H).

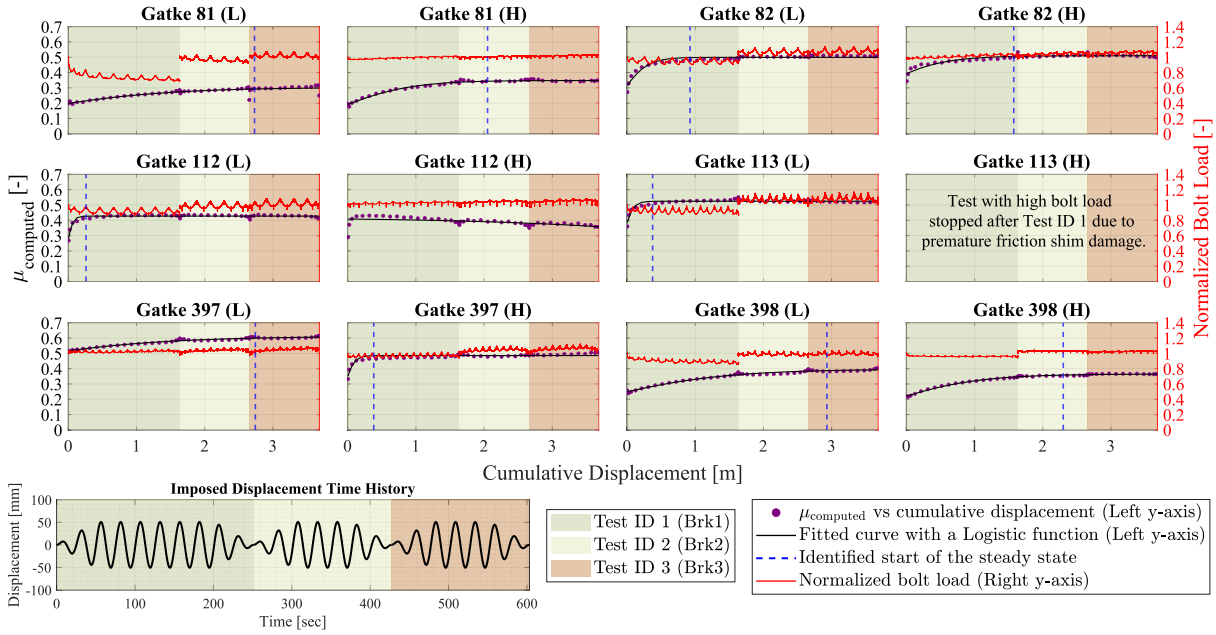

Figure 2.18. Assessment of the break-in effect

Except for Test Groups Gatke 112 (H) and Gatke 113 (H), the identified steady-state coefficients of friction, i.e., parameters L for the fitted Logistic function, are termed μ_{ss} and are summarized in Table 2.5. The mean coefficients of friction from Test ID 4 (termed $\overline{\mu_4}$) are also summarized in Table 2.5 and the relative difference between μ_{ss} and $\overline{\mu_4}$ is computed as $\delta_{ss\text{-}4} = \frac{\overline{\mu_4} - \mu_{ss}}{\mu_{ss}}$ and is reported in Table 2.5. It is noted that for all test groups, the magnitude of $\delta_{ss\text{-}4}$ was less than 10%, which proved that upon the establishment of the break-in effect, the coefficient of friction reached a relatively constant level and also, the fitted Logistic function overall captured the break-in response of the friction interfaces. The relative difference between the initial coefficients of friction from Test ID 1 (termed μ_{ini}) and μ_{ss} is computed as $\delta_{ini\text{-}ss} = \frac{\mu_{ss} - \mu_{ini}}{\mu_{ini}}$ and is also reported in Table 2.5.

In this study, the start of the steady state is defined as when the derivative of the fitted Logistic function, $\frac{d\mu}{dx}$, reaches 0.01. The cumulative displacements at the start of the steady state,

Table 2.5. Summary of Break-in Effect Assessment Results

Test Group	Initial COF from Test ID 1 μ_{ini}	Logistic Function Regression Analysis			Mean COF from Test ID 4 $\overline{\mu_4}$	Relative Difference Computation	
		R^2	Identified Steady-State COF μ_{ss}	Identified Steady-State Cumulative Displacement [m]		$\delta_{ss\text{-}4}$[a]	$\delta_{ini\text{-}ss}$[b]
Gatke 81 (L)	0.213	0.83	0.303	2.730	0.326	7.51%	42.27%
Gatke 81 (H)	0.194	0.98	0.348	2.051	0.355	1.92%	79.15%
Gatke 82 (L)	0.272	0.92	0.499	0.924	0.518	3.73%	83.30%
Gatke 82 (H)	0.343	0.88	0.510	1.574	0.490	-3.85%	48.67%
Gatke 112 (L)	0.268	0.90	0.427	0.259	0.421	-1.52%	59.65%
Gatke 112 (H)	0.289	0.32	N/A	N/A	0.356	N/A	N/A
Gatke 113 (L)	0.378	0.88	0.525	0.375	0.527	0.40%	38.88%
Gatke 113 (H)				N/A			
Gatke 397 (L)	0.518	0.96	0.613	2.742	0.608	-0.80%	18.35%
Gatke 397 (H)	0.332	0.82	0.486	0.382	0.509	4.85%	46.27%
Gatke 398 (L)	0.265	0.97	0.397	2.930	0.422	6.48%	49.78%
Gatke 398 (H)	0.221	0.99	0.365	2.300	0.380	4.19%	65.29%

[a] $\delta_{ss\text{-}4} = (\overline{\mu_4} - \mu_{ss})/\mu_{ss}$.
[b] $\delta_{ini\text{-}ss} = (\mu_{ss} - \mu_{ini})/\mu_{ini}$.

termed the identified steady-state cumulative displacement, are summarized in Table 2.5 and are plotted in Figure 2.18 in dashed blue lines. From Table 2.5 and Figure 2.18, it is observed that the break-in effect depends on the material constituents of the composite friction materials and the normal load level. Cotton-fiber-reinforced composite friction materials (Gatke 112 and 113) had shorter steady-state cumulative displacements than glass-fiber-reinforced composite friction materials (Gatke 81, 82, 397, and 398), which indicated a faster establishment of the break-in effect. This is because for the composite-metallic friction interfaces tested in this study, the break-in effect is mainly attributed to the worn-out of surface asperities, which induces an increase in the real contact area and the adhesive friction [87] [127] [128] [129]. Cotton fibers had a lower hardness than glass fibers, which potentially made the worn-out of surface asperities easier than that of glass fibers. Except for Gatke 82, a higher normal load overall resulted in a faster break-in process. This is because a higher normal load potentially enhanced the process of wearing out surface asperities.

Figure 2.18 also presents the normalized bolt load ($\frac{N}{N_{target}}$) history within the break-in tests. It can be observed that bolt load loss was most significant within break-in tests one (Brk1) and was reduced as break-in tests continued. The bolt load variation reflected the wear mechanism of the friction interface. At the beginning of sliding, besides the break-in process, the wear-in process also happened, in which a steady-state wear rate was to be reached [87]. According to the non-linear model of the wear behavior [130], the wear rate was higher at the beginning of sliding. A higher wear rate increased the wear volume, causing the friction shims to be thinner. This mechanism induced a higher bolt load loss as observed in break-in tests one. As the cumulative displacement increased, the wear rate was reduced, making the increase of the wear volume slower and therefore, induced a smaller bolt load loss as observed in break-in tests two and three.

Effect of Sliding Velocity

Figure 2.19 shows the assessment of the effect of sliding velocities on the response of the friction interface. In Figure 2.19, each black circular marker represents the mean $\mu_{computed}$ of one

sliding travel, and the computation method of $\mu_{computed}$ was the same as in Section 2.4.4. The x-axis, starting from zero, represents the testing period of Test IDs 5∼10 with the ten seconds dwell time between tests being excluded. Figure 2.19 shows the evolution of $\mu_{computed}$ in Test IDs 5∼10. In Figure 2.19, light red lines represent the time history of the absolute sliding velocity, which was computed from the recorded displacement response. It is noted that for test groups with high normal load, the peak sliding velocity of Test IDs 7 and 8 was lower than the target imposed peak sliding velocity in Figure 2.8. This was attributed to the stalling of the testing machine caused by the hydraulic supply capacity limitation.

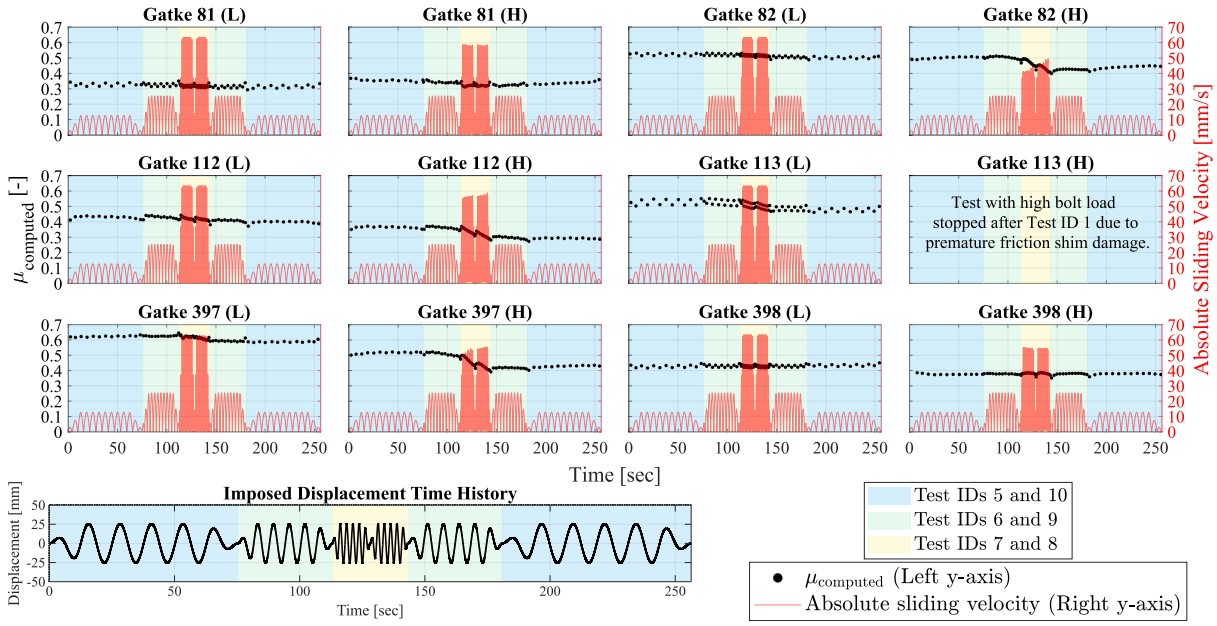

Figure 2.19. Assessment of effect of sliding velocity (Test IDs 5∼10)

The mean coefficient of friction for Test ID i, termed $\overline{\mu_i}$, is summarized in Table 2.6 for Test IDs 5∼10 for all test groups except for Test Group Gatke 113 (H). The relative difference between mean coefficients of friction for Test ID i ($\overline{\mu_i}$) within Test IDs 5∼10 and the mean coefficient of friction for Test ID 5 ($\overline{\mu_5}$) is computed as $\delta_{i\text{-}5} = \frac{\overline{\mu_i} - \overline{\mu_5}}{\overline{\mu_5}}$. The computed relative difference for all test groups except for Test Group Gatke 113 (H) is also reported in Table 2.6 and is shown in Figure 2.20. From Figure 2.19 and Table 2.6, it is observed that except for Test Groups Gatke 398 (L) and (H), an increase in the sliding velocity overall induced a decrease in

the coefficient of friction μ. Figure 2.20 shows that the decrease in μ was more significant in test groups with high normal load than test groups with low normal load. Figure 2.20 also shows that for test groups with glass-fiber-reinforced composite friction materials such as Test Groups Gatke 81 (H), Gatke 82 (H), and Gatke 397 (H), μ exhibited an increase in follow-up tests with lower sliding velocities; while for test groups with cotton-fiber-reinforced composite friction materials such as Test Groups Gatke 112 (L) and (H), a further decrease in μ was observed in follow-up tests with lower sliding velocities.

Table 2.6. Summary of Mean COF ($\overline{\mu_i}$) and Relative Difference between $\overline{\mu_i}$ and $\overline{\mu_5}$ ($\delta_{i\text{-}5}$) for Test IDs 5$\sim$10

Test Group	$\overline{\mu_5}$ ($\delta_{5\text{-}5}$)	$\overline{\mu_6}$ ($\delta_{6\text{-}5}$)	$\overline{\mu_7}$ ($\delta_{7\text{-}5}$)	$\overline{\mu_8}$ ($\delta_{8\text{-}5}$)	$\overline{\mu_9}$ ($\delta_{9\text{-}5}$)	$\overline{\mu_{10}}$ ($\delta_{10\text{-}5}$)
Gatke 81 (L)	0.33 (0.00%)	0.32 (-3.03%)	0.32 (-3.03%)	0.32 (-3.03%)	0.31 (-6.06%)	0.32 (-3.03%)
Gatke 81 (H)	0.35 (0.00%)	0.35 (0.00%)	0.32 (-8.57%)	0.32 (-8.57%)	0.33 (-5.71%)	0.34 (-2.86%)
Gatke 82 (L)	0.52 (0.00%)	0.52 (0.00%)	0.52 (0.00%)	0.51 (-1.92%)	0.51 (-1.92%)	0.50 (-3.85%)
Gatke 82 (H)	0.50 (0.00%)	0.51 (2.00%)	0.48 (-4.00%)	0.44 (-12.00%)	0.42 (-16.00%)	0.44 (-12.00%)
Gatke 112 (L)	0.43 (0.00%)	0.43 (0.00%)	0.42 (-2.33%)	0.42 (-2.33%)	0.41 (-4.65%)	0.40 (-6.98%)
Gatke 112 (H)	0.37 (0.00%)	0.36 (-2.70%)	0.34 (-8.11%)	0.31 (-16.22%)	0.30 (-18.92%)	0.29 (-21.62%)
Gatke 113 (L)	0.53 (0.00%)	0.53 (0.00%)	0.51 (-3.77%)	0.50 (-5.66%)	0.48 (-9.43%)	0.48 (-9.43%)
Gatke 113 (H)				N/A		
Gatke 397 (L)	0.62 (0.00%)	0.63 (1.61%)	0.62 (0.00%)	0.61 (-1.61%)	0.59 (-4.84%)	0.59 (-4.84%)
Gatke 397 (H)	0.52 (0.00%)	0.51 (-1.92%)	0.47 (-9.62%)	0.43 (-17.31%)	0.42 (-19.23%)	0.43 (-17.31%)
Gatke 398 (L)	0.43 (0.00%)	0.43 (0.00%)	0.43 (0.00%)	0.43 (0.00%)	0.43 (0.00%)	0.43 (0.00%)
Gatke 398 (H)	0.38 (0.00%)	0.38 (0.00%)	0.38 (0.00%)	0.38 (0.00%)	0.38 (0.00%)	0.38 (0.00%)

Similar velocity-dependent variation of the coefficient of friction has been observed in past experimental tests of composite-metallic friction interfaces [2] [131]. Bowden and Tabor's adhesive friction theory [83] [132] is introduced herein to explain the observed velocity-dependent variation of the coefficient of friction. Figure 2.21 presents a schematic explanation of Bowden and Tabor's adhesive friction theory. The theory suggests that when two surfaces are in contact under a certain normal pressure, the contact happens at the highest peaks, and the real contact area is much smaller than the total contact area. Locally, the normal stress could be high enough so that plastic deformation of the materials occurs. Adhesion junctions are formed at the contact points. When sliding occurs between these two surfaces, the friction force generated at the friction interface comes from two sources: shearing of the adhesion junctions, and the

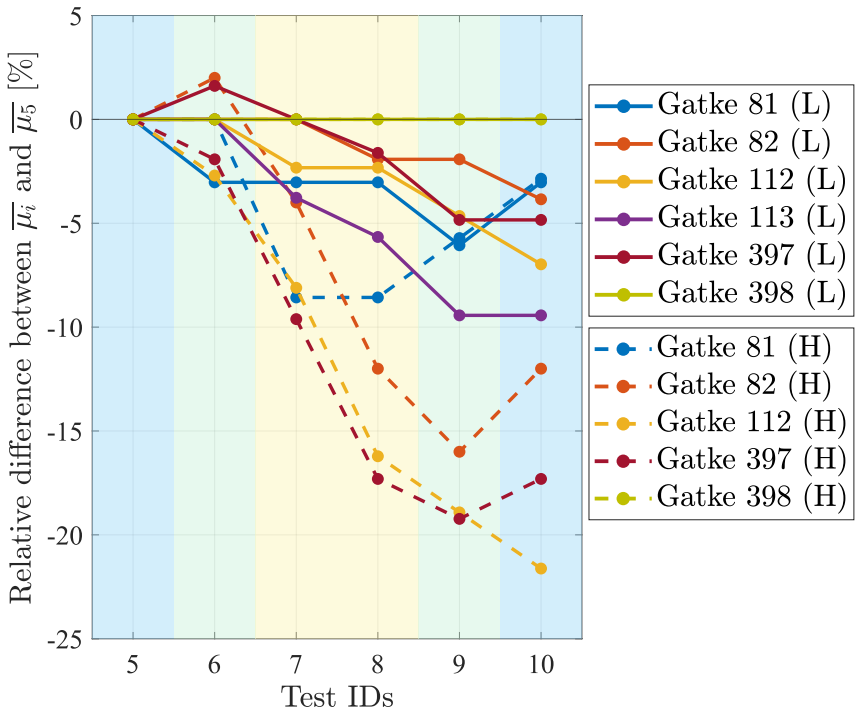

Figure 2.20. Relative difference between $\overline{\mu_i}$ and $\overline{\mu_5}$ in Test IDs 5∼10

plowing of hard materials into soft materials. For composite-metallic friction interfaces used in structural engineering applications, the contribution of plowing could be considered negligible. Figure 2.22 (a) presents the state of the friction interface after the establishment of the break-in effect (i.e., the friction interface reached a steady state as defined in Section 2.4.4) as at the beginning of Test ID 5, represented schematically by a single adhesion junction. In this state, the normal force is termed N; the friction force is termed f_{ss}; the real contact area is termed $A_{j,ss}$; the normal pressure developed at this adhesion junction is termed σ_{ss}; the shear strength of this adhesion junction is termed τ_{ss}; the coefficient of friction of the friction interface, which is the steady state coefficient of friction, is termed μ_{ss}. By force equilibrium, the friction interface has:

$$\begin{aligned} N &= A_{j,ss}\sigma_{ss} \\ f_{ss} &= A_{j,ss}\tau_{ss} \\ \mu_{ss} &= \frac{f_{ss}}{N} = \frac{A_{j,ss}\tau_{ss}}{A_{j,ss}\sigma_{ss}} = \frac{\tau_{ss}}{\sigma_{ss}} \end{aligned} \tag{2.3}$$

Figure 2.22 (b) presents the state of the friction interface under an increased sliding velocity during Test IDs 7∼8. In the discussion of the effect of the sliding velocity on the response of the friction interface, the normal load N is assumed to remain relatively constant. A detailed discussion on the variation of the normal load is presented in Section 2.4.4. Under a higher sliding velocity, the wear rate increased. The increased wear rate resulted in increased generation and accumulation of wear particles at the friction interface. The accumulation of wear particles potentially reduced the shear strength of the adhesion junction from τ_{ss} to τ_f ($\tau_f < \tau_{ss}$). In addition, the increased wear rate potentially caused the real contact area to reduce from $A_{j,ss}$ to $A_{j,f}$ [2], resulting in an increased normal pressure at the adhesion junction ($\sigma_f > \sigma_{ss}$). For this new state, the friction interface has:

$$\mu_f = \frac{\tau_f}{\sigma_f} < \frac{\tau_{ss}}{\sigma_{ss}} = \mu_{ss} \tag{2.4}$$

Equation 2.4 explained the observed decrease in the coefficient of friction μ associated with the increase in the sliding velocity in Test IDs 7∼8 as shown in Figures 2.19 and 2.20.

Figure 2.22 (c) presents the state of the friction interface under a lower sliding velocity during Test IDs 9∼10. Under a lower sliding velocity, the wear rate decreased and in the meantime, previously generated wear particles got evacuated from the friction interface. The evacuation of wear particles potentially induced an increase in the shear strength of the adhesion junction from τ_f to τ_s ($\tau_s > \tau_f$). In addition, under a lower sliding velocity, the rejuvenation of the friction interface potentially caused the real contact area to increase from $A_{j,f}$ to $A_{j,s}$ [2], resulting in a decrease in the normal pressure at the adhesion junction ($\sigma_s < \sigma_f$). For this new state, the friction interface has:

$$\mu_s = \frac{\tau_s}{\sigma_s} > \frac{\tau_f}{\sigma_f} = \mu_f \tag{2.5}$$

Equation 2.5 explained the observed increase in the coefficient of friction μ associated with a lower sliding velocity in Test IDs 9∼10 as shown in Figures 2.19 and 2.20.

In summary, the above explanation highlights the competing effect of two processes: wear particles generation and accumulation at the friction interface versus wear particles evacuation from the friction interface. When the sliding velocity was relatively high, the rate of wear particles generation and accumulation at the friction interface was effectively higher than the rate of wear particles evacuation from the friction interface, and this tended to induce a decrease in the coefficient of friction (as during Test IDs 7∼8). In contrast, when the sliding velocity was relatively low, the rate of wear particles generation and accumulation at the friction interface was effectively lower than the rate of wear particles evacuation from the friction interface, and this tended to induce an increase in the coefficient of friction (as during Test IDs 9∼10).

Based on the explanation above, the effect of material constituents on the velocity-dependent frictional behavior is discussed herein. In Test IDs 9∼10, the difference between the frictional behavior of friction interfaces with glass-fiber-reinforced composite friction materials and those with cotton-fiber-reinforced composite friction materials can be potentially explained as follows: Glass fibers have higher hardness than cotton fibers, and therefore, glass fibers potentially enhanced the evacuation of wear particles from the friction interface. For friction interfaces with glass-fiber-reinforced composite friction materials, a larger percentage of increase in the coefficient of friction was thus observed in Test IDs 9∼10. For friction interfaces with cotton-fiber-reinforced composite friction materials, the effect of the evacuation of wear particles was less significant; consequently, a similar or further decrease in the coefficient of friction was observed in Test IDs 9∼10.

In addition to the observations above, comparing the results of Test Groups Gatke 81 (H) and Gatke 82 (H), it is found that Gatke 81 (H) exhibited a less reduction in the coefficient of friction in Test IDs 7∼8 and a larger percentage of increase in the coefficient of friction in Test IDs 9∼10. Hypothetically this was attributed to the contribution of acrylic fibers and aramid fibers in Gatke 81. Comparing the results of Test Groups Gatke 81 (H), Gatke 82 (H) and Gatke 397 (H), it is found that Gatke 81 (H) and Gatke 82 (H) exhibited a larger percentage of increase in the coefficient of friction in Test IDs 9∼10 than Gatke 397 (H). Hypothetically the

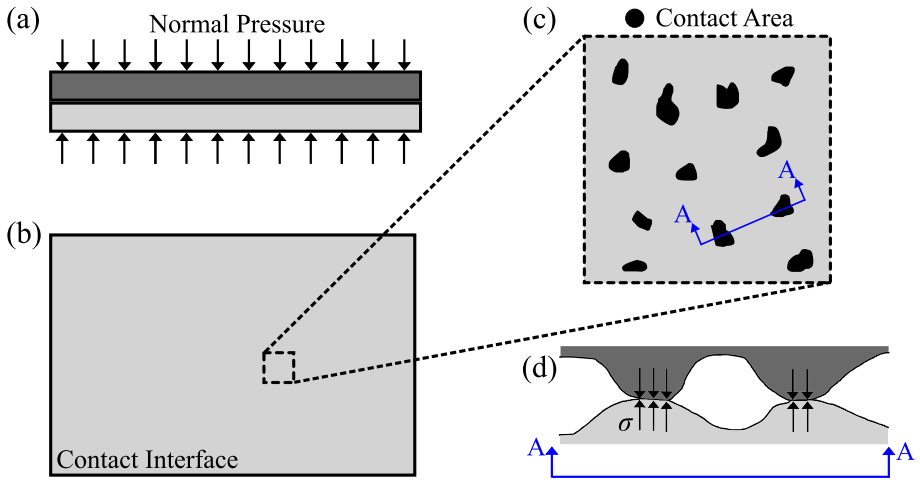

Figure 2.21. Schematic explanation of Bowden and Tabor's adhesive friction theory: (a) Two plates are clamped together under a certain normal pressure (b) Top view of the contact interface (c) Zoomed-in top view of the contact interface, with real contact areas being exaggerated (d) Zoomed-in elevation view of the contact interface at Section A-A; a normal pressure of σ is developed at the adhesion junction

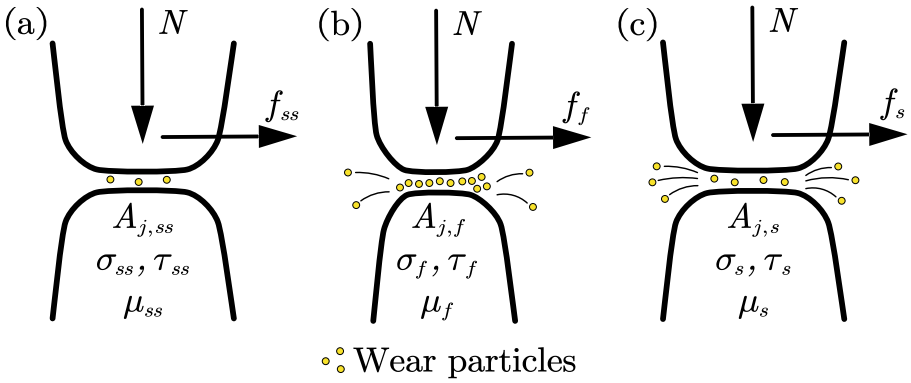

Figure 2.22. Schematic representation of the state of the friction interface (a) at the beginning of Test ID 5 (b) during Test IDs 7∼8 and (c) during Test IDs 9∼10

presence of abrasive particles (yellow iron oxide, green chromium (III) oxide, and aluminum oxide) in Gatke 81 and 82 enhanced the evacuation of wear particles. It is noteworthy that Gatke 398 exhibited the least significant velocity-dependent frictional behavior among the composite friction materials tested in this study. In both Gatke 398 (L) and (H), the average coefficient of friction $\overline{\mu}$ was the same for all tests within Test IDs 5$\sim$10. Hypothetically this was attributed to the contribution of graphite, Teflon, and molybdenum disulfide (MoS_2), which assisted in controlling the wear rate of the friction interface under different sliding velocities.

Oscillation in the Friction Force Response

Figure 2.23 (a) and (b) present the absolute sliding velocity history and the corresponding recorded friction force history of one selected representative sliding travel from Test IDs 6 and 12 in Test Groups Gatke 398 (H) and Gatke 112 (H). From Figure 2.23 (a) and (b), it can be observed that oscillation occurred in the friction force response of Gatke 398 and was associated with lower sliding velocities. Although not shown, the same observation applied to Gatke 81, 82, and 397. It is also observed that oscillation did not occur in the friction force response of Gatke 112, regardless of the sliding velocity. Although not shown, the same observation applied to Gatke 113.

Oscillation in the friction force response associated with lower sliding velocities was attributed to the stick-slip behavior of the friction interface. The stick-slip behavior of composite-metallic friction interfaces has been studied and was attributed to the change of the surface topography of the friction interface [131] [133] [134]. For friction interfaces with glass-fiber-reinforced composite friction materials, the accumulation of wear particles tended to be more localized as hard glass fibers at the friction interface facilitated the accumulation of wear particles around them. The localized accumulation and evacuation of wear particles enhanced the stick-slip behavior of the friction interface, inducing oscillation in the friction force response under low sliding velocities [131] [134]. In contrast, for friction interfaces with cotton-fiber-reinforced composite friction materials, the accumulation and evacuation of wear particles tended to be

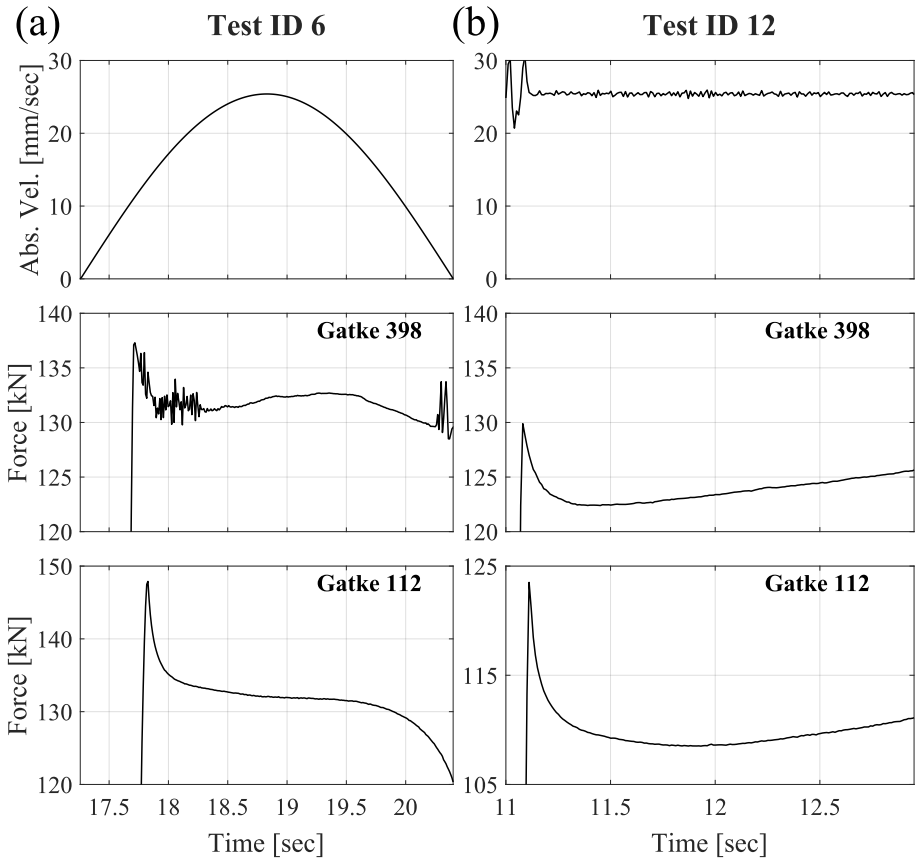

Figure 2.23. (a) Absolute sliding velocity history and recorded friction force history of one selected representative sliding travel from Test ID 6 in Test Groups Gatke 398 (H) and Gatke 112 (H) (b) Absolute sliding velocity history and recorded friction force history of one selected representative sliding travel from Test ID 12 in Test Groups Gatke 398 (H) and Gatke 112 (H)

more uniform across the friction interface, as softer cotton fibers provided limited supports for localized accumulation of wear particles. Therefore, the stick-slip behavior of friction interfaces with cotton-fiber-reinforced composite friction materials was insignificant. It should be noted that for earthquake structural engineering applications, the frequency of the oscillation in the friction force response is high relative to the frequencies of interest at the structural and nonstructural component level and the magnitude of the oscillation is low relative to typical force demands of friction-based structural components. The effect of the stick-slip behavior of composite-metallic friction interfaces could be considered insignificant for earthquake structural engineering applications.

Response of Friction Interfaces under Earthquake-type Input Excitation

Figure 2.24 shows the recorded force versus displacement responses of the tested friction interfaces under earthquake-type input excitation. For all the tested friction interfaces, the shape of the force-displacement response was close to a rectangle and thus could be idealized as a Coulomb-type force-displacement response. The force-displacement response shows the pinching displacement at zero force due to the gap between the steel channel and the friction shim. The pinching displacement at zero force was considered small and could be further reduced by a tighter tolerance control in machining the steel channels.

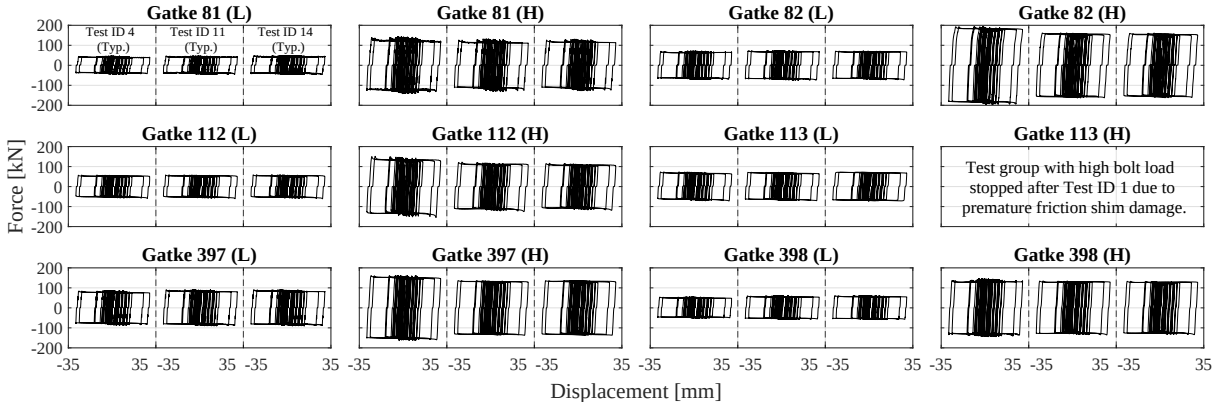

Figure 2.24. Force-displacement responses of the tested friction interfaces under earthquake-type input excitation (Test IDs 4, 11, and 14)

Figure 2.25 shows the evolution of the coefficient of friction of the tested friction interfaces with respect to the increase of the cumulative displacement under earthquake-type input excitation. In Figure 2.25, each circular marker represents the mean $\mu_{computed}$ of one sliding travel and its corresponding mean cumulative displacement within this sliding travel. The computation method was the same as in Section 2.4.4. The mean coefficients of friction within each Test ID ($\overline{\mu}$) are reported in the figure. It can be observed that within each Test ID, the coefficient of friction maintained at a relatively constant level, which was consistent with the rectangular force-displacement responses as shown in Figure 2.24. For some test groups, a difference in $\overline{\mu}$ between Test IDs can be observed, and the difference is attributed to the effect of the sliding history. As described in Section 2.3.3, between Test IDs 4 and 11, Test IDs 5∼10 assessed the effect of sliding velocities on the response of the friction interface. In some test groups, the effect of sliding velocity from Test IDs 5∼10 got carried over to follow-up tests, i.e., Test IDs 11 and 14. The details of velocity-dependent frictional behavior have been discussed in Section 2.4.4.

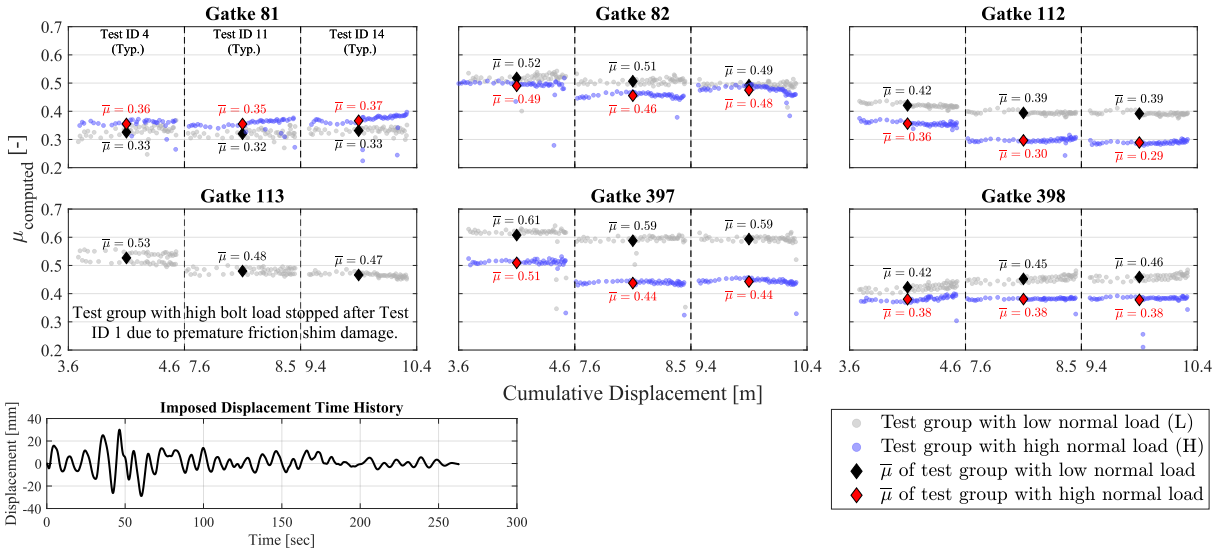

Figure 2.25. Evolution of μ of the friction interfaces under earthquake-type input excitation (Test IDs 4, 11, and 14)

From Figure 2.25, the effect of the normal load level on the magnitude of the coefficient

of friction can also be observed. Gatke 81 (H) exhibited a higher coefficient of friction than Gatke 81 (L). Hypothetically this was attributed to the contribution of aramid fibers. In contrast, for Gatke 82, 112, 397, and 398, a decrease in the coefficient of friction was observed when the normal load was increased from low to high.

Effect of Dwell Time

Figure 2.26 shows the data used to assess the effect of the dwell time on the frictional behavior. The relative difference between the mean coefficient of friction of the prior test (termed $\overline{\mu}_{pr}$) and the mean coefficient of friction of its corresponding posterior test (termed $\overline{\mu}_{po}$) was computed as $\frac{\overline{\mu}_{po}-\overline{\mu}_{pr}}{\overline{\mu}_{pr}}$ and was plotted against its corresponding dwell time (DT10s, DT10m, and DT30m). As shown in the imposed displacement time history plot (truncated to the first 100 seconds for presentation purposes) of one prior test and its corresponding posterior test, to exclude the effect of the cumulative displacement on the coefficient of friction, for prior tests, the last four sliding travels were selected for the computation of $\overline{\mu_{pr}}$, and for posterior tests, the first four sliding travels were selected for the computation of $\overline{\mu_{po}}$.

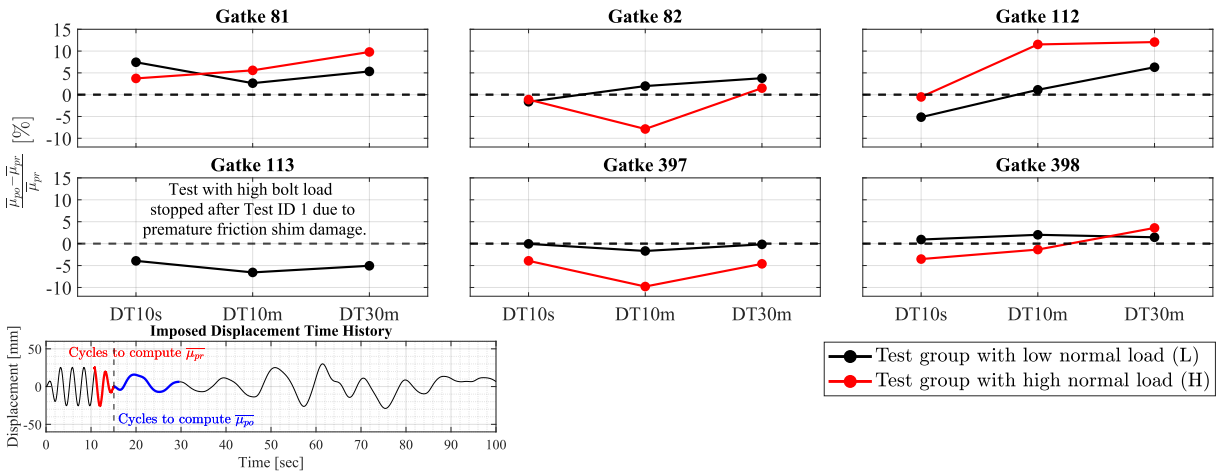

Figure 2.26. Assessment of the effect of dwell time (Test IDs 15∼20)

Figure 2.26 shows that the dwell time overall increased the coefficient of friction in cases of Gatke 81, 82, 112, and 398. Comparing the result of DT30m with DT10s and DT10m, it is observed that a longer dwell time overall induced a larger increase in the coefficient of

friction. The increase in the coefficient of friction was less than 10% except for Gatke 112 (H). The increase in the coefficient of friction associated with the dwell time can be attributed to the increase in the real contact area between two contact surfaces of the friction interface [2] [83] [135]. Figure 2.26 also shows that for Gatke 113 and 397, the dwell time induced a decrease in the coefficient of friction in all cases. The effect of dwell time on the response of friction interfaces formed by Gatke 113 and Gatke 397 in contact with low-carbon structural steel requires further investigation.

Bolt Load Variation

Figure 2.27 (a) shows the time history of the normalized bolt load (N/N_{target}) in all test groups. In Figure 2.27 (a), the bolt load time histories during the bolt retightening process and the dwell time were excluded. The normalized bolt load variation was similar in all tests. The instantaneous sliding velocity appeared to affect the bolt load. An increase in instantaneous sliding velocities resulted in a relatively small increase in the bolt load, such as in Test IDs 7 and 8. A lower instantaneous sliding velocity overall resulted in a decrease in the bolt load, such as in Test IDs 9 and 10. Figure 2.27 (b) shows the time history of the normalized bolt load of Test IDs 7 and 8 in Test Group Gatke 398 (H) as an example to further discuss this effect. In Figure 2.27 (b), the time history of the normalized bolt load during the dwell time between Test ID 7 and Test ID 8 is also presented. The colorbar defines the magnitude of the instantaneous sliding velocity. As the instantaneous velocity increased, the instantaneous bolt load increased. As the instantaneous velocity decreased, the instantaneous bolt load decreased. An overall increase of the bolt load was observed during the duration of Test ID 7 and during the duration of Test ID 8. A reduction in the bolt load was observed during the dwell time between Test ID 7 and Test ID 8.

Section 2.4.4 explains the effect of sliding velocities on the accumulation and evacuation of wear particles. The same mechanics can be adopted here to explain the variation of bolt load with respect to the variation of the instantaneous sliding velocity, as follows: When the instantaneous sliding velocity increased, the wear rate increased. As a result, the rate of

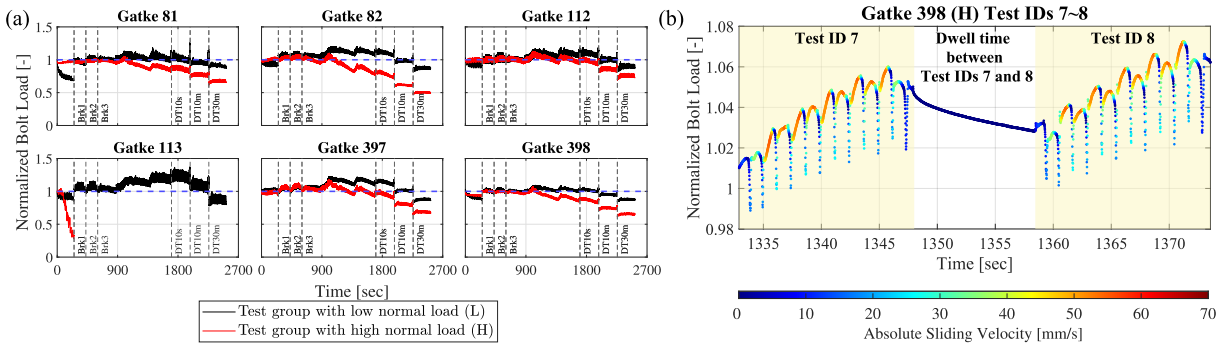

Figure 2.27. (a) Normalized bolt load time history of all test groups and (b) Normalized bolt load time history of Test IDs 7 and 8 in Test Group Gatke 398 (H); the color of the marker is defined based on the instantaneous absolute sliding velocity

accumulation of wear particles at the friction interface increased. As the cumulative sliding under relatively high instantaneous sliding velocities increased, the unstructured accumulation of wear particles effectively increased the total thickness of the bolted assembly, which in turn led to bolt elongation and an increase in the bolt load. Under a relatively low instantaneous sliding velocity, the effect of the evacuation of wear particles became more significant than the effect of the accumulation of wear particles. As the cumulative sliding under relatively low instantaneous sliding velocities increased, the evacuation of wear particles reduced the total thickness of the bolted assembly, which in turn led to bolt shortening and a decrease in the bolt load. As shown in Figure 2.27 (b), during Test IDs 7 and 8, the effect of the unstructured accumulation of wear particles in the friction interface during relatively high-velocity sliding motions outweighs the effect of the evacuation of wear particles during relative low-velocity sliding motions. Therefore, the increase in the bolt load was cumulative and an overall increased bolt load during the durations of Test IDs 7 and 8 was observed. The increase in the bolt load during the durations of Test IDs 7 and 8 could be considered small (approximately 5%) in the context of earthquake structural engineering applications. The bolt load loss during dwell time was attributed to the compaction of unstructured accumulated wear particles.

As demonstrated in Section 2.4.4, relatively high-velocity sliding motions overall induced a decrease in the coefficient of friction μ. As explained in this section, relatively high-velocity

sliding motions overall resulted in an increase in the bolt load N. According to Coulomb's friction equation $f = \mu N$, it can be observed that the effect of sliding velocities on μ and N cancels out each other on the product f. Therefore, for a friction-based structural component, the friction force generated is possible to maintain relatively constant under high sliding velocities. Figure 2.28 presents the recorded force response time history of the friction interface in Test Group Gatke 112 (H) and in Test IDs 5 and 7 as an example, plotted in the normalized time scale for comparison purposes. From Table 2.6, it is learned that the coefficient of friction of this friction interface was reduced by 8.11% in Test ID 7 compared with Test ID 5. In the sliding travel highlighted in Figure 2.28, the average sliding force (termed f_{avg}) of this sliding travel in Test ID 5 was 129.3 kN and the same quantity in Test ID 7 was 122.4 kN. The reduction in the sliding force was 5.3%, lower than 8.11%, because of the effect of the increase in the bolt load as explained above. Practically, the sliding force generated by the friction interface in this case can be considered relatively constant in Test IDs 5 and 7.

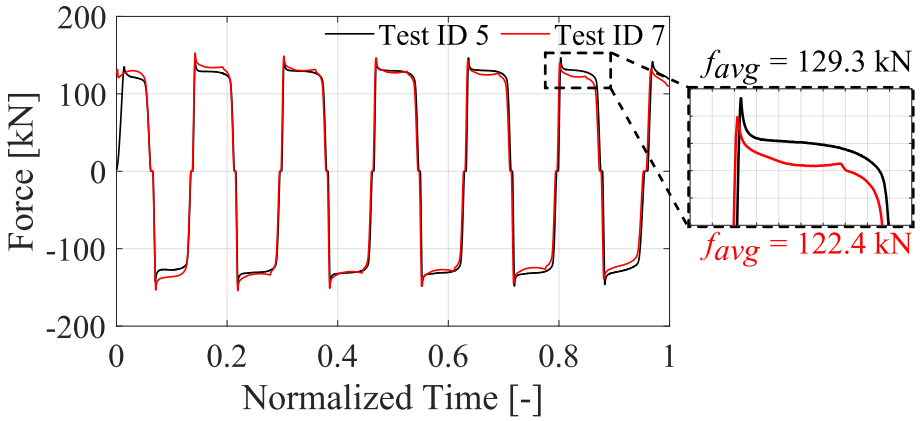

Figure 2.28. Recorded force response time history of Test IDs 5 and 7 from Test Group Gatke 112 (H)

In addition to the observations above, it is also observed that the normal load level had an impact on the bolt load loss. Test groups under high normal load exhibited more normalized bolt load loss toward the end of the loading protocol than test groups under low normal load. This is because the higher normal load induced more wear of the composite material friction shims and consequently resulted in a more significant reduction in the total thickness of the bolted

assembly, which in turn led to a more significant decrease in the bolt load toward the end of the loading protocol.

2.5 Conclusions

This chapter presented an experimental study focused on characterizing the mechanical properties of composite friction materials and the tribological properties of composite to low-carbon structural steel friction interfaces for use in friction-based structural components for earthquake structural engineering applications. A systematic testing program was proposed. The testing program included the coupon tensile test, the plate bearing test, the bolt relaxation test, and the friction test. The friction test considered the normal load level, loading frequencies, sliding velocities, velocity profiles (earthquake vs. sinusoidal vs. linear), and sliding histories (the cumulative displacement, the dwell time, and previous sliding events) as the testing parameters. The effect of these parameters on the friction sliding force, the bolt load, and the experimentally derived coefficient of friction was presented. Six types of phenolic-resin-based fiber-reinforced composite friction materials were tested using the proposed testing program. Based on the experimental testing results, the following conclusions were made:

- The flash compression molding process may result in manufacturing of materials with regions of lower concentration of phenolic resin than anticipated. This potential manufacturing imperfection was shown to exacerbate delamination of the composite material, characterized by bond failure observed during the coupon tensile test.

- The percentage of bolt load loss due to the creep effects in the composite friction materials ranged from 4.5% to 15%. Possible flash compression molding manufacturing defects can lead to a lower concentration of phenolic resin, resulting in lower bonding and adhesion between the matrix and fibers. This mechanism can induce exacerbated through-thickness creep effects, and consequently an increased percentage of bolt load loss. The bolt

relaxation test results highlighted the importance of quality control in the manufacturing of composite friction materials for friction-based structural components.

- The break-in effect depends on the material constituents of the composite friction materials and the normal load level. Cotton-fiber-reinforced composite friction materials compared with glass-fiber-reinforced composite friction materials required less cumulative sliding to establish a steady-state coefficient of friction. A higher normal load increased the wear rate for both cotton- and glass-fiber-reinforced composite friction materials. As a result, a steady-state coefficient of friction was reached with less cumulative sliding.

- Friction tests with different sliding velocities showed a general trend where an increase in the sliding velocity led to a reduction in the coefficient of friction while lower sliding velocities overall resulted in an increase in the coefficient of friction. The reduction in the coefficient of friction was attributed to higher wear rates under higher sliding velocities and accumulation of wear particles, which decreased the shear strength of the adhesion junction and potentially the real contact area. The increase in the coefficient of friction was attributed to the evacuation of wear particles, which increased the shear strength of the adhesion junction, and potentially an increase in the real contact area. A higher normal load was shown to enhance the velocity-dependent frictional behavior.

- Constituents of composite materials appeared to affect velocity-dependent behavior of composite-metallic friction interfaces. The presence of glass fibers and abrasive particles such as yellow iron oxide, green chromium (III) oxide, and aluminum oxide in the material constituent appeared to enhance the evacuation of wear particles. Among the friction interfaces tested in this study, the friction interface with the composite friction material Gatke 398 (consisting of phenolic resin, glass fibers, graphite, Teflon and molybdenum disulfide MoS_2) in contact with low-carbon structural steel exhibited the most stable frictional behavior under different sliding velocities. Hypothetically this was attributed to the contribution of graphite, Teflon, and molybdenum disulfide MoS_2.

- Friction interfaces with glass-fiber-reinforced composite friction materials exhibited oscillations in the force response at low sliding velocities due to the stick-slip behavior of the friction interface. The stick-slip behavior was attributed to the localized accumulation and evacuation of wear particles, which was enhanced by hard glass fibers. In contrast, friction interfaces with cotton-fiber-reinforced composite friction materials did not exhibit oscillations in the force response. The effect of the stick-slip behavior of composite-metallic friction interfaces could be considered insignificant for earthquake structural engineering applications.

- The increased dwell time increased the coefficient of friction with the exception of the test cases that used Gatke 113 and Gatke 397, which require further investigation.

- The friction-based structural component with composite-metallic friction interfaces tested in this study exhibited velocity-dependent bolt load variation because of the wear mechanism of the friction interface. Higher sliding velocities tended to induce an increase in the bolt load due to increased wear debris generation and accumulation while lower sliding velocities tended to induce a reduction in the bolt load due to wear debris evacuation. In addition, a higher normal load overall induced more wear of the composite friction material and therefore, induced more bolt load loss toward the end of the test.

- Considering the results of the mechanical and tribological characterization of materials presented in this study, composite materials that consist of phenolic resin, glass fibers, graphite, Teflon and molybdenum disulfide MoS_2 are among the most suitable materials for use in friction-based structural components for earthquake structural engineering applications. More in-depth studies can be conducted using techniques such as Scanning Electron Microscopy (SEM) and Energy-dispersive X-ray (EDX) to gain a better understanding of the micro-level friction mechanism of this type of material; this will support the future development of high-performance composite friction materials for earthquake structural engineering applications.

Acknowledgments

Chapter 2, in full, is a reprint of the material as it appears in: Chen, K., Tsampras, G., Cheruvalath, S., & Thundathil, M. (2025). Experimental characterization of mechanical and tribological properties of composite materials for friction-based force-limiting structural components. *Composites Part B: Engineering*, 302, 112472. Credits are distributed as follows: Kaixin Chen: Writing – original draft, Visualization, Validation, Software, Methodology, Investigation, Formal analysis, Data curation, Conceptualization. Georgios Tsampras: Writing – review & editing, Supervision, Resources, Project administration, Methodology, Investigation, Funding acquisition, Data curation, Conceptualization. Shivaglal Cheruvalath: Writing – review & editing, Resources, Investigation. Mary Thundathil: Writing – review & editing, Resources, Investigation.

Chapter 3

Low-Cost Friction-Based Structural Components With Reduced Sensitivity to Machining Tolerances and Accelerated Repairability

3.1 Overview and Scope of Study

Based on the design considerations and challenges presented in Chapter 1, the objective of the study presented in this chapter is to present the development and experimental characterization of a novel yet practical design concept of a slotted-bolted friction-based structural component that is low-cost, less sensitive to machining tolerances, and easily repairable. The design concept is presented, and the experimental results are discussed. The experimental testing program consisted of two test phases. The first test phase was component-level connection tests. The second test phase was a full-scale shaking table test where the proposed friction-based component was designed as the force-limiting connection between a re-centering steel braced frame and sliding slabs. Throughout the experimental testing program, the performance of the friction-based force-limiting connection designed using this concept was assessed. The repairability of the connection was specifically examined during the shaking table test and is also discussed in this chapter. To provide insights into the practical implementation of buildings equipped with friction-based connections designed with this concept, this study also assesses and reports the

reference time required for manufacturing, assembling, installing, and repairing the proposed connection.

3.2 Design Concept

3.2.1 Connection Configuration

Figure 3.1 presents the schematic representation of the exploded view and the assembly of the proposed friction-based force-limiting connection, which has a slotted-bolted configuration. Two ends of this connection are termed the fixed end and the sliding end, respectively. On the fixed end, two steel channels and one internal connection plate are connected using six structural bolts and bolt assemblies including nuts and flat washers for structural applications. The structural bolts are expected to be ASTM F3125 Gr.A325 medium-strength steel heavy hex head bolts which are commonly used for structural applications in the United States. For each steel channel, a rectangular-shaped opening is created in the channel, in which the friction shim is hosted. Sliding occurs on the end where friction shims are hosted, termed the sliding end. On the sliding end, the friction shims are clamped against the slotted internal sliding plate by initially loose steel washer plates (termed steel washer plates in Figure 3.1 and herein) and one structural bolt (termed the friction bolt herein) and its bolt assemblies including one nut and one flat washer for structural applications. The friction bolt is also expected to be an ASTM F3125 Gr.A325 structural bolt. The friction interface is formed between the friction shims and the internal sliding plate. The friction bolt and bolt assemblies apply the normal load acting on the friction interface, and loose steel washer plates are clamped to distribute the applied normal load onto friction shims. The friction shims are expected to be made of fiber-reinforced non-metallic composite friction materials [2, 136]. The internal connection plate, the internal sliding plate, and the steel washer plates are expected to be made of commercially available structural steel such as A36 or A572 Gr.50 steel used in the United States. The steel channels are commercially available hot-rolled steel channels, also made of structural steel.

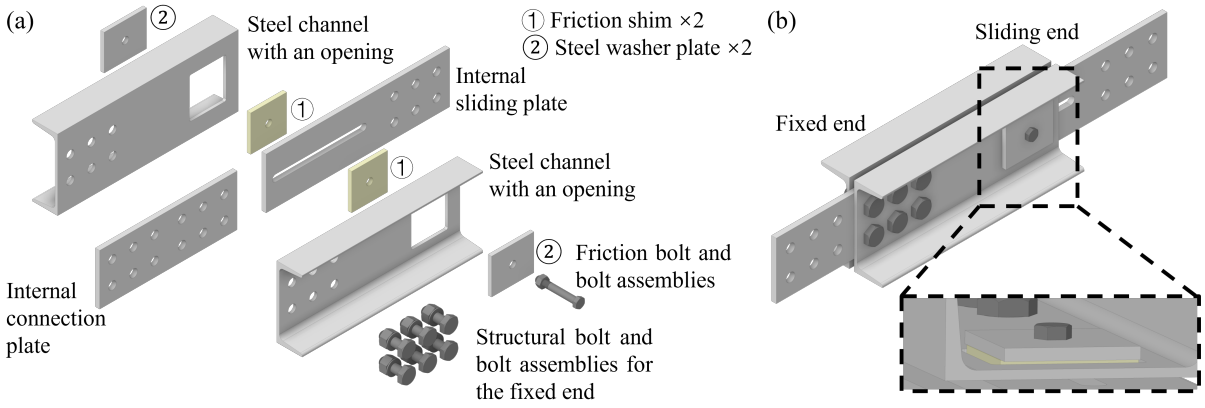

Figure 3.1. Schematic representation of the proposed friction-based force-limiting connection: (a) Exploded view (b) Assembly

Figure 3.2 presents the load path of the friction-based connection, considering the connection under tension as a demonstration. Assuming that the normal load acting on the friction interface is N and the coefficient of friction of the friction interface is μ, based on Coulomb's friction equation, the connection generates a friction force $f = 2\mu N$ when sliding, as shown in Figure 3.2 (a). For this connection, the parts on the fixed end, i.e., the internal connection plate, two steel channels, and six structural bolts and their assemblies, are expected to remain static relative to each other. On the sliding end, when the steel channels start moving relative to the internal sliding plate, the steel channels make contact with the edge of the friction shims and push the friction shims to move relative to the internal sliding plate and to activate the sliding friction mechanism, as shown in Figure 3.2 (b). Therefore, when sliding occurs, the friction shim is under the normal load from bolt pretension, the edge bearing force from the steel channel, and the sliding friction force from the friction interface, as shown in Figure 3.2 (c). The bearing force $f_{bearing}$ is distributed on the cross section of the friction shim over an area of $A_{contact}$ and $A_{contact}$ is equal to the product of the thickness of the web of the steel channel and the height of the friction shim. During sliding, the steel channels are not expected to make contact with steel washer plates (as the friction shim thickness is greater than the web thickness of the steel channel) and the internal sliding plate.

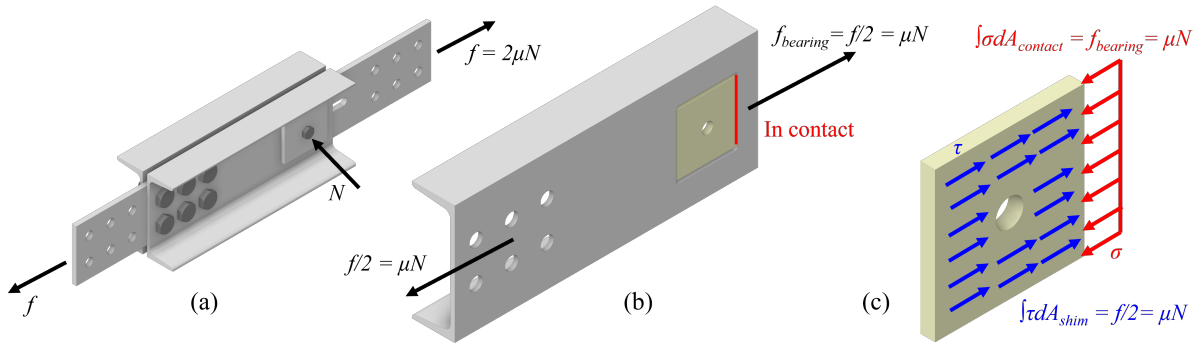

Figure 3.2. Load path of the friction-based connection: (a) The connection generates a tensile force of $f = 2\mu N$. (b) Schematic free body diagram of the steel channel when in contact with the friction shim in the opening (c) Schematic free body diagram of the friction shim (The normal load acting on the friction shim is not shown in the figure)

In practical design, the required sliding force of this connection should be determined through system-level structural analysis or by following specific design methods, such as those outlined in Section 3 of Chou et al. [137] or in Tsampras and Sause [138]. A detailed discussion of how to determine the required sliding force is beyond the scope of this study. At the component level, damage limit states of the connection parts should be considered, and the parts should be sized based on the required sliding force. On the fixed end, the connection between the internal connection plate and the steel channels should be designed as a slip-critical connection in accordance with Section J3 of AISC 360-22 [139], and the strength requirements of both the structural bolts and plates should be satisfied. On the sliding end, given the required sliding force (f) and the selected material pair for the friction interface (μ), the required bolt pretension acting on the friction interface (N) can be calculated using Coulomb's friction equation ($N = f/\mu$). The resulting nominal normal pressure acting on the friction shim should be checked. Past research [2, 136] has suggested that for friction shims made of fiber-reinforced composite materials, 13.5 MPa is a reasonable reference upper limit for the nominal normal pressure. The friction shim should have sufficient bearing strength to resist the bearing action from contact with the steel channel, as well as adequate shear strength to resist the in-plane shear stress induced by the friction force. The steel channels and the internal sliding plate should have sufficient

design tensile and compressive strengths to resist connection forces, and the design tensile and compressive strengths can be computed following Sections D and E of AISC 360-22 [139], respectively. Note that when the friction shim is in contact with the steel channel and when the connection is in tension, as shown in Figure 3.2 (b), stress concentration could be developed locally at the outer edge of the steel channel in the direction of loading close to the opening, and result in critical regions of high stress. This effect should be taken into account when detailing the steel channel.

The design concept shown in Figure 3.1 has several advantages. First, the parts of this connection, i.e., the steel plates and hot-rolled steel channels, are commercially available and relatively low-cost. Second, the sliding friction mechanism is activated through the bearing action between the steel channel and the edge of the friction shim. In contrast, for the conventional design of slotted-bolted friction-based structural components shown in Figure 1.2, the bearing action typically occurs between the friction bolt and the friction shim. The bearing action between the friction bolt and the friction shim leads to the variation of the axial strain in the bolt and potential damage to the friction shims (see Figure 1.7 (a)). The activation of sliding through bearing between the edge of the friction shim and the steel channel, as shown in Figure 3.2 (b) and (c), reduces the chance of friction shim damage and reduces the variation of the axial strain in the friction bolt. In addition, the initially loose steel washer plates are clamped to apply confining pressure on the friction shim that helps prevent the development of damage due to bearing. Third, the design with loose steel washer plates mitigates the effect of non-parallel plates on applying the normal load as demonstrated in Figure 1.8. This allows for a more accurate normal load estimate when applying the normal load using the calibrated wrench method in practice. Fourth, the design with loose steel washer plates increases the flexibility between the internal sliding plate and the assembly with friction shims, steel washer plates, and the friction bolt and its assemblies. The increased flexibility mitigated the effect of the contact between the internal surface of the slot and the friction bolt on the response of the connection; therefore, the parts of the connection, i.e., the internal sliding plate, the steel channels, and the steel washer plates, do

not need to be machined following a low geometric tolerance with respect to their flatness and parallelism. Compared to the example conventional design in Figure 1.2, this design concept reduces the time and cost of machining the parts. Lastly, compared to the example conventional design of slotted-bolted friction-based components in Figure 1.2 of which the repairing and inspection requires to remove the external clamping plate, the design with loose steel washer plates allows for quicker inspection and replacement of the friction shims after an earthquake if needed.

3.2.2 Preliminary Numerical Assessment of the Design Concept

As an intermediate step in the development of the proposed friction-based connection, a numerical simulation was performed in the ANSYS Mechanical finite element software [140], with the objective of preliminarily assessing both the expected kinematics of the connection and its anticipated force–displacement response. In the numerical simulation, the internal connection plate, the steel channels, the friction shims, and the steel washer plates were explicitly simulated using eight-node solid finite elements. The bolts for the fixed end, the friction bolt, and the bolt assemblies were not explicitly simulated. The pretension of the friction bolt was 50 kN, being simulated as a constant force boundary condition distributed to the nodes on the surface of the elements in the steel washer plates. The contact interfaces between the modeled parts were explicitly simulated using pair-based contact definition. A contact pair was defined between each surface of the friction shims and the adjacent surface of the internal sliding plate; for those contact pairs, a Coulomb-type frictional behavior was defined with a constant coefficient of friction equal to 0.4. The sliding force of the connection was computed using the modified version of Coulomb's friction equation $f = n_b n_s \mu N$, where n_b was the number of the friction bolt and was equal to 1; n_s was the number of the friction interface that contributes to the sliding friction force and was equal to 2; μ was the expected coefficient of friction, 0.4; and N was the normal load acting on the friction interface provided by one bolt, which was 50 kN. The resulting sliding force of the connection f was equal to 40 kN.

In the numerical simulation, static structural analysis was performed. Figure 3.3 presents the imposed displacement time history of the analysis and the resulting force-displacement response of the connection. In the force-displacement response plot, positive force indicates tension in the connection. The force-displacement response overall resembled a Coulomb-type frictional behavior. In the force-displacement response, zero-force pinching displacement was observed due to the gap between the friction shim and the steel channel. In practice, the zero-force pinching displacement in the force-displacement response can be reduced by enforcing a tighter tolerance when machining the opening on the steel channel. The maximum principal stresses in the connection when the imposed displacement was equal to +75 mm and when the connection was under tension is also presented in Figure 3.3. From the maximum principal stresses results, critical regions of high stress can be identified and they are at the outer edge of the steel channel in the direction of loading close to the opening and at the inner corner of the opening. The magnitude of the maximum principal stresses at these regions can be reduced by increasing the radius of the inner corner of the opening and by increasing the width of material between the inner and outer edge of the steel channel.

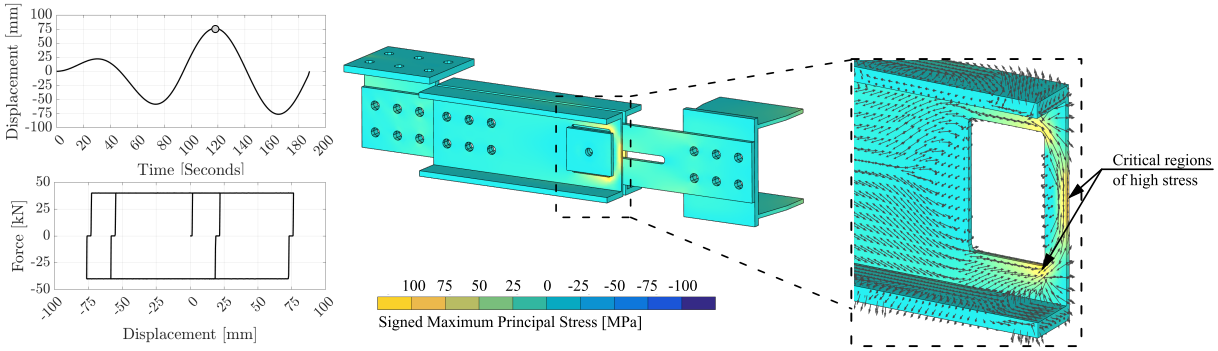

Figure 3.3. Numerical simulation of the proposed friction-based connection

3.3 Experimental Program

3.3.1 Summary of Testing Phases

Table 3.1 presents the testing phases of this experimental study. Test Phase 1 included component-level connection tests conducted at the University of California San Diego and consisted of three test groups. The main objective of Test Phase 1 was to experimentally validate the proposed friction-based connection design and to support Test Phase 2. Test Phase 2 was conducted at the National Center for Research on Earthquake Engineering (NCREE) in Taiwan, which was the shaking table tests of a three-story, re-centering steel braced frame with sliding slabs, where the proposed friction-based connection was designed to work as the force-limiting connection between the steel frame and sliding slabs. Test Phase 2 also included pre-shaking table tests or post-shaking table tests of the connection. The target connection sliding force was 40 kN in all tests. The target connection sliding force was estimated based on the force required to be transferred between the steel frame and sliding slabs. Per Section 3.2.1, if needed, a higher connection sliding force can be achieved by increasing the normal load acting on the friction interface, and the parts of the connection can be sized and detailed accordingly. For example, Chen et al. [136] detailed a connection following the same design concept for the characterization of the tribological properties of phenolic-resin-based composite materials that required a connection sliding force of more than 200 kN.

3.3.2 Test Phase 1: Component-level Connection Test

Manufacturing of the Connection Specimen

This section presents the manufacturing process of the parts of the connection specimen used in Test Phase 1. The connection specimens used in Test Phase 2 were manufactured following a similar process. For the connection specimen used in Test Phase 1, the steel channels, the internal sliding plate, the internal connection plate, and the steel washer plates, were all made of A36 low-carbon structural steel. A Computer Numerical Controlled (CNC) subtractive

Table 3.1. Test phases of the proposed friction-based connection

Test Phase	Test Group	No. of Tests	Objectives
1 Component-level connection test	1	63	Preliminary experimental evaluation of the feasibility of the proposed friction-based connection design
	2	32	Investigation of the friction bolt load variation and the response of the friction-based connection under earthquake-type input excitation
	3	7	Verification of the proposed break-in process for the friction-based connection
2 Shaking table test	1	6	Pre-shaking-table-test break-in process of the friction-based connection
	2	8	Shaking table test of a steel frame equipped with proposed friction-based connections
	3	6	Post-shaking-table-test investigation of the response of the friction-based connection
	4	2	Connection test 10 months after the shaking table test to assess the aging effect

manufacturing approach was used for machining the steel parts. The toolpath programming was completed using Autodesk Fusion 360 [141] and the machining of the steel parts was completed in the machining shop of the University of California San Diego using a HAAS VF4 vertical machining center [142]. The steel channels for the connection specimen were commercially available C10×15.3 hot-rolled steel channels, of which the cross-sectional dimensions followed the AISC Steel Construction Manual [92]. The length of each channel was 635 mm (25 inch). The machining process of the steel channel involved creating the rectangular-shaped opening and the bolt holes on the channel. The rectangular-shaped opening had a dimension of 130 mm × 143 mm to host the friction shim of which the dimension was 127 mm × 127 mm × 12.7 mm (5 inch × 5 inch × 0.5 inch). A 2D pocket toolpath was selected and programmed to complete the machining task. The internal sliding plate had a dimension of 508 mm × 203.2 mm × 12.7 mm (20 inch × 8 inch × 0.5 inch) and was cut from a raw material stock plate having a dimension of 609.6 mm × 254 mm × 12.7 mm (24 inch × 10 inch × 0.5 inch). The machining process of the internal sliding plate involved two steps: the first step was to create the slot on the plate using the

2D pocket toolpath and the second step was to use the 2D contour toolpath to cut the internal sliding plate off the raw material stock plate. It is worth noting that for the internal sliding plate, geometric tolerances with respect to its flatness and parallelism were not enforced; the surfaces of the internal sliding plate associated with the friction interface were not face milled during the machining process. The internal connection plate had a dimension of 355.6 mm $\times$ 203.2 mm $\times$ 12.7 mm (14 inch $\times$ 8 inch $\times$ 0.5 inch) and was also cut from a raw material stock plate having a dimension of 609.6 mm $\times$ 254 mm $\times$ 12.7 mm (24 inch $\times$ 10 inch $\times$ 0.5 inch). The machining of the internal connection plate involved creating bolt holes on the plate using the 2D pocket toolpath and cutting the plate off the raw material stock plate using the 2D contour toolpath. The steel washer plate had a dimension of 152.4 mm $\times$ 152.4 mm $\times$ 12.7 mm (6 inch $\times$ 6 inch $\times$ 0.5 inch) and the raw material stock plate had the same dimension. The machining process of the steel washer plate just required creating the bolt hole on the plate using the 2D pocket toolpath. Table 3.2 summarizes the reference machining time of the parts. The reference machining time considers only the time spent on machining operations but does not take the time spent on other operations (for example, workholding setup and probing) into account. In the machining of all the steel parts, a TiAlN-coated 4-flute carbide end mill with a diameter of 12.7 mm (0.5 inch) was used for all the machining operations. For 2D pocket toolpaths, the cutting parameters used were: spindle speed = 1,000 RPM, resulting in a surface speed of 0.665 m/s (130.9 ft/min); cutting feed rate = 1,016 mm/min (40 inch/min), resulting in a chip load of 0.254 mm per tooth (0.01 inch per tooth); the cutting depth was 1.27 mm (0.05 inch) per pass. For 2D contour toolpaths, the cutting parameters used were: spindle speed = 4,393 RPM, resulting in a surface speed of 2.921 m/s (575 ft/min); cutting feed rate = 1,517.4 mm/min (59.74 inch/min), resulting in a chip load of 0.0864 mm per tooth (0.0034 inch per tooth); the cutting depth was 2.54 mm (0.1 inch) per pass.

For the friction-based connection tested in this study, the friction interface was formed by low-carbon structural steel (A36 steel) in contact with the composite friction material Gatke 398 [143] manufactured by ScanPac Mfg., Inc., which consisted of phenolic resin matrix, E-

Table 3.2. Information about the machining of the parts of the connection specimen used in Test Phase 1

Manufacturing machine	Part	Number of parts machined	Reference machining time [min]
HAAS VF-4	Steel channel	2	89.2
	Internal sliding plate	1	23.4
	Internal connection plate	1	28.8
	Steel washer plate	2	3.7
Onefinity CNC milling system	Friction shim	16	281.8

glass fiber cloth reinforcement, lubricants including graphite, Teflon, and molybdenum disulfide (MoS_2), and fillers. A systematic characterization of the mechanical and tribological properties of six composite friction materials showed that the Gatke 398 to low-carbon structural steel friction interface exhibits stable frictional behavior [136]. The friction shim had a dimension of 127 mm $\times$ 127 mm $\times$ 12.7 mm (5 inch $\times$ 5 inch $\times$ 0.5 inch). The thickness of the friction shim should be enough to prevent the steel channel from getting in contact with the steel washer plate. A dry CNC subtractive manufacturing approach was used to machine the friction shims. A three-axis Onefinity [144] CNC milling system with a diamond-coated end mill was used for the machining process. Details regarding the Gatke 398 material properties, specimen preparation, and cutting parameters have been provided in Chen et al. [136].

Assembly of the Connection

Figure 3.4 demonstrates the assembly process of the proposed friction-based connection. The parts of the connection were initially roughly positioned for preliminary alignment. The structural bolts and bolt assemblies were then inserted on the fixed end and loosely tightened to position the internal connection plate with respect to the two steel channels. On the sliding end, the internal sliding plate was elevated to its designated position. The friction shims were then placed in the openings on the steel channels against the internal sliding plate and the steel washer plates were also held in position. The friction bolt and its bolt assemblies were then put in and the friction bolt was loosely tightened to assemble the sliding end. Once all parts were properly

positioned, the bolts for the fixed end were tightened at their minimum pretension level to ensure that there was no relative movement between the parts on the fixed end. The friction bolt was then tightened to the designed target normal load level based on the specific required sliding force of the connection. For the connection used in this study, as previously mentioned, the target connection sliding force was 40 kN. For the Gatke 398 to low-carbon structural steel friction interface, a reference coefficient of friction μ was 0.4 [2, 136, 143]. The target normal load was calculated to be 50 kN (approximately 30% of the minimum pretension of the friction bolt in this case) and the normal load could be applied using a manual torque wrench to pretension the friction bolt, as shown in Figure 3.4. For higher target normal loads, an electric or hydraulic torque wrench might be required for the pretensioning process. The entire assembly process was completed by a single worker and took approximately three minutes.

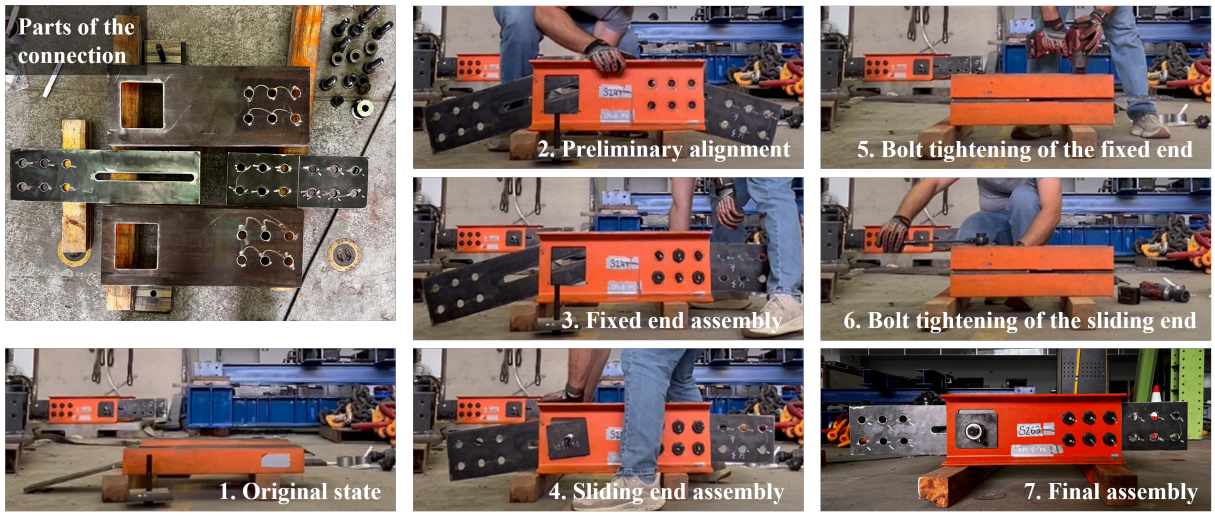

Figure 3.4. Connection assembly demonstration

Connection Test Setup and Instrumentation

Figure 3.5 presents the connection test setup of Test Phase 1. The connection tests conducted in Test Phase 2 adopted a similar test setup. The connection tests were conducted using a universal testing machine (UTM). The instrumentation of the connection test was adapted to the objective of each test group. In all connection tests, the connection displacement and the

connection force were recorded using the UTM controller. The connection deformation and sliding motion were effectively equal to the UTM actuator displacement. The connection force was effectively equal to the UTM actuator load. In addition to the force and displacement data, imaging data was collected in Test Group 1. Digital Image Correlation (DIC) method was used to compute the full-field strain responses using the imaging data. The strain field computed using the Test Group 1 imaging data was compared with the strain field computed using the numerical model. Imaging data was not collected in follow-up connection tests. In Test Groups except for Test Group 1, a through-hole bolt load cell was used to monitor the bolt load of the friction bolt throughout the test.

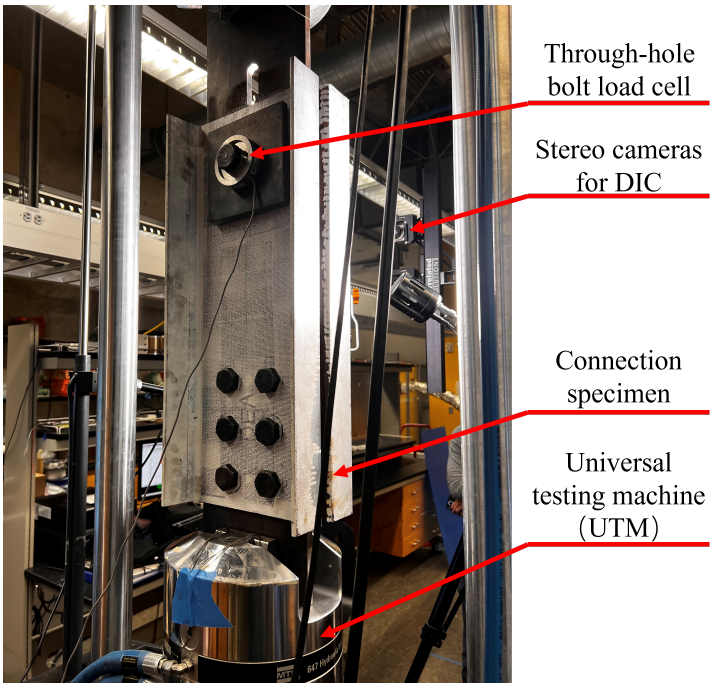

Figure 3.5. Representative connection test setup

Results

Test Phase 1 Test Group 1 served as a preliminary experimental evaluation of the feasibility of the proposed friction-based connection design. Sixty-three displacement-controlled cyclic tests were completed and ramped sinusoidal displacement time histories were used as

the input excitation. Two loading frequencies (0.03 Hz and 0.20 Hz), six peak displacements (10 mm, 20 mm, 30 mm, 40 mm, 50 mm, and 58 mm), and seven levels of the applied torque T (bolt was not preloaded (0 N-m), bolt was hand tightened, 81 N-m, 163 N-m, 183 N-m, 203 N-m, and 217 N-m) on the friction bolt were considered. Figure 3.6 (a) presents selected connection force-displacement response results of Test Phase 1 Test Group 1. In Figure 3.6 (a), each subplot corresponds to one level of the applied torque on the friction bolt (from top left to bottom right: bolt was not preloaded (0 N-m), 81 N-m, 163 N-m, and 203 N-m). Blue lines represent force-displacement responses of the connection in tests having a loading frequency of 0.03 Hz and a peak displacement of 10 mm; black lines represent force-displacement responses of the connection in tests having a loading frequency of 0.03 Hz and a peak displacement of either 40 mm or 50 mm; red lines represent force-displacement responses of the connection in tests having a loading frequency of 0.20 Hz and a peak displacement of either 40 mm or 50 mm. The result of the T = 0 N-m case shows that when the friction bolt was not preloaded, the friction force between the parts of this connection could be considered negligible. The results of the rest of the tests show that regardless of the loading frequency, the peak displacement, and the value of the applied torque on the friction bolt, the proposed friction-based connection exhibited stable force-displacement responses (i.e., the connection generated a relatively constant sliding friction force without exhibiting the uncontrolled displacement-dependent variable friction force shown in Figure 1.3 (b)). The force-displacement response of the proposed connection was close to a rectangle; therefore, a Coulomb-type frictional behavior idealization could be used for this connection in practical design. Importantly, with this novel design concept, the force-displacement response of the connection did not exhibit an uncontrolled variable friction force as shown in Figure 1.3 (b) even when the parts were not machined following a low geometric tolerance with respect to their flatness and parallelism.

The commercial software Vic-3D [145] was used for the DIC analysis in Test Phase 1 Test Group 1. Figure 3.6 (b) shows a selected representative DIC analysis result. The frame selected was from Test 34 of Test Group 1 when the applied torque T was equal to 163 N-m and

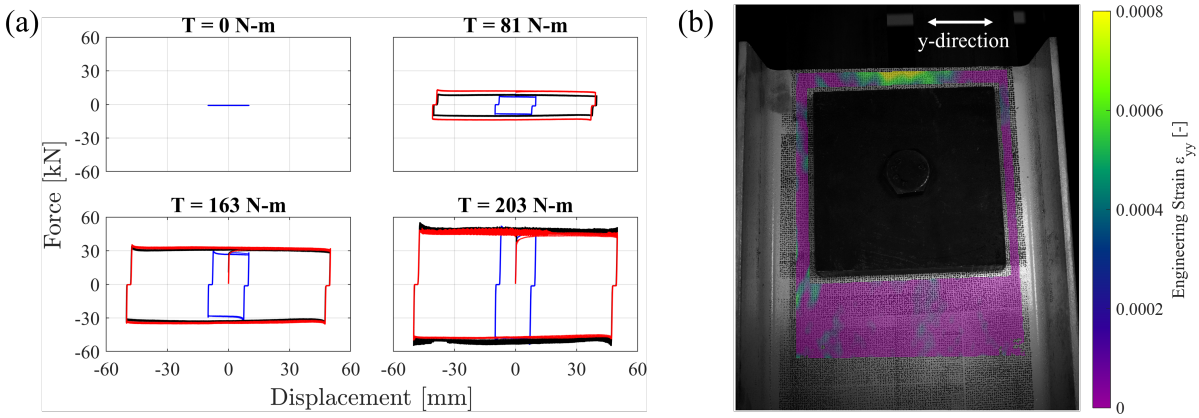

Figure 3.6. (a) Selected force-displacement responses of the connection in Test Phase 1 Test Group 1 (b) Selected DIC analysis results of Test Group 1

represented a moment when the connection was in tension. The contour map of the engineering strain ε_{yy} is shown in Figure 3.6 (b). The DIC analysis results provided experimental validation of the numerical simulation (Figure 3.3), confirming that high stress concentrations developed near the outer edge of the steel channel adjacent to the opening in the direction of loading without exceeding the yield strain limit.

Gatke 398 friction shims conditions were inspected throughout the testing. Figures 3.7 (a) and (b) present the representative surface and edge appearance of Gatke 398 friction shims before and after the test, respectively. The Gatke 398 friction shims were observed to be damage free. No mechanical failure or damage was observed on the surface of the friction shim which formed the friction interface, or the edge of the friction shim where the bearing action between the steel channel and the friction shim was established. Black wear marks were observed on the surface of the friction shim that formed the friction interface, which resulted from the thermo-oxidative degradation process of the phenolic resin constituent [136, 104].

Following Test Group 1, Test Group 2 was conducted to further investigate the connection response, taking earthquake-type input excitation and the variation of the friction bolt load into consideration. Table 3.3 presents the loading protocol of Test Group 2. In Test Group 2, Tests 1, 2, 3, 13, 14, and 15 had expected seismic-induced responses of a friction-based structural

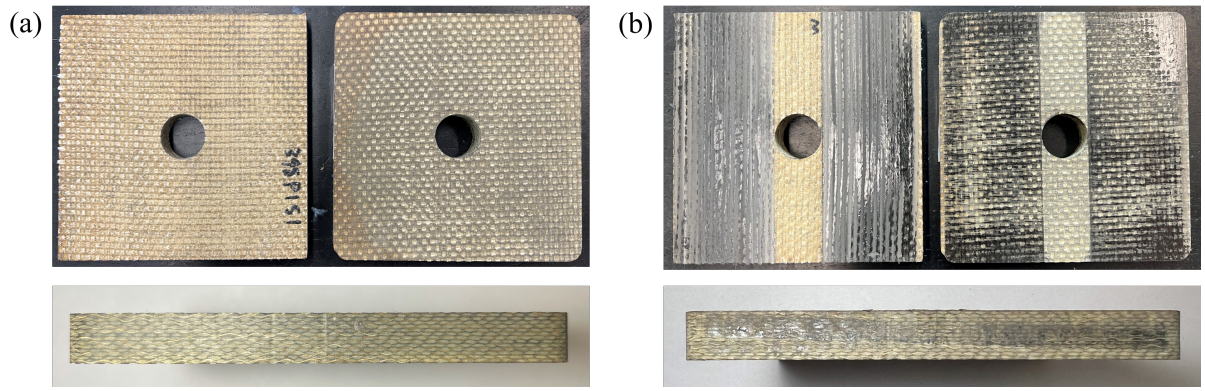

Figure 3.7. Representative surface and edge appearance of Gatke 398 friction shims (a) before a test and (b) after a test

connection as the imposed displacement time histories of the input excitation. The imposed displacement time histories for these tests were responses of a friction-based structural connection from numerical earthquake simulations of the steel frame in Test Phase 2 [146] considering three levels of ground motion intensities (Design Basis Earthquake (DBE), Maximum Considered Earthquake (MCE) and 1.5 times Maximum Considered Earthquake (1.5×MCE)). The sliding velocity imposed by the displacement histories was scaled down to be limited below the testing machine's capacity by elongating the duration of the displacement histories. The velocity-dependent frictional behavior of the Gatke 398 to low-carbon structural steel friction interface has been discussed in Chapter 2. As discussed in Section 3.3.2, the target normal load provided by the friction bolt was 50 kN and the bolt load of the friction bolt was monitored using the through-hole bolt load cell throughout the test. Between tests, the friction bolt was retightened to the target normal load level if bolt load loss was observed.

Figure 3.8 presents selected results of Test Group 2. The force-displacement response of the friction-based connection was plotted for tests having expected seismic-induced responses as the input excitation. It is observed that under earthquake-type input excitation, the proposed friction-based connection exhibited a stable force-displacement response that could be idealized as a Coulomb-type frictional behavior. Comparing Test 1 with Test 14, Test 2 with Test 15, and Test 3 with Test 13, noticeable difference in the magnitude of the connection sliding force can be

Table 3.3. Loading protocol of Test Phase 1 Test Group 2

Test ID	Input Type	Peak Displ. [mm]	Peak Vel. [mm/sec]	Loading Freq. [Hz]	Descriptions
0	Ramped Sine	50	7.6	0.0243	Bolt was not preloaded, as a pre-test setup check
1	EQ-DBE	22	∼28	-	Assess the connection response at DBE level earthquake
2	EQ-MCE	31	∼35	-	Assess the connection response at MCE level earthquake
3	EQ-1.5MCE	52	∼36	-	Assess the connection response at 1.5×MCE level earthquake
4∼12	Ramped Sine	Various	Various	Various	Assess the connection response under ramped sinusoidal motions with various peak displacements, peak sliding velocities, and loading frequencies
13	EQ-1.5MCE	52	∼36	-	Assess repeatability of the connection response at 1.5×MCE level earthquake, compared to Test 3
14	EQ-DBE	22	∼28	-	Assess repeatability of the connection response at DBE level earthquake, compared to Test 1
15	EQ-MCE	31	∼35	-	Assess repeatability of the connection response at MCE level earthquake, compared to Test 2

observed. Figure 3.9 presents the evolution of the magnitude of the connection sliding force with respect to the cumulative displacement that the friction interface of the connection underwent. In Figure 3.9, different tests are separated by vertical dashed lines. The bolt load variation, defined as the relative difference between the bolt load at the beginning and at the end of the test, is plotted in the same figure. A negative bolt load variation means that there was a bolt load loss in this test. Figure 3.9 shows that at the beginning of the test when the cumulative displacement was relatively small, the connection sliding force was lower than the target connection sliding force (40 kN). As the cumulative displacement increased, the connection sliding force increased and reached a relatively constant level equal to the target connection sliding force. Moreover, it is observed that the bolt load loss was more significant at the beginning of the test and was reduced as the cumulative displacement increased.

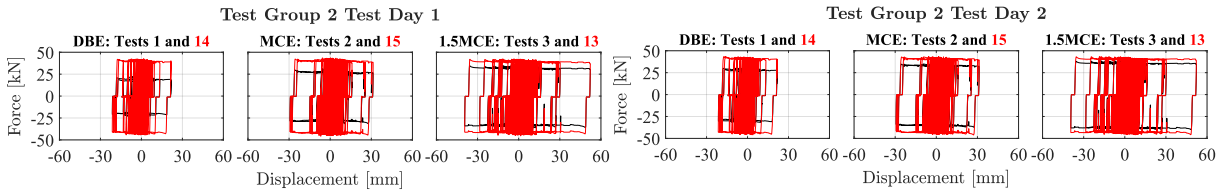

Figure 3.8. Selected results of Test Phase 1 Test Group 2: force-displacement responses of the connection under earthquake-type input excitation (Tests 1, 2, 3, 13, 14, and 15)

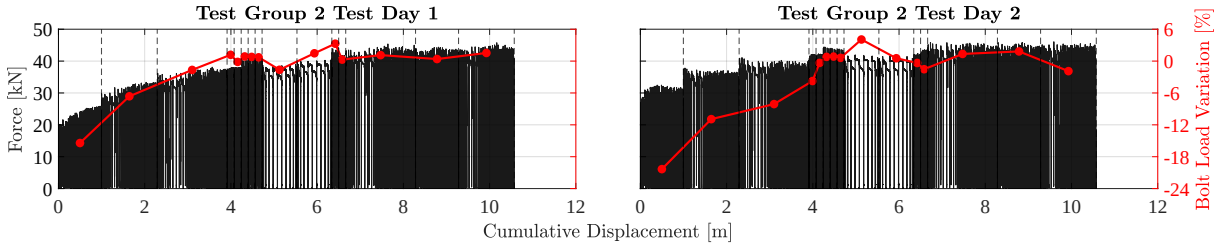

Figure 3.9. Results of Test Phase 1 Test Group 2: evolution of the connection force with respect to the cumulative displacement and the variation of the bolt load in each test (tests are separated using dashed lines)

The observed evolution of the connection force and the bolt load variation with respect to the cumulative displacement of the friction interface was attributed to the break-in effect of the friction interface. When two surfaces are first brought into contact under the normal load

and start sliding relative to each other, the break-in process happens. Changes in the coefficient of friction and the wear rate of a friction interface usually happen at this stage due to changes in the surface conditions [147]. The break-in process depends on the cumulative displacement and as the cumulative displacement increases, the response of the friction interface will reach a relatively steady state [147], in which the coefficient of friction and the wear rate will reach a relatively constant level. Chen et al. [136] studied the break-in effect of composite-metallic friction interfaces for earthquake engineering applications. For the Gatke 398 to low-carbon structural steel friction interface used in this study, the break-in effect was attributed to the wearing of surface asperities and an increase in the adhesive friction at the beginning of sliding, and as a result, the friction interface exhibited an increase in the coefficient of friction upon reaching the steady state. This explains the evolution of the connection sliding force observed in Figure 3.9. In addition, Chen et al. [136] showed that due to the break-in effect, composite metallic friction interfaces have a higher wear rate at the beginning of sliding. A higher wear rate increases the wear volume, causing the friction shims to be thinner, and consequently causing a shortening of the friction bolt and inducing a higher bolt load loss at the beginning of sliding. As the cumulative displacement increased, the wear rate was reduced; therefore, the increase in the wear volume became slower and as a result, the induced bolt load loss became lower. This explains the evolution of the bolt load variation observed in Figure 3.9. The break-in effect observed in Test Group 2 highlighted the importance of breaking in the friction shims before installing the connection onto the structure, so that the friction interface of the connection can reach a relatively steady state and the connection can generate a relatively constant connection sliding force with a relatively low bolt load loss.

As observed in Figure 3.9, at a cumulative displacement of about 4 meters, the connection sliding force reached a relatively constant level and the bolt load variation was effectively close to zero. Based on this result, a break-in loading protocol as shown in Figure 3.10 was proposed for the friction-based connection in this study. The proposed break-in loading protocol consisted of three sets of break-in tests having ramped sinusoidal waves as the imposed displacement time

history of the input excitation. Between the break-in tests and at the end of the break-in loading protocol, the friction bolt was retightened to the original target bolt load if bolt load loss was observed. The peak sliding velocity imposed by the proposed break-in loading protocol was 7.62 mm/s. The total cumulative displacement imposed by the proposed break-in loading protocol was 4 meters. Note that this proposed break-in loading protocol was developed for the specific material pair (composite material Gatke 398 in contact with low-carbon structural steel) used in the friction interface for this connection, and for a specific normal pressure level (for the connection tested, the target normal load was 50 kN and the resulting target nominal normal pressure was 3.8 MPa). If the material pair for the friction interface is different or if a different normal pressure is applied, the break-in loading protocol may need to be revised accordingly [136].

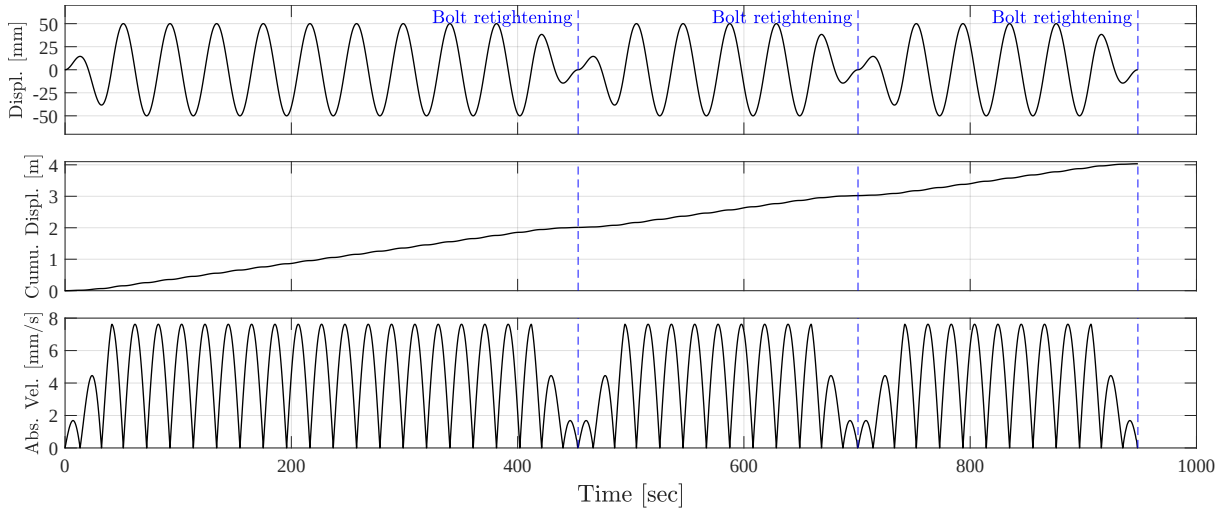

Figure 3.10. Proposed break-in loading protocol for the friction-based connection in this study. From top to bottom: imposed displacement time history; cumulative displacement time history; absolute sliding velocity time history

Following Test Group 2, Test Group 3 was conducted to verify the proposed break-in loading protocol in Figure 3.10. Table 3.4 presents the loading protocol of Test Group 3. Tests 1, 2, and 3 were break-in tests following the break-in loading protocol in Figure 3.10. Tests 4, 5, and 6 were follow-up tests with expected seismic-induced responses as the displacement histories of the input excitation. Following the break-in loading protocol in Figure 3.10, the friction bolt

was retightened to the target normal load level (50 kN) between Tests 1 and 2, Tests 2 and 3, and after the completion of Test 3, if bolt load loss was observed. Figure 3.11 (a) presents the force-displacement response of the connection in Test Group 3. It can be observed that the connection generated a lower sliding force in Test 1 and the connection sliding force increased in Tests 2 and 3 as the break-in effect was established. In Tests 4, 5, and 6, the connection sliding force was maintained at a relatively constant level of about 40 kN. Figure 3.11 (b) presents the time histories of the imposed displacement, the recorded connection sliding force and the bolt load, and the computed coefficient of friction $\mu_{computed}$. Upon the establishment of the break-in effect after Test 3, the coefficient of friction of the sliding interface reached a relatively constant level. Hence, Test Group 3 verified the effectiveness of the proposed break-in loading protocol.

Table 3.4. Loading protocol of Test Group 3

Test ID	Input Type	Peak Displ. [mm]	Peak Vel. [mm/sec]	Descriptions
1	Ramped Sine	50	7.6	Break-in test one to establish the break-in effect
2	Ramped Sine	50	7.6	Break-in test two to establish the break-in effect
3	Ramped Sine	50	7.6	Break-in test three to establish the break-in effect
4	EQ-DBE	22	∼28	Post-break-in-process assessment of the connection response at DBE level earthquake
5	EQ-MCE	31	∼35	Post-break-in-process assessment of the connection response at MCE level earthquake
6	EQ-1.5MCE	52	∼36	Post-break-in-process assessment of the connection response at 1.5×MCE level earthquake

Summary of Test Phase 1 Results

Throughout a series of component-level connection tests, Test Phase 1 showed that the proposed friction-based connection exhibited a stable force-displacement response that could be idealized as a Coulomb-type frictional behavior under different loading conditions and for various force demands. Furthermore, it demonstrated that by using the novel design concept with loose steel washer plates, the stable Coulomb-type frictional behavior could be achieved without enforcing tight geometric tolerances when machining the parts. Test Phase 1 also highlighted that the break-in effect of the composite-metallic friction interface influenced the

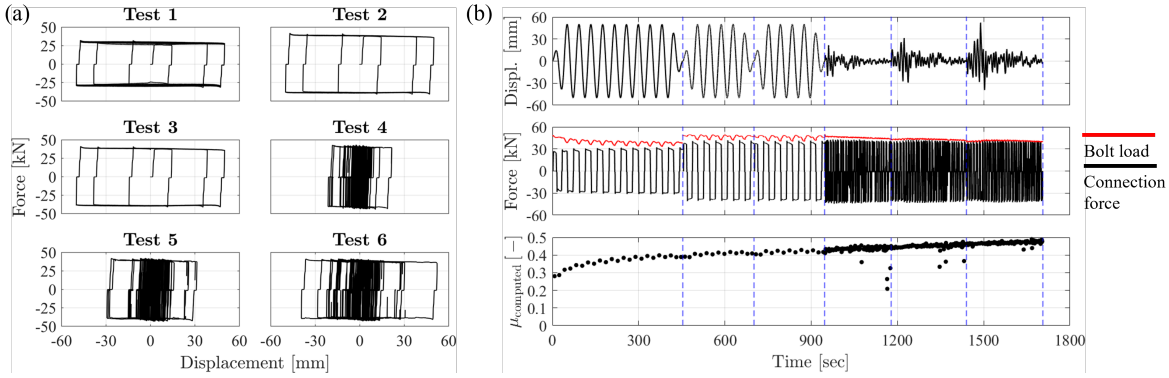

Figure 3.11. Results of Test Phase 1 Test Group 3: (a) Force-displacement responses of the connection in Test Group 3 (b) Time history results of Test Group 3 (tests are separated by dashed blue lines). From top to bottom: imposed displacement time history; recorded connection sliding force and bolt load time histories; computed coefficient of friction $\mu_{computed}$ time history

early-stage response of the friction-based connection. After the break-in effect was established, the connection exhibited a relatively constant connection sliding force and a relatively low bolt load loss. Based on these results, a break-in loading protocol was proposed and verified for use in Test Phase 2 shaking table tests so that breaking in of the friction shims could be performed before installing the friction-based connections onto the structure.

3.3.3 Test Phase 2: Shaking Table Test

Test Phase 2 was a shaking table test conducted at the National Center for Research on Earthquake Engineering (NCREE) in Taiwan, in which a full-scale three-story, re-centering steel braced frame with sliding slabs was tested. In this frame specimen, the proposed friction-based connection was used as the force-limiting connection to limit the force transferred between the sliding slabs and the steel frame. Spring devices were used with friction-based connections in the frame specimen; they were designed to provide the re-centering capability when the slabs moved. Shaking table tests results demonstrated that, compared with the conventional frame design, the frame specimen incorporating friction-based force-limiting connections, spring devices, and sliding slabs exhibited reduced slab acceleration, roof frame drift, and base shear demands, and thereby having the potential to limit damage to nonstructural components and to support the

objective of post-earthquake functional recovery [137]. The detailed discussion about the design of the re-centering braced frame, the test setup, and the test response of the frame specimen and the spring devices, can be found in Chou et al. [137]. Only basic information about the shaking table test is provided in Section 3.3.3 to facilitate follow-up discussions. In contrast, this study focuses specifically on the friction-based connection used in this shaking table test, including its installation process, the instrumentation plan, and the connection response throughout the pre-shaking-table-test preparation, the shaking table test, and the post-shaking-table-test evaluation.

Shaking Table Test Setup

Figure 3.12 (a) presents an overview of the re-centering steel frame specimen that had three stories. The sliding slabs were termed based on the story above it; from top to bottom, they were termed RFL, 3FL, and 2FL. At each story, two friction-based connections were used to transfer the force between the steel frame and sliding slabs. They were placed on the west and east side of the steel beams of the lateral force resisting system (LFRS). The friction-based connection was termed based on the sliding slab to which it was connected and its reference position with respect to the steel beam. For example, the friction-based connection 3FL-W represented the friction-based connection connecting to the Sliding slab (3FL) and was installed on the west side of the steel beam in the LFRS system. Six friction-based connections were used in this frame (i.e., friction-based connections RFL-W/E, 3FL-W/E, and 2FL-W/E). For RFL and 3FL friction-based connections, the target connection sliding force was 40 kN; for 2FL friction-based connections, the target connection sliding force was 20 kN. The shaking table tests were conducted along the north-south direction of the frame (i.e., the motion was one-dimensional); therefore, the friction-based connections were also oriented in the north-south direction.

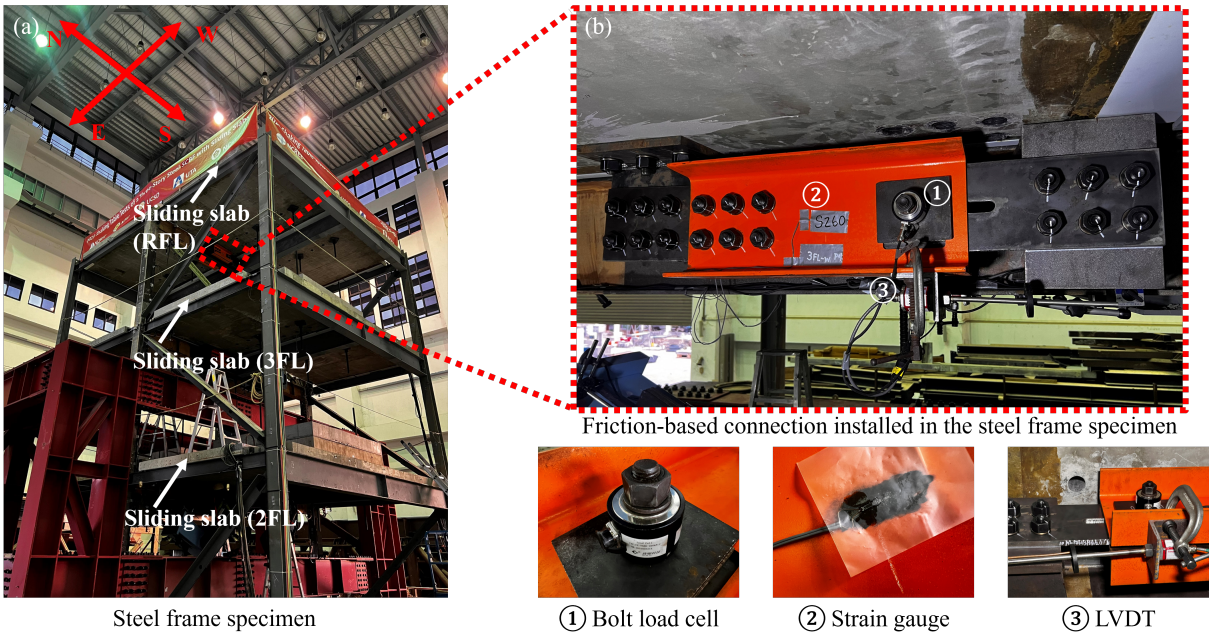

Figure 3.12. Test Phase 2 shaking table test (a) overview of the steel frame specimen and (b) instrumentation related to the friction-based connection

Installation of the Connection onto the Frame Specimen

Figure 3.13 demonstrates the installation process of the friction-based connection onto the steel frame specimen. In the shaking table test setup, the sliding end of the connection was connected to the steel beam, while the fixed end of the connection was connected to the concrete sliding slab. Steel connection plates were used on both ends of the friction-based connection to connect the ends of the connection with the steel beam and the sliding slab, as shown in Figure 3.13. To install the connection, first the connection was lifted roughly to its designated position by a crane. After aligning one bolt hole on the sliding end with the connection plate, a bolt was inserted to temporarily connect the sliding end with the connection plate and the inserted bolt was also used as a temporary pivot point, as shown in Figure 3.13. The connection was then rotated about this pivot point to align the bolt holes on the fixed end with its corresponding steel connection plate. Once aligned, a temporary fixing tool was placed on the fixed end to hold the connection in position. At this stage, the bolt holes on both ends were properly aligned and the connection was in its designated position. The final step was to insert all the bolts on both ends

and to tighten the bolts so that the friction-based connection was properly connected with the connection plates. In this test, the connecting bolts on both ends were tightened to a slip-critical condition. Figure 3.13 also presents the final state of the installation process when the connection was installed on the frame specimen. The entire installation process was completed by three workers, taking approximately eight to twelve minutes.

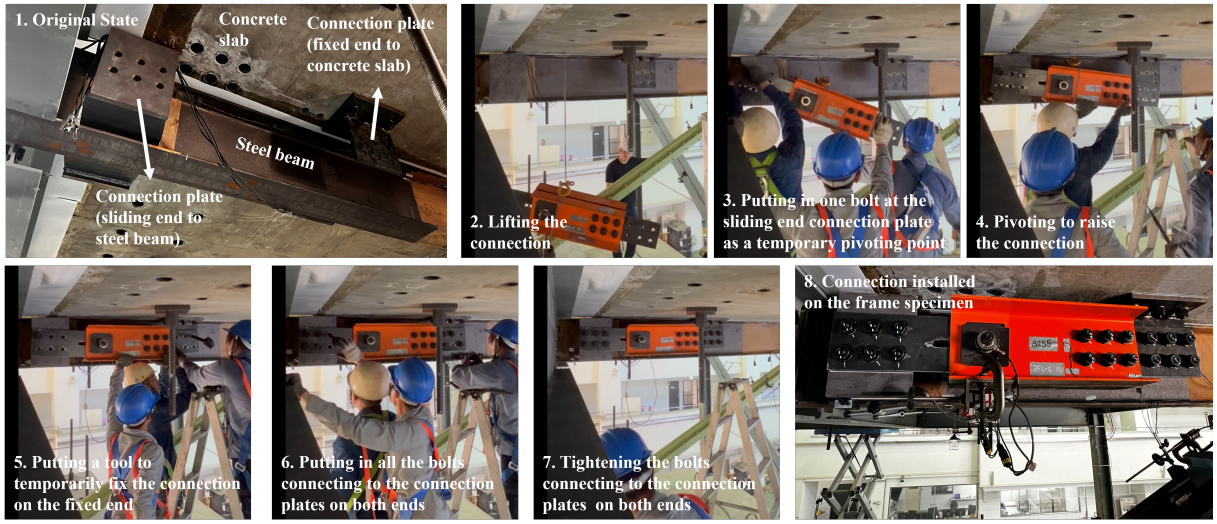

Figure 3.13. Demonstration of the connection installation process

Instrumentation

Figure 3.12 (b) presents the instrumentation setup for the friction-based connection in Test Phase 2 shaking table tests. Three types of instruments were used for the friction-based connection. The bolt load cell was used to monitor the load variation of the friction bolt throughout the shaking table test. A Linear Variable Differential Transformer (LVDT) was used to measure the connection displacement. Strain gauges were mounted on both steel channels of the connection as an indirect method for estimating the connection force. However, this approach was later found to be unreliable due to difficulties in accurately calibrating the relationship between the measured strain and the actual connection force. In addition, some strain gauges might become loose and slipped relative to the steel channel during the test, resulting in measurement errors.

Results

Before installing six friction-based connections onto the frame specimen, all connections underwent the break-in loading protocol proposed in Test Phase 1 (Figure 3.10) as the pre-shaking-table-test preparation step and this was denoted as Test Phase 2 Test Group 1. Figure 3.14 presents the result of one of the connections. It can be observed that towards the end of the break-in loading protocol, the connection sliding force increased to the target connection sliding force (±40 kN) and the sliding force was maintained at a relatively constant level. In addition, the bolt load loss of the friction bolt decreased as the break-in process continued. Although not shown, the testing results of the other five connections were similar. The six friction-based connections after the break-in process in Test Phase 2 Test Group 1 were considered ready for the shaking table tests in Test Group 2.

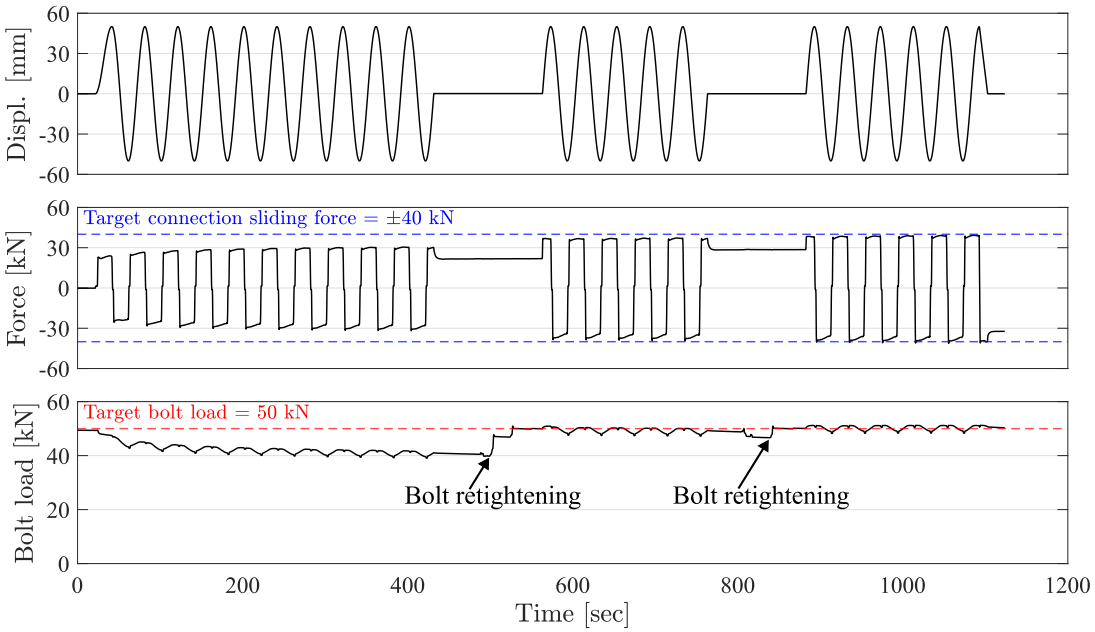

Figure 3.14. Selected results of Test Phase 2 Test Group 1 of one representative connection. From top to bottom: imposed displacement time history; connection sliding force time history; and friction bolt load time history

In the shaking table test (Test Phase 2 Test Group 2), the selected ground motion was obtained from the September 18, 2022, Guanshan and Chihshang Earthquake, which was

recorded at the EYUL-EW station close to a collapsed building [148]. Eight tests were conducted with ground motions having different intensities by scaling the peak ground acceleration (PGA). Table 3.5 presents the testing sequence of the shaking table test. The test intensity was obtained by normalizing the measured PGA of the shaking table platen to the design PGA at the DBE level (0.24 g) and the MCE level (0.32 g). The measured PGA of the shaking table platen is also presented in Table 3.5. Between tests, the specimen was inspected to assess the condition of all members including beams, columns, braces, and friction-based connections; no additional actions (e.g., retightening the friction bolts) were performed.

Table 3.5. Testing sequence of the shaking table test

Test	Test Intensity	PGA [g]	Test	Test Intensity	PGA [g]
1	6% DBE	-0.02	5	98% MCE	-0.32
2	35% DBE	-0.08	6	-120% MCE	0.38
3	70% DBE	-0.17	7	166% MCE	0.53
4	92% DBE	-0.22	8	-161% MCE	-0.51

Figure 3.15 shows the measured displacement time history, the cumulative displacement time history, and the absolute sliding velocity time history of the RFL-W and RFL-E friction-based connections throughout the shaking table test. The responses of the RFL friction-based connections were of interest because they had higher peak displacement demands than the 3FL and 2FL friction-based connections. From Figure 3.15, it is observed that since the shaking table test motion was along the plane of the LFRS (north-south direction) and given that the steel frame specimen was essentially symmetric about the north-south axis, RFL-W and RFL-E friction-based connections had nearly identical responses.

The displacement time history shows that during Tests 1 and 2 (6% DBE and 35% DBE), there was negligible relative displacement on the sliding ends of the connections. The connection displacement became noticeable from Test 3 (70% DBE) afterward. A peak connection displacement of -69.2 mm was observed in Test 7 (166% MCE). Due to the re-centering mechanism of the frame and the slabs, the residual displacement of the connection after each test remained

relatively small, consistently less than 6 mm. The cumulative displacement time history was derived from the recorded connection displacement time history. The cumulative displacement time history started from 4.1 m to take into account the cumulative displacement of the friction interface during the pre-shaking-table-test break-in process in Test Group 1. The cumulative displacement time history confirmed the previous observation that the connection displacement was negligible in Tests 1 and 2 and became noticeable from Test 3 afterward. The total cumulative displacement of eight tests was approximately 0.85 m for RFL connections. The absolute sliding velocity time history was also derived from the recorded connection displacement time history. The peak absolute sliding velocity that the connection underwent throughout the shaking table test was observed in Test 7 (166% MCE), of approximately 525 mm/s.

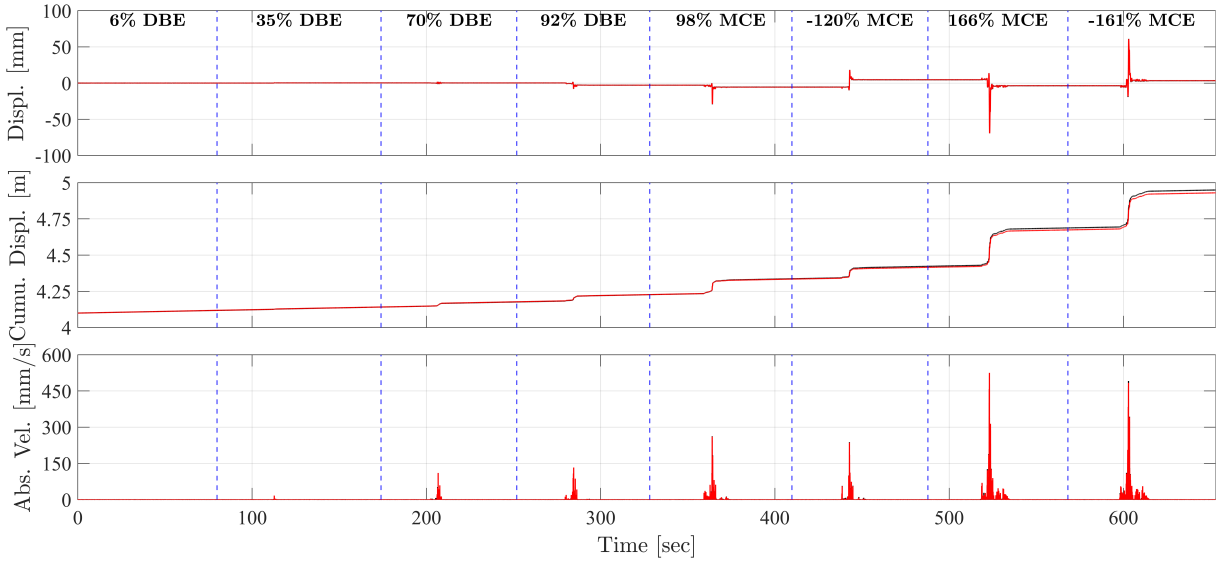

Figure 3.15. Selected results of the shaking table test: displacement time history, cumulative displacement time history, and absolute sliding velocity time history of RFL-W (in black) and RFL-E (in red) friction-based connections

Figure 3.16 presents the friction bolt load time history of all the friction-based connections in the frame specimen. The difference in recorded testing durations between the bolt load time history in Figure 3.16 and the displacement time history in Figure 3.15 was attributed to the use of separate data acquisition channels for LVDTs and bolt load cells. The data acquisition channels for these two instruments were started and stopped at different times, resulting in a

difference in the recorded testing durations. The displacement response and the friction bolt load time history were processed separately, and no synchronization was performed. As shown in Figure 3.16, the bolt load variation during Tests 1 and 2 was negligible. The first noticeable bolt load loss occurred in Test 3. A possible explanation for the observed bolt load loss in Test 3 was that, as shown in Figure 3.15, the connection displacement became noticeable in Test 3, which means that the steel channel made contact with the friction shim, pushed the friction shim to move relative to the internal sliding plate, and activated the sliding friction mechanism. During the assembly process, when the friction shim was placed into the opening of the steel channel, it was possible that the edge of the friction shim was not perfectly aligned with the edge of the opening of the steel channel. The contact between the steel channel and the edge of the friction shim potentially created a self-aligning mechanism and forced the edge of the friction shim to align with the edge of the opening of the steel channel. This process potentially induced a slight in-plane rotation of the friction shim and might consequently result in the observed bolt load loss in Test 3. The cumulative bolt load loss from the beginning to the end of the testing sequence is also reported in Figure 3.16 for each connection. For all the connections, the amount of the bolt load loss at the end of the testing sequence was similar, being about 5 kN. The cumulative bolt load loss throughout the testing sequence was primarily attributed to the wear of the friction shims [136].

Although there was no observed mechanical failure or damage associated with the Gatke 398 friction shims, the replacement of friction shims was still demonstrated after the completion of all shaking table tests, while the friction-based connection remained installed on the frame specimen. This was to experimentally justify the advantage of the design concept of this connection, that the design with loose steel washer plates allows quick inspection and replacement of the friction shims. Figure 3.17 presents the friction shim replacement process. To replace the friction shims, the friction bolt was first loosened. Then the bolt load cell and the steel washer plate were removed, making the friction shim exposed. The friction shim could then be removed from the connection for inspection, and could be replaced if necessary. After placing

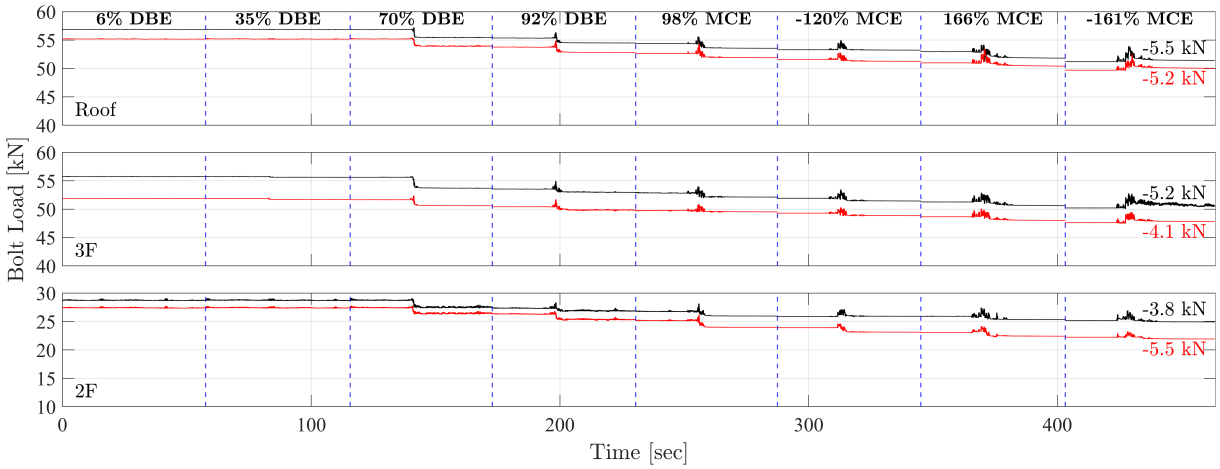

Figure 3.16. Friction bolt load time history of all the friction-based connections in this frame specimen throughout the shaking table test. From top to bottom: friction bolts for RFL connections, for 3FL connections, and for 2FL connections. Responses in black are for -W connections and responses in red are for -E connections.

the friction shim back to the connection, the steel washer plate and the bolt load cell were placed back. The friction bolt was then retightened to the designed normal load level to complete the assembly process. The entire friction shim replacement process was completed by two workers and took approximately three minutes.

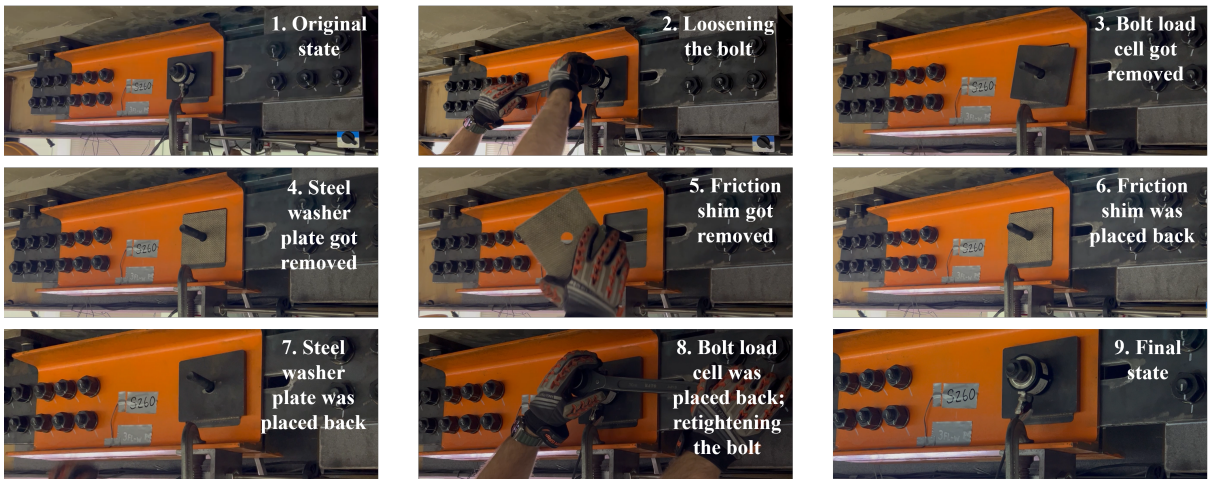

Figure 3.17. Friction shim replacement demonstration after the completion of the shaking table tests while the friction-based connection remained installed on the frame specimen

The limitation of Test Group 2 was that the use of strain gauges as an indirect measurement for estimating the connection force was found to be unreliable for estimating the force

response of the connection during shaking table tests. To address this limitation, follow-up connection tests were conducted in Test Group 3 as a post-shaking-table-test evaluation process to provide a supporting evidence of the response of the connection during the shaking table tests. In Test Group 3, one of the friction-based connections with a target connection sliding force of 40 kN was removed from the steel frame specimen and was subjected to six displacement-controlled cyclic tests to verify the connection response during the shaking table test. Out of the six tests, one test had linear ramped waves as the imposed displacement time history of the input excitation while the remaining five tests used recorded connection displacement responses from Tests 4 to 8 in the shaking table test as the imposed displacement time history of the input excitation. The recorded connection displacement responses used were from an RFL friction-based connection.

Figure 3.18 presents the force-displacement response of the connection in Test Group 3. It is observed that in the six tests conducted in Test Group 3, the friction-based connection exhibited a stable force-displacement response and the connection sliding force was maintained at a relatively constant level of about 40 kN. Hence, the results of Test Group 3 provided supporting evidence that the force-displacement response of the connection was stable throughout the shaking table test.

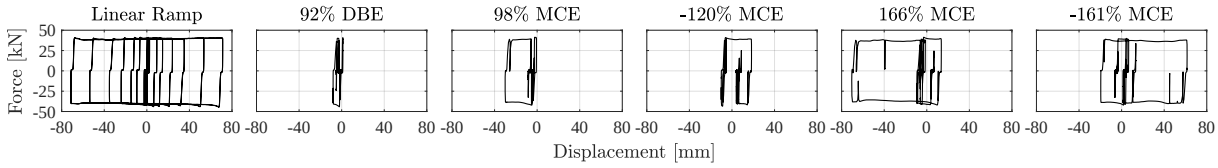

Figure 3.18. Force-displacement responses of the connection in Test Phase 2 Test Group 3

Approximately ten months after the shaking table test, Test Group 4 was conducted to investigate the possible influence of environmental exposure and aging effects on the response of the friction-based connection. During the period between the shaking table test and Test Group 4, the connection specimen was stored in the lab without any protection. The friction bolt was hand-tightened during the storage process and was retightened to the target normal load level of 50 kN before the start of Test Group 4. In Test Group 4, two tests were conducted. Both

tests used linear ramped waves as the imposed displacement time history of the input excitation. Figure 3.19 presents the force-displacement response of the connection in Test Group 4. The results showed that the friction-based connection exhibited a stable force-displacement response and the connection sliding force was maintained at a relatively constant level of about 40 kN.

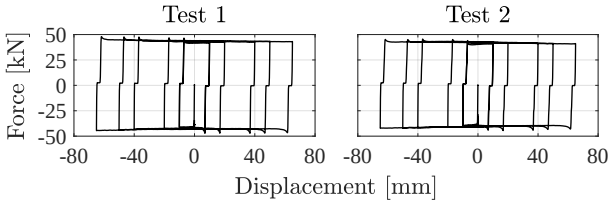

Figure 3.19. Force-displacement responses of the connection in Test Phase 2 Test Group 4

Summary of Test Phase 2 Results

Test Phase 2 successfully implemented the use of the proposed friction-based connection in the three-story re-centering steel frame specimen for the shaking table test. The connection successfully accommodated a relative displacement of approximately 70 mm between the steel frame and the sliding slab. The bolt load loss of the friction bolt of the connection was relatively low. The repairability of the connection was demonstrated by replacing the friction shims while the friction-based connection remained installed on the frame specimen. The pre-shaking-table-test preparation and post-shaking-table-test evaluation tests further demonstrated that after the break-in effect was established, the connection exhibited a stable force-displacement response and the connection sliding force was relatively constant. Test Group 4 results indicated that ten months of storage had no noticeable impact on the force-displacement response of the connection, which enhanced the confidence in the long-term performance of the proposed friction-based connection.

3.4 Conclusions

This chapter presents the development and experimental characterization of a novel yet practical design concept for friction-based structural components intended for use as energy

dissipation devices or force-limiting connections in earthquake-resistant structures. The proposed connection has a slotted-bolted configuration and the main difference between this design and the conventional design of slotted-bolted friction-based components is that, in this design, initially loose plates are used to establish the clamping mechanism. This design concept offers two key advantages. First, The connection has stable force-displacement responses and generates relatively constant sliding forces without enforcing tight geometric tolerances in the machining of the parts. Secondly, the design with loose steel washer plates allows quick inspection and replacement of friction shims if needed.

To verify this design concept, a numerical simulation was conducted to assess the expected kinematics and force-displacement responses of the connection. Critical regions of high stress were identified to facilitate the design and detailing of the parts. A friction-based structural component, which has a required sliding force of 40 kN, was designed with the proposed design concept and tested. Two test phases including component-level connection tests (99 tests in total) and a full-scale shaking table test of a three-story re-centering steel braced frame (8 tests in total), in which the proposed friction-based connection was designed as the force-limiting connection between the steel frame and the sliding slab, were performed. Based on the results of the experimental study, the following conclusions were made:

- Without enforcing tight geometric tolerances in the machining of the parts, the friction-based force-limiting connection designed with loose steel washer plates exhibited stable force-displacement responses. The connection tested in this study generated a relatively constant sliding friction force equal to the required sliding force (40 kN) without exhibiting the uncontrolled displacement-dependent variable friction force. Hence, it was demonstrated that compared with the conventional design of slotted-bolted friction-based components, the proposed design concept with loose steel washer plates can save both manufacturing time and cost.

- The break-in effect of the composite-metallic friction interface influenced the early-stage

response of the friction-based connection. It is recommended to break in the composite friction shim before installing the connection onto the structure so that the friction interface of the connection can reach a relatively steady state and the connection can generate a relatively constant connection sliding force with a relatively low bolt load loss.

- For the connection tested in this study (friction interface: Gatke 398 to low-carbon structural steel; nominal normal pressure: 3.8 MPa), the break-in loading protocol used was the following: Break-in test 1 (ramped sinusoidal waves with a cumulative displacement of 2 meters) $\rightarrow$ Bolt retightening $\rightarrow$ Break-in test 2 (ramped sinusoidal waves with a cumulative displacement of 1 meter) $\rightarrow$ Bolt retightening $\rightarrow$ Break-in test 3 (ramped sinusoidal waves with a cumulative displacement of 1 meter) $\rightarrow$ Bolt retightening. The ramped sinusoidal waves used had a peak displacement of 50.8 mm and a peak sliding velocity of 7.62 mm/s. The break-in loading protocol resulted in a total cumulative displacement of 4 meters.

- Throughout the shaking table test, the proposed friction-based connection successfully accommodated a relative displacement of approximately 70 mm between the steel frame and the sliding slab, under a peak sliding velocity of approximately 525 mm/s, with a relatively low bolt load loss (5 kN).

- The inspection and replacement of the friction shims for the friction-based connection designed with loose steel washer plates could be performed relatively easily without removing the connection from the structure. Compared with the conventional design, of which the inspection and replacement process requires removal of external clamping plates, the proposed design concept with loose steel washer plates allows a quicker inspection and repairing process, which potentially enhances the practicality of the connection in real applications and supports the long-term functionality of earthquake-resistant buildings equipped with friction-based connections.

- The two test phases showed no failure or damage in the parts of the proposed friction-based components even after multiple displacement time histories.
- Reference times for manufacturing, assembling, installing, and repairing of one connection are as follows: Manufacturing: 180 minutes; Assembling: 3 minutes; Installing: 8$\sim$12 minutes; Repairing: 3 minutes.

In conclusion, the proposed design concept with loose steel washer plates provides a low-cost, less sensitive to machining tolerances, and easily repairable solution for designing friction-based structural components in earthquake engineering applications. Potential future work includes (1) component-level connection tests under higher required sliding forces and (2) system-level shaking table tests for structures equipped with the proposed connection under multi-directional seismic excitation.

Acknowledgments

Chapter 3, in full, is a reprint of the material as it appears in: Chen, K., Tsampras, G., Chou, C. C., Lin, H. Z., Wu, C. J., Córdova, A., Uang, C. M., & Chao, S. H. (2026). Low-Cost Friction-Based Force-Limiting Connection With Reduced Sensitivity to Machining Tolerances and Accelerated Repairability. *Earthquake Engineering & Structural Dynamics*. Credits are distributed as follows: Kaixin Chen: writing – original draft and editing, Visualization, Experiments, Data curation and analysis, Methodology, Investigation. Georgios Tsampras: writing – original draft and editing, Research need and scope conceptualization, Friction-based connection design concept, manufacturing and experiments, Resources, Funding acquisition and project administration (UC San Diego), Methodology, Investigation, Data curation and analysis. Chung-Che Chou: writing – review and editing, Resources, Experiments, Resources, Funding acquisition and project administration (NCREE), Methodology, Investigation, Sliding floor shake table testing lead, Shake table testing data curation. Huang-Zuo Lin: writing – review, Experiments, Data curation, Methodology, Investigation. Chi-Jeng Wu: writing – review, Experiments, Data curation, Methodology, Investigation. Alvaro Córdova: writing – review,

Experiments, Data curation, Methodology, Investigation. Chia-Ming Uang: writing – review and editing, Sliding floor design conceptualization, Methodology, Investigation. Shih-Ho Chao: writing – review and editing, Sliding floor design conceptualization, Methodology, Investigation.

Chapter 4

Friction-Based Structural Components with Predetermined Discrete Variable Friction Forces at Target Design Displacement Levels

4.1 Overview

This chapter presents the development of a friction-based structural component designed to develop predetermined discrete variable friction forces at target displacement levels. The concept of practical force-limiting connections, core wall structures, and the implementation of force-limiting connections in core wall structures are first discussed as the background and the motivation of the study presented in this chapter. Previously developed connections capable of developing multiple discrete variable force levels at target displacement levels are also reviewed.

4.2 Background

4.2.1 Practical Force-Limiting Connections

Practical force-limiting connections have been developed with the goal of limiting the seismic-induced horizontal forces transferred from the floors to the vertical elements of planar seismic force-resisting systems in earthquake-resistant buildings and limit the higher-mode effects [149, 150, 70, 151, 2, 3, 138, 152, 153, 154]. A force-limiting connection consists of a friction

device or a buckling-restrained brace and low-damping rubber bearings. The force-limiting connections are designed to accommodate the seismic-induced three-dimensional kinematic requirements between floors and planar seismic force-resisting systems. The low-damping rubber bearings provide out-of-plane stability to the planar walls of the seismic force-resisting system and post-elastic stiffness to the force-limiting connections. The post-elastic stiffness in the force-limiting connections limits the seismic-induced displacement of the floors relative to the planar seismic force-resisting system. A force-limiting connection that consists of a friction device and low-damping rubber bearings installed in an example building with rocking walls [2, 3] has been presented in Figure 1.4 (b). The seismic response of buildings with force-limiting connections between gravity load resisting systems and reinforced concrete planar walls [149, 150, 70, 151, 2, 138], planar rocking walls [2, 3, 152, 153, 154], and self-centering concentrically braced steel frames [149, 138] has been studied. The use of force-limiting connections in these buildings (1) limits the seismic-induced force and acceleration responses, (2) reduces the variability in the force and acceleration responses due to the ground motion variability, and (3) mitigates the effects of higher-mode responses on the dynamic response of buildings [70]. Similar observations have been made for the seismic response of buildings with dissipative floor connectors between the gravity load resisting system and steel concentrically braced frames [155]. The dissipative floor connectors consist of rubber bearings and a friction device [156].

4.2.2 Friction-based Force-limiting Connections in Core Wall Buildings

The reinforced concrete core wall system is a widely used seismic force-resisting system for tall buildings because of its high lateral stiffness and its capacity for dissipating energy [157, 158, 159, 160, 161, 162]. In addition to reinforced concrete, core walls can also be formed using cross-laminated timber structural walls [163] or concrete filled composite plate structural walls [164, 165, 166]. In contrast to planar seismic force-resisting systems that are not stable out-of-plane if they are not braced, core walls are stable without lateral bracing. In the core

wall system, the wall piers are typically connected by reinforced concrete coupling beams along the height of the structure [167]. The core wall system is designed in a way that the nonlinear inelastic mechanism takes place at the coupling beams and at the base of the walls, with the rest of the structure designed to remain linear elastic [167]. Similar to buildings with planar seismic force-resisting systems, the inelastic response at the core wall base reduces the first mode response. However, the higher-mode effects are not reduced by the inelastic response at the wall base [168] and they may amplify the seismic-induced story shear forces and floor accelerations.

Force-limiting connections between the floors of the flexible gravity load resisting system and the stiff core wall could be used to mitigate the higher-mode effects on the dynamic response of tall buildings and contribute to the accelerated post-earthquake recovery of these buildings to a target level of functionality. However, the force-limiting connections developed for buildings with planar walls cannot be used in buildings with core walls. The reason is that the three-dimensional kinematic requirements in force-limiting connections between the floors and the core wall are different from the three-dimensional kinematic requirements in force-limiting connections between floors and planar walls. The high stiffness of the rubber bearings under compression would constrain the relative movement between the floors and the core wall, making the force-limiting connection ineffective, as shown schematically in Figure 4.1. In the already developed force-limiting connection for planar wall buildings, the functions of rubber bearings are (1) to provide out-of-plane stability to the planar walls and (2) to provide post-elastic stiffness to the force-limiting connection to prevent the potentially excessive connection deformation. Shake-table experimental seismic simulations of a half-scale, four-story reinforced concrete flat-plate structural wall structure with force-limiting connections conducted at the NHERI experimental facility at UC San Diego [169] showed that pounding of the slabs and the planar walls is expected at the maximum-considered-level of earthquake ground motion [3]. As a result, rubber bumpers are required to transfer the pounding forces. The rubber bumpers are used in addition to the friction devices and the low-damping rubber bearings. The use of conventional friction devices with constant force transferred between the floors of the flexible gravity load

resisting system and the stiff core wall without the use of low-damping rubber bearings and bumpers would result in large displacement of the floor relative to the core wall and potentially uncontrolled pounding forces at the maximum-considered-level of earthquake ground motions.

Considering the above-mentioned limitations related to the use of the already developed force-limiting connections in core wall buildings, there is a need for a structural connection that can develop predetermined forces at target design displacement levels with the goal of limiting the force and acceleration responses of core wall buildings without inducing excessive displacement demand in the connections.

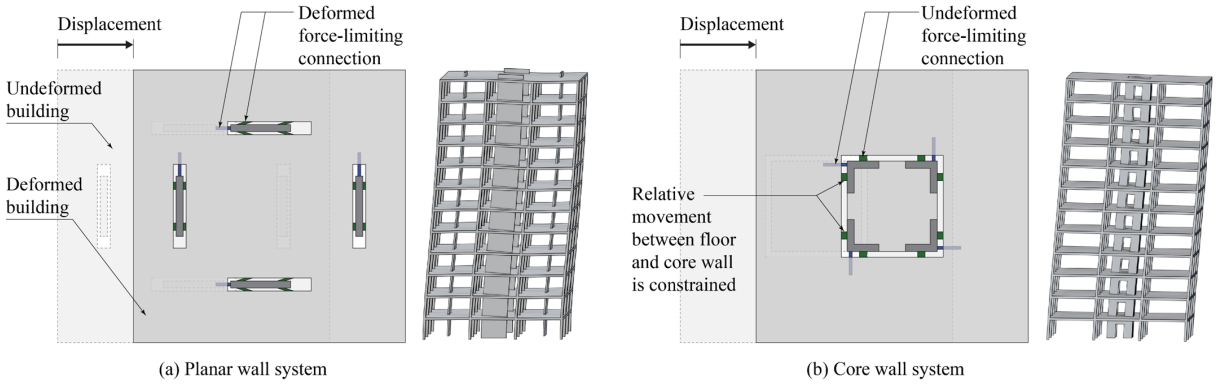

Figure 4.1. In contrast with the planar wall system, the relative movement between the floors and the core wall system is constrained by the rubber bearings. The planar wall system is shown in (a) and the core wall system is shown in (b).

4.2.3 Structural Connections Capable of Developing Multiple Discrete Variable Force Levels at Target Displacement Levels

Early conceptual work in structural connections capable of developing multiple resistance levels at target displacement levels can be traced to Weidlinger and Ettouney [170]. In their study, a connection concept termed *sequential connections* was proposed. Sequential connections were introduced at selected structural joints along the seismic load path to permit controlled slip. The term *sequential* reflects the fact that the resulting force-displacement response of the connection does not follow an elastic-perfectly plastic response typical of conventional friction connections, but instead develops through successive slip and resistance segments, resulting in

a step-like force-displacement response. This behavior was proposed to be achieved through relatively simple connection details, such as bolts in slotted holes. Using numerical analyses of a single-degree-of-freedom model, Weidlinger and Ettouney [170] showed that such step-like force-displacement responses could improve the seismic response of a structure by reducing the peak displacement and the residual deformation. Weidlinger [171] subsequently interpreted sequential connections as a form of passive structural control and further examined the selection of optimal design parameters for such connections. Numerical earthquake simulation results further indicated that by incorporating such step-like force-displacement responses, the peak inelastic response of a structure could be reduced by about 20% to 50%, again highlighting the potential benefit of this structural connection concept [171].

Structural connection concepts capable of developing multiple discrete variable force levels at target displacement levels have received increasing research attention in recent years for two main reasons. First, as discussed above, increasing the connection force at target design displacement levels can help limit excessive connection deformation. Second, such force-displacement responses offer the possibility of multi-level earthquake protection, in which different resistance mechanisms or force levels are activated under seismic excitations of different intensities. Past studies on such concepts are summarized in Table 4.1. In these studies, additional connection resistance is activated only after a target connection displacement is reached, typically through relatively simple physical mechanisms such as gap closure and subsequent bearing contact between components. By delaying the engagement of the additional force-resisting component, the connections are able to develop multiple discrete variable force levels at target displacement levels and thus exhibit a step-like force-displacement response.

Among the studies summarized in Table 4.1, friction-based connections and hybrid connections involving friction form an important subset. In many of these concepts, developing discrete variable force levels at target displacement levels is achieved by connecting a friction-based component, commonly in a slotted-bolted configuration, in series with another component whose activation force is larger than the sliding force of the friction-based component. The

Table 4.1. Summary of previous studies on structural connections capable of developing multiple discrete force levels at target displacement levels

Author(s)	Year	Device type	Working mechanism	Author(s)	Year	Device type	Working mechanism
Cheraghi and Zahrai [172]	2016	Metallic	Translational	Huang et al. [173]	2024	Friction	Rotational
Lee et al. [174]	2016	Hybrid friction + metallic	Shear-type	Kazemi et al. [175]	2024	Metallic	Translational
Pan et al. [176]	2017	Metallic	Translational	Ke et al. [177]	2024	Metallic	Translational
Yan et al. [178]	2018	Hybrid lead extrusion + friction	Translational	Liu et al. [179]	2024	Metallic	Translational
Naeem and Kim [180]	2019	Metallic	Shear-type	Sha et al. [181]	2024	Friction	Translational
Ranaei and Aghakouchak [182]	2019	Hybrid viscoelastic + metallic	Shear-type	Xiong et al. [183]	2024	Metallic	Translational
Ghorbani and Rofooei [184]	2020	Friction	Translational	Yang et al. [185]	2024	Friction	Translational
Wang et al. [186]	2020	Friction	Translational	Yang et al. [187]	2024	Friction	Translational
Wang et al. [188]	2020	Metallic	Translational	Yang et al. [189]	2024	Metallic	Shear-type
Friis et al. [190]	2021	Friction	Translational	Yang et al. [191]	2024	Viscous fluid	Translational
Golmoghany and Zahrai [192]	2021	Hybrid friction + metallic	Shear-type	Yu et al. [193]	2024	Hybrid friction + metallic	Sliding Bearing
Jiang et al. [194]	2021	Metallic	Translational	Bai et al. [195]	2025	Hybrid friction + nitrogen gas spring damper (NGS)	Translational
Kiani and Hashemi [196]	2021	Metallic	Shear-type	Dong et al. [197]	2025	Friction	Rotational
Shahbazi and Moaddab [198]	2021	Friction	Translational	Lie et al. [199]	2025	Hybrid friction + metallic	Translational
Sun et al. [200]	2021	Hybrid viscous + lead	Shear-type	Luo et al. [201]	2025	Friction	Translational
Chen et al. [202]	2022	Metallic	Shear-type	Pan et al. [203]	2025	Hybrid viscoelastic + metallic	Shear-type
Dai et al. [204]	2023	Hybrid friction + metallic	Translational	Sakai et al. [205]	2025	Hybrid friction + metallic	Translational
Jiang et al. [206]	2023	Friction	Translational	Tian et al. [207]	2025	Hybrid friction + metallic	Translational
Ke et al. [208]	2023	Hybrid friction + metallic	Translational	Wei et al. [209]	2025	Metallic	Rotational
Li et al. [210]	2023	Metallic	Translational	Wu et al. [211]	2025	Hybrid viscoelastic + friction	Translational
Lu et al. [212]	2023	Hybrid friction + metallic	Translational	Zhang et al. [213]	2025	Metallic	Translational
Yang et al. [214]	2023	Hybrid friction + metallic	Rotational	Tan et al. [215]	2026	Metallic	Shear-type
Chang Chien and Guo [216]	2024	Friction	Translational	Zhou et al. [217]	2026	Hybrid friction + metallic	Rotational
Dong et al. [218]	2024	Friction	Translational				

activation force of the second component may correspond, for example, to the sliding force of another friction-based component or to the yield force of a metallic component. Once the target displacement level is reached, the movement of the bolts associated with the first friction-based component is restrained by the slot length, causing the connection force to increase beyond the sliding force of that component and consequently activating the second component [174, 184, 190, 198, 204, 208, 185, 195]. Although utilizing bolt-slot contact provides a simple way to develop discrete variable force levels at target displacement levels, this approach also has several limitations. First, once the slot geometry is determined, the target displacement levels for the activation of additional connection resistance cannot be adjusted easily. Moreover, the repeated bearing action between the bolts and the slot may result in damage to the connection components, which may compromise the long-term practicality of the connection.

4.3 Scope of Study

This chapter presents a simple and practical structural connection able to develop pre-determined discrete variable friction forces at target design displacement levels. As a result, a performance-based discrete variable limiting force-displacement response can be achieved. The innovative connection is termed Modified Friction Device (*Modified FD*). The term *Modified* is to distinguish its force-displacement response with those of conventional friction devices, of which constant friction forces are typically expected. In the following sections, the schematics of the physical embodiment of the Modified FD are presented. The components and the assembly of the Modified FD are discussed. The mechanics of the Modified FD are explained. Results from static structural analyses of two types of finite element models of the Modified FD are presented. The first model is developed using solid finite elements and it is termed *Solid Model*. The Solid Model is used to assess the expected kinematics and the expected force-displacement response of the Modified FD. The second model is developed using a truss finite element and it is termed *Truss Model*. The Truss Model can be used to efficiently simulate the force-displacement

response of the Modified FD in numerical earthquake simulations of structural systems. The force-displacement response of the Modified FD computed using a numerical earthquake simulation of an eighteen-story reinforced concrete core wall building model is presented. The seismic response of the building model with Modified FDs is compared with the seismic response of the building model with monolithic connections and the seismic response of the building model with friction devices with constant friction forces. The results presented in this study show that it is possible to develop a simple and practical structural connection with predetermined discrete variable force-displacement response to limit the seismic-induced horizontal forces transferred between the floors of the flexible gravity load resisting system and the core wall piers in high-performance earthquake resilient buildings.

4.4 Modified FD

4.4.1 Components and Assembly

Figure 4.2 shows a sketch of the components, the exploded view, the assembly, and the front view of the Modified FD. The Modified FD consists of an internal plate, two external plates, four bearing plates, four friction shims between the external plates and the internal plate (termed friction shims for external plates), four friction shims between the bearing plates and the internal plate (termed friction shims for bearing plates), ten structural bolts with flat washers and nuts, and a spherical bearing. The number of bearing plates, friction shims, and bolts can be adjusted to achieve the variations of the predefined discrete variable friction force-displacement response discussed in the following sections. The end clevises used to attach a Modified FD on the floor and the seismic force-resisting system are not shown in Fig. 5. The plates and the clevises are made of structural steel ASTM A572 Grade 50. The friction shims are made of composite material similar to the laminated glass fiber fabric with graphite composite materials [219] used in friction devices developed for force-limiting connections [2].

Pretension load is applied to the bolts to clamp the external plates, the bearing plates, the

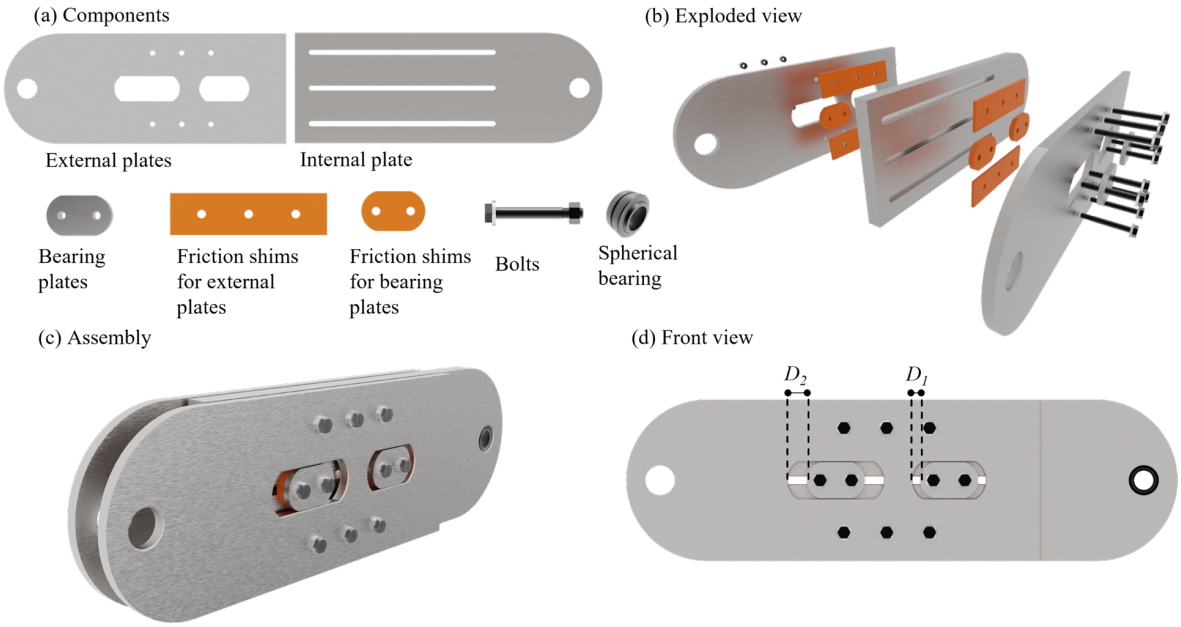

Figure 4.2. Schematics of the Modified FD (a) components, (b) exploded view, (c) assembly, and (d) front view with initial gap dimensions D_1 and D_2 between the bearing plates and the slots in the external plates.

friction shims, and the internal plate. The bolted components create the assembly of the Modified FD. Friction interfaces are established in the contact surfaces between the internal plate and the friction shims. The bolt load results in normal force on the friction interfaces between the friction shims and the internal plate. The friction shims for the external plates are not expected to move relative to the external plates. The friction shims for the bearing plates are not expected to move relative to the bearing plates. The slots in the internal plate allow the longitudinal motion of the friction shims, the external plates, and the bearing plates relative to the internal plate. The bearing plates and the associated friction shims are positioned within slots in the external plates, and they are not expected to move relative to the internal plate until the bearing plates are in contact with the external plates. The first gap distance between the bearing plates and the slots in the external plates is termed D_1, and the second gap distance between the bearing plates and the slots in the external plates is termed D_2 , as shown in Figure 4.2. The spherical bearings at the end of the Modified FD and the clevis allow the rotational motions and restrain the translational motions within the plane of the plates. As a result, the Modified FD is expected to develop axial

load along its longitudinal direction and zero moments at the ends.

4.4.2 Expected Kinematics and Force-displacement Response

Figure 4.3 shows the expected kinematics and the expected force-displacement response of the Modified FD. The term ”expected” is used because the kinematics and force-displacement response have not been validated through experimental testing. The following parameters define the expected kinematics and the expected force-displacement response: the first gap between the bearing plates and the slot in each external plate is termed D_1; the second gap between the bearing plates and the slot in each external plate is termed D_2; the friction force generated by the frictional interface between the internal plate and the friction shims for the external plates is termed F_1; the friction force generated by the frictional interface between the internal plate and the friction shims for the bearing plates in the slots associated with D_1 is termed F_2 ; the friction force generated by the frictional interface between the internal plate and the friction shims for the bearing plates in the slots associated with D_2 is termed F_3 ; and the elastic stiffnesses are termed K_1, K_2, and K_3. K_1 simulates the flexibility of the components of the Modified FD that are designed to have a linear elastic force-displacement response, and the shear flexibility of the friction shims associated with external plates. The linear elastic components include the clevis plates, the external plates, the internal plate, and the pins. K_2 and K_3 simulate the flexibility of the components of the Modified FD that are designed to have a linear elastic force-displacement response, the shear flexibility of the friction shims associated with external plates, and the shear flexibility of the friction shims associated with D_1 and D_2, respectively. Six phases define the expected kinematics of the Modified FD that result in the expected force-displacement response. The expected kinematics and the expected force-displacement response described below assume that the translational motion of the external plates is restrained (i.e., pinned condition at the ends of the external plates) and that a displacement along the longitudinal direction of the Modified FD is applied at the end of the internal plates. Positive displacement results in axial tension in the Modified FD and negative displacement results in axial compression in the Modified FD.

The following section presents the six phases. The discussion of the kinematics in the six phases ignores the elastic deformations F_1/K_1, F_2/K_2, and F_3/K_3 assuming $K_1 = K_2 = K_3 \approx \infty$. The rigid body kinematics of the Modified FD components are considered.

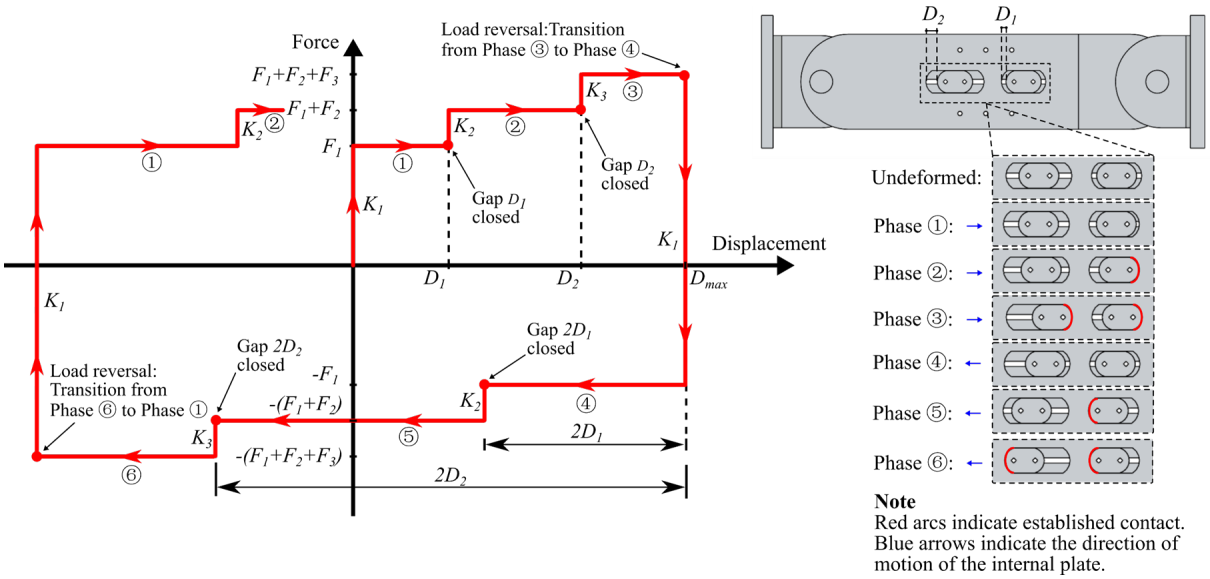

Figure 4.3. Expected kinematics and expected force-displacement response in the Modified FD.

Phase 1 – Sliding along the positive direction of motion with friction force F_1: The increase of the imposed displacement in the Modified FD results in increasing force with stiffness K_1. When the force in the Modified FD becomes equal to F_1, the friction shims for the external plates and the external plates start moving relative to the internal plate. The sliding at the frictional interface between the internal plate and the friction shims for the external plates results in F_1. F_1 can be estimated using Coulomb theory, $F_1 = n_s N_1 \mu_{s1}$, where $n_s = 2$ is the number of friction interfaces; $N_1$is the total load from the six bolts acting normal to the friction interfaces between the friction shims for the external plates and the internal plate; μ_{s1} is the coefficient of friction in the friction interfaces between the friction shims for the external plates and the internal plate.

Phase 2 – Sliding along the positive direction of motion with friction force $F_1 + F_2$: Assuming $K_1 \approx \infty$, once the value of displacement reaches D_1, the external plates contact the bearing plates located in the slots associated with D_1. As the displacement in the Modified

FD increases, the force in the Modified FD increases with stiffness K_2. When the force in the Modified FD becomes equal to $F_1 + F_2$, the bearing plates and the friction shims in the slots associated with D_1 start moving relative to the internal plate. The sliding at the frictional interface between the internal plate and the friction shims in the slots associated with D_1 results in F_2. F_2 can be estimated using Coulomb theory, $F_2 = n_s N_2 \mu_{s2}$, where N_2 is the total load from the two bolts acting normal to the friction interfaces between the friction shims in the slots associated with D_1 and the internal plate; μ_{s2} is the coefficient of friction in the friction interfaces between the friction shims in the slots associated with D_1 and the internal plate. The total force in the Modified FD during this phase is $F_1 + F_2$.

Phase 3 – Sliding along the positive direction of motion with friction force $F_1 + F_2 + F_3$: Assuming $K_1 = K_2 \approx \infty$, once the value of the displacement reaches D_2, the external plates contact the bearing plates located in the slots associated with D_2. As the displacement in the Modified FD increases, the force in the Modified FD increases with stiffness K_3. When the force in the Modified FD becomes equal to $F_1 + F_2 + F_3$, the bearing plates and the friction shims in the slots associated with D_2 start moving relative to the internal plate. The sliding at the frictional interface between the internal plate and the friction shims in the slots associated with D_2 results in F_3. F_3 can be estimated using Coulomb theory, $F_3 = n_s N_3 \mu_{s3}$, where N_3 is the total load from the two bolts acting normal to the friction interfaces between the friction shims in the slots associated with D_2 and the internal plate; μ_{s3} is the coefficient of friction in the friction interfaces between the friction shims in the slots associated with D_2 and the internal plate. The total force in the Modified FD during this phase is $F_1 + F_2 + F_3$. The motion continues until the Modified FD reaches the maximum imposed displacement $D_{\max}$.

Phase 4 – Sliding along the negative direction of motion with friction force -F_1: The reversal of the imposed displacement reduces the force in the Modified FD with elastic stiffness K_1. When the force in the Modified FD becomes equal to -F_1, the internal plate starts moving relative to the external plates along the negative direction. The friction shims for the bearing plates are not expected to move relative to the internal plate during this phase. The internal plate

moves relative to the friction shims for the external plates and the external plates, resulting in a force with magnitude equal to F_1.

Phase 5 – Sliding along the negative direction of motion with friction force $-(F_1+F_2)$: Assuming $K_1 \approx \infty$, once the value of displacement reaches $D_{\max}$- $2D_1$, the external plates contact the bearing plates located in the slots associated with D_1. As the displacement in the Modified FD decreases, the force in the Modified FD decreases with stiffness K_2. When the force in the Modified FD becomes equal to $-(F_1+F_2)$, the internal plate starts moving relative to the bearing plates and the friction shims in the slots associated with D_1. The sliding at the frictional interface between the internal plate and the friction shims in the slots associated with D_1 results in a force with magnitude equal to F_2. The total force in the Modified FD during this phase is $-(F_1+F_2)$.

Phase 6 – Sliding along the negative direction of motion with friction force $-(F_1+F_2+F_3)$: Assuming $K_1 = K_2 \approx \infty$, once the value of displacement reaches $D_{\max}$- $2D_2$, the external plates contact the bearing plates located in the slots associated with D_2. As the displacement in the Modified FD decreases, the force in the Modified FD decreases with stiffness K_3. When the force in the Modified FD becomes equal to $-(F_1+F_2+F_3)$, the internal plate starts moving relative to the bearing plates and the friction shims in the slots associated with D_2. The sliding at the frictional interface between the internal plate and the friction shims in the slots associated with D_2results in a force with magnitude equal to F_3. The total force in the Modified FD during this phase is $-(F_1+F_2+F_3)$.

Compared with friction-based connections that use bolt-slot contact to develop discrete variable force levels at target displacement levels, as summarized in Table 4.1, the Modified FD offers two distinct advantages. First, the displacement-related design parameters, D_1 and D_2, can be relatively easily adjusted by changing the lengths of the bearing plates. Second, the step-like force-displacement response of the Modified FD is achieved through bearing action between the external plates and the bearing plates, rather than through bolt-slot contact. This avoids direct bearing between bolts and slot edges, which is more prone to damaging either the bolts or the slotted plates.

4.5 Numerical Simulations of the Modified FD

Experimental characterization of the kinematics and the force-displacement response of the Modified FD is required. However, finite element analyses can be used for rapid digital prototyping of the Modified FD. For this reason, the Solid Model and the Truss Model defined in Section 2 are developed. The Solid Model is used to assess the expected kinematics and the expected force-displacement response of the Modified FD. The Truss Model is used to efficiently simulate the force-displacement response of the Modified FD in numerical earthquake simulations of structural systems. This section presents the results from the static structural analyses of the Solid Model and the Truss Model.

4.5.1 Description of the Solid Model

Figure 4.4 shows the undeformed geometry of the Solid Model developed in ANSYS Mechanical finite element software [160] and its exploded view, front view, and top view. The Solid Model explicitly simulates the internal plate, the external plates, the bearing plates, the friction shims, the clevises, and the pins using 24,962 eight-node solid finite elements. In this model, the overall lengths (i.e., their longest dimensions along the x-direction) of the external plates are 122.56 cm, their thicknesses (i.e., their dimensions along the y-direction) are 2.54 cm and their heights (i.e., their dimensions along the z-direction) are 41.91 cm; the overall length of the internal plate is 127.64 cm, its thickness is 5.08 cm and its height is 41.91 cm; the overall lengths of the bearing plates are 15.56 cm, their thicknesses are 1.52 cm and their heights are 9.68 cm; the dimensions of the friction shims for the external plates are 38.1 cm $\times$ 1.02 cm $\times$ 10.16 cm (x $\times$ y $\times$ z); the overall lengths of the friction plates associated with the bearing plates are 15.56 cm, their thicknesses are 2.03 cm and their heights are 9.68 cm; the diameters of both pins are 7.8 cm. The bolts are assumed to be ASTM A325 structural bolts with a diameter of 19.05 mm. The minimum pretension of each bolt is 124.55 kN. ASTM A572 Grade 50 is considered for the steel plates. The Solid Model does not explicitly simulate the bolts and

the associated washers and nuts used to apply the normal force on the friction interfaces. The preload of the bolts is simulated as a constant force boundary condition distributed to the nodes on the surface of the elements in the external plates and the bearing plates. The surfaces that the simulated bolt load is applied are highlighted with green color in the front view shown in Fig. 7 and they represent the common surface areas between the washers and the external plates and the common surface areas between the washers and the bearing plates. Zero displacement boundary condition is enforced at all the degrees of freedom of the nodes located on the surface of the single clevis located closer to the origin of the global x-axis. In a building application, the single clevis would have been attached to a core wall pier. As a result, the enforced boundary condition is a simplification. The simplified boundary condition is acceptable considering that the objective of the analysis of the Solid Model is to assess the expected kinematics and the expected force-displacement response of the Modified FD. For the same reason, simplified nonzero displacement boundary condition is enforced at the degrees of freedom along the global x-axis of the nodes on the surface of the double clevis further away from the origin of the global x-axis.

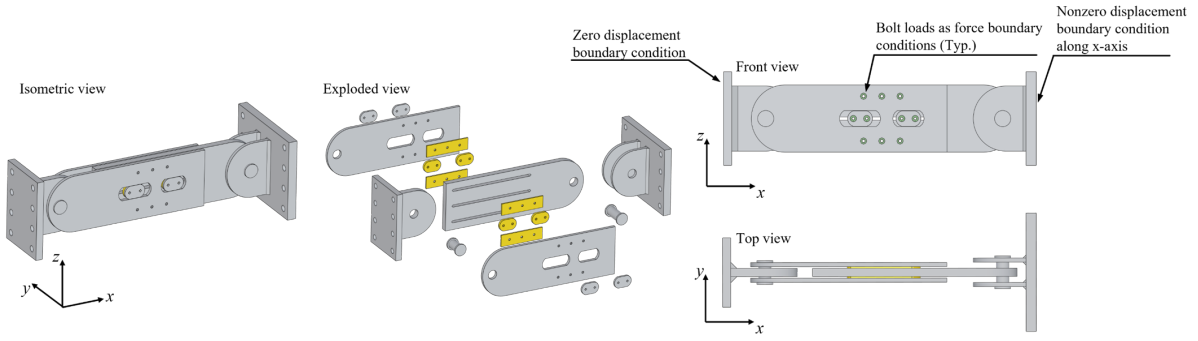

Figure 4.4. Finite element model developed to assess the expected kinematics and the expected force-displacement response of the Modified FD.

The Solid Model explicitly simulates the contact interfaces between the modeled components of the Modified FD using pair-based contact definition with 44,805 surface-to-surface contact elements. A contact pair is defined between each curved surface of a bearing plate and the adjacent curved surface in the slot of the external plate. These contact pairs are assumed

to be frictionless. A contact pair is defined between each surface of the friction shims and the adjacent surface of the internal plate. The stress normal to the surfaces is related to the shear stress that defines the limit for the initiation of sliding using the Coulomb friction model with a constant friction coefficient equal to 0.4. The assumed friction coefficient is justified based on past experimental observations [2] of a friction device with friction interfaces established between steel and laminated glass fiber fabric with graphite composite friction shims [219]. The friction shims are assumed to be bonded on the bearing plates and the external plates. This assumption is justified considering that the bearing action of the bolts on the friction shims enforces the kinematic compatibility between the friction shims and the bearing plates and between the friction shims and the external plates. Past research has shown that it is possible to accomplish this kinematic compatibility without damaging the friction shims due to the expected bearing stresses acting on the friction shims [2]. A contact pair is defined between each surface of the pins and the surface of the internal plate where bearing is expected to occur. Similarly, a contact pair is defined between each surface of the pins and the surface of the external plates where bearing is expected to occur. A constant friction coefficient equal to 0.3 is assumed for the steel pin to steel plates contact interfaces. The components of the Modified FD are designed to remain linear elastic. All materials are simulated using a linear elastic constitutive stress-strain relationship. The structural steel is assumed to have a modulus of elasticity equal to 200 GPa and a Poisson's ratio equal to 0.3. The composite friction material is assumed to have a modulus of elasticity equal to 6.9 GPa and a Poisson's ratio equal to 0.4. The example parameters considered for the design of the Modified FD used to develop the Solid Model are D_1 = 2 cm, D_2 = 5 cm, F_1 = 600 kN, F_2 = 200 kN, and F_3 = 200 kN. The calculation of F_1, F_2, and F_3 follows Coulomb theory, for example, $F_1 = n_s N_1 \mu_{s1}$, where n_s = 2 is the number of friction interfaces; N_1 is the total load from the six bolts acting normal to the friction interfaces, N_1 = 6 $\times$ 124.55 kN = 747.30 kN, given the minimum pretension of each bolt is 124.55 kN; μ_{s1} = 0.4 is the assumed coefficient of friction at the friction interface. Standard oversize holes were considered for all the pin holes. As a result, the difference between the nominal diameter of the holes and the nominal

diameter of the pins is equal to Δ_{dn} = 0.16 cm = 1/16 inches. A static structural analysis of the Modified FD is performed and the stiffness matrix is updated at each converged step of analysis to account for the updated geometry. The following section shows the results from the static structural analysis of the Solid Model.

4.5.2 Solid Model Analysis Results

Static structural analysis of the Solid Model is performed. The analysis is executed in two steps. Results from the analysis are shown in Figure 4.5. The force boundary conditions that simulate the bolt pretension loads are applied in the first step of analysis. In the second step of analysis, the sinusoidal displacement shown in Figure 4.5 (a) is applied along the global x-axis at the degrees of freedom with the nonzero displacement boundary condition shown in Figure 4.4. Figure 4.5 (b) shows the relationship of the applied displacement and the total reaction force along the global x-axis multiplied by -1. Positive force in the plot indicates tension in the Solid Model. The force-displacement relationship also shows the pinching displacement at zero force due to the difference between the nominal diameter of the holes and the nominal diameter of the pins. Figure 4.5 (c) shows the maximum principal stresses in the Solid Model at the first step of analysis and the ten sub-steps of the second step of analysis. In the first step, stresses develop in the Solid Model only due to the simulated bolt pretension. In the second step, the stress distribution at each sub-step is used to discuss the kinematics associated with the computed force-displacement response of the Solid Model. Sub-steps 0, 1, 4, and 7 are associated with force magnitude F_1 since contact has not been established between the bearing plates and the external plates. The gap distance D_1 has closed in sub-steps 2, 5, and 8. Two out of the four bearing plates are in contact with the two external plates. The increased magnitude of the maximum principal compressive stresses in the contact areas between two bearing plates and the two external plates is indicated with dark blue color as shown in Figure 4.5 (c). Sub-steps 2, 5, and 8 are associated with a force magnitude equal to $F_1 + F_2$. The gap distance D_2 has closed in sub-steps 3, 6, and 9. All bearing plates are in contact with the two external plates and high

magnitude maximum principal compressive stresses are observed in the contact areas between the bearing plates and the external plates. Sub-steps 3, 6, and 9 are associated with a force magnitude equal to $F_1 + F_2 + F_3$. The simulated kinematics and the computed force-displacement relationship verify that it is possible to develop predetermined discrete variable friction forces at target design displacements with the proposed Modified FD.

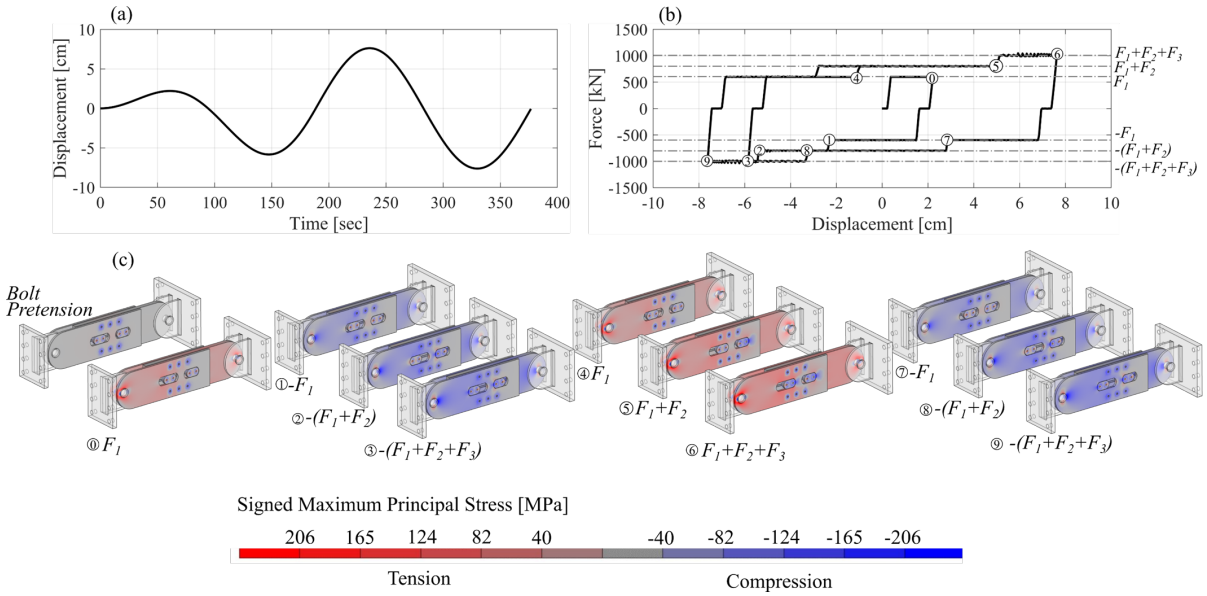

Figure 4.5. Static structural analysis of the Solid Model shows that it is possible to develop predetermined friction forces at target design displacements with the proposed Modified FD.

4.5.3 Description of the Truss Model

The Truss Model simulates the force-displacement response of the Modified FD in OpenSees [220] using a corotational truss element. Figure 4.6 shows the schematic representation of the Truss Model. A reference unit area is assigned to the truss element, termed A_{truss}. The length of the truss element is equal to the total approximate length of the Modified FD, termed L_{truss}. A uniaxial material termed *Aggregate Material* is assigned to the truss element. The term "Aggregate" is used for the uniaxial material to indicate that its stress-strain relationship is simulated by combining the stress-strain relationships of seven primary uniaxial materials. The stress of the Aggregate Material is equal to the internal force in the truss element normalized

by A_{truss}. The strain of the Aggregate Material is equal to the axial deformation of the truss element divided by L_{truss}. The use of a normalized force-displacement response as the stress-strain relationship of a uniaxial material assigned to a truss element is a common modeling approach in OpenSees [151, 220]. Figure 4.6 (b) shows the schematic representation of the combination of the seven primary uniaxial materials used to develop the Aggregate Material. The primary uniaxial materials in Figure 4.6 (b) are represented as springs and their normalized force-displacement behavior is defined in the following paragraphs.

The primary uniaxial materials termed *Friction 1*, *Friction 2*, and *Friction 3* simulate the normalized force-displacement behavior of the frictional interfaces that result in F_1, F_2, and F_3. The normalized force-displacement relationships of Friction 1, Friction 2, and Friction 3 are shown in Figure 4.6 (c), Figure 4.6 (d), and Figure 4.6 (e), respectively. Friction 1, Friction 2, and Friction 3 are modeled using the *Steel01* uniaxial material in OpenSees. Their normalized elastic stiffness simulates the elastic shear stiffness of the friction shims, $K_{shear,i} = n_{fpi} \times G \times A_{fpi}/t_{fpi}$, normalized by (A_{truss}/L_{truss}). The subscript i = 1, 2, and 3 indicates the number associated with Friction 1, Friction 2, and Friction 3, respectively.n_{fpi} is the number of friction shims associated with the development of the friction forces F_i. G is the expected shear modulus of the material of the friction shims assuming that the same material is used for all the friction shims. A_{fpi} is the surface area of the associated friction shim. t_{fpi} is the thickness of the associated friction shim. Figure 4.7 shows the schematic representation of the geometric terms A_{fpi} and t_{fpi} for i = 1, 2, and 3. The transition from the elastic to the post-elastic normalized force-displacement response simulates the slip between the friction shims and the internal plate associated with the friction force F_i for i = 1, 2, and 3 normalized by A_{truss}.

The primary uniaxial materials, termed *Gap* D_1 and *Gap* D_2, simulate the contact behavior between the bearing plates and the external plates. They are modeled using the *ElasticMultiLinear* uniaxial material in OpenSees. The normalized force-displacement relationships of Gap D_1 and Gap D_2 are shown in Figure 4.6 (f) and Figure 4.6 (g), respectively. The pinching displacement behavior at an approximately zero normalized force is simulated with a small, normalized

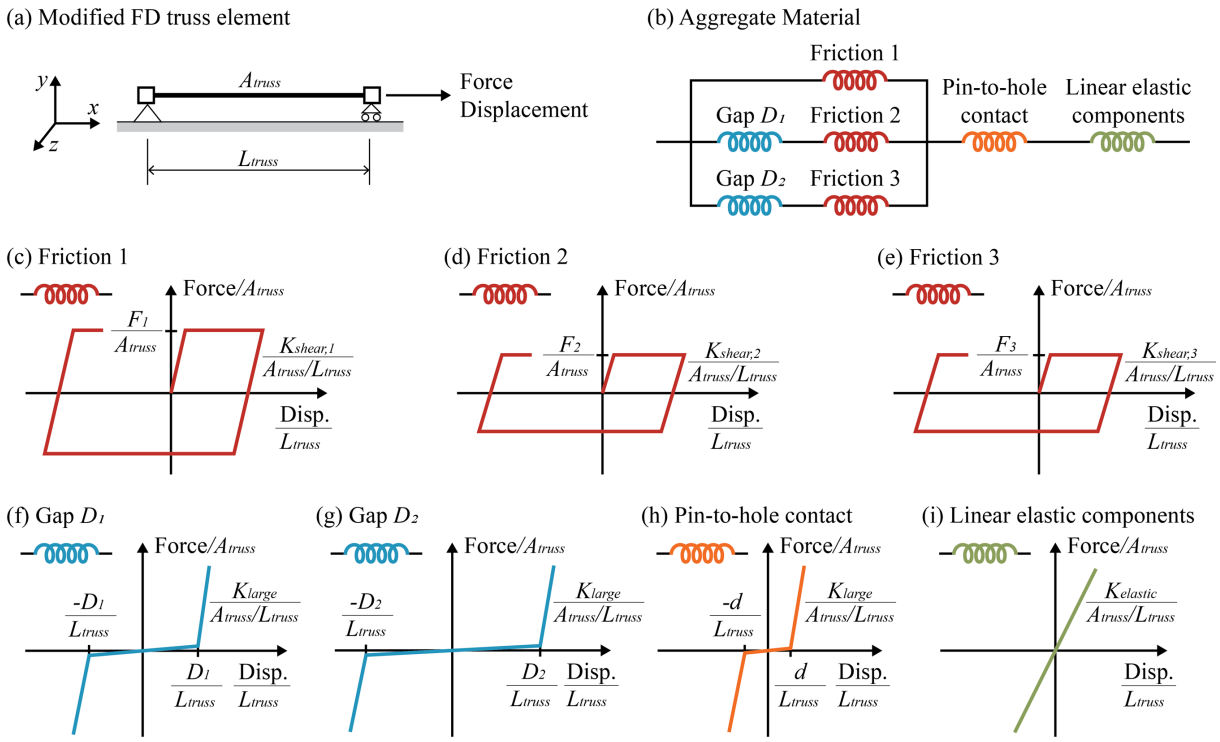

Figure 4.6. Schematic representation of the Modified FD Truss Model and the associated material definitions.

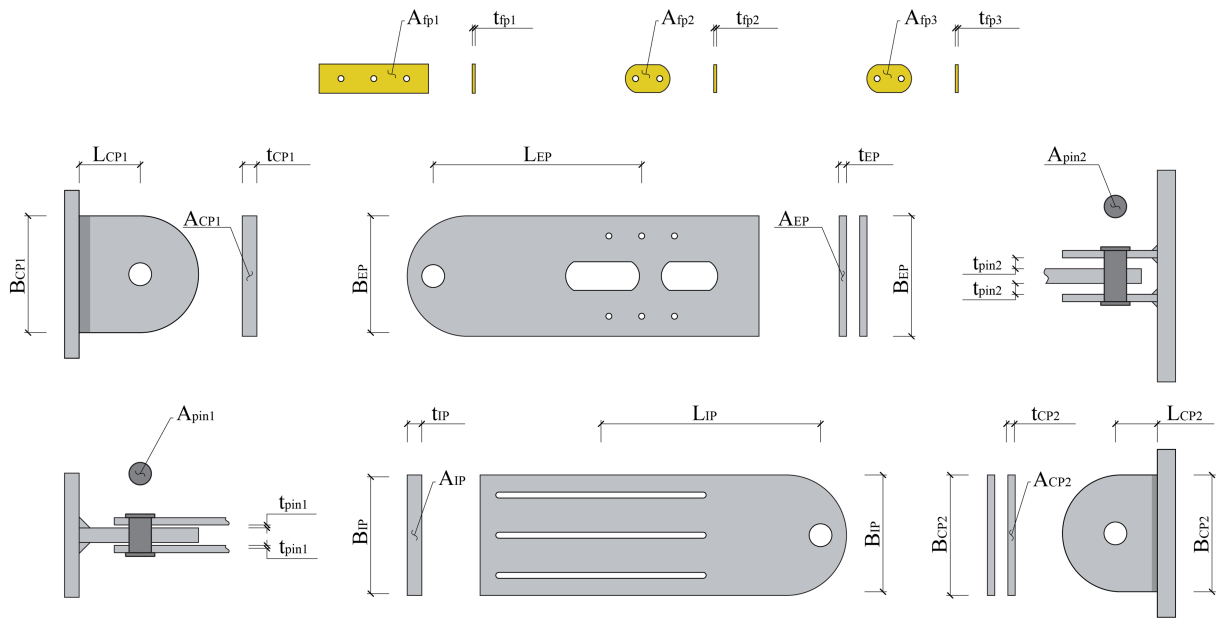

Figure 4.7. Schematic representation of the geometric terms used to estimate the stiffness of the components of the Modified FD simulated with the Truss Model.

stiffness relative to the normalized elastic stiffness of the Modified FD. The small, normalized stiffness is assigned to the normalized force-displacement region between the normalized gap lengths -D_j/L_{truss} and $D_j/L_{truss}$where j = 1 or 2 indicates the gap distance D_1 or D_2, respectively. A large, normalized stiffness relative to the normalized elastic stiffness of the Modified FD is used to simulate the normalized contact stiffness between the bearing plates and the external plates.

The primary uniaxial material, termed *Pin-to-hole contact*, simulates the contact behavior between the pins and associated holes in the clevises, the external plates, and the internal plates. Figure 4.6 (h) shows the normalized force-displacement relationship of the *ElasticMultiLinear* uniaxial material used to simulate this contact behavior. The pinching displacement behavior at an approximately zero normalized force is simulated with a small, normalized stiffness relative to the normalized elastic stiffness of the Modified FD. The small, normalized stiffness is assigned to the normalized force-displacement region between the normalized gap lengths $-d/L_{truss} = -(4 \times \Delta_{dn})/L_{truss}$ and $d/L_{truss} = (4 \times \Delta_{dn})/L_{truss}$. A large, normalized stiffness relative to the normalized elastic stiffness of the Modified FD is used to simulate the contact stiffness between the pins, the clevises, and the plates.

The primary uniaxial material, termed *Linear Elastic Components*, simulates the flexibility of the components of the Modified FD that are designed to have a linear elastic force-displacement response. Fig. 9(i) shows the normalized force-displacement relationship of the *Elastic* uniaxial material used in OpenSees. The flexibility of the elastic components is estimated as a combination of the elastic components in series as follows:

$$1/K_{elastic} = 1/K_{CP1} + 1/K_{Pin1} + 1/K_{EPs} + 1/K_{IP} + 1/K_{Pin2} + 1/K_{CP2}$$

where $K_{CP1} = E_{steel} \times A_{CP1}/L_{CP1}$ is the estimate of the axial stiffness of the single clevis plate; $K_{Pin1} = 2 \times G_{steel} \times A_{Pin1}/t_{Pin1}$ is the estimate of the shear stiffness of the pin connecting the external plates with the single clevis plate; $K_{EPs} = 2 \times E_{steel} \times A_{EP}/L_{EP}$ is the

estimate of the axial stiffness of the two external plates; $K_{IP} = E_{steel} \times A_{IP}/L_{IP}$ is the estimate of the axial stiffness of the internal plate; $K_{Pin2} = 2 \times G_{steel} \times A_{Pin2}/t_{Pin2}$ is the estimate of the shear stiffness of the pin connecting the double clevis plate with the internal plate; and $K_{CP2} = 2 \times E_{steel} \times A_{CP2}/L_{CP2}$ is the estimate of the axial stiffness of the double clevis plate. For all the terms above, A, L, and t relate to the size of components of the Modified FD and the clevis plates. Figure 4.7 shows the schematic representations of the geometric terms used to compute the estimate of the stiffness of each elastic component that was considered in the computation of the flexibility of the linear elastic components. E_{steel} and G_{steel} are the modulus of elasticity and the shear modulus of steel, respectively. The parameters for the example Modified FD model analyzed in Section 4.5.1 are the following: for the structural steel, $E_{steel} = 200$ GPa and $G_{steel} = 77$ GPa; for the single clevis plate, $B_{CP1} = 40.64$ cm, $t_{CP1} = 5.08$ cm, $A_{CP1} = B_{CP1} \times t_{CP1} = 206.45$ cm^2, and $L_{CP1} = 17.46$ cm; for the pin connecting the external plates with the single clevis plate, $A_{Pin1} = 47.78$ cm^2 and $t_{Pin1} = 1.27$ cm; for the external plates, $B_{EP} = 41.91$ cm, $t_{EP} = 2.54$ cm, $A_{EP} = B_{EP} \times t_{EP} = 106.45$ cm^2, and $L_{EP} = 72.64$ cm; for the internal plate, $B_{IP} = 41.91$ cm, $t_{IP} = 5.08$ cm, $A_{IP} = B_{IP} \times t_{IP} = 212.9$ cm^2, and $L_{IP} = 72.64$ cm; for the pin connecting the double clevis plate with the internal plate, $A_{Pin2} = 47.78$ cm^2 and $t_{Pin2} = 3.81$ cm; for the double clevis plate, $B_{CP2} = 40.64$ cm, $t_{CP2} = 2.54$ cm, $A_{CP2} = B_{CP2} \times t_{CP2} = 103.23$ cm^2, and $L_{CP2} = 14.61$ cm.

4.5.4 Truss Model Analysis Results

Static structural analyses of the Truss Model are performed to compare the computed force-displacement response with the force-displacement response computed from the static structural analyses of the Solid Model. The axial degree of freedom at one node of the Truss Model is fixed. The displacement history shown in Fig. 8(a) is applied at the second axial degree of freedom of the Truss Model. The Truss Model assumes the design parameters considered in Section 4.5.1: D_1 = 2 cm; D_2 = 5 cm; F_1 = 600 kN; F_2 = F_3 = 200 kN. Figure 4.8 shows results from two analysis cases. The first analysis case assumes standard oversized pin holes

with a 0.16 cm = 1/16 inches difference between the diameter of the pin holes and the diameter of the pins. This analysis case is termed *Standard Oversize*. The second analysis case assumes a 0.00 cm difference between the diameter of the pin holes and the diameter of the pins. This analysis case is termed *Zero Oversize*. The Zero Oversize analysis case represents an ideal design case with machining requirements subjected to low tolerance. Low tolerance machining of the components of the Modified FD can be accomplished by using Computer Numerical Control (CNC) subtracting manufacturing methods. Figure 4.8 (a) and Figure 4.8 (b) compare the force-displacement response of the Truss Model and the force-displacement response of the Solid Model for the Standard Oversize analysis case and the Zero Oversize analysis case, respectively. The comparison of the results shows that the Truss Model approximates reasonably well the force-displacement response computed using the Solid Model. As a result, the Truss Model can be used to simulate the expected force-displacement response of the Modified FD in numerical earthquake simulations of core wall building models.

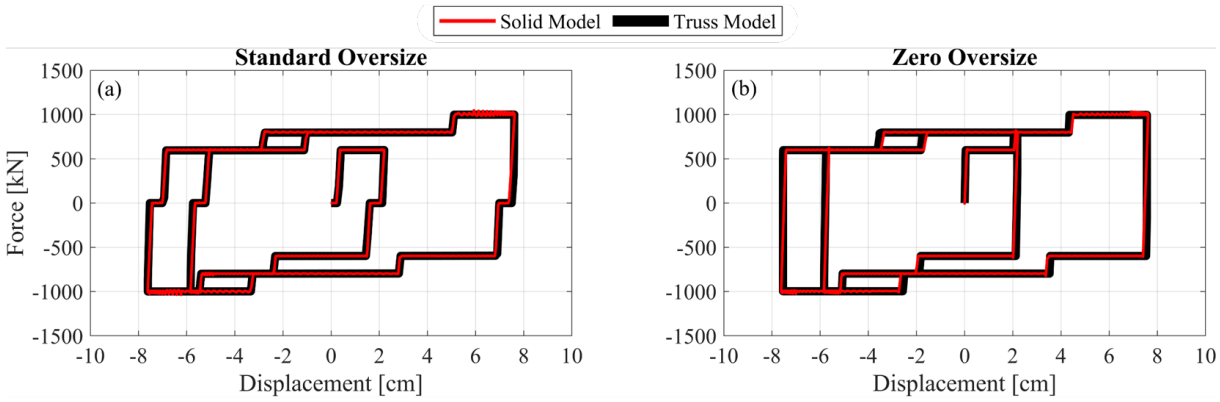

Figure 4.8. Comparison of the force-displacement response computed using the Solid Model and the Truss Model assuming standard oversized pin holes and zero oversized pin holes.

Five additional static structural analyses of the Truss Model are conducted to show the effect of the variation of the design parameters D_1, D_2, F_1, F_2, and F_3 in the expected force-displacement response of the Modified FD. Table 1 lists the design parameters considered in the six analysis cases discussed in this section.

The Baseline Model assumes the design parameters discussed in the Zero Oversize

Table 4.2. Design parameters considered in six variations of the Truss Model

Case of Design Parameters [-]	D_1 [cm]	D_2 [cm]	F_1 [kN]	F_2 [kN]	F_3 [kN]
Baseline Model	2.00	5.00	600	200	200
DP1	3.56	5.00	600	200	200
DP2	2.00	6.35	600	200	200
DP3	2.00	5.00	800	200	200
DP4	2.00	5.00	600	400	200
DP5	2.00	5.00	600	200	400

analysis case. DP1 assumes that the bearing plate in the slot associated with D_1 is replaced by a bearing plate that is 3.12 cm shorter compared to the bearing plate assumed in Baseline Model. DP2 assumes that the bearing plate in the slot associated with D_2 is replaced by a bearing plate that is 2.70 cm shorter compared to the bearing plate assumed in Baseline Model. DP1 and DP2 can be accomplished by replacing the associated bearing plates without revising the design of the remaining components of the Modified FD. DP3 assumes that F_1 is changed from 600 kN to 800 kN, which represents a case when the number of bolts contributing to F_1 is increased from six to eight. DP4 assumes that F_2 is changed from 200 kN to 400 kN, which represents a case when the number of bolts contributing to F_2 is increased from two to four. DP5 assumes that F_3 is changed from 200 kN to 400 kN, which represents a case when the number of bolts contributing to F_3 is increased from two to four. Static structural analyses are conducted using the displacement history shown in Figure 4.5 (a). Figure 4.9 (a) shows the force-displacement response computed from the analysis of the Baseline Model. Figure 4.9 (b) through (f) compare the force-displacement response of the baseline model with the force-displacement responses computed from the analysis of DP1, DP2, DP3, DP4, and DP5. The results demonstrate that the expected performance of the Modified FD is possible to be controlled by selecting the design parameters that lead to predefined forces at target displacement levels.

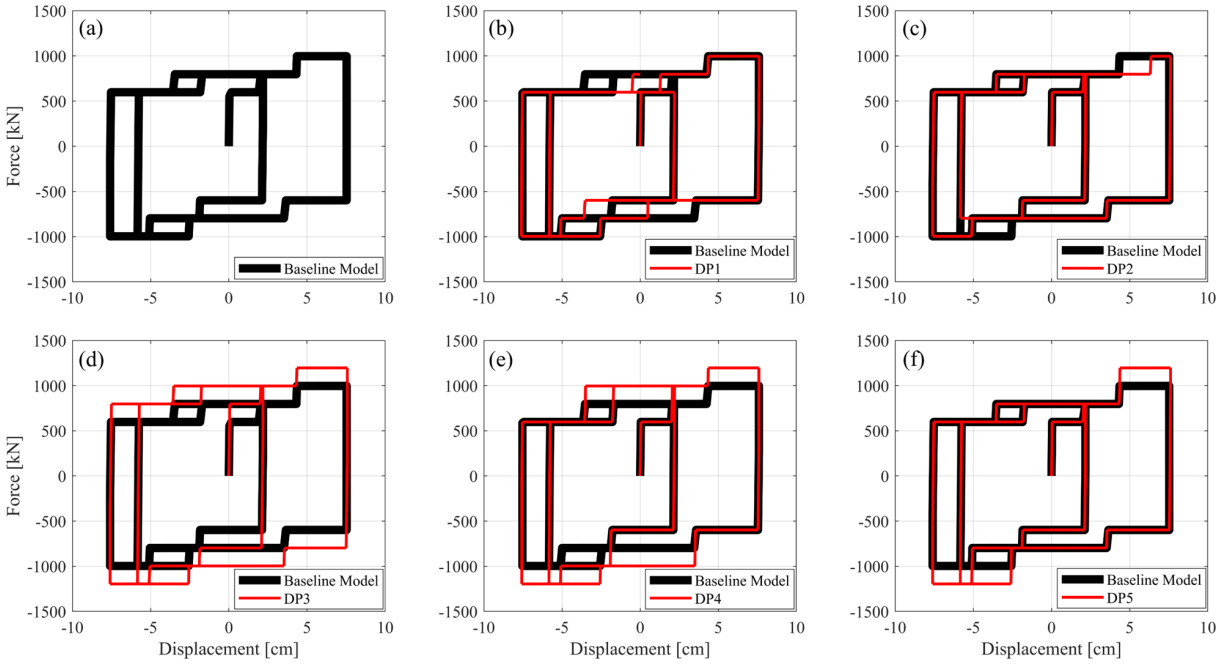

Figure 4.9. The force-displacement responses from six analysis cases of the Truss Model show that the expected performance of the Modified FD is possible to be controlled by selecting the design parameters that lead to predefined discrete variable forces at target displacement levels.

4.6 Seismic Demands in Modified FDs from Numerical Earthquake Simulation of Core Wall Building

In this section, the expected force and displacement seismic demands in the Modified FD are computed using results from a numerical earthquake simulation of a model of a reinforced concrete core wall building with Modified FDs. The computed displacement demands can be used as applied displacement histories in future testing for the experimental characterization of the kinematics and the force-displacement response of the Modified FD. The Modified FD between each floor and core wall pier is simulated using a Truss Model. The seismic response of the building model with Modified FDs is compared with the seismic response of the building model with monolithic connections and the seismic response of the building model with friction devices with constant friction forces. It is shown that it is possible to develop discrete variable limiting forces transferred between the floors of the flexible gravity load resisting system and the core wall piers within design target displacement levels. The detailed assessment of the seismic

response of core wall buildings with Modified FD is outside the scope of this study.

4.6.1 Numerical Model of Example Building

An eighteen-story reinforced concrete core wall building is adopted from a reference report by Tauberg et al. [160]. The seismic force-resisting system of the building is a core wall with four L-shaped wall piers connected by coupling beams along the height of the structure, as shown in Figure 4.10. The typical story height is 3.0 m (i.e., 10 ft), the length of the wall is 2.7 m (i.e., 9 ft), and the aspect ratio of the coupling beam is 3.0 with a length of 2.3 m (i.e., 7.5 ft) and a height of 0.8 m (i.e., 30 in). The slab is 0.2 m (i.e., 8 in) thick with a 1.8 m (i.e., 6 ft) cantilever slab overhang. Twelve gravity columns are located along the edge of the slab with a 9.1 m (i.e., 30 ft) distance. The structure was designed for Seismic Design Category (SDC) $D_{\max}$ as defined in FEMA P695.

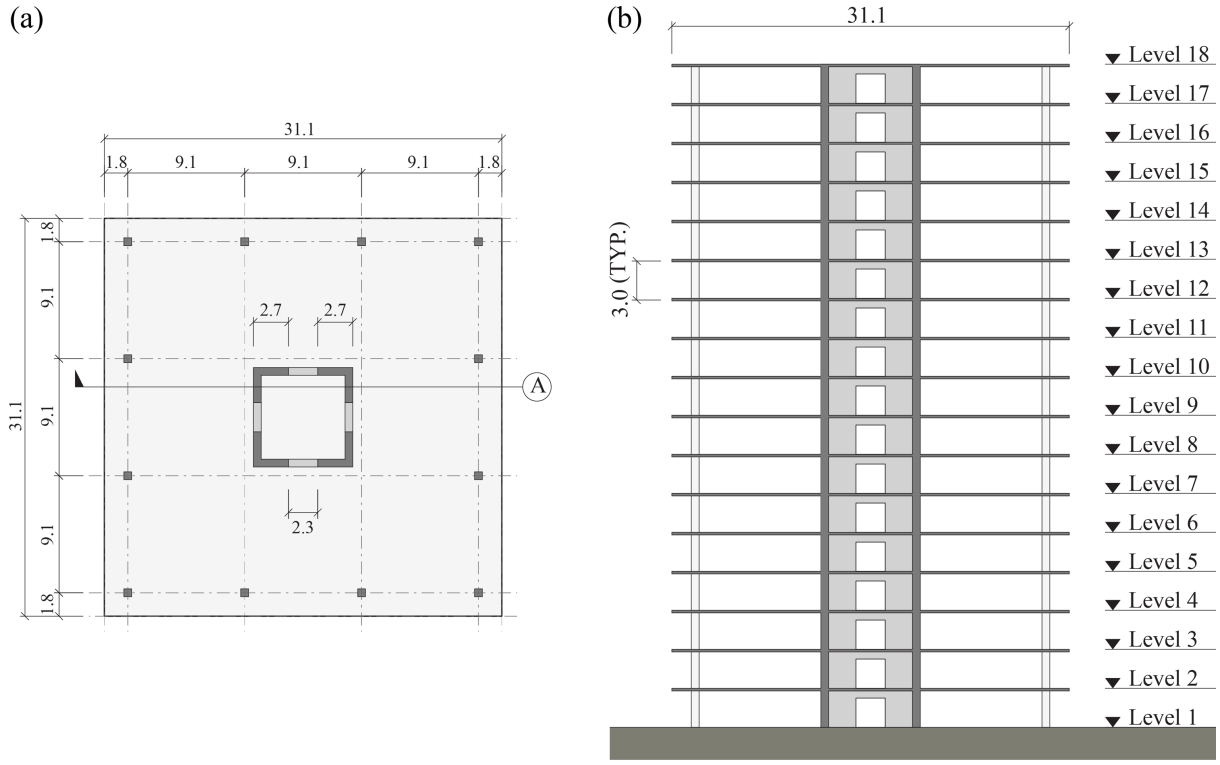

Figure 4.10. (a) Typical floor plan and (b) section A of the eighteen-story building (all dimensions are in meters).

A three-dimensional numerical model of this eighteen-story core wall building with added Modified FDs between the floors and the core wall piers was developed in OpenSees. Figure 4.11 shows the schematic representation of the eighteen-story core wall building with the Modified FDs, the numerical model of the eighteen-story core wall building, and a typical simulated floor in the numerical model of the eighteen-story core wall building. The four piers of the core wall in each story of the building model are simulated using force-based nonlinear elements with fiber sections. The inelastic response of the coupling beams that are connecting the wall piers is simulated using lumped plasticity zero-length elements. The gravity columns are simulated using four linear elastic beam-column elements with section properties that aggregate the cracked section properties of the gravity columns. Rigid in-plane behavior is assumed for the diaphragms. The Truss Model is used to simulate the Modified FD. The Modified FD design parameters used in the model are D_1 = 2.0 cm, D_2 = 5.0 cm, and $F_2 = F_3$ = 200 kN. The values of F_1 on the 18th floor, 17th floor, 16th floor, 15th floor, and 1st – 14th floor are 1262 kN, 1082 kN, 902 kN, 722 kN, and 614 kN, respectively. The values of F_1 at each floor were computed using a force-based method proposed by Tsampras and Sause [138]. This method is modified from the ASCE/SEI 7-16 [80] alternative seismic design force method for floor diaphragms. Numerical earthquake simulations [138] demonstrated that using this method in designing reinforced concrete planar wall buildings with force-limiting connections would result in reasonable connection deformation demands and relatively uniform distribution connection deformation demands over the height of the building.

The building model was subjected to a ground motion recorded at Shin-Osaka station during the 1995 earthquake in Kobe, Japan, scaled to the design level of the expected earthquake ground motion. The two horizontal components of the scaled ground acceleration, SHI000 (H1) and SHI090 (H2), are shown in Figure 4.12 (a) and Figure 4.12 (b), respectively. Figure 4.12 (c) shows the response spectra of the scaled ground motion and the design spectrum with a 5% damping ratio. The natural periods of the first, second, and third translational modes of the building model properties are also plotted in Fig. 15(c). H1 and H2 are applied at the base of the

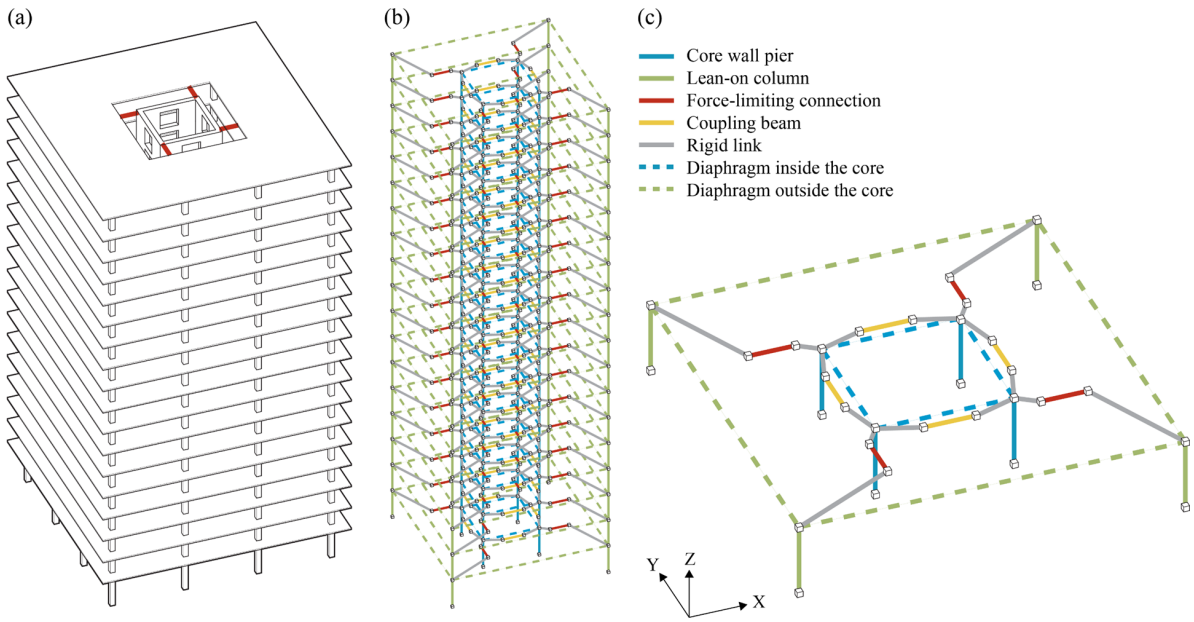

Figure 4.11. Schematic representation of (a) the eighteen-story core wall building with the Modified FDs, (b) the numerical model of the eighteen-story core wall building and (c) a typical floor simulated in the numerical model of the building.

building model along the global X- and Y- directions, respectively.

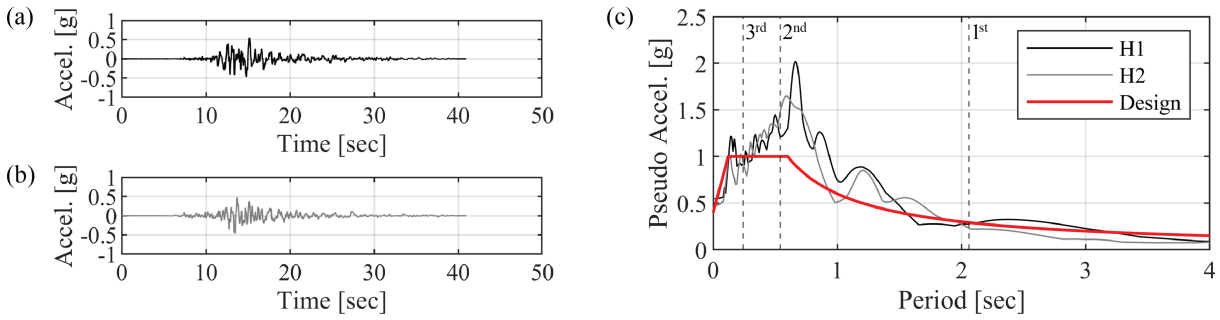

Figure 4.12. Scaled ground acceleration of the two horizontal components (a) SHI000 (H1) and (b) SHI090 (H2), and (c) pseudo acceleration response spectra of scaled ground motions and design spectrum with a 5% damping ratio. The dashed lines are associated with the natural periods of the first, second, and third translational modes of the building model.

4.6.2 Seismic Response of the Modified FD in the Example Building Model

Figure 4.13 shows the force and displacement seismic responses of the Modified FD computed using analysis results from the numerical earthquake simulation. Figure 4.13(a) shows

the peak (i.e., absolute maximum) response of the Modified FD connection displacement and connection forces over the height of the building model. The peak responses are computed at each floor level. The black lines are associated with the peak responses in the global X-direction, and the red lines are associated with the peak responses in the global Y-direction. The peak connection forces show the activation of different force levels at different floors to limit the displacement demand. For example, due to the contribution of the second and higher translational mode responses in the total dynamic response of the building, the peak connection deformation is the largest near floor levels from 3 to 6, and larger connection forces are activated at the corresponding floor levels to limit the large displacement demand. Figure 4.13(b) shows the force-displacement responses of the Modified FD at floor levels 5, 14, and 18, representing the largest response, the smallest response, and the response at the roof, respectively. On the 5th floor, the connection force reached $F_1 + F_2 + F_3$ and $F_1 + F_2$ in the global X- and Y-directions, respectively. On the 14th floor, where the deformation is the smallest, only the connection force F_1 was activated in both the global X- and Y-directions. On the 18th floor, the connection force reached $F_1 + F_2$ and F_1 in the global X- and Y-directions, respectively. The numerical earthquake simulation results show that it is possible to limit the forces transferred from the floors to the core wall piers in a controlled manner through the expected predetermined discrete variable force-displacement response of the Modified FD simulated using the Truss Model.

The seismic responses of the eighteen-story reinforced concrete core wall building model with three types of connections are compared. The first type of connection assumes conventional monolithic connections between the floors and the core wall system; the second type of connection assumes the use of friction devices with constant friction forces, termed FD; the third type of connection assumes the use of Modified FDs. The monolithic connections are simulated using a linear-elastic force-displacement response with high elastic stiffness to approximate a rigid behavior. The FDs are simulated using elastic-perfectly plastic force-displacement response (i.e., zero post-elastic stiffness). The elastic stiffness of the FDs is equal to the elastic stiffness of the Modified FDs. The post-elastic force of the FDs is equal

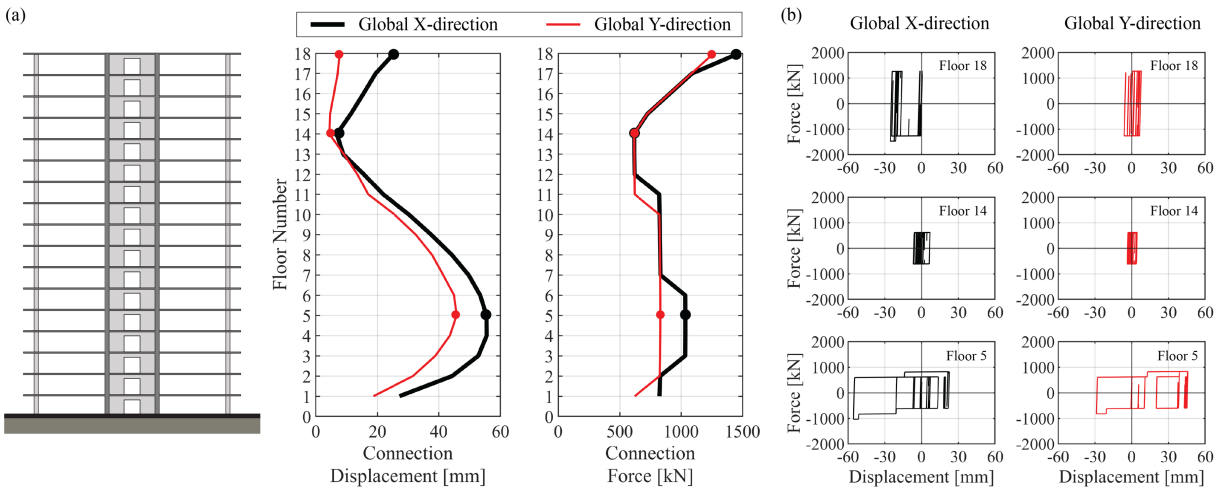

Figure 4.13. Peak force and peak displacement responses in the Modified FD along the global X- and Y-directions, and (b) the force-displacement response of the Modified FD at floor levels 5, 14, and 18.

to F_1 discussed in Section 4.6.1. Figure 4.14 shows the peak floor total acceleration, the peak connection displacement, and the peak connection force in global X- and Y-directions over the height of the building model. The use of FDs or Modified FDs reduces the peak floor total acceleration and the peak connection force compared to the use of monolithic connections. In addition to the reduction of acceleration and force responses, the use of Modified FDs effectively reduces the peak connection displacement compared to the use of FDs. The peak connection displacement of the monolithic connections is close to zero due to the high connection stiffness.

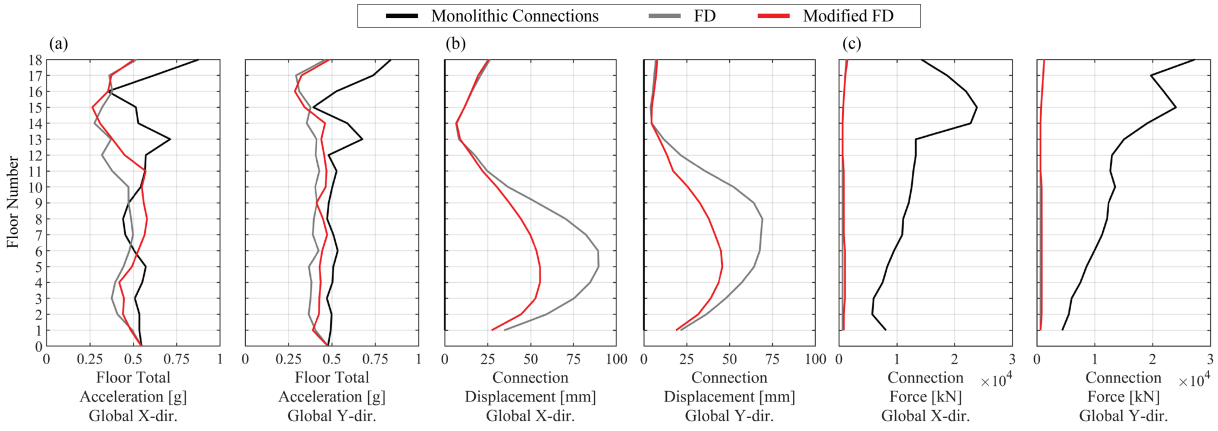

Figure 4.14. Peak floor total acceleration, peak connection displacement, and peak connection force in global X- and Y-directions.

The numerical earthquake simulation results showed that the use of the Modified FDs can limit the seismic-induced horizontal forces transferred from the floors to the core wall of the example building model without inducing excessive connection displacement demand. Further research is required to determine the effect of the characteristics of earthquake strong ground motions in the seismic response of multistory reinforced concrete core wall buildings with Modified FDs and to determine the values of the design parameters of the Modified FD that result in target seismic performance of core wall buildings.

4.7 Conclusions

A simple and practical structural connection that develops predetermined discrete variable friction forces at target design displacement levels was presented. The innovative connection was termed Modified Friction Device (Modified FD). Modified FDs are used to transfer the seismic-induced horizontal forces from the floors to the core wall seismic force-resisting system of a building. The schematics of the physical embodiment of the Modified FD were presented. The components and the assembly of the Modified FD were discussed. The mechanics of the Modified FD were explained. Results from numerical simulations of a solid finite element model of the Modified FD validated the expected kinematics and the expected force-displacement response of the Modified FD. A truss finite element model was developed in OpenSees. It was shown that the truss model simulates efficiently and reasonably well the expected force-displacement response of the Modified FD. Numerical earthquake simulations of an eighteen-story reinforced concrete core wall building model with three types of connections (i.e., conventional monolithic connections, friction devices with constant friction forces, and the Modified FD) were conducted using OpenSees. The numerical earthquake simulation results showed that the use of the Modified FDs can limit the seismic induced horizontal forces transferred from the floors to the core wall of the example building model without inducing excessive connection displacement demand.

Further research is required to determine the effect of the characteristics of earthquake

strong ground motions in the seismic response of multistory reinforced concrete core wall buildings with Modified FDs and to determine the values of the design parameters of the Modified FD that result in target seismic performance of core wall buildings. Experimental characterization of the kinematics and the force-displacement response of the Modified FD is required.

Acknowledgments

Chapter 4, in full, is a reprint of the material as it appears in: Chen, K., Tsampras, G., & Lee, K. (2023). Structural connection with predetermined discrete variable friction forces. *Resilient Cities and Structures*, 2(1), 1–17. Credits are distributed as follows: Kaixin Chen: Writing – original draft, Visualization, Validation, Software, Methodology, Investigation, Truss model analysis, Conceptualization. Georgios Tsampras: Writing – original draft, Supervision, Resources, Project administration, Methodology, Solid model analysis, Conceptualization. Kyoungyeon Lee: Writing – original draft, Visualization, Software, Methodology, Investigation, Numerical simulation of the core wall structure.

Chapter 5

Experimental Characterization of Friction-Based Structural Components with Predetermined Discrete Variable Friction Forces at Target Design Displacement Levels

5.1 Scope of Study

Chapter 5 focuses on the component-level experimental characterization of the Modified FD introduced in Chapter 4. The objectives are to validate the fabrication and assembly processes, experimentally characterize the structural response of the Modified FD subjected to cyclic displacement loading histories, and experimentally demonstrate the practical adjustability of the design parameters.

For completeness and to provide context for the experimental characterization presented in this chapter, the configuration and expected force-displacement response of the Modified FD introduced in Chapter 4 are briefly reviewed in Figure 5.1. As shown in Figure 5.1 (a), the Modified FD consists of two external plates, an internal plate, four bearing plates, eight friction shims (four for the external plates and four for the bearing plates), and pretensioned bolts that provide the normal load acting on the friction interface. For each external plate, two openings are created to host the bearing plates. At target displacement levels, the external plates come

into contact with the bearing plates, which then cause the bearing plates to move relative to the internal plate and in turn to activate the associated sliding friction mechanism. The expected force-displacement response of the Modified FD is shown in Figure 5.1 (d). The response is characterized by five design parameters, D_1, D_2, F_1, F_2, and F_3 (assuming elastic stiffness $K_1 = K_2 = K_3 \approx \infty$). As shown in Figure 5.1 (c), the displacement-related design parameters D_1 and D_2 represent the shorter and longer distances between the bearing plate and the external plate, respectively. The force-related design parameters F_1, F_2, and F_3 are the sliding friction forces contributed by friction shims for the external plates, friction shims for the bearings plates associated with D_1, and friction shims for the bearings plates associated with D_2, respectively.

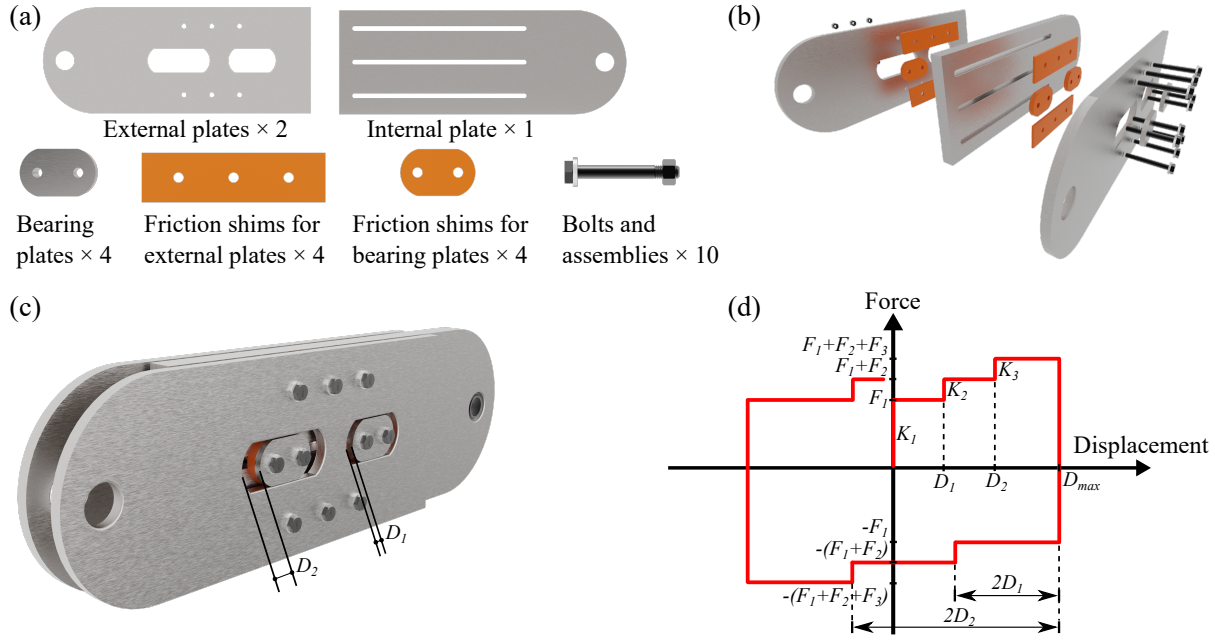

Figure 5.1. Schematic representation of the Modified Friction Device (Modified FD) introduced in Chapter 4: (a) components, (b) exploded view, (c) assembly, showing design parameters D_1 and D_2, and (d) force-displacement response with design parameters D_1, D_2, F_1, F_2, and F_3 (assuming elastic stiffness $K_1 = K_2 = K_3 \approx \infty$).

5.2 Experimental Testing

The experimental characterization of the Modified FD was conducted in two stages: preliminary studies followed by full-scale connection tests. In this chapter, preliminary stud-

ies refer to connection tests conducted at force levels lower than those expected in full-scale building applications. These preliminary studies were conducted first to assess the connection kinematics, experimentally evaluate the adjustability of design parameters, verify the intended force-displacement response with predetermined discrete variable friction forces at target displacement levels, and identify practical issues related to fabrication, assembly, and testing before proceeding to the full-scale tests. The full-scale connection tests were then conducted using force and displacement demand levels representative of those estimated for Modified FDs in full-scale building applications [123].

5.2.1 Preliminary Studies

Connection Configuration

Three configurations of the Modified FD were tested in the preliminary studies, namely PS-C1 (preliminary study configuration one), PS-C1R (preliminary study configuration one - revised), and PS-C2 (preliminary study configuration two). The schematic representation of the PS-C1 specimen is shown in Figure 5.2. Photos of the parts of the PS-C1 specimen and the specimen assembly are shown in Figure 5.3. The configuration of PS-C1 is primarily consistent with that of the Modified FD shown in Figure 5.1. Both the internal plate and external plates had a dimension of 635 mm $\times$ 254 mm $\times$ 12.7 mm (25 inch $\times$ 10 inch $\times$ 0.5 inch). Three bolt holes were created at the end of the external plates to connect the external plates to the end connection plates using three 19.05 mm (3/4 inch) diameter bolts, thereby allowing the end connection to be gripped by the testing machine actuator. These three bolts were pretensioned using the Turn-of-Nut Method [95] by 120°. The internal plate, external plates, bearing plates, and end connection plates were all made of A36 low-carbon structural steel. Two bearing plate lengths were considered, as shown in Figure 5.3 (d), to demonstrate the adjustability of design parameters D_1 and D_2. The shorter bearing plates had a length of 127 mm (5 inch) while the longer bearing plates had a length of 137 mm (5.4 inch). The difference in bearing plate lengths resulted in a difference of 5 mm (0.2 inch) in either design parameters D_1 or D_2, depending on

the cases of design parameters considered. The edges of the bearing plates in contact with the external plates were machined into a curved shape, following the configuration shown in Figure 4.2. The friction shims used in the preliminary studies were made of the composite friction material Gatke 112 [143] manufactured by ScanPac Mfg., Inc. Gatke 112 consisted of phenolic resin matrix, cotton fiber cloth reinforcement, and fillers. A systematic characterization of the mechanical and tribological properties of Gatke 112 can be found in Chapter 2. The friction interfaces were established between Gatke 112 friction shims and the slotted internal plate; the surface of the internal plate in the PS-C1 specimen was not specially treated. The friction shims for external plates had a dimension of 190.5 mm × 63.5 mm × 12.7 mm (7.5 inch × 2.5 inch × 0.5 inch) while the friction shims for bearing plates had the same dimension and shape as the shorter bearing plates. The end-to-end length of the PS-C1 specimen was 914.4 mm (36 inch).

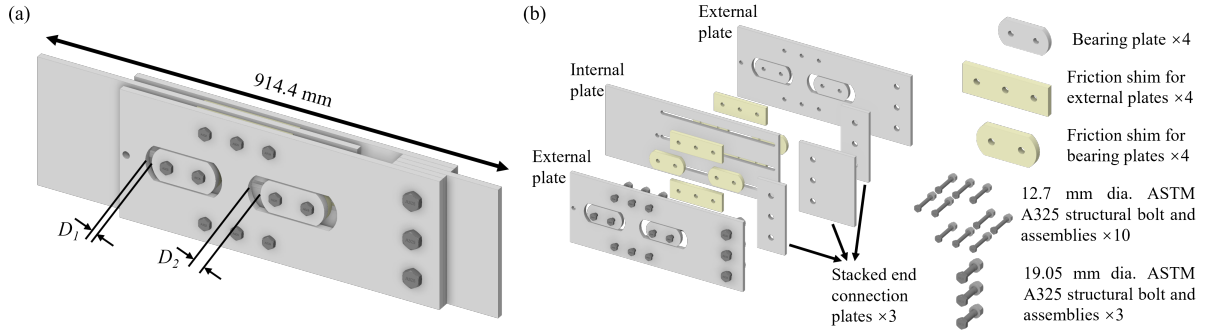

Figure 5.2. Schematic representation of the PS-C1 specimen: (a) assembly, and (b) exploded view.

Cases of design parameters considered for PS-C1 are presented in Table 5.1. A total of six cases were tested. The baseline design of PS-C1, denoted PS-C1 BL, had the following combination of nominal design parameters: D_1 equal to 12.7 mm (0.5 inch), D_2 equal to 25.4 mm (1.0 inch), F_1 equal to 106.8 kN (24 kips), and both F_2 and F_3 equal to 35.6 kN (8 kips). Note that the calculation of nominal design parameters F_1, F_2, and F_3 followed the modified version of Coulomb's friction equation [88] $f = \mu N = n_b n_s \mu N_b$. Here, n_b is the number of bolts providing the normal load acting on the friction interface (those bolts are termed friction bolts herein); as shown in Figure 5.2, n_b was equal to six for F_1 and equal to two for both

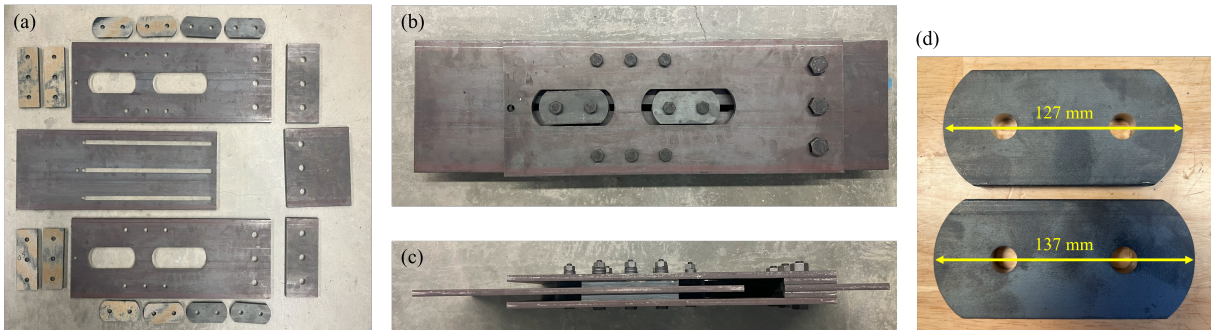

Figure 5.3. Photos of (a) parts of the PS-C1 specimen, (b) front view of the PS-C1 specimen assembly, (c) top view of the PS-C1 specimen assembly, and (d) shorter and longer bearing plates for adjusting D_1 and D_2.

F_2 and F_3. n_s is the number of the friction interface that contributes to the sliding friction force, and was equal to 2 for F_1, F_2, and F_3. μ is the expected coefficient of friction. As previously described, the friction interface in the preliminary studies was Gatke 112 in contact with low-carbon structural steel; therefore, a nominal coefficient of friction μ equal to 0.5 was assumed [136]. N_b is the normal load provided by one friction bolt. In the preliminary studies, ASTM F3125 Gr. A325 structural bolts with a diameter of 12.7 mm (1/2 inch) were used as the friction bolts. For PS-C1 BL, a nominal value of N_b equal to 17.8 kN (4 kips) was considered (approximately one-third of the minimum pretension of the friction bolt). Hence, F_1 can be calculated as $F_1 = 6 \times 2 \times 0.5 \times 17.8 = 106.8$ kN. F_2 and F_3 can be calculated in the same way. DP1 to DP5 (where DP stands for design parameters) represent five additional cases of design parameter combinations, each with one design parameter being adjusted compared to PS-C1 BL. As previously described, D_1 and D_2 were adjusted by using longer bearing plates. F_1, F_2, and F_3 were adjusted by changing the pretension of the friction bolt.

The schematic representation of the PS-C1R specimen is presented in Figure 5.4 (a). The configuration of PS-C1R was generally similar to that of PS-C1, except for two main modifications. First, the contact edges between external plates and bearing plates were modified from a curved shape to straight edges. Second, pockets were machined into both the external plates and the bearing plates to host the friction shims. Photos of the revised parts in the PS-C1R

Table 5.1. Cases of design parameters considered in PS-C1 testing

Case of design parameters	Nominal design parameters				
	D_1 [mm]	D_2 [mm]	F_1 [kN]	F_2 [kN]	F_3 [kN]
BL	12.7	25.4	106.8	35.6	35.6
DP1	7.62	25.4	106.8	35.6	35.6
DP2	12.7	20.32	106.8	35.6	35.6
DP3	12.7	25.4	80.0	35.6	35.6
DP4	12.7	25.4	106.8	26.7	35.6
DP5	12.7	25.4	106.8	35.6	26.7

specimen, along with the corresponding parts in the PS-C1 specimen for comparison, are shown in Figure 5.4 (b). The reasons for these modifications are discussed further in Section 5.2.1.

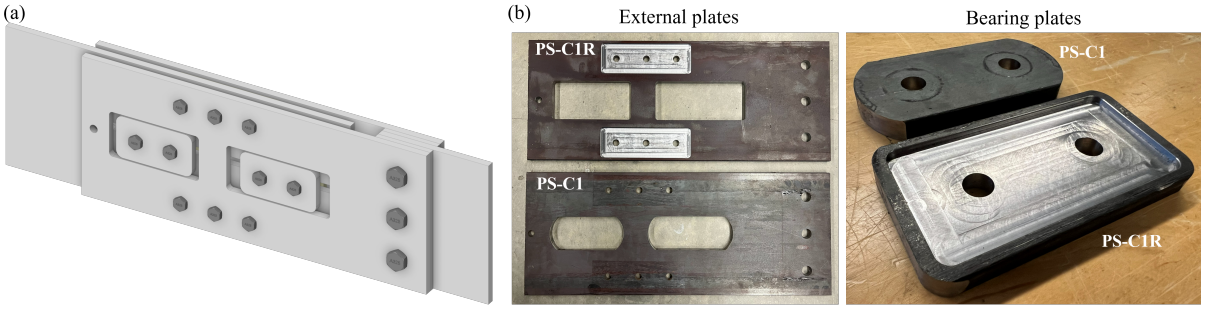

Figure 5.4. (a) Schematic representation of the PS-C1R specimen assembly and, (b) changes on the PS-C1R configuration compared with PS-C1.

The schematic representation of the PS-C2 specimen is shown in Figure 5.5. Photos of the individual parts of the PS-C2 specimen and the specimen assembly are shown in Figure 5.6. The design of PS-C2 followed the design concept proposed in Chapter 3, in which initially loose washer plates were used. Different from PS-C1 and PS-C1R which used flat steel plates, PS-C2 used commercially available steel sections as the internal and external plates. A W16×36 section with a length of 571.5 mm (22.5 inch) was designed as the internal plate and two C12×20.7 channels having a length of 698.5 mm (27.5 inch) were designed as the external plates. The W section was made of A992 Grade 50 steel, while the channels were made of A36 steel. The cross-sectional dimensions of the W16×36 section and the C12×20.7 channels followed the AISC Steel Construction Manual [92].

At the fixed end of the assembly, the two channels and one internal connection plate were connected using six 22.2 mm (7/8 inch) diameter bolts. Similar to PS-C1 and PS-C1R, this design allowed the end connection to be gripped by the testing machine actuator. During assembly, a torque of 542 Newton·meter (400 pound·foot) was applied to tighten each of the six bolts so that relative displacement did not happen between the two steel channels and the internal connection plate. For each steel channel, four rectangular-shaped openings were created to host the friction shims. The surface of the W section was sandblasted, and slots were created on the web of the W section. Friction shims were placed in the openings on the steel channel, and the friction interfaces were established between the friction shims and the web of the W section. Same as in PS-C1 and PS-C1R, ten ASTM F3125 Gr. A325 structural bolts having a diameter of 12.7 mm (0.5 inch) were used as the friction bolts in PS-C2. Initially loose steel washer plates were clamped to distribute the applied normal load onto the friction shims.

In PS-C2, the sliding friction mechanism was activated through the bearing action between the web of the steel channel and the edge of the friction shims. The four friction shims with three bolt holes were associated with F_1, and each had a dimension of 152.4 mm $\times$ 50.8 mm $\times$ 12.7 mm (6 inch $\times$ 2 inch $\times$ 0.5 inch). The distance between the web of the channel and friction shims for F_1 was tightly controlled to be practically zero, so that the sliding friction mechanism associated with F_1 would be activated once longitudinal relative displacement was imposed between the steel channel and the W section. The other four friction shims with two bolt holes were associated with either F_2 or F_3. For PS-C2, design parameters D_1 and D_2 were the distance, in the undeformed configuration, between the web of the channel and the friction shims associated with F_2 and F_3, respectively, as shown in Figure 5.5 (a). Therefore, instead of adjusting the length of the bearing plates as in PS-C1 and PS-C1R, in PS-C2, D_1 and D_2 were adjusted by using friction shims of different lengths. For PS-C2, two cases of design parameter combinations were considered, namely PS-C2 BL and PS-C2 DP1. PS-C2 BL and PS-C2 DP1 were designed to have the same D_1 and D_2 as PS-C1 BL and PS-C1 DP1, respectively. In PS-C2 BL, the four friction shims associated with F_2 and F_3 had the same dimension of 101.6 mm $\times$

50.8 mm × 12.7 mm (4 inch × 2 inch × 0.5 inch). In PS-C2 DP1, to adjust D_1, the length of the two friction shims associated with F_2 were increased to 111.76 mm (4.4 inch), as shown in Figure 5.5 (b). The end-to-end length of PS-C2 was 952.5 mm (37.5 inch).

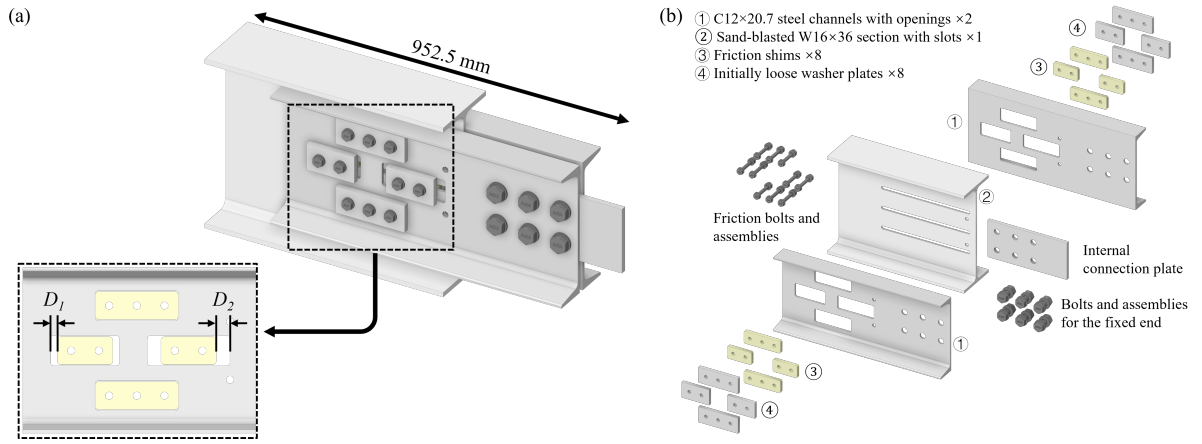

Figure 5.5. Schematic representation of the PS-C2 specimen: (a) assembly, and (b) exploded view.



Figure 5.6. Photos of (a) parts of the PS-C2 specimen (bolts and associated assemblies are not shown), (b) PS-C2 specimen assembly, and (c) shorter and longer friction shims to adjust design parameters D_1 and D_2.

Test Setup and Instrumentation

Figure 5.7 (a) presents an overview of the experimental testing setup for the preliminary studies. Photos of the PS-C1, PS-C1R, and PS-C2 specimens on the testing machine are shown in Figure 5.7 (b). The preliminary studies were conducted using a universal testing machine (UTM) (MTS 370.25 servo-hydraulic load frame). The actuator force and displacement data were

collected using a load cell and a Temposonics linear displacement transducer, respectively. These data were filtered and recorded with 100 Hz sample rate through the onboard MTS FlexTest 40 controller data acquisition card. The actuator displacement and force is effectively equal to the connection displacement and force, respectively. Imaging data was collected using stereo cameras throughout the tests. For PS-C1 and PS-C1R, one of the external plates and two bearing plates were spray-painted in white and then a black speckle pattern was applied. For PS-C2, the same preparation was applied to one of the steel channels and two washer plates. The surface preparation facilitated subsequent Digital Image Correlation (DIC) analysis of the imaging data to obtain full-field displacement and strain related data. In addition to the force, displacement, and imaging data, through-hole bolt load cells as shown in Figure 5.7 (c) were used to monitor the bolt load of the friction bolts throughout the tests.

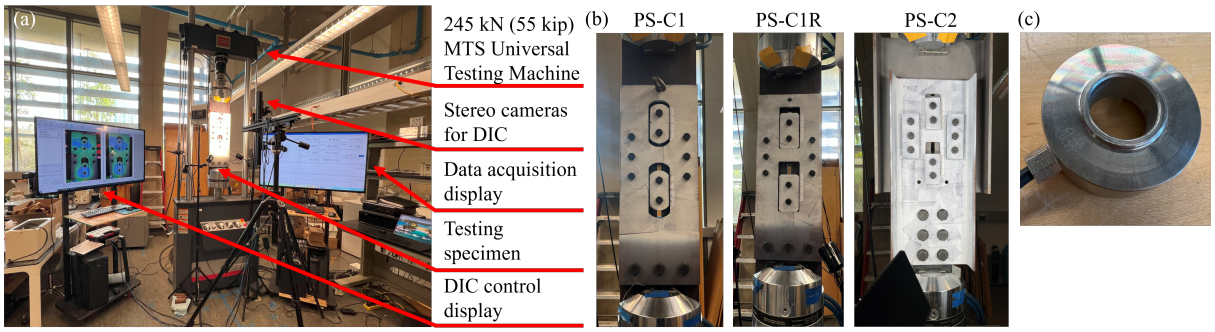

Figure 5.7. (a) Overview of the experimental testing setup for the preliminary studies, (b) photos of PS-C1, PS-C1R, and PS-C2 specimens on the testing machine, and (c) through-hole bolt load cell for monitoring the bolt load.

Loading Protocol

The loading protocol for the preliminary studies is presented in Table 5.2. The characteristics of each test, including the type of input excitation, the peak displacement, the peak sliding velocity, the loading frequency, and a brief description, are also summarized in Table 5.2. All tests were cyclic and displacement-controlled. Test 0-0 was a pre-test setup check in which the friction bolts were not preloaded. Test 0-1 was conducted to establish the break-in effect of the friction interface, so that the friction interface could reach a relatively steady state

and the coefficient of friction could become relatively stable [136, 147]. For each of the tested configuration, Tests 0-0 and 0-1 were conducted once at the beginning of the testing series. In contrast, Tests 1 to 10 were conducted repeatedly for each case of the design parameter combinations.

Tests 1 to 8 used ramped sinusoidal displacement time histories as the input excitation. The peak displacements of Tests 1 to 8 were defined based on the design parameters D_1 and D_2 of PS-C1 BL where $D_1 = 12.7$ mm (0.5 inch) and $D_2 = 25.4$ mm (1.0 inch). Tests 1 and 2 had a peak displacement D_{max} equal to 7.62 mm (0.3 inch). Since D_{max} was smaller than D_1 (of PS-C1 BL, herein), the external plates were not expected to make contact with the bearing plates, and the connection was therefore expected to develop a peak force of F_1. Tests 3 to 5 had a peak displacement D_{max} equal to 19.05 mm (0.75 inch). Since D_{max} was greater than D_1 while smaller than D_2, the external plates were expected to make contact with the bearing plates associated with F_2, but not those associated with F_3, and the connection was therefore expected to develop a peak force of $F_1 + F_2$. Tests 6 to 8 had a peak displacement D_{max} equal to 38.1 mm (1.5 inch). Since D_{max} was greater than D_2, the external plates were expected to make contact with all the bearing plates and thus, the connection was expected to develop a peak force of $F_1 + F_2 + F_3$. Two levels of peak sliding velocities were considered in Tests 1 to 8; the slower one was 12.7 mm/sec (0.5 inch/sec) and the faster one was 50.8 mm/sec (2.0 inch/sec).

Tests 9 and 10 had expected seismic-induced responses of a friction-based structural connection as the imposed displacement time histories of the input excitation. The imposed displacement time histories for these two tests were the response of a friction-based structural connection from numerical earthquake simulations of a steel re-centering braced frame [137, 146, 221]. The imposed displacement time histories of Tests 9 and 10 had a peak displacement of 30.1 mm (1.185 inch) which was larger than D_2; therefore, the connection was expected to develop a peak force of $F_1 + F_2 + F_3$. Between tests, inspection was conducted and the bolt loads of the friction bolts was adjusted to the target bolt load levels. Figure 5.8 shows the imposed displacement histories for Tests 1 to 10, together with the cumulative displacement and absolute

sliding velocity time histories of each test. For reference, $\pm D_1$ and $\pm D_2$ of PS-C1 BL are also shown in the plot of the imposed displacement time histories.

Table 5.2. Loading protocol for the preliminary studies

Test ID	Input type	Peak displ. [mm]	Peak vel. [mm/sec]	Loading freq. [Hz]	Descriptions
0-0	Ramped Sine	50.80	12.7	0.0398	Pre-test setup check
0-1	Ramped Sine	50.80	12.7	0.0398	Break-in effect establishment
1	Ramped Sine	7.62	12.7	0.2653	Assess the connection response when the bearing plates are not in contact with the external plates, under a relatively slow sliding velocity
2	Ramped Sine	7.62	50.8	1.0610	Assess the connection response when the bearing plates are not in contact with the external plates, under a relatively fast sliding velocity
3	Ramped Sine	19.05	12.7	0.1061	Assess the connection response when only the bearing plates associated with F_2 are in contact with the external plates, under a relatively slow sliding velocity

Continued on next page

Table 5.2. Loading protocol for the preliminary studies (continued)

Test ID	Input type	Peak displ. [mm]	Peak vel. [mm/sec]	Loading freq. [Hz]	Descriptions
4	Ramped Sine	19.05	12.7	0.1061	Assess the repeatability of the connection response compared to Test 3
5	Ramped Sine	19.05	50.8	0.4244	Assess the connection response when only the bearing plates associated with F_2 are in contact with the external plates, under a relatively fast sliding velocity
6	Ramped Sine	38.10	12.7	0.0531	Assess the connection response when the bearing plates associated with both F_2 and F_3 are in contact with the external plates, under a relatively slow sliding velocity
7	Ramped Sine	38.10	12.7	0.0531	Assess the repeatability of the connection response compared to Test 6
8	Ramped Sine	38.10	50.8	0.2122	Assess the connection response when the bearing plates associated with both F_2 and F_3 are in contact with the external plates, under a relatively fast sliding velocity

Continued on next page

Table 5.2. Loading protocol for the preliminary studies (continued)

Test ID	Input type	Peak displ. [mm]	Peak vel. [mm/sec]	Loading freq. [Hz]	Descriptions
9	Earthquake	30.10	20.0	N/A	Assess the connection response under an earthquake-type input excitation
10	Earthquake	30.10	20.0	N/A	Assess the repeatability of the connection response under an earthquake-type input excitation, compared to Test 9

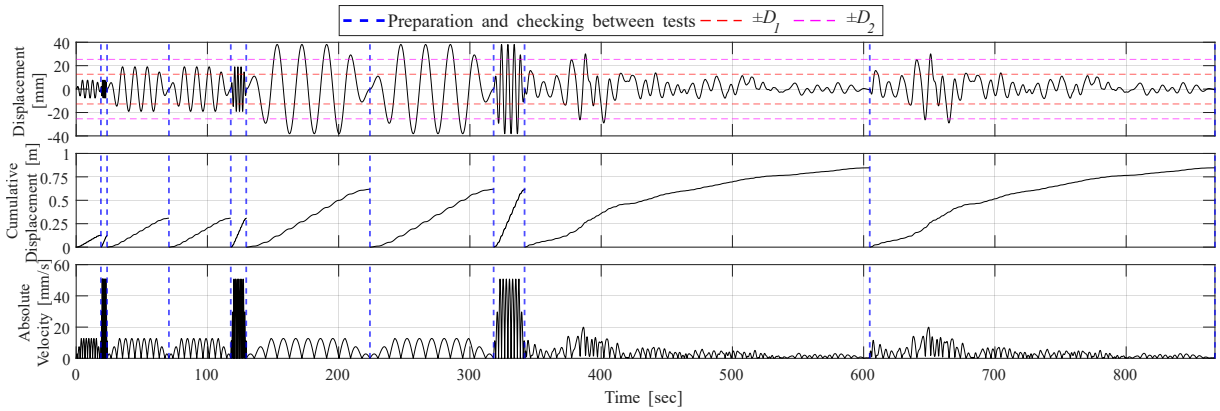

Figure 5.8. Loading protocol for the preliminary studies. From top to bottom: imposed displacement time history; cumulative displacement time history; absolute sliding velocity time history.

Results

Figure 5.9 presents the force-displacement response of the PS-C1 specimen. Only the case of design parameter combination DP5 is presented for demonstration purposes. From Figure 5.9, it is shown that the force-displacement response of the PS-C1 specimen was as anticipated. In Tests 1 and 2, the connection exhibited a rectangular-shaped force-displacement response, which resembled a Coulomb-type frictional behavior and was similar to that of a conventional friction-based connection. In Tests 3 to 5 and Tests 6 to 8, the connection developed a peak force of $F_1 + F_2$ and $F_1 + F_2 + F_3$, respectively, and the discrete variable force levels were developed at target designed displacement levels. The kinematics of the Modified FD was thus experimentally validated.

Figure 5.10 demonstrates the adjustability of the design parameters of the Modified FD. For each case of design parameter combinations, Test 7 was selected for comparison. The response of PS-C1 BL in Test 7 is plotted in black and is also plotted in each subplot for comparison with the response of PS-C1 DP1$\sim$5. Figure 5.10 shows that the performance of the Modified FD is possible to be controlled through the selection of design parameters that lead to predetermined discrete force levels at target displacement levels.

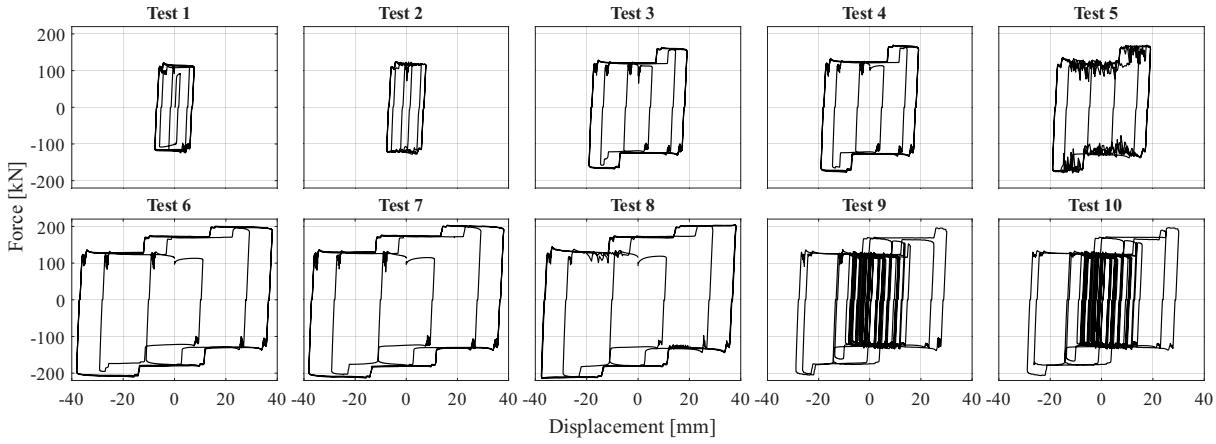

Figure 5.9. Selected force-displacement responses of the PS-C1 specimen (with the case of design parameters DP5)

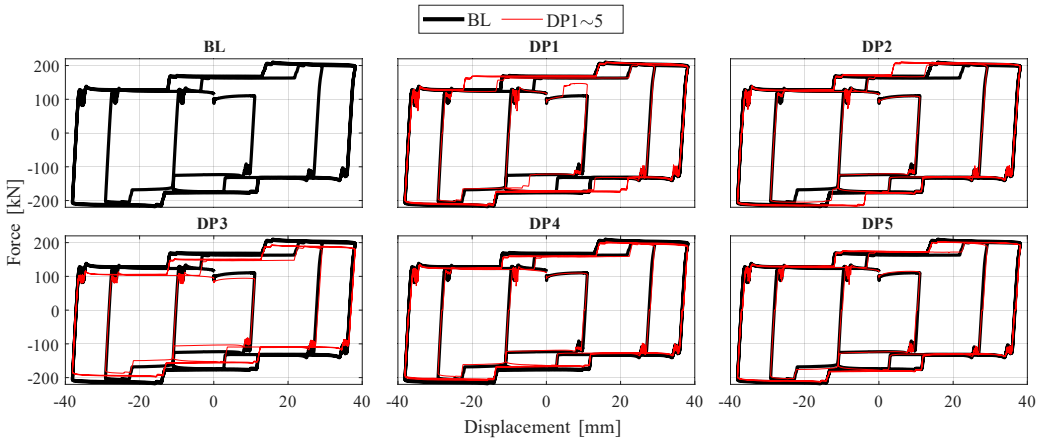

Figure 5.10. Demonstration of the design parameters adjustability of PS-C1 using Test 7

Figure 5.11 presents the numbering plan of bolt load cells used in PS-C1 tests. In the testing of PS-C1, eight of the ten friction bolts were instrumented. As shown in the numbering plan, four of the six friction bolts for the friction shims associated with F_1 were instrumented with LC#3$\sim$6; the two friction bolts for the friction shims associated with F_2 were instrumented with LC#7 and LC#8; and the two friction bolts for the friction shims associated with F_3 were instrumented with LC#9 and LC#10. Figure 5.11 also presents the bolt load variation results from the testing of PS-C1 BL. The bolt load variation is defined as the relative difference between the bolt load at the beginning and at the end of the test. A negative bolt load variation indicates bolt load loss occurred during the test.

From Figure 5.11, it is observed that the trends of the bolt load variation of LC#7 and LC#8 throughout the PS-C1 BL testing series was overall similar. The largest bolt load loss was observed in Test 3. This is because, in Test 3, the external plates first made contact with the bearing plates associated with F_2, to which the friction bolts instrumented with LC#7 and LC#8 were connected. This bearing action potentially caused in-plane rotation of the bearing plates and their associated assemblies, as shown in Figure 5.12 (a), and resulted in the bolt load loss observed in LC#7 and LC#8 during Test 3. The same explanation applies to the bolt load loss observed in LC#9 and LC#10 during Test 6. Once the in-plane rotation was established, the bolt load variation of LC#7$\sim$10 remained at a relatively low level, approximately within $\pm$5%. For the friction bolts associated with F_1 and instrumented with LC#3$\sim$6, it is observed that the trends of the bolt load variation of LC#3 and LC#5 were overall similar, and those of LC#4 and LC#6 were also overall similar. It is found that the bolt load variation of LC#3$\sim$6 was mainly associated with the out-of-plane deformation of the connection specimen, the details of which are discussed later.

Although the kinematics of the Modified FD were successfully validated through the testing of the PS-C1 specimen, several limitations of this configuration were observed during testing. As described previously, the bearing action between the external plates and the bearing plates caused in-plane rotation of the bearing plates and their associated assemblies. Once the

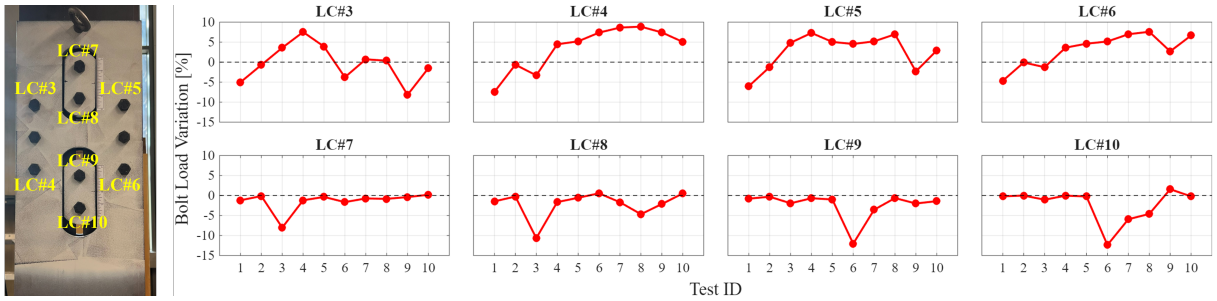

Figure 5.11. PS-C1 bolt load cells numbering plan and PS-C1 BL testing bolt load variation results

bearing plates became tilted, as shown in Figure 5.12 (a), the contact between the external plate and the bearing plate became off-centered, as indicated by the contact marks in Figure 5.12 (b). This in-plane rotation also led to gouging between the side of the bearing plate and the external plate, as indicated by the contact marks shown in Figure 5.12 (c), and to the relative movement between the bearing plate and its associated friction shim, as shown in Figure 5.12 (d). Another limitation was observed during load reversal. As shown in Figure 5.12 (e), high-frequency variation in the force response can be observed during load reversal. This high-frequency variation in the force response was found to be associated with the stick-slip mechanism of the friction interface between the friction shim and the external plate. As explained in Tsampras et al. [2] and Chen et al. [136], because of the break-in effect of the composite-metallic friction interface, for slotted-bolted friction-based connections, the friction interface between the friction shim and the internal slotted plate undergoes a larger cumulative displacement and the increase in the cumulative displacement leads to an increase in the coefficient of friction, larger than that of the friction interface between the friction shim and the external clamping plate. Therefore, sliding tends to happen between the friction shim and the external plate. Figure 5.12 (f) shows the appearance of Gatke 112 friction shims associated with F_1 before testing. Apparent wear marks were observed on the friction shims surfaces in contact with the internal plate after testing, as shown in Figure 5.12 (g). Wear marks were also observed on the friction shims surfaces in contact with the external plate, as shown in Figure 5.12 (h), which proved that sliding occurred

between the friction shim and the external plate. The stick-slip mechanism associated with this sliding resulted in the observed high-frequency variation in the force response during load reversal. In addition to the limitations discussed above, high-frequency variation in the force response was also observed in tests with relatively high sliding velocities, namely Tests 2, 5, and 8 in Figure 5.9. This high-frequency variation was later found to be associated with the out-of-plane deformation of the connection specimen. The details are discussed in the PS-C1R results.

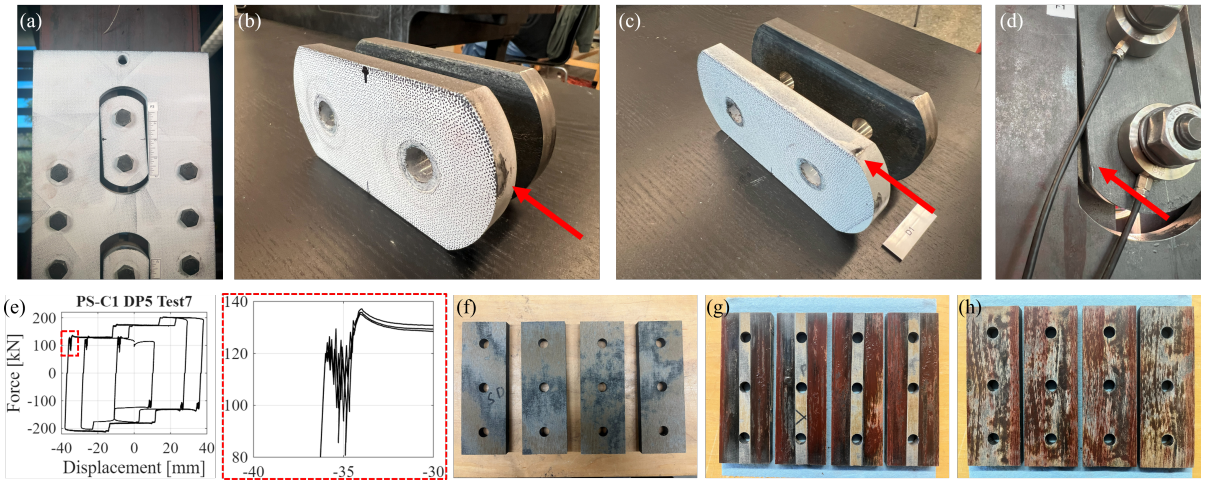

Figure 5.12. Observations from PS-C1 testing: (a) bearing plates getting tilted during the testing, (b) off-centered contact due to tilted bearing plate, (c) gouging between the side of the bearing plate and the external plate due to tilted bearing plate, (d) relative movement between the bearing plate and the friction shim associated with it, (e) high-frequency variation in the force response observed upon force reversal, (f) Gatke 112 friction shims before testing, (g) Gatke 112 friction shims surfaces in contact with the internal plate after testing, and (h) Gatke 112 friction shims surfaces in contact with the external plate after testing

To address the observed limitations, the modifications described previously and shown in Figure 5.4 were incorporated into PS-C1R. Specifically, the contact edges between external plates and bearing plates were modified from a curved shape to straight edges. These straight edges created a self-aligning mechanism and helped maintain the bearing plates in an upright position relative to the external plates when contact occurred. In addition, pockets were machined into both the external plates and the bearing plates to host the friction shims. This configuration restrained the relative movement between the friction shims and the external plates, as well as

between the friction shims and the bearing plates. Figure 5.13 presents the force-displacement response of the PS-C1R specimen. For Tests 1 to 5, the design parameters of PS-C1R followed the PS-C1 BL case. However, high-frequency variation in the force response was observed during Tests 2 and 5 and this variation led to vibration of the test setup. For safety reasons, starting from Test 6, the nominal target bolt loads of all the friction bolts were reduced from 17.8 kN to 10 kN. Overall, PS-C1R exhibited a smoother transition during load reversal, indicating the effectiveness of the pocket configuration. Inspection of the specimen also showed that the bearing plates did not become tilted throughout the testing series. However, significant high-frequency variation in the force response was still observed in Tests 2, 5, and 8, when a relatively high sliding velocity was imposed.

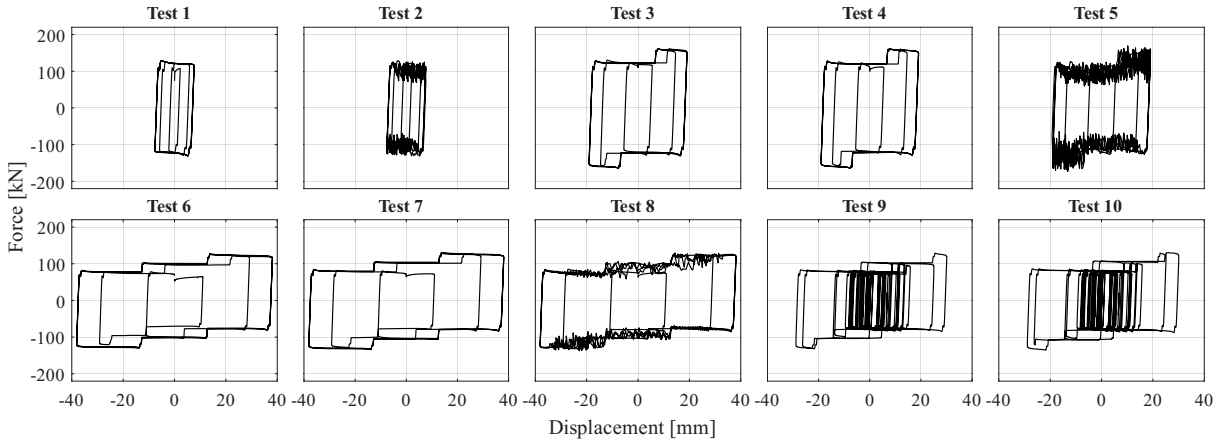

Figure 5.13. Force-displacement responses of the PS-C1R specimen

DIC analysis was conducted to investigate the cause of the observed high-frequency variation in the force response, and the results indicated that this variation was potentially related to out-of-plane deformation of the connection specimen. Figure 5.14 presents selected DIC analysis results of the PS-C1R specimen. A reference point was selected on the bearing plate associated with D_2, as shown in Figure 5.14. The figure also presents the out-of-plane displacement time history of this reference point during Tests 4 and 5. For comparison purposes, the time histories from both tests are plotted on a normalized time scale. The normalized imposed displacement time history of the connection is also included for reference. Because

the bearing plate associated with D_2 was not expected to come into contact with the external plate during Tests 4 and 5, it was expected to remain stationary throughout both tests. However, Figure 5.14 shows that, in Test 4, the reference point exhibited an out-of-plane displacement of approximately -0.1 mm when the connection was under compression, and an out-of-plane displacement of approximately +0.05 mm when the connection was under tension. Because this bearing plate was clamped together with the internal plate, the out-of-plane displacement of the reference point reflects the out-of-plane deformation of the internal plate. These results indicate that, during Test 4, the internal plate bent inward (with respect to the view shown in Figure 5.14) when the connection was under compression and bent outward when the connection was under tension. As described in Chapter 4, when the Modified FD is used in practice, spherical bearings are expected to be installed at both ends. With spherical bearings, the end boundary condition is expected to allow rotational motions while restraining translational motions, so that the Modified FD is expected to develop axial load along its longitudinal direction and zero moments at the ends. In the preliminary studies, however, spherical bearings were not used. Instead, the internal plate and the end connection plate of the specimen were directly gripped by the testing machine actuator, which created a near-fixed boundary condition. Considering the potential minor misalignment between the two grips of the testing machine, as well as imperfections in the specimen assembly from manufacturing tolerances, out-of-plane deformation of the connection specimen was induced during testing. This out-of-plane deformation also contributed to the bolt load variation observed in LC#3$\sim$6, as shown in Figure 5.11. Moreover, Figure 5.14 shows that, under a relatively high loading velocity as in Test 5, both the amplitude and frequency of the out-of-plane deformation increased. This high-frequency out-of-plane deformation potentially led to frictional instability at the friction interface and consequently, to the observed high-frequency variation in the force response as in Tests 2, 5, and 8.

Due to concerns regarding the out-of-plane deformation of the specimen, which originated from imperfections in the test setup, the nominal target bolt loads of the friction bolts in the PS-C2 testing were limited to 5 kN. This was considered acceptable because the main objective

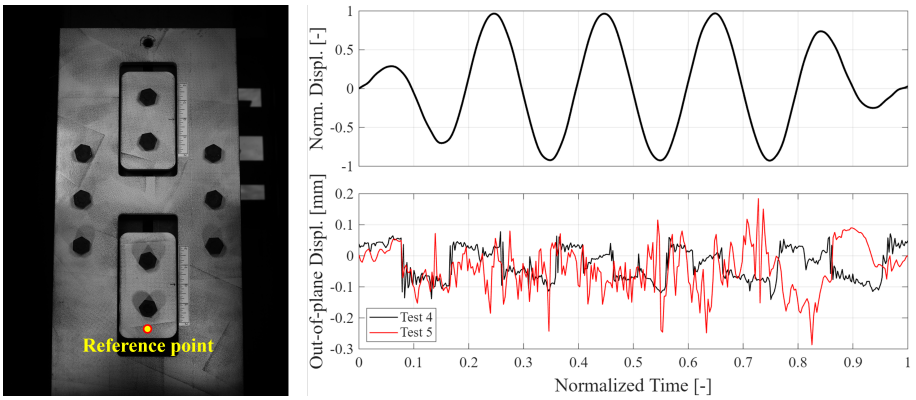

Figure 5.14. Selected DIC analysis results from the PS-C1R testing

of these tests was to demonstrate the feasibility of the PS-C2 configuration. Figure 5.15 presents the force-displacement response of the PS-C2 specimen. Similar to PS-C1, PS-C2 also exhibited force-displacement responses with predetermined discrete variable friction forces at target displacement levels. Therefore, the kinematics of the Modified FD with the PS-C2 configuration were also experimentally validated. Note that, as previously described, the adjustment of the displacement-related design parameters D_1 and D_2 in PS-C2 was achieved by using friction shims of different lengths. The demonstration of this adjustment is shown in Figure 5.16 (a) and (b), and the comparison of the force displacement responses of PS-C2 BL and PS-C2 DP1 in Test 7 is shown in Figure 5.16 (c).

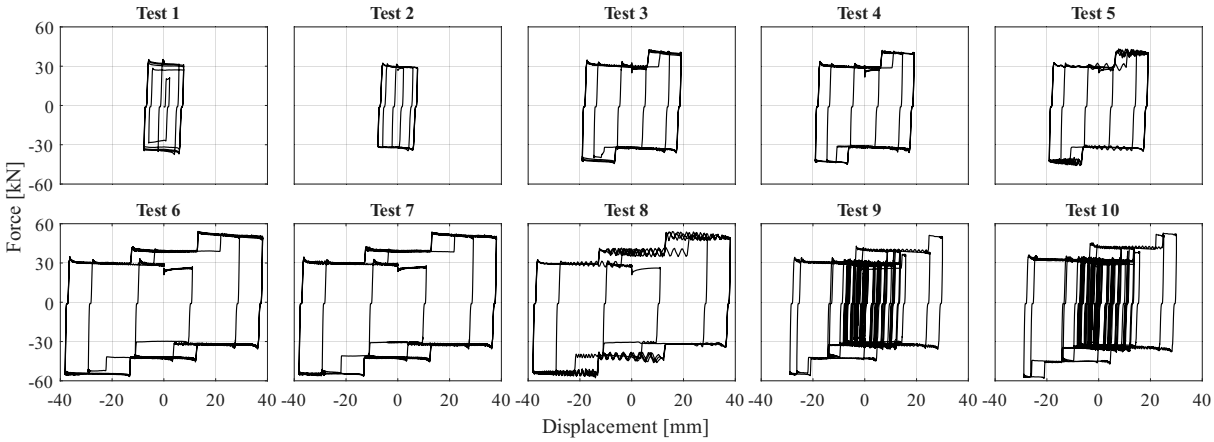

Figure 5.15. Force-displacement responses of the PS-C2 specimen (with design parameters PS-C2 BL)

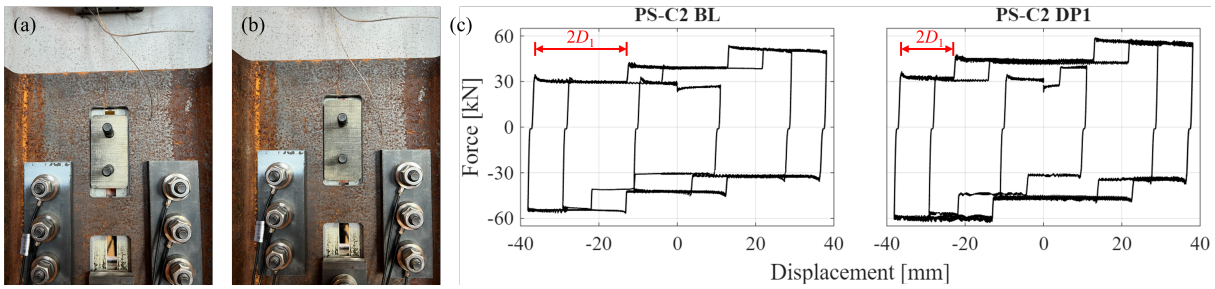

Figure 5.16. Demonstration of adjusting design parameters for PS-C2: (a) shorter friction shims for larger D_1 in PS-C2 BL, (b) longer friction shims for smaller D_1 in PS-C2 DP1, and (c) comparison of the force-displacement response of PS-C2 BL and PS-C2 DP2 in Test 7

Summary of Results from the Preliminary Studies

The preliminary studies showed that the proposed Modified FD exhibited the intended force-displacement response with predetermined discrete variable friction forces at target displacement levels, thereby experimentally validating the kinematics of the connection concept. The testing of PS-C1 demonstrated that the response of the Modified FD could be controlled through the selection of design parameters and that the adjustment of these parameters could be implemented through relatively simple operations. At the same time, the tests also revealed several practical limitations in the PS-C1 configuration. Based on these observations, the PS-C1R configuration was developed and showed improved behavior. DIC analysis further indicated that the remaining high-frequency variation in the force response at relatively high sliding velocities was potentially related to out-of-plane deformation induced by imperfections in the test setup. Finally, the testing of PS-C2 demonstrated the feasibility of an alternative configuration using commercially available steel sections and design concept with initially loose washer plates, and further confirmed the intended response of the Modified FD. Overall, these results verified the feasibility of the Modified FD design concept, demonstrated the practicality of adjusting its design parameters, identified fabrication-, assembly-, and testing-related issues, and provided the basis for improving the connection design for subsequent full-scale connection testing.

5.2.2 Full-scale Connection Testing

Connection Configuration

The schematic representation of the full-scale Modified FD specimen is presented in Figure 5.17. The specimen was designed into a brace configuration with pin-pin boundary conditions to utilize an existing damper test setup in the Powell lab of the University of California San Diego. As shown in Figure 5.17 (a), the pin-to-pin distance of the full-scale Modified FD specimen was 3.4 m. The full-scale Modified FD specimen was designed to have a peak displacement capacity of $\pm$ 101.6 mm (4 inch). Figure 5.17 (b) shows the exploded view of the full-scale Modified FD specimen. The specimen consisted of a channel component, a W-section component, and parts including twelve initially loose washer plates, twelve friction shims, including four longer ones and eight shorter ones, two PTFE shims, and bolts and their assemblies including nuts and washers. The design of the functioning part of the full-scale Modified FD specimen generally followed that of the PS-C2 specimen. One notable difference was that, near the ends of the two channels, two PTFE shims were placed between the channels and the web of the W-section, and were connected to the channels using loose structural bolts. This design was intended to restrain the out-of-plane deformation of the channels and also maintain the distance between the channels and the web of the W-section, thereby reducing the potential for gouging between the components.

Photos of the channel component are shown in Figure 5.18. The channel component consisted of two C15$\times$40 channels, each having a length of 1346.2 mm (53 inch). The channels were made of A36 steel and were welded to a base plate with dimensions of 482.6 mm $\times$ 330.2 mm $\times$ 50.8 mm (19 inch $\times$ 13 inch $\times$ 2 inch). Same as the design concept of the PS-C2 specimen, openings were created on both channels to host the friction shims. A rectangular A36 steel plate with dimensions of 381 mm $\times$ 152.4 mm $\times$ 19.05 mm (15 inch $\times$ 6 inch $\times$ 0.75 inch) was placed between the two channels to maintain the plumbness of the channels and the distance between them during the welding process. A36 steel stiffeners were welded to

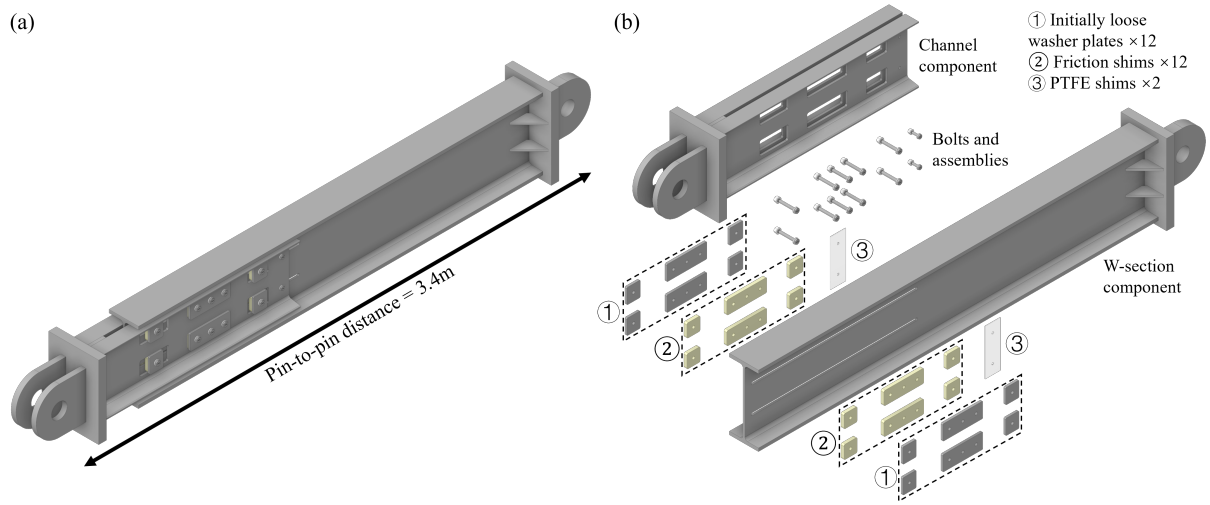

Figure 5.17. Schematic representation of the full-scale Modified FD specimen (a) assembly and (b) exploded view

strengthen the connection between the two channels and the base plate and to facilitate force transfer. On the other side of the base plate, two clevis plates were welded to the base plate, forming a double-plate clevis connection. Both the clevis plates and the base plate were made of A572 Gr.50 steel. As shown in Figure 5.18 (b) and (c), one of the two channels was spray-painted in white and speckled, to facilitate the DIC data collection process.

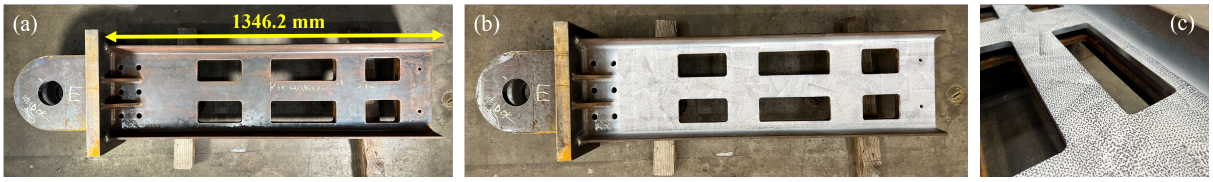

Figure 5.18. (a) Photo of the channel component and (b)(c) speckled channel component for DIC data collection

Photos of the W-section component are shown in Figure 5.19. The W-section component consisted of one W18×71 section, having a length of 2667 mm (105 inch). The W-section was made of ASTM A992 Gr.50 steel and was welded to a base plate with dimensions of 533.4 mm × 304.8 mm × 50.8 mm (21 inch × 12 inch × 2 inch). Following the design concept of the PS-C2 specimen, the web of the W-section was slotted to accommodate the relative movement between the components during frictional sliding. Similar to the channel component, A36 steel

stiffeners were welded to strengthen the connection between the W-section and the base plate and to facilitate force transfer. On the other side of the base plate, one clevis plate was welded to the base plate and formed a single-plate clevis connection. Both the clevis plate and the base plate were made of A572 Gr.50 steel. Since the web of the W-section was used to establish the friction interface, a wire brush was used to remove dust and rust from the surface. The as-received condition of the W-section surface is shown in Figure 5.19 (b) while the appearance of the W-section surface after cleaning is shown in Figure 5.19 (c).

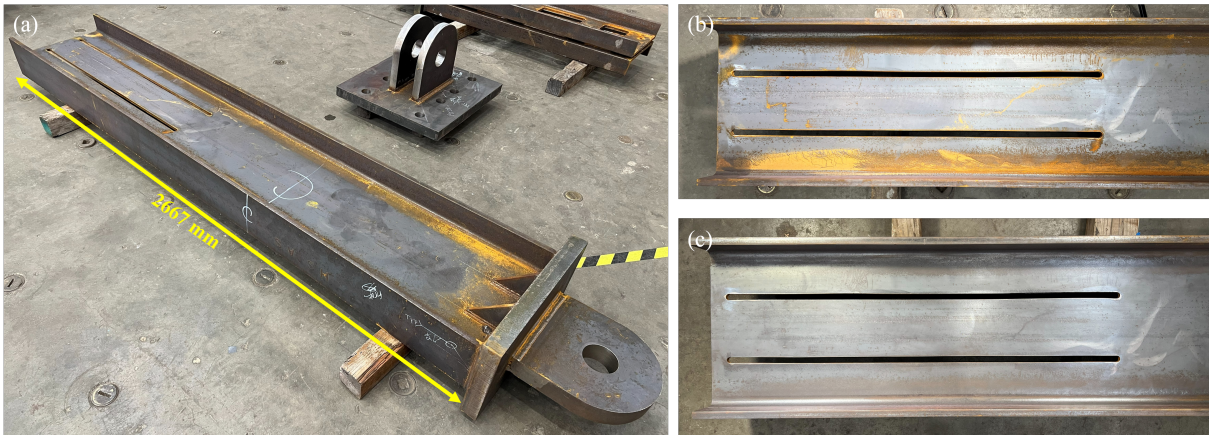

Figure 5.19. (a) Photo of the W-section component, (b) as-received condition of the W-section surface, and (c) W-section surface after cleaning

Figure 5.20 shows the photos of the parts used in the full-scale Modified FD specimen. Figures 5.20 (a) and (b) show the longer and shorter washer plates, respectively. These washer plates were used to distribute the normal load acting on the corresponding longer and shorter friction shims shown in Figures 5.20 (c) and (d). All washer plates were made of A36 steel. Figures 5.20 (c) and (d) show the friction shims used in the full-scale Modified FD specimen. Same as the preliminary studies, friction shims used in the full-scale Modified FD specimen were made of the composite friction material Gatke 112. The longer friction shims, shown in Figure 5.20 (c), had nominal dimensions of 266.7 mm $\times$ 88.9 mm $\times$ 19.05 mm (10.5 inch $\times$ 3.5 inch $\times$ 0.75 inch) and were designed to accommodate three friction bolts. These friction shims were associated with the design parameter F_1. The shorter friction shims, shown in Figure 5.20

(d), had nominal dimensions of 88.9 mm × 88.9 mm × 19.05 mm (3.5 inch × 3.5 inch × 0.75 inch) and were designed to accommodate one friction bolt. They were associated with the design parameters F_2 or F_3. As discussed for the PS-C2 specimen, the displacement-related design parameters D_1 and D_2 in this configuration were adjusted by using friction shims of different lengths. As shown in Figure 5.20 (e), additional friction shims with dimensions of 101.6 mm × 88.9 mm × 19.05 mm (4 inch × 3.5 inch × 0.75 inch) were machined to demonstrate the adjustability of D_1 and D_2. The PTFE shims placed between the channels and the web of the W-section are shown in Figure 5.20 (f). The friction bolts used in the full-scale Modified FD testing, although not shown in Figure 5.20, were ASTM F3125 Gr.A325 structural bolts with a diameter of 15.875 mm ($\frac{5}{8}$ inch).

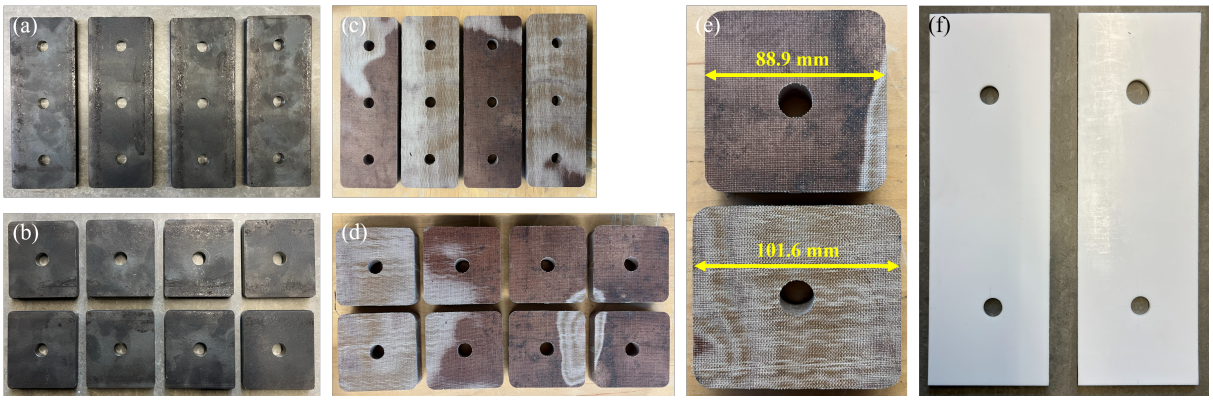

Figure 5.20. Photo of the parts of the full-scale Modified FD: (a) longer washer plates, (b) shorter washer plates, (c) longer friction shims (for F_1), (d) shorter friction shims (for F_2 and F_3), (e) friction shims of different lengths for adjusting D_1 and D_2, and (f) 3.2 mm ($\frac{1}{8}$ inch) thickness PTFE shims

Cases of design parameters considered for the full-scale Modified FD testing are presented in Table 5.3. Similar to the testing of the PS-C1 specimen, a total of six cases were tested. The baseline design, denoted FS BL, had the following combination of nominal design parameters: D_1 equal to 25.4 mm (1.0 inch), D_2 equal to 50.8 mm (2.0 inch), F_1 equal to 507 kN (114 kips), and both F_2 and F_3 equal to 169 kN (38 kips). The calculation of nominal design parameters F_1, F_2, and F_3 followed the modified version of Coulomb's friction equation [88] $f = \mu N = n_b n_s \mu N_b$. Here, n_b is the number of friction bolts and it was equal to six for F_1 and equal to two for both F_2

and F_3. n_s is the number of the friction interface that contributes to the sliding friction force, and was equal to 2 for F_1, F_2, and F_3. μ is the expected coefficient of friction and was assumed to be 0.5. N_b is the normal load provided by one friction bolt. For the FS BL case, N_b was taken as 84.5 kN (19 kips) for all friction bolts, corresponding to the minimum pretension [92] of a 15.875 mm ($\frac{5}{8}$ inch) diameter A325 structural bolt. DP1 to DP5 represent five additional cases of design parameter combinations, each with one design parameter being adjusted compared to FS BL. As previously described, D_1 and D_2 were adjusted by using friction shims with different lengths. F_1, F_2, and F_3 were adjusted by reducing the bolt load of all friction bolts associated with the corresponding design parameter to half of the baseline value, namely 42.25 kN (9.5 kips).

Table 5.3. Cases of design parameters considered in full-scale Modified FD testing

Case of design parameters	**Nominal design parameters**				
	D_1 [mm]	D_2 [mm]	F_1 [kN]	F_2 [kN]	F_3 [kN]
BL	25.4	50.8	507	169	169
DP1	19.05	50.8	507	169	169
DP2	25.4	44.45	507	169	169
DP3	25.4	50.8	253.5	169	169
DP4	25.4	50.8	507	84.5	169
DP5	25.4	50.8	507	169	84.5

Test Setup and Instrumentation

Figure 5.21 (a) presents the schematic representation of the full-scale Modified FD test setup. Only the essential components are shown in this figure. Other parts such as connecting bolts, threaded rods, and the vertical and lateral restraints of the load beam, are not shown in Figure 5.21 (a). Two actuators were used in the test setup and were referred to as Actuator (W) and Actuator (E) based on their relative locations on the west and east sides, respectively. At the north end, the actuators were connected to fixture adapters, which were connected to a strong concrete reaction wall. At the south end, the actuators were connected to a W14×257 load beam, which was considered nearly rigid in this setup. The load beam was supported on two concrete

blocks anchored to the strong floor. The full-scale Modified FD specimen was placed in the middle of the two actuators. The channel component of the Modified FD was connected to the load beam through a single-plate clevis, marked as ③ in Figure 5.21. At the north end, the W-section component of the Modified FD was connected to the wall-end fixture adapter through a double-plate clevis, marked as ② in Figure 5.21, and the wall-end fixture adapter was connected to the strong reaction wall. During testing, both actuators were displacement-controlled and imposed nearly identical displacements at each time step, thereby creating a uniaxial loading condition for the Modified FD specimen. Figure 5.21 (b) shows the photo of the actual test setup, including the vertical and lateral restraints of the load beam. A photo of the full-scale Modified FD specimen installed in the test setup is shown in Figure 5.22.

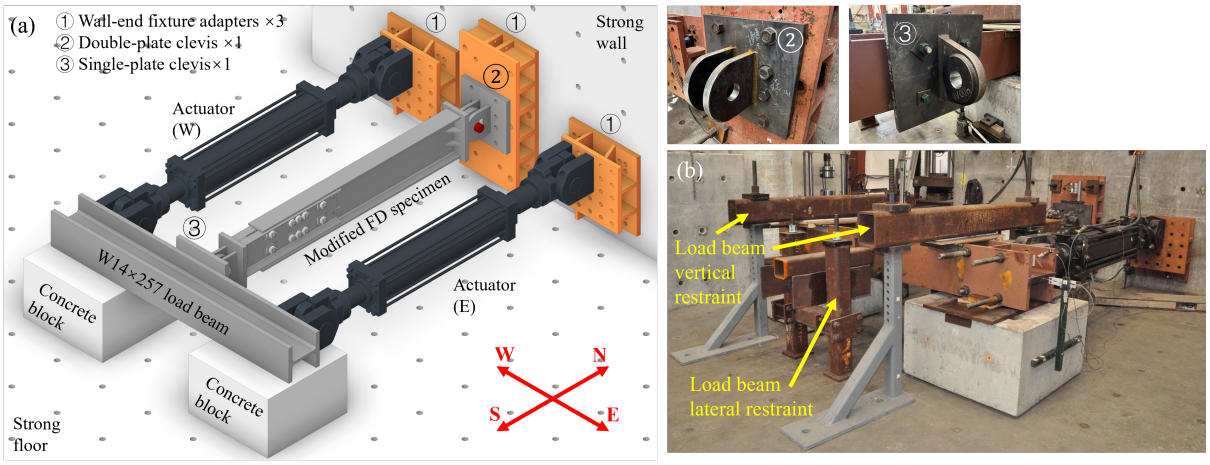

Figure 5.21. (a) Schematic representation of the test setup, and (b) photo of the actual test setup

Figure 5.23 (a) presents the schematic representation of the instrumentation plan for the full-scale Modified FD test. Six displacement transducers were used, as shown in Figure 5.23 (b). T01 and T02 measured the relative displacement between the channel component and the W-section component at the top and bottom of the assembly, respectively. The average of T01 and T02 was taken as the effective connection displacement of the Modified FD specimen. The difference between T01 and T02 was used to assess the relative rotation between the channel component and the W-section component. T03 and T04 measured the relative displacement



Figure 5.22. Photo of the full-scale Modified FD specimen in the test setup

between the W-section component and the wall-end double-plate clevis. These measurements were used to capture potential deformation at this pin connection due to machining tolerances, the shear flexibility of the pin, and the axial flexibility of the clevis plates. The difference between T03 and T04 was used to assess the rotation at this pin connection. Similarly, T05 and T06 measured the relative displacement between the channel component and the beam-end single-plate clevis, and the difference between T05 and T06 was used to assess the rotation at this pin connection. Each friction bolt was instrumented with one through-hole bolt load cell, as shown in Figure 5.23 (c). The numbering indices of the through-hole bolt load cells are shown in Figure 5.23 (d). The friction bolts associated with F_1 were instrumented with LC1 to LC6; the friction bolts associated with F_2 were instrumented with LC7 and LC8; and the friction bolts associated with F_3 were instrumented with LC9 and LC10. For the pin connection at the end of the W-section component, an instrumented load pin, shown in Figure 5.23 (e), was used to directly measure the connection force of the Modified FD specimen. The photo of the instrumented load pin installed in the test setup is shown in Figure 5.23 (f). In addition, as previously described, one of the two channels was spray-painted in white and speckled to facilitate DIC data collection. Figure 5.23 (g) shows the photo of the DIC setup. In addition to the instruments described above, the displacement and load readings from the two actuators were also recorded.

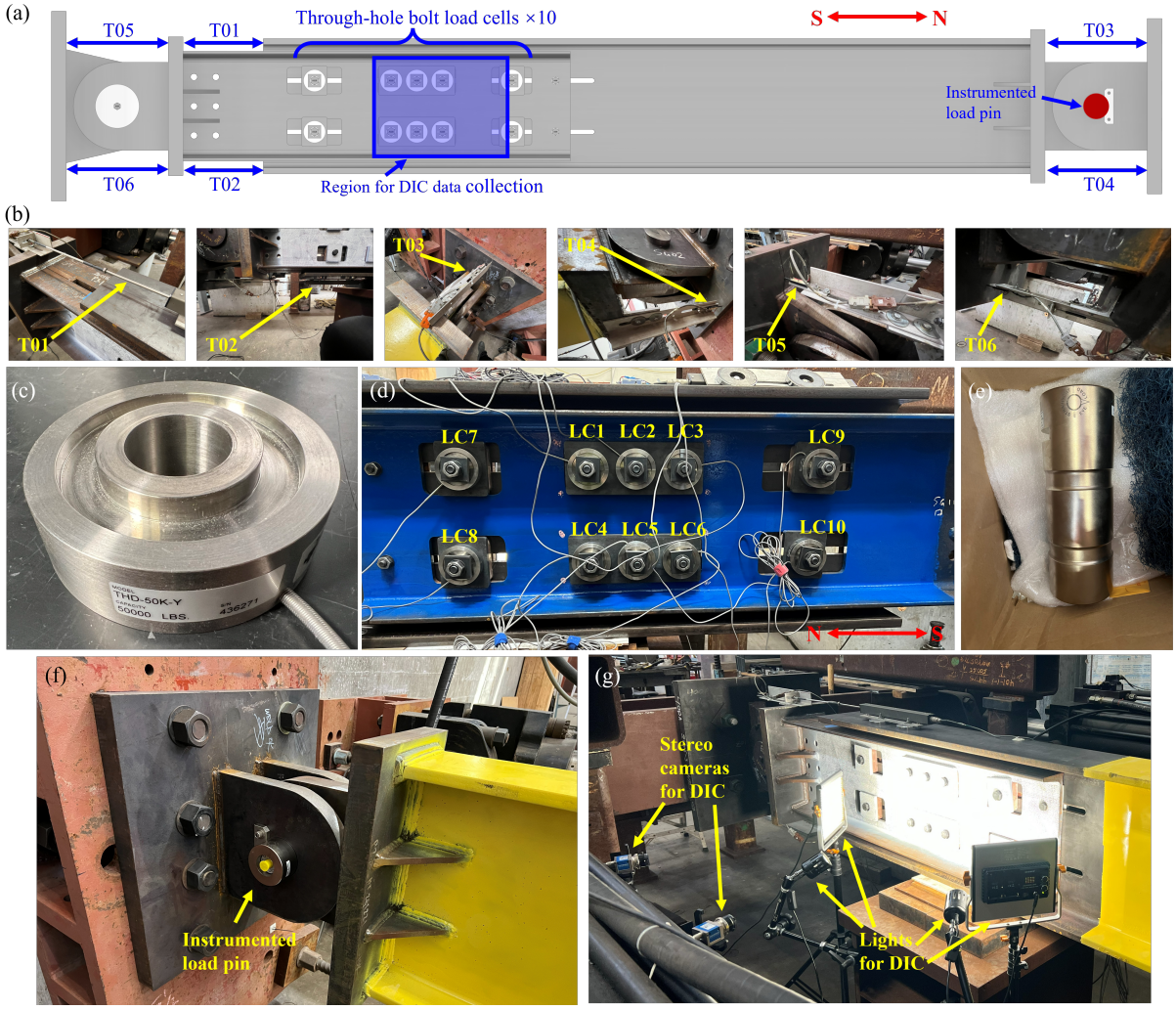

Figure 5.23. (a) Schematic representation of the full-scale Modified FD test instrumentation plan, (b) photos of displacement transducers, (c) photo of one through-hole bolt load cell, (d) photo of through-hole bolt load cells on the specimen and their numbering indices, (e) photo of the instrumented load pin, (f) photo of the instrumented load pin installed in the setup, and (g) photo of DIC setup

Loading Protocol

The loading protocol for the full-scale Modified FD testing is shown in Table 5.4. All tests were cyclic and displacement-controlled. Test Phase 1 was conducted to establish the break-in effect of the Gatke 112 friction shims. The applied normal pressure and sliding distance were selected based on the test results presented in Chapter 2. Test Phase 2 was the main testing phase of the Modified FD. Tests 2.1 to 2.5 were conducted for cases DP1 to DP5 to demonstrate the adjustability of the design parameters of the full-scale Modified FD, using the same imposed displacement time history. Tests 2.6-1 to 2.6-8 were conducted for the FS BL case. Tests 2.6-1 to 2.6-6 used ramped sinusoidal waves with different peak displacements as the imposed displacement time histories to demonstrate the sequential development of connection force levels equal to F_1, $F_1 + F_2$, and $F_1 + F_2 + F_3$. Tests 2.6-7 and 2.6-8 used an earthquake-type input excitation as the imposed displacement time history. The imposed displacement time history for Tests 2.6-7 and 2.6-8 was obtained from Tests 9 and 10 of the testing of PS-C1 and was also truncated to shorten the testing duration. The peak displacement of this time history was scaled to 76.2 mm (3 inch) and the peak sliding velocity imposed by this displacement time history was reduced to 5.08 mm/sec (0.2 inch/sec) by elongating the testing period. Except for Test 2.7, the peak sliding velocity of all tests was limited to 5.08 mm/sec (0.2 inch/sec) based on the hydraulic supply capacity of the actuators. Test 2.7 was conducted to assess the connection response considering a wind-load excitation. In Test 2.7, the Modified FD was first loaded until the connection force reached 222.4 kN (50 kips). A sinusoidal input excitation was then imposed to induce a connection force of 222.4 kN $\pm$ 111.2 kN (50 kips $\pm$ 25 kips) at a frequency of 0.5 Hz. The connection remained elastic throughout this test. The test was terminated after 1000 load cycles were completed. Between tests, the bolt loads of all the friction bolts were adjusted to the target reference level, namely either 84.5 kN or 42.25 kN, depending on the upcoming test.

Table 5.4. Loading protocol for full-scale Modified FD testing

Test ID	Input Type	Peak Displ. [mm]	Peak Vel. [mm/s]	Loading Freq. [Hz]	Description
Test Phase 1					
1-1	Ramped sine	101.6	5.08	0.008	Break-in effect establishment of Gatke 112 friction shims
1-2	Ramped sine	101.6	5.08	0.008	Break-in effect establishment of Gatke 112 friction shims
Test Phase 2					
2.1	Ramped sine	101.6	5.08	0.008	Test of the DP3 case using a sinusoidal wave with 101.6 mm peak displacement
2.2	Ramped sine	101.6	5.08	0.008	Test of the DP4 case using a sinusoidal wave with 101.6 mm peak displacement
2.3	Ramped sine	101.6	5.08	0.008	Test of the DP5 case using a sinusoidal wave with 101.6 mm peak displacement
2.4	Ramped sine	101.6	5.08	0.008	Test of the DP1 case using a sinusoidal wave with 101.6 mm peak displacement
2.5	Ramped sine	101.6	5.08	0.008	Test of the DP2 case using a sinusoidal wave with 101.6 mm peak displacement

Continued on next page

Table 5.4. Loading protocol for full-scale Modified FD testing (continued)

Test ID	Input Type	Peak Displ. [mm]	Peak Vel. [mm/s]	Loading Freq. [Hz]	Description
2.6-1	Ramped sine	19.05	5.08	0.0424	Test of the BL case, considering an expected connection force equal to F_1
2.6-2	Ramped sine	19.05	5.08	0.0424	Test of the BL case, considering an expected connection force equal to F_1; repetition
2.6-3	Ramped sine	38.1	5.08	0.0212	Test of the BL case, considering an expected connection force equal to $F_1 + F_2$
2.6-4	Ramped sine	38.1	5.08	0.0212	Test of the BL case, considering an expected connection force equal to $F_1 + F_2$; repetition
2.6-5	Ramped sine	101.6	5.08	0.008	Test of the BL case, considering an expected connection force equal to $F_1 + F_2 + F_3$
2.6-6	Ramped sine	101.6	5.08	0.008	Test of the BL case, considering an expected connection force equal to $F_1 + F_2 + F_3$; repetition
2.6-7	Earthquake-type	76.2	5.08	N/A	Test of the BL case, considering an earthquake-type input excitation
2.6-8	Earthquake-type	76.2	5.08	N/A	Test of the BL case, considering an earthquake-type input excitation; repetition

Continued on next page

Table 5.4. Loading protocol for full-scale Modified FD testing (continued)

Test ID	Input Type	Peak Displ. [mm]	Peak Vel. [mm/s]	Loading Freq. [Hz]	Description
2.7	Ramped sine	N/A	N/A	0.5	Displacement-controlled wind load test with 1000 cycles

The imposed displacement time history used for Tests 1-1, 1-2, 2.1 to 2.5, and 2.6-5 to 2.6-6 is plotted in Figure 5.24 (a). The imposed displacement time histories for Tests 2.6-1 to 2.6-8 are plotted in Figure 5.24 (b). In Figure 5.24 (b), the imposed displacement time history of each test was separated by blue dashed vertical lines. $\pm D_1$ and $\pm D_2$ of the FS BL case were also plotted for reference. It should be noted that the imposed displacement time history refers to the command sent to the actuators. Because of machining tolerances at the pinhole connections, the axial flexibility of the clevis plates, the shear flexibility of the pins, and the axial flexibility of the Modified FD itself, the actual effective connection displacement experienced by the Modified FD was slightly smaller than the imposed actuator displacement. However, the difference was found to be overall small based on the measured data.

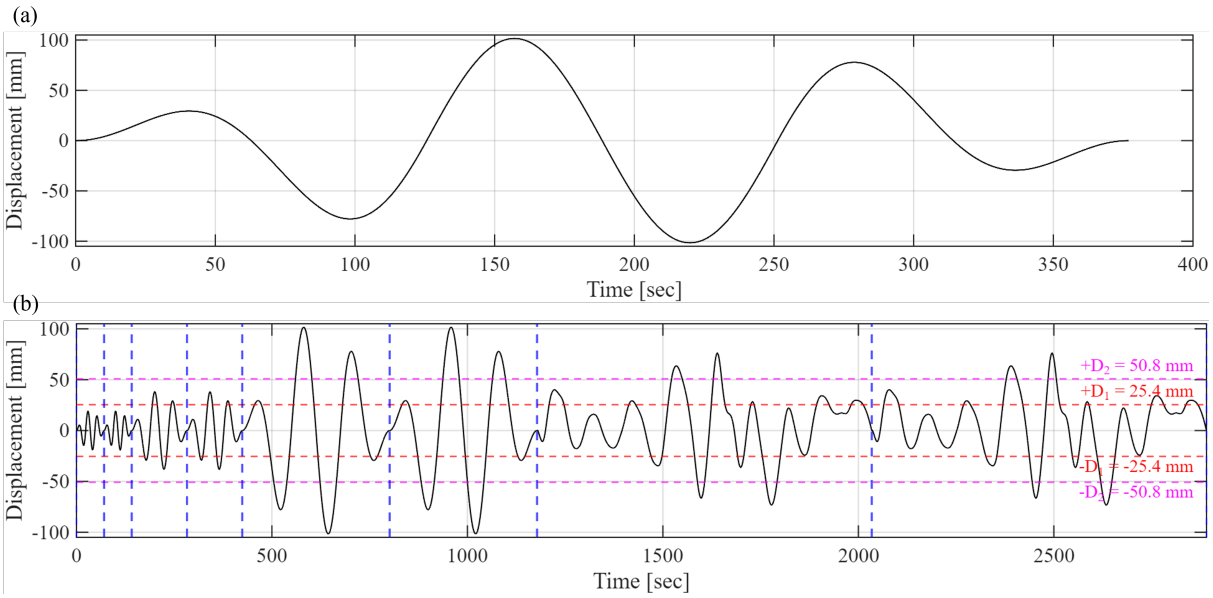

Figure 5.24. (a) The imposed displacement time history used for Tests 1-1, 1-2, 2.1∼2.5, and 2.6-5∼6, and (b) the imposed displacement time history for Tests 2.6-1 to 2.6-8

Results

Figure 5.25 presents the force-displacement response of the full-scale Modified FD from Tests 2.6-1 to 2.6-8, in which the design parameters of the Modified FD followed the FS BL case. As shown in Figure 5.25, the force-displacement response of the full-scale Modified FD

was generally consistent with the anticipated response. In Tests 2.6-1 and 2.6-2, Tests 2.6-3 and 2.6-4, and Tests 2.6-5 to 2.6-8, the Modified FD developed peak connection force levels corresponding to F_1, $F_1 + F_2$ and $F_1 + F_2 + F_3$, respectively. The force-displacement response also exhibited a pinching displacement at zero force due to the gap between the steel channel and the friction shims. This pinching displacement could potentially be reduced by enforcing tighter tolerance control when creating the openings on the steel channels. Overall, the Modified FD exhibited stable force-displacement responses throughout the testing, under both sinusoidal and earthquake-type input excitations. Therefore, the intended kinematics of the full-scale Modified FD were experimentally validated.

It should also be noted that the measured connection force levels were generally larger than the nominal design force levels listed in Table 5.3. This difference was mainly attributed to variations in the coefficient of friction at the friction interfaces. The nominal design force levels were calculated using an expected coefficient of friction of 0.5, whereas the actual coefficient of friction of the friction interface could vary because of variability in the material properties of the friction shims. Overall, the difference between the measured and nominal force levels was considered reasonable and did not affect the validation of the intended kinematics and sequential force development of the Modified FD.

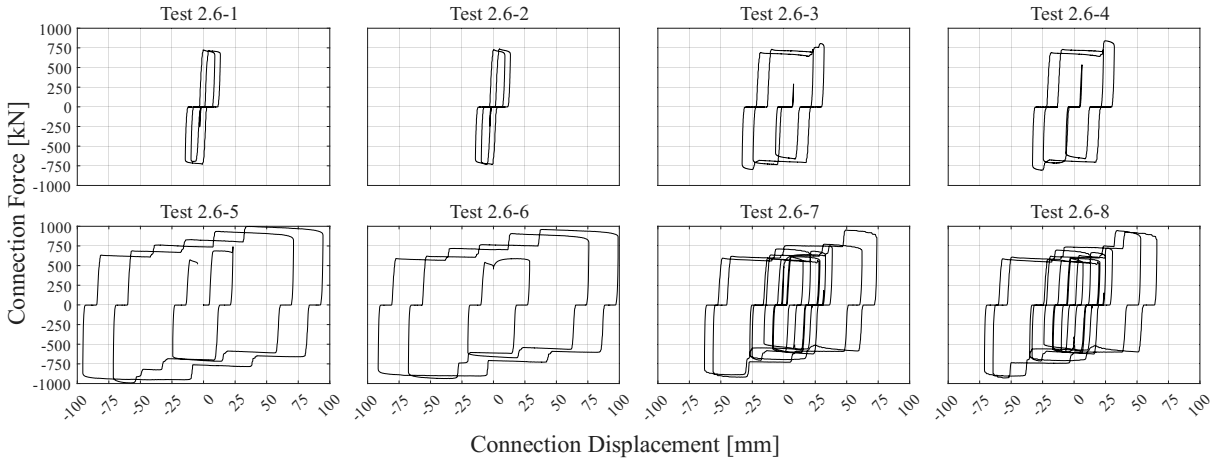

Figure 5.25. Force-displacement response of the full-scale Modified FD (FS BL case)

Figure 5.26 demonstrates the adjustability of the design parameters of the full-scale Modified FD. For each case of design parameter combinations, the response of the FS BL case is plotted in black for comparison. The results show that, at the full-scale level, the response of the Modified FD can still be controlled through the selection of design parameters that lead to predetermined discrete force levels at target displacement levels. This adjustability can be achieved through relatively simple operations, such as replacing friction shims with different lengths to adjust the displacement-related design parameters or adjusting the friction bolt load levels to adjust the force-related design parameters. When the Modified FD is designed following the concept presented in Chapter 3, these adjustments can be performed conveniently even after the Modified FD is installed in a structure.

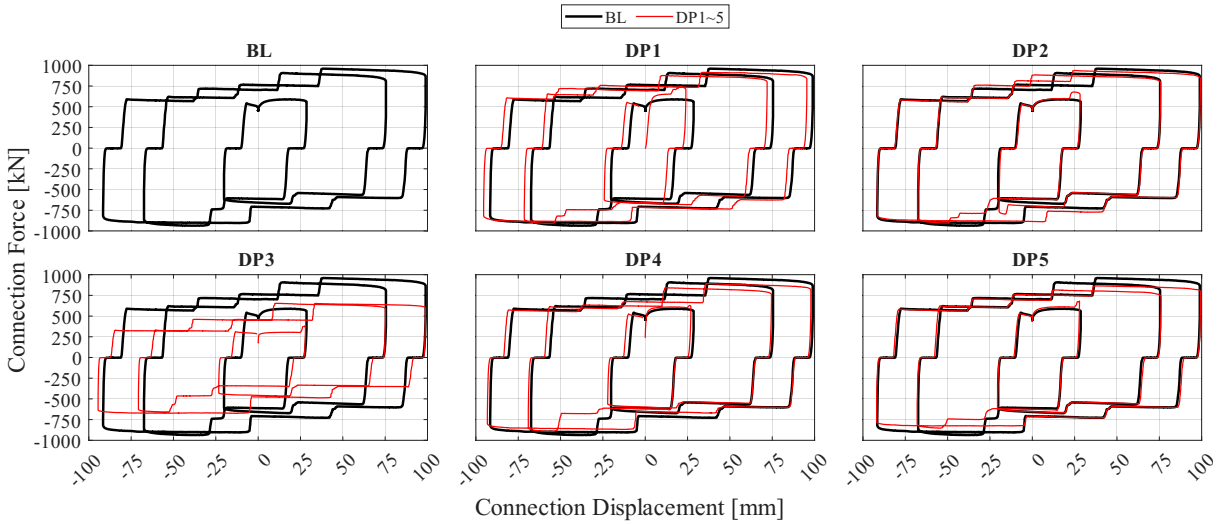

Figure 5.26. Comparison of full-scale Modified FD design cases

Figure 5.27 presents the bolt load results from Test 2.6-6. Note that the numbering indices of the through-hole bolt load cells have been shown in Figure 5.23 (d). Figure 5.27 (a) presents the imposed displacement time history of Test 2.6-6 for reference. Figure 5.27 (b) presents the bolt load time histories of LC1 to LC6. It is observed that the changes in LC2 and LC5 were insignificant throughout the test. In contrast, noticeable bolt load variations were observed in LC1, LC3, LC4, and LC6 when the Modified FD was under compression. LC1 and LC4 exhibited similar trends, whereas LC3 and LC6 exhibited similar but opposite trends relative

to LC1 and LC4. Specifically, when the Modified FD was under compression, the bolt loads in LC3 and LC6 increased, while those in LC1 and LC4 decreased. The increase in individual bolt load reached up to approximately 50%.

The observed bolt load variation was potentially associated with out-of-plane deformation of the specimen. As shown in Figure 5.23 (d), LC1 and LC4 were positioned symmetrically about the longitudinal axis of the Modified FD, which was also the loading direction. Similarly, LC3 and LC6 formed another symmetric pair. When the Modified FD was under compression, the channel section likely experienced out-of-plane deformation. This deformation was restrained by the longer washer plate, and the corresponding restraining action potentially induced out-of-plane bending of the longer washer plate. As a result, the friction bolts instrumented by LC3 and LC6 likely experienced increased elongation, which led to an increase in the bolt load. In contrast, the friction bolts instrumented by LC1 and LC4 were likely shortened, which led to a decrease in the bolt load.

Although the bolt load in an individual friction bolt could vary by as much as approximately 50%, the variation in the sum of the bolt loads was much smaller, as shown in Figure 5.27 (c). Therefore, the overall force-displacement response of the Modified FD remained stable. It is also worth noting that the bolt load variations in LC7 to LC10 were relatively insignificant throughout the test, as shown in Figure 5.27 (d) and Figure 5.27 (e).

Figure 5.28 presents the evolution of the Modified FD connection stiffness during the wind-load test, i.e., Test 2.7. The stiffness was calculated for each half cycle by performing a linear regression of the connection force against the connection displacement. Specifically, the data between two adjacent force extrema were used, and the slope of the best-fit line was taken as the connection stiffness for that half cycle. As shown in Figure 5.28, no stiffness degradation was observed during the wind-load test. Instead, the stiffness gradually increased from approximately 675 kN/mm and eventually converged to approximately 750 kN/mm.

The reason for this gradual stiffness increase is not fully clear based on the currently available data. It may be related to connection-level mechanisms, such as changes in contact

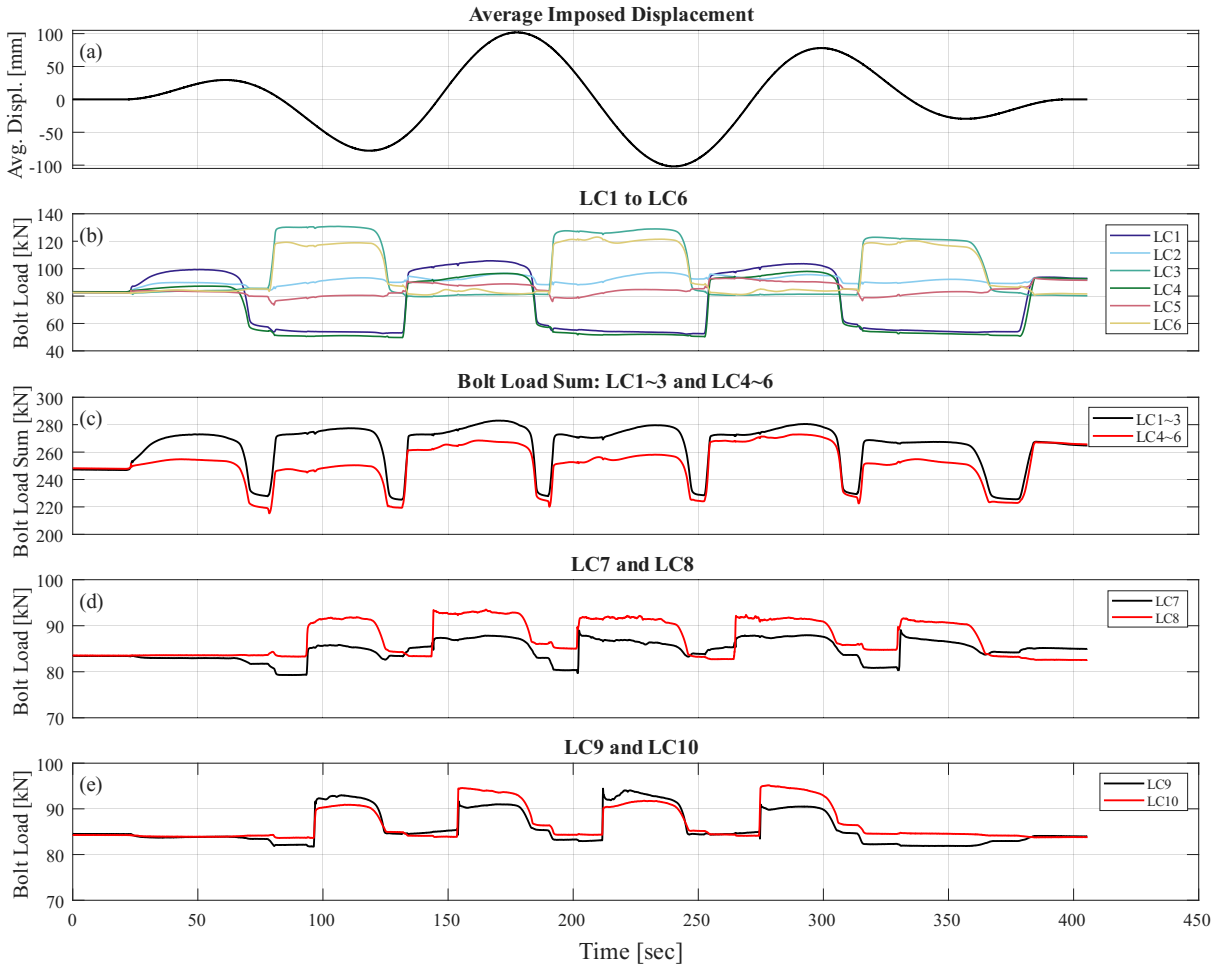

Figure 5.27. Bolt load results from Test 2.6-6: (a) imposed displacement time history of Test 2.6-6, (b) time history of LC1 to LC6, (c) time history of the sum of LC1 to LC3 and LC4 to LC6, (d) time history of LC7 and LC8, and (e) time history of LC9 and LC10

conditions within the Modified FD, minor redistribution of deformation among the specimen components during repeated loading, or local changes at the friction interfaces. Further investigation would be needed to identify the underlying mechanism. Nevertheless, the evolution of stiffness indicates that the Modified FD remained stable under the repeated wind-load excitation and did not exhibit stiffness degradation over the 1000 load cycles.

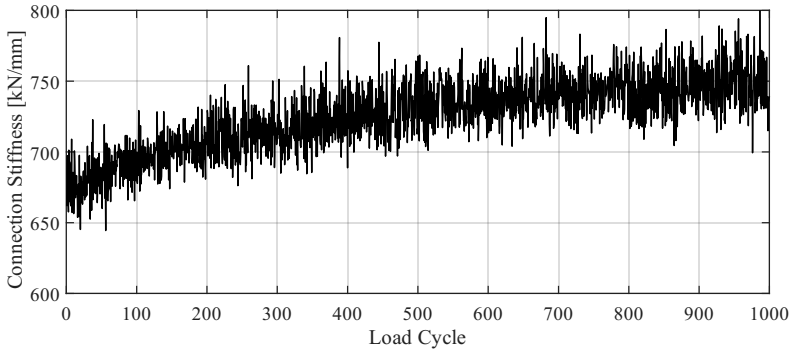

Figure 5.28. Evolution of the Modified FD connection stiffness during the wind load test

Summary of Full-scale Connection Testing

The full-scale connection testing verified that the proposed Modified FD could develop the intended discrete variable force levels at target displacement levels under both sinusoidal and earthquake-type input excitations, thereby experimentally validating the kinematics of the connection concept at the full-scale level. The tests also confirmed that the response of the Modified FD could be adjusted by changing the design parameters through relatively simple operations, including using friction shims with different lengths and adjusting friction bolt load levels. The wind-load test further showed that the Modified FD remained stable and did not exhibit stiffness degradation over 1000 load cycles. Overall, the full-scale testing verified the feasibility of the Modified FD concept at the full-scale level and confirmed the practicality of adjusting its design parameters for future implementation.

5.3 Conclusions

This chapter presents the component-level experimental characterization of the Modified FD introduced in Chapter 4. The objectives were to validate the fabrication and assembly processes, experimentally characterize the structural response of the Modified FD subjected to cyclic displacement loading histories, and experimentally demonstrate the practical adjustability of the design parameters. To achieve these objectives, the experimental program was conducted in two stages: preliminary studies followed by full-scale connection testing. The preliminary studies were conducted first at force levels lower than those expected in full-scale applications, to evaluate the connection concept, examine alternative configurations, and support the development of the full-scale specimen. The full-scale tests were then conducted using force and displacement demand levels representative of those expected in full-scale building applications. Based on the experimental results, the following conclusions were made:

- The Modified FD exhibited the intended force-displacement response with predetermined discrete variable friction force levels at target displacement levels. The sequential development of force levels corresponding to F_1, $F_1 + F_2$, and $F_1 + F_2 + F_3$ was observed in both the preliminary studies and the full-scale connection tests. Therefore, the kinematics of the Modified FD connection concept were experimentally validated.

- The response of the Modified FD could be controlled through the selection and adjustment of design parameters. The displacement-related design parameters, D_1 and D_2, could be adjusted by changing the lengths of the bearing plates or friction shims, depending on the connection configuration. The force-related design parameters, F_1, F_2, and F_3, could be adjusted by changing the friction bolt load levels. The experimental testing results demonstrated the adjustability of the design parameters of the Modified FD.

- The testing of the PS-C1 specimen in the preliminary studies identified several fabrication-, assembly-, and testing-related issues in this configuration, including in-plane rotation

of bearing plates, local gouging, relative movement between friction shims and their corresponding washer plates, and high-frequency force variations at relatively high sliding velocities. Based on these observations, the PS-C1R configuration was developed using straight contact edges and pockets for hosting the friction shims, and exhibited improved connection response. The testing of the PS-C2 specimen further demonstrated the feasibility of an alternative configuration using commercially available steel sections and initially loose washer plates in the design and detailing of the Modified FD.

- DIC analysis indicated that the high-frequency variation in the force response observed at relatively high sliding velocities was potentially related to out-of-plane deformation induced by imperfections in the test setup. This observation highlighted the importance of boundary conditions, and the test setup alignment when testing friction-based components.

- The full-scale Modified FD exhibited stable force-displacement responses under both sinusoidal and earthquake-type input excitations. Although the measured connection force levels were generally slightly higher than the nominal design force levels because of variations in the coefficient of friction, the intended sequential force development and connection kinematics were consistently observed.

- The wind-load test showed that the full-scale Modified FD remained stable and did not exhibit stiffness degradation over 1000 load cycles. This result indicated that the connection could remain elastic and stable under the prescribed repeated service-level loading.

- Bolt load measurements showed that individual friction bolts could experience noticeable load variations, particularly for the bolts associated with F_1 in the full-scale specimen. However, the variation in the sum of the bolt loads was overall insignificant, and the overall force-displacement response of the Modified FD remained stable.

In conclusion, the experimental program verified the feasibility of the Modified FD concept through preliminary studies and full-scale component-level connection testing. The results

confirmed that the Modified FD can provide predetermined discrete variable friction force levels at target displacement levels and that its design parameters can be adjusted through relatively simple operations. The testing also identified practical issues and connection-level mechanisms that should be considered in future design improvement and practical implementation of the Modified FD. It should be acknowledged, however, that the full-scale tests were conducted at relatively low velocities because of limitations of the hydraulic supply capacity. Future full-scale tests at higher velocities are needed to further evaluate the response of the Modified FD and to support its implementation under realistic seismic demands.

Chapter 6

Summary and Conclusions

6.1 Summary

This dissertation investigated friction-based structural components as a class of seismic response modification components for earthquake-resistant structures. The research was motivated by material- and component-level research gaps related to the short- and long-term force-displacement response of friction-based structural components. At the material level, this dissertation characterized the mechanical and tribological properties of selected composite friction materials for composite-metallic friction interfaces. At the component level, this dissertation developed and experimentally characterized friction-based structural components that are intended to reduce sensitivity to machining tolerances, improve inspection and repair procedures, and achieve intended force-displacement responses under cyclic loading.

6.1.1 Research Goal

The overarching goal of this dissertation was to improve the understanding, design, and performance of friction-based structural components in both short- and long-term operation, and ultimately to democratize and advance their applications in earthquake-resistant buildings. This research goal was addressed through material-level and component-level experimental studies.

6.1.2 Research Objectives

The research objectives were:

- To experimentally characterize selected composite friction materials and composite-metallic friction interfaces for use in friction-based structural components.
- To improve the understanding of the mechanical and tribological properties of composite friction materials and composite to low-carbon structural steel friction interfaces under conditions relevant to earthquake structural engineering applications, considering both short- and long-term operation.
- To develop and assess a practical friction-based structural component design concept with reduced sensitivity to machining tolerances and accelerated repairability.
- To develop and evaluate a friction-based structural component (termed the *Modified Friction Device*, or *Modified FD*) capable of developing predetermined discrete variable friction forces at target design displacement levels.
- To experimentally validate the kinematics, force-displacement response, and design-parameter adjustability of the proposed Modified FD.

6.1.3 Research Scope

The following research tasks were performed to achieve the research objectives:

- Chapter 2 presented the experimental characterization of mechanical and tribological properties of composite materials for friction-based structural components. Six phenolic-resin-based fiber-reinforced composite friction materials were tested. Coupon tensile tests and plate bearing tests were conducted to characterize the tensile and bearing strengths of the materials. Bolt relaxation tests were conducted to assess the through-thickness creep behavior of the composite materials and the resulting bolt load loss. Friction tests

were conducted to characterize the tribological properties of composite to low-carbon structural steel friction interfaces under testing parameters relevant to earthquake structural engineering applications, including the normal load level, loading frequencies, sliding velocities, velocity profiles, cumulative displacement, dwell time, and the sliding history.

- Chapter 3 presented the development and experimental characterization of a low-cost friction-based component design concept with reduced sensitivity to machining tolerances and accelerated repairability. The design concept, load path, component detailing, and preliminary numerical assessment were presented. The experimental testing program consisted of component-level connection tests and a full-scale shaking table test, where the proposed friction-based component was designed as the force-limiting connection between a re-centering steel braced frame and sliding slabs. The repairability of the proposed connection was specifically examined during the shaking table test. Reference times required for manufacturing, assembling, installing, and repairing the proposed connection were also assessed and reported, to demonstrate the practicality of the design concept.

- Chapter 4 presented the development of the Modified FD. The schematics of the physical embodiment of the Modified FD were presented. The components, assembly, and mechanics of the Modified FD were discussed. Static structural analyses of a solid finite element model and a truss finite element model were conducted to assess the expected kinematics and force-displacement response of the Modified FD. The adjustability of the design parameters of the Modified FD was discussed and numerically demonstrated.

- Chapter 5 presented the component-level experimental characterization of the Modified FD. The experimental program was conducted in two stages: preliminary studies followed by full-scale connection testing. The preliminary studies were conducted first to validate the expected kinematics and force-displacement response of the Modified FD, examine the practical adjustability of the design parameters, identify fabrication-, assembly-, and testing-related issues, and support the development of the full-scale Modified FD specimen.

Three configurations, namely PS-C1, PS-C1R, and PS-C2, were tested in the preliminary studies. Full-scale connection tests were then conducted using force and displacement demand levels representative of those expected in full-scale building applications.

6.1.4 Research Findings of Chapter 2

- The flash compression molding process may result in manufacturing of materials with regions of lower concentration of phenolic resin than anticipated. This potential manufacturing imperfection was shown to exacerbate delamination of the composite material, characterized by bond failure observed during the coupon tensile test.

- The percentage of bolt load loss due to the creep effects in the composite friction materials ranged from 4.5% to 15%. Possible flash compression molding manufacturing defects can lead to a lower concentration of phenolic resin, resulting in lower bonding and adhesion between the matrix and fibers. This mechanism can induce exacerbated through-thickness creep effects, and consequently an increased percentage of bolt load loss. The bolt relaxation test results highlighted the importance of quality control in the manufacturing of composite friction materials for friction-based structural components.

- The break-in effect depends on the material constituents of the composite friction materials and the normal load level. Cotton-fiber-reinforced composite friction materials compared with glass-fiber-reinforced composite friction materials required less cumulative sliding to establish a steady-state coefficient of friction. A higher normal load increased the wear rate for both cotton- and glass-fiber-reinforced composite friction materials. As a result, a steady-state coefficient of friction was reached with less cumulative sliding.

- Friction tests with different sliding velocities showed a general trend where an increase in the sliding velocity led to a reduction in the coefficient of friction while lower sliding velocities overall resulted in an increase in the coefficient of friction. The reduction in the coefficient of friction was attributed to higher wear rates under higher sliding velocities

and accumulation of wear particles, which decreased the shear strength of the adhesion junction and potentially the real contact area. The increase in the coefficient of friction was attributed to the evacuation of wear particles, which increased the shear strength of the adhesion junction, and potentially an increase in the real contact area. A higher normal load was shown to enhance the velocity-dependent frictional behavior.

- Constituents of composite materials appeared to affect velocity-dependent behavior of composite-metallic friction interfaces. The presence of glass fibers and abrasive particles such as yellow iron oxide, green chromium (III) oxide, and aluminum oxide in the material constituent appeared to enhance the evacuation of wear particles. Among the friction interfaces tested in this study, the friction interface with the composite friction material Gatke 398, consisting of phenolic resin, glass fibers, graphite, Teflon, and molybdenum disulfide MoS_2, in contact with low-carbon structural steel exhibited the most stable frictional behavior under different sliding velocities. Hypothetically, this was attributed to the contribution of graphite, Teflon, and molybdenum disulfide MoS_2.

- Friction interfaces with glass-fiber-reinforced composite friction materials exhibited oscillations in the force response at low sliding velocities due to the stick-slip behavior of the friction interface. The stick-slip behavior was attributed to the localized accumulation and evacuation of wear particles, which was enhanced by hard glass fibers. In contrast, friction interfaces with cotton-fiber-reinforced composite friction materials did not exhibit oscillations in the force response. The effect of the stick-slip behavior of composite-metallic friction interfaces could be considered insignificant for earthquake structural engineering applications.

- The increased dwell time increased the coefficient of friction, with the exception of the test cases that used Gatke 113 and Gatke 397, which require further investigation.

- The friction-based structural component with composite-metallic friction interfaces tested

in this study exhibited velocity-dependent bolt load variation because of the wear mechanism of the friction interface. Higher sliding velocities tended to induce an increase in the bolt load due to increased wear debris generation and accumulation while lower sliding velocities tended to induce a reduction in the bolt load due to wear debris evacuation. In addition, a higher normal load overall induced more wear of the composite friction material and therefore, induced more bolt load loss toward the end of the test.

- Relatively high-velocity sliding motions overall induced a decrease in the coefficient of friction μ and an increase in the bolt load N. According to Coulomb's friction equation $f = \mu N$, the effect of sliding velocities on μ and N tends to cancel out each other on the product f. Therefore, for a friction-based structural component, the friction force generated is possible to maintain relatively constant under high sliding velocities.

- Considering the results of the mechanical and tribological characterization of materials presented in this study, composite materials that consist of phenolic resin, glass fibers, graphite, Teflon, and molybdenum disulfide MoS_2 are among the most suitable materials for use in friction-based structural components for earthquake structural engineering applications.

6.1.5 Research Findings of Chapter 3

- A novel yet practical design concept for friction-based structural components intended for use as energy dissipation devices or force-limiting connections in earthquake-resistant structures was developed and experimentally characterized. The proposed connection has a slotted-bolted configuration. The main difference between this design and the conventional design of slotted-bolted friction-based components is that, in this design, initially loose plates are used to establish the clamping mechanism.

- This design concept offers two key advantages. First, the connection has stable force-displacement responses and generates relatively constant sliding forces without enforcing

tight geometric tolerances in the machining of the parts. Second, the design with loose steel washer plates allows quick inspection and replacement of friction shims if needed.

- A numerical simulation was conducted to assess the expected kinematics and force-displacement responses of the connection. Critical regions of high stress were identified to facilitate the design and detailing of the parts.

- A friction-based structural component, which has a required sliding force of 40 kN, was designed with the proposed design concept and tested. Two test phases, including component-level connection tests (99 tests in total) and a full-scale shaking table test of a three-story re-centering steel braced frame (8 tests in total), were performed. In the shaking table test, the proposed friction-based connection was designed as the force-limiting connection between the steel frame and the sliding slab.

- Without enforcing tight geometric tolerances in the machining of the parts, the friction-based force-limiting connection designed with loose steel washer plates exhibited stable force-displacement responses. The connection tested in this study generated a relatively constant sliding friction force equal to the required sliding force, 40 kN, without exhibiting the uncontrolled displacement-dependent variable friction force. Hence, it was demonstrated that compared with the conventional design of slotted-bolted friction-based components, the proposed design concept with loose steel washer plates can save both manufacturing time and cost.

- The break-in effect of the composite-metallic friction interface influenced the early-stage response of the friction-based connection. It is recommended to break in the composite friction shim before installing the connection onto the structure so that the friction interface of the connection can reach a relatively steady state and the connection can generate a relatively constant connection sliding force with relatively low bolt load loss.

- For the connection tested in this study, with a Gatke 398 to low-carbon structural steel

friction interface and a nominal normal pressure of 3.8 MPa, the break-in loading protocol consisted of three ramped sinusoidal break-in tests, with bolt retightening after each break-in test. Break-in test 1 had a cumulative displacement of 2 meters, and Break-in tests 2 and 3 each had a cumulative displacement of 1 meter. The ramped sinusoidal waves used had a peak displacement of 50.8 mm and a peak sliding velocity of 7.62 mm/s. The break-in loading protocol resulted in a total cumulative displacement of 4 meters.

- Throughout the shaking table test, the proposed friction-based connection successfully accommodated a relative displacement of approximately 70 mm between the steel frame and the sliding slab, under a peak sliding velocity of approximately 525 mm/s, with a relatively low bolt load loss of 5 kN.

- The inspection and replacement of the friction shims for the friction-based connection designed with loose steel washer plates could be performed relatively easily without removing the connection from the structure. Compared with the conventional design, of which the inspection and replacement process requires removal of external clamping plates, the proposed design concept with loose steel washer plates allows a quicker inspection and repairing process, which potentially enhances the practicality of the connection in real applications and supports the long-term functionality of earthquake-resistant buildings equipped with friction-based connections.

- The two test phases showed no failure or damage in the parts of the proposed friction-based components even after multiple displacement time histories.

- Reference times for manufacturing, assembling, installing, and repairing one connection were reported. The reference manufacturing time was 180 minutes, the assembling time was 3 minutes, the installing time was 8 to 12 minutes, and the repairing time was 3 minutes.

- The proposed design concept with loose steel washer plates provides a low-cost, less

sensitive to machining tolerances, and easily repairable solution for designing friction-based structural components in earthquake engineering applications.

6.1.6 Research Findings of Chapter 4

- A simple and practical structural connection designed to develop predetermined discrete variable friction forces at target displacement levels was presented. The innovative connection was termed *Modified Friction Device*, or *Modified FD*.

- The schematics of the physical embodiment of the Modified FD were presented. The components and the assembly of the Modified FD were discussed. The mechanics of the Modified FD were explained.

- Results from numerical simulations of a solid finite element model of the Modified FD validated the expected kinematics and the expected force-displacement response of the Modified FD.

- A truss finite element model was developed in OpenSees. The truss model simulated efficiently the expected force-displacement response of the Modified FD.

- The adjustability of the design parameters of the Modified FD was discussed and numerically demonstrated.

6.1.7 Research Findings of Chapter 5

- The Modified FD exhibited the intended force-displacement response with predetermined discrete variable friction force levels at target displacement levels. The sequential development of force levels was observed in both the preliminary studies and the full-scale connection tests. Therefore, the kinematics of the Modified FD connection concept were experimentally validated.

- The response of the Modified FD could be controlled through the selection and adjustment of design parameters. The displacement-related design parameters could be adjusted by changing the lengths of the bearing plates or friction shims, depending on the connection configuration. The force-related design parameters could be adjusted by changing the friction bolt load levels. The experimental testing results demonstrated the adjustability of the design parameters of the Modified FD.

- The testing of the PS-C1 specimen in the preliminary studies identified several fabrication-, assembly-, and testing-related issues in this configuration, including in-plane rotation of bearing plates, local gouging, relative movement between friction shims and their corresponding washer plates, and high-frequency force variations at relatively high sliding velocities. Based on these observations, the PS-C1R configuration was developed using straight contact edges and pockets for hosting the friction shims, and exhibited improved connection response. The testing of the PS-C2 specimen further demonstrated the feasibility of an alternative configuration using commercially available steel sections and initially loose washer plates in the design and detailing of the Modified FD.

- DIC analysis indicated that the high-frequency variation in the force response observed at relatively high sliding velocities was potentially related to out-of-plane deformation induced by imperfections in the test setup. This observation highlighted the importance of boundary conditions and test setup alignment when testing friction-based components.

- The full-scale Modified FD exhibited stable force-displacement responses under both sinusoidal and earthquake-type input excitations. Although the measured connection force levels were generally slightly higher than the nominal design force levels because of variations in the coefficient of friction, the intended sequential force development and connection kinematics were consistently observed.

- The wind-load test showed that the full-scale Modified FD remained stable and did not

exhibit stiffness degradation over 1000 load cycles. This result indicated that the connection could remain elastic and stable under the prescribed repeated service-level loading.

- Bolt load measurements showed that individual friction bolts could experience noticeable load variations, particularly for the bolts associated with F_1 in the full-scale specimen. However, the variation in the sum of the bolt loads was overall insignificant, and the overall force-displacement response of the Modified FD remained stable.

- The experimental program verified the feasibility of the Modified FD concept through preliminary studies and full-scale component-level connection testing. The results confirmed that the Modified FD can provide predetermined discrete variable friction force levels at target displacement levels and that its design parameters can be adjusted through relatively simple operations. The testing also identified practical issues and connection-level mechanisms that should be considered in future design improvement and practical implementation of the Modified FD.

- The full-scale tests were conducted at relatively low velocities because of limitations of the hydraulic supply capacity. Future full-scale tests at higher velocities are needed to further evaluate the response of the Modified FD and to support its implementation under realistic seismic demands.

6.2 Conclusions

- A systematic testing program was developed to characterize composite friction materials and composite to low-carbon structural steel friction interfaces for use in friction-based structural components. The testing program included coupon tensile tests, plate bearing tests, bolt relaxation tests, and friction tests, and provided information on the mechanical and tribological properties of the tested composite friction materials.

- The experimental results showed that the material constituents and manufacturing process of composite friction materials affect their mechanical properties and through-thickness

creep behavior. Possible flash compression molding manufacturing defects can lead to a lower concentration of phenolic resin, which can result in lower bonding and adhesion between the matrix and fibers and potentially exacerbate through-thickness creep behavior.

- The tribological properties of composite to low-carbon structural steel friction interfaces were affected by the material constituents of the composite friction materials and testing parameters including normal load level, sliding velocity, velocity profile, cumulative displacement, dwell time, and previous sliding events. Constituents such as reinforcing fibers and friction modifiers were shown to influence the velocity-dependent behavior of the friction interfaces. Among the tested friction interfaces, the Gatke 398 to low-carbon structural steel friction interface exhibited the most stable frictional behavior under different sliding velocities.

- A low-cost friction-based structural component design concept with reduced sensitivity to machining tolerances and accelerated repairability was developed and experimentally characterized. The proposed design uses loose steel washer plates to establish the clamping mechanism and generated relatively constant sliding forces without enforcing tight geometric tolerances in the machining of the parts.

- The friction-based force-limiting connection designed with loose steel washer plates was shown to be practical in both component-level tests and a full-scale shaking table test. The connection generated a required sliding force of 40 kN, accommodated a relative displacement of approximately 70 mm between the steel frame and the sliding slab under a peak sliding velocity of approximately 525 mm/s, and exhibited relatively low bolt load loss. The inspection and replacement of friction shims could be performed without removing the connection from the structure.

- A simple and practical structural connection, termed the *Modified Friction Device* or *Modified FD*, was developed to provide predetermined discrete variable friction forces

at target design displacement levels. The component-level experimental characterization of the Modified FD validated the expected kinematics, force-displacement response, and the adjustability of design parameters. The full-scale Modified FD exhibited stable force-displacement responses under sinusoidal, earthquake-type, and repeated wind-load input excitations, supporting the feasibility of this design concept for future implementation in earthquake-resistant buildings.

6.3 Original Contributions

- The development of a systematic experimental framework for characterizing composite friction materials and composite-metallic friction interfaces for earthquake structural engineering applications was achieved. The framework supports the assessment of mechanical and tribological properties of composite friction materials for use in friction-based structural components.

- The experimental assessment of the mechanical and tribological properties of six composite friction materials was conducted following the proposed experimental framework. The experimental results revealed the effect of material constituents and manufacturing defects on the properties of composite friction materials, and supported the identification of suitable constituents for composite friction materials used in friction-based structural components for earthquake structural engineering applications.

- The component-level experimental assessment of a low-cost friction-based structural component design concept with loose washer plates was conducted. The proposed design concept was shown to generate stable force-displacement responses without enforcing tight geometric tolerances in the machining of the parts, while allowing accelerated inspection and replacement of friction shims.

- The component-level experimental assessment of a simple and practical friction-based structural component (the Modified FD), capable of developing predetermined discrete

variable friction forces at target design displacement levels, was conducted. The tests validated the intended kinematics, force-displacement response, and the adjustability of design parameters of the Modified FD. Stable force-displacement responses under sinusoidal, earthquake-type, and repeated wind-load input excitations were demonstrated.

6.4 Future Research

6.4.1 Material-level

- The mechanism proposed in Chapter 2 regarding the generation, accumulation, and evacuation of wear particles at the friction interface is broadly consistent with the mechanisms proposed in previous studies [83, 2] and with the experimental observations obtained in this study. Nevertheless, it remains a hypothesis supported primarily by indirect macroscopic evidence, including the evolution of the coefficient of friction and the bolt load time histories. More in-depth studies can be conducted using techniques such as Scanning Electron Microscopy and Energy-dispersive X-ray spectroscopy to gain a better understanding of the micro-level friction mechanism of composite friction materials. This will further validate the proposed mechanism and potentially support the future development of high-performance composite friction materials for earthquake structural engineering applications.

- The friction test presented in Chapter 2 did not explicitly consider the potential contribution of frictional heat to the observed variation in the bolt load. Future studies could use bolts instrumented with strain gauges and thermocouples to quantify temperature changes and assess the contribution of thermally induced bolt elongation, complementing the wear particles accumulation mechanism discussed in this dissertation.

- The peak sliding velocity considered in the friction test presented in Chapter 2 was 63.5 mm/s (2.5 inch/s), which was limited by the hydraulic supply capacity of the test machine. Future studies should extend the friction testing program to higher sliding velocities to

further characterize the velocity-dependent frictional behavior and assess whether the mechanisms discussed in this dissertation remain applicable over a broader velocity range.

- Future studies should investigate alternative break-in procedures that potentially reduce the required pre-processing effort while providing a stable frictional response, thereby improving the practicality of friction-based components when using composite-metallic friction interfaces. Long-term testing is also needed to determine whether the effect of the initial break-in process is maintained over time and whether an additional break-in process is required in long-term operation.

- Further research on the effects of manufacturing process is recommended. Specifically, composite friction materials manufactured using positive cavity molding techniques can be tested and compared with flash-molded materials to better understand the effects of manufacturing process and quality control on the mechanical and tribological properties of composite friction materials.

6.4.2 Component-level

- The peak sliding velocity considered in the full-scale Modified FD testing was 5.08 mm/s (0.2 inch/s), which was limited by the hydraulic supply capacity of the two actuators in the existing test setup. Although the response of a friction-based component is governed primarily by the behavior of the friction interface, which was assessed through the material-level study presented in Chapter 2, full-scale tests of the Modified FD at higher velocities are still recommended to further evaluate its response and to support its implementation under realistic seismic demands.

6.4.3 System-level

- Further research is recommended to develop design guidelines for structural systems equipped with Modified FDs. In particular, simple and efficient procedures are needed for

determining and optimizing the design parameters of the Modified FD, including D_1, D_2, F_1, F_2, and F_3, to achieve target seismic performance in different structural applications.

Bibliography

[1] National Geophysical Data Center / World Data Service (NGDC/WDS), "NCEI/WDS Global Significant Earthquake Database." NOAA National Centers for Environmental Information. Accessed: 2026-05-29.

[2] G. Tsampras, R. Sause, R. B. Fleischman, and J. I. Restrepo, "Experimental study of deformable connection consisting of friction device and rubber bearings to connect floor system to lateral force resisting system," *Earthquake Engineering & Structural Dynamics*, vol. 47, pp. 1032–1053, Apr. 2018.

[3] Z. Zhang, R. B. Fleischman, J. I. Restrepo, G. Guerrini, A. Nema, D. Zhang, U. Shakya, G. Tsampras, and R. Sause, "Shake-table test performance of an inertial force-limiting floor anchorage system," *Earthquake Engineering & Structural Dynamics*, vol. 47, no. 10, pp. 1987–2011, 2018.

[4] G. Tsampras and R. Sause, "Development and Experimental Validation of Deformable Connection for Earthquake-Resistant Building Systems with Reduced Floor Accelerations," tech. rep., Lehigh University, 2015.

[5] C. Christopoulos and A. Filiatrault, *Principles of passive supplemental damping and seismic isolation*. IUSS Press, 2006.

[6] T. T. Soong and G. F. Dargush, *Passive energy dissipation systems in structural engineering*. Wiley, 1997.

[7] P. Clark, R. Bassett, and J. Bradshaw, "Plate friction load control devices-their application and potential.," *Proceedings of the Institution of Civil Engineers*, vol. 55, no. 2, pp. 335–352, 1973.

[8] Y. Loo, R. Upfold, and D. Banks, "The behavior of an earthquake energy absorber for bridge decks," in *Proceedings of the Sixth Austrialian Conference on the Mechanics of Structures and Materials, Christchurch, NZ*, pp. 365–371, 1977.

[9] Y. C. Kurama, "Simplified seismic design approach for friction-damped unbonded post-tensioned precast concrete walls," *Structural Journal*, vol. 98, no. 5, pp. 705–716, 2001.

[10] A. S. Pall, *Limited slip bolted joints: a device to control the seismic response of large panel structures*. PhD thesis, Concordia University, 1979.

[11] C. Bora, M. G. Oliva, S. D. Nakaki, and R. Becker, "Development of a precast concrete shear-wall system requiring special code acceptance," *PCI journal*, vol. 52, no. 1, p. 122, 2007.

[12] B. G. Morgen, *Friction-damped unbonded post-tensioned precast concrete moment frame structures for seismic regions*. PhD thesis, University of Notre Dame, 2007.

[13] B. G. Morgen and Y. C. Kurama, "Seismic response evaluation of posttensioned precast concrete frames with friction dampers," *Journal of structural engineering*, vol. 134, no. 1, pp. 132–145, 2008.

[14] L.-l. Song, T. Guo, and C. Chen, "Experimental and numerical study of a self-centering prestressed concrete moment resisting frame connection with bolted web friction devices," *Earthquake Engineering & Structural Dynamics*, vol. 43, no. 4, pp. 529–545, 2014.

[15] O. Pekau and R. Guimond, "Controlling seismic response of eccentric structures by friction dampers," *Earthquake engineering & structural dynamics*, vol. 20, no. 6, pp. 505–521, 1991.

[16] B. Morgen and Y. Kurama, "A friction damper for post-tensioned precast concrete beam-to-column joints," *PCI Journal*, vol. 49, no. 4, pp. 112–133, 2004.

[17] L. Ferrara, R. Felicetti, G. Toniolo, and C. Zenti, "Friction dissipative devices for cladding panels in precast buildings: An experimental investigation," *European journal of environmental and civil engineering*, vol. 15, no. 9, pp. 1319–1338, 2011.

[18] S. Cherry and A. Filiatrault, "Seismic response control of buildings using friction dampers," *Earthquake Spectra*, vol. 9, no. 3, pp. 447–466, 1993.

[19] B. Dal Lago, F. Biondini, and G. Toniolo, "Friction-based dissipative devices for precast concrete panels," *Engineering Structures*, vol. 147, pp. 356–371, 2017.

[20] T. Koshikawa, "Moment and energy dissipation capacities of post-tensioned precast concrete connections employing a friction device," *Engineering Structures*, vol. 138, pp. 170–180, 2017.

[21] S. Yildirim, G. Asik, B. Erkus, Y. Tonguc, and I. Mualla, "Seismic retrofit of single story precast reinforced concrete structures with infill walls using friction dampers," in *Proceedings of the second European conference on earthquake engineering and seismoilogy*, p. 10, 2014.

[22] M. N. Eldin, A. J. Dereje, and J. Kim, "Seismic retrofit of rc buildings using self-centering pc frames with friction-dampers," *Engineering Structures*, vol. 208, p. 109925, 2020.

[23] A. Naeem and J. Kim, "Seismic retrofit of 3000 kva power transformer using friction dampers and prestressed tendons," *Structures*, vol. 32, pp. 641–650, 2021.

[24] Y. Cui, Q. Tang, T. Wu, and T. Wang, "Seismic performance of bending-type frictional steel truss coupling beams," *Earthquake Engineering & Structural Dynamics*, vol. 51, no. 3, pp. 673–687, 2022.

[25] Y. Cui, Q. Tang, T. Wu, T. Okazaki, and T. Wang, "Mechanism and experimental validation of frictional steel truss coupling beams," *Journal of Structural Engineering*, vol. 148, no. 9, p. 04022129, 2022.

[26] A. S. Pall and C. Marsh, "Response of friction damped braced frames," *Journal of the Structural Division*, vol. 108, no. 6, pp. 1313–1323, 1982.

[27] A. Filiatrault and S. Cherry, "Performance evaluation of friction damped braced steel frames under simulated earthquake loads," *Earthquake spectra*, vol. 3, no. 1, pp. 57–78, 1987.

[28] I. D. Aiken, J. Kelly, and A. Pall, "Seismic response of a nine-story steel frame with friction damped cross-bracing," tech. rep., University of California Berkeley, 1988.

[29] G. Anagnostides, *Design of economical means of enhancing the energy-absorption capability of braced frame structures*. PhD thesis, University of London. Imperial Colledge of Science and Technology., 1988.

[30] G. Anagnostides and A. Hargreaves, "Shake table testing on an energy absorption device for steel braced frames," *Soil Dynamics and Earthquake Engineering*, vol. 9, no. 3, pp. 120–140, 1990.

[31] T. Fitzgerald, T. Anagnos, M. Goodson, and T. Zsutty, "Slotted bolted connections in aseismic design for concentrically braced connections," *Earthquake spectra*, vol. 5, no. 2, pp. 383–391, 1989.

[32] R. Giacchetti, A. Whittaker, V. V. Bertero, and H. Aktan, "Seismic response of a dmrsf retrofitted with friction slip devices," in *Proceedings of the First International Meeting on Base Isolation and Passive Energy Dissipation*, 1989.

[33] R. Tremblay, *Seismic behavior and design of friction concentrically braced frames for steel buildings*. PhD thesis, University of British Columbia, 1993.

[34] C. E. Grigorian, T.-S. Yang, and E. P. Popov, "Slotted bolted connection energy dissipators," *Earthquake Spectra*, vol. 9, no. 3, pp. 491–504, 1993.

[35] H.-H. Khoo, C. Clifton, J. Butterworth, G. MacRae, and G. Ferguson, "Influence of steel shim hardness on the sliding hinge joint performance," *Journal of Constructional Steel Research*, vol. 72, pp. 119–129, 2012.

[36] H. Bagheri, A. Hashemi, P. Zarnani, P. Quenneville, Z. Yan, G. Clifton, G. MacRae, R. Dhakal, X. Zhao, L. Jia, and P. Xiang, "A low-damage steel structure using resilient slip friction joint for a full-scale shaking table test," in *Proceedings of the 17th world conference on earthquake engineering (17WCEE)*, p. 12, 2020.

[37] J. C. C. Golondrino, G. A. MacRae, J. G. Chase, G. W. Rodgers, and G. C. Clifton, "Seismic behaviour of symmetric friction connections for steel buildings," *Engineering Structures*, vol. 224, p. 111200, 2020.

[38] J. C. C. Golondrino, G. A. MacRae, J. G. Chase, G. W. Rodgers, A. C. N. Scott, and G. C. Clifton, "Steel building friction connection seismic performance–corrosion effects," *Structures*, vol. 19, pp. 96–109, 2019.

[39] J. C. C. Golondrino, G. MacRae, J. Chase, G. Rodgers, and G. Clifton, "Application of brake pads on asymmetrical friction connection (afc)," in *Proceedings of the New Zealand Society for Earthquake Engineering Conference*, 2013.

[40] G. MacRae, X. Zhao, L. Jia, G. Clifton, R. Dhakal, P. Xiang, S. Ramhormozian, and G. Rodgers, "The china-nz robust friction building shaking table testing overview," in *17th World conference on earthquake engineering*, 2020.

[41] S. Ramhormozian, G. Clifton, and G. MacRae, "The asymmetric friction connection with belleville springs in the sliding hinge joint," in *Proceedings of the New Zealand Society for Earthquake Engineering Conference*, 2014.

[42] P. Rojas, J. Ricles, and R. Sause, "Seismic performance of post-tensioned steel moment resisting frames with friction devices," *Journal of structural engineering*, vol. 131, no. 4, pp. 529–540, 2005.

[43] G. D. Petty, "Evaluation of a friction component for a post-tensioned steel connection," Master's thesis, Lehigh University, 1999.

[44] K.-C. Tsai, C.-C. Chou, C.-L. Lin, P.-C. Chen, and S.-J. Jhang, "Seismic self-centering steel beam-to-column moment connections using bolted friction devices," *Earthquake Engineering & Structural Dynamics*, vol. 37, no. 4, pp. 627–645, 2008.

[45] H.-J. Kim and C. Christopoulos, "Friction damped posttensioned self-centering steel moment-resisting frames," *Journal of Structural Engineering*, vol. 134, no. 11, pp. 1768–1779, 2008.

[46] M. Wolski, J. M. Ricles, and R. Sause, "Experimental study of a self-centering beam–column connection with bottom flange friction device," *Journal of Structural Engineering*, vol. 135, no. 5, pp. 479–488, 2009.

[47] Y.-C. Lin, R. Sause, and J. Ricles, "Seismic performance of a large-scale steel self-centering moment-resisting frame: Mce hybrid simulations and quasi-static pushover tests," *Journal of Structural Engineering*, vol. 139, no. 7, pp. 1227–1236, 2013.

[48] A. Filiatrault, "Analytical predictions of the seismic response of friction damped timber shear walls," *Earthquake engineering & structural dynamics*, vol. 19, no. 2, pp. 259–273, 1990.

[49] Z. Li, F. Chen, M. He, R. Zhou, Y. Cui, Y. Sun, and G. He, "Lateral performance of self-centering steel–timber hybrid shear walls with slip-friction dampers: Experimental investigation and numerical simulation," *Journal of structural engineering*, vol. 147, no. 1, p. 04020291, 2021.

[50] W. Y. Loo, C. Kun, P. Quenneville, and N. Chouw, "Experimental testing of a rocking timber shear wall with slip-friction connectors," *Earthquake engineering & structural dynamics*, vol. 43, no. 11, pp. 1621–1639, 2014.

[51] R. Tyler, "Test on a brake lining damper for structures," *Bulletin of the New Zealand Society for Earthquake Engineering*, vol. 18, no. 3, pp. 280–284, 1985.

[52] I. D. Aiken, *Earthquake simulator testing and analytical studies of two energy-absorbing systems for multistory structures*. PhD thesis, University of California, Berkeley, 1990.

[53] I. D. Aiken, D. K. Nims, A. S. Whittaker, and J. M. Kelly, "Testing of passive energy dissipation systems," *Earthquake spectra*, vol. 9, no. 3, pp. 335–370, 1993.

[54] D. K. Nims, P. J. Richter, and R. E. Bachman, "The use of the energy dissipating restraint for seismic hazard mitigation," *Earthquake spectra*, vol. 9, no. 3, pp. 467–489, 1993.

[55] A. Filiatrault, R. Tremblay, and R. Kar, "Performance evaluation of friction spring seismic damper," *Journal of Structural Engineering*, vol. 126, no. 4, pp. 491–499, 2000.

[56] B. Chi and C. Uang, "Dynamic testing of full-scale slotted bolted connections," tech. rep., Department of Structural Engineering: University of California San Diego, 2000.

[57] S. Jaisee, F. Yue, and Y. H. Ooi, "A state-of-the-art review on passive friction dampers and their applications," *Engineering Structures*, vol. 235, p. 112022, 2021.

[58] T. Sun, L. Peng, X. Ji, and X. Li, "Development of a negative stiffness friction damping device with an amplification mechanism," *Engineering Structures*, vol. 275, p. 115286, 2023.

[59] K. Shirai, T. Ito, and M. Kikuchi, "Seismic response control effects for reinforced-concrete buildings incorporating a passive variable friction device," *Journal of Building Engineering*, vol. 62, p. 105388, 2022.

[60] S. Zhu, *Seismic behavior of framed structural systems with self-centering friction damping braces*. PhD thesis, Lehigh University, 2007.

[61] C. Christopoulos, R. Tremblay, H.-J. Kim, and M. Lacerte, "Self-centering energy dissipative bracing system for the seismic resistance of structures: development and validation," *Journal of structural engineering*, vol. 134, no. 1, pp. 96–107, 2008.

[62] J. Erochko, C. Christopoulos, and R. Tremblay, "Design and testing of an enhanced-elongation telescoping self-centering energy-dissipative brace," *Journal of Structural Engineering*, vol. 141, no. 6, p. 04014163, 2015.

[63] C.-C. Chou and Y.-C. Chen, "Development of steel dual-core self-centering braces: quasi-static cyclic tests and finite element analyses," *Earthquake Spectra*, vol. 31, no. 1, pp. 247–272, 2015.

[64] A. M. Asfaw, L. Cao, O. E. Ozbulut, and J. Ricles, "Development of a shape memory alloy-based friction damper and its experimental characterization considering rate and temperature effects," *Engineering Structures*, vol. 273, p. 115101, 2022.

[65] "Pall dynamics," 2025. Accessed: 2025-09-02.

[66] "Quaketek," 2025. Accessed: 2025-09-02.

[67] "Damptech," 2025. Accessed: 2025-09-02.

[68] "Oiles corporation," 2025. Accessed: 2025-09-02.

[69] "Tectonus," 2025. Accessed: 2025-09-02.

[70] G. Tsampras, R. Sause, D. Zhang, R. B. Fleischman, J. I. Restrepo, D. Mar, and J. Maffei, "Development of deformable connection for earthquake-resistant buildings to reduce floor accelerations and force responses," *Earthquake Engineering & Structural Dynamics*, vol. 45, no. 9, pp. 1473–1494, 2016.

[71] A. Mokha, M. Constantinou, and A. Reinhorn, "Teflon bearings in base isolation i: Testing," *Journal of Structural Engineering*, vol. 116, no. 2, pp. 438–454, 1990.

[72] J. C. Golondrino, G. A. MacRae, J. G. Chase, G. W. Rodgers, and G. C. Clifton, "Behaviour of asymmetrical friction connections using different shim materials," in *Proceedings of 2012 NZSEE Conference*, New Zealand Society for Earthquake Engineering., 2012.

[73] M. Latour, V. Piluso, and G. Rizzano, "Experimental analysis on friction materials for supplemental damping devices," *Construction and Building Materials*, vol. 65, pp. 159–176, Aug. 2014.

[74] Y. Qin, K.-X. Zhao, G.-P. Shu, and L. Ke, "Experimental study on frictional behavior of different structural materials," *Structures*, vol. 49, pp. 557–569, Mar. 2023.

[75] C. E. Grigorian, T. S. Yang, and E. P. Popov, "Slotted bolted connection energy dissipators," *Earthquake spectra*, vol. 9, no. 3, pp. 491–504, 1993.

[76] H. Liu, L.-J. Jia, Y.-A. Lin, and P. Xiang, "Effects of interface conditions on tribological and hysteretic behaviors of symmetric friction connections," *Engineering Structures*, vol. 302, p. 117405, Mar. 2024.

[77] H. Li, Y. Yin, and S. Wang, "Studies on seismic reduction of story-incresed buildings with friction layer and energy-dissipated devices," *Earthquake Engineering & Structural Dynamics*, vol. 32, pp. 2143–2160, Nov. 2003.

[78] B. G. Morgen and Y. C. Kurama, "Characterization of two friction interfaces for use in seismic damper applications," *Materials and Structures*, vol. 42, pp. 35–49, Jan. 2009.

[79] R. W. Chan and W. Tang, "Serviceability conditions of friction dampers for seismic risk mitigations," *Structures*, vol. 35, pp. 500–510, Jan. 2022.

[80] American Society of Civil Engineers, *Minimum Design Loads and Associated Criteria for Buildings and Other Structures (ASCE/SEI 7-22)*, 2022.

[81] M. T. Lie, "Earthquake energy absorbers," Master's thesis, University of Wollongong, 1983.

[82] H. J. Kim, *Self-centering steel moment-resisting frames with energy dissipating systems*. PhD thesis, University of Toronto, 2007.

[83] F. Bowden and D. Tabor, *The Friction and Lubrication of Solids*. Oxford University Press, 2001.

[84] Z. Li, M. He, H. Dong, Z. Shu, and X. Wang, "Friction performance assessment of Non-Asbestos Organic (NAO) composite-to-steel interface and Polytetrafluoroethylene (PTFE) composite-to-steel interface: Experimental evaluation and application in seismic resistant structures," *Construction and Building Materials*, vol. 174, pp. 272–283, June 2018.

[85] M. Paronesso and D. G. Lignos, "Experimental study of sliding friction damper with composite materials for earthquake resistant structures," *Engineering Structures*, vol. 248, p. 113063, Dec. 2021.

[86] J. Gao, Y. Yuan, T. Qiu, C.-L. Wang, and Z. Qu, "Performance optimization and loading rate-dependency of friction dampers with non-metallic friction materials," *Journal of Building Engineering*, vol. 54, p. 104609, Aug. 2022.

[87] P. J. Blau, *Friction science and technology: from concepts to applications*. Boca Raton, FL: CRC Press, 2009.

[88] C. A. Coulomb, *Théorie des Machines Simples (Theory of Simple Machines)*. Paris: Bachelier, 1821.

[89] C. J. Black, N. Makris, and I. D. Aiken, "Component testing, seismic evaluation and characterization of buckling-restrained braces," *Journal of Structural Engineering*, vol. 130, no. 6, pp. 880–894, 2004.

[90] R. DesRoches, J. McCormick, and M. Delemont, "Cyclic properties of superelastic shape memory alloy wires and bars," *Journal of Structural Engineering*, vol. 130, no. 1, pp. 38–46, 2004.

[91] G. Tsampras and R. Sause, "Reducing the magnitude and variability of seismic-induced acceleration and force responses in steel buildings with controlled rocking base mechanism and force-limiting connections," *Resilient Cities and Structures*, vol. 4, no. 4, pp. 143–157, 2025.

[92] American Institute of Steel Construction, *Steel Construction Manual*. American Institute of Steel Construction, 16 ed., 2023.

[93] M. Latour, V. Piluso, and G. Rizzano, "Free from damage beam-to-column joints: Testing and design of DST connections with friction pads," *Engineering Structures*, vol. 85, pp. 219–233, Feb. 2015.

[94] G. Tsampras and R. Sause, "Full-scale, components test of inertial force-limiting floor anchorage systems for seismic resistant building structures using a friction device and carbon fiber reinforced low damping rubber bearings." DesignSafe-CI dataset, 2014. Accessed: 2025-04-29.

[95] Research Council on Structural Connections, *Specification for Structural Joints Using High-Strength Bolts (RCSC Specification)*. Chicago, IL: American Institute of Steel Construction, 2020.

[96] J. Lv, Y. Xiao, and Y. Xue, "Time-temperature-dependent response and analysis of preload relaxation in bolted composite joints," *Journal of Reinforced Plastics and Composites*, vol. 37, no. 7, pp. 460–474, 2018.

[97] D. Weerth and C. Ortloff, "Creep considerations in reinforced plastic laminate bolted connections," in *Army symposium on solid mechanics*, pp. 137–54, 1986.

[98] S. D. Thoppul, R. F. Gibson, and R. A. Ibrahim, "Phenomenological modeling and numerical simulation of relaxation in bolted composite joints," *Journal of composite materials*, vol. 42, no. 17, pp. 1709–1729, 2008.

[99] V. Caccese, K. A. Berube, M. Fernandez, J. D. Melo, and J. P. Kabche, "Influence of stress relaxation on clamp-up force in hybrid composite-to-metal bolted joints," *Composite Structures*, vol. 89, no. 2, pp. 285–293, 2009.

[100] A. Scattina, D. Roncato, G. Belingardi, and G. Martino, "Investigation of creep phenomenon on composite material for bolt connections," *Composite structures*, vol. 134, pp. 378–383, 2015.

[101] I. H. Mualla and B. Belev, "Performance of steel frames with a new friction damper device under earthquake excitation," *Engineering Structures*, vol. 24, no. 3, pp. 365–371, 2002.

[102] S. Veismoradi, S. M. M. Yousef-beik, P. Zarnani, and P. Quenneville, "Development and parametric study of a new self-centering rotational friction damper," *Engineering Structures*, vol. 235, p. 112097, 2021.

[103] A. B. Francavilla, M. Latour, G. Rizzano, F. Nigro, and V. Piluso, "Experimental assessment of the hysteretic response of resilient low-damage friction joints with different belleville disk springs configurations," *Soil Dynamics and Earthquake Engineering*, vol. 180, p. 108617, 2024.

[104] R. Cox, *Engineered Tribological Composites*. Warrendale, PA: SAE International, Nov. 2011.

[105] N. Hentati, F. Makni, and R. Elleuch, "Braking performance of friction materials: A review of manufacturing process impact and future trends," *Tribology - Materials, Surfaces & Interfaces*, vol. 17, no. 2, pp. 136–157, 2023.

[106] G. Nicholson, *Facts about Friction: A Friction Material Manual Almost All You Need to Know about Manufacturing*. Gedoran, 1995.

[107] R. A. Tatara, *Applied plastics engineering handbook*, ch. 17, pp. 389–424. William Andrew Publishing, 2024.

[108] SAE International, *Brake Lining Quality Test Procedure (SAE J661 202110)*, 2021.

[109] "Gatke." Accessed: 2023-11-30.

[110] "Harvey Tool." Accessed: 2024-09-19.

[111] "Makita." Accessed: 2024-09-19.

[112] D20 Committee, "Standard test method for tensile properties of plastics," tech. rep., ASTM International, 2022.

[113] E. J. Barbero, *Introduction to composite materials design*. CRC press, 2010.

[114] "MTS." Accessed: 2024-03-19.

[115] D30 Committee, "Standard test method for bearing response of polymer matrix composite laminates," tech. rep., ASTM International, 2023.

[116] American Institute of Steel Construction, *Steel construction manual*, 15 ed., 2017.

[117] S. D. Thoppul, J. Finegan, and R. F. Gibson, "Mechanics of mechanically fastened joints in polymer–matrix composite structures – A review," *Composites Science and Technology*, vol. 69, pp. 301–329, Mar. 2009.

[118] "Hytorc." Accessed: 2024-09-19.

[119] F16 Committee, "Standard specification for hardened steel backup and reaction washers inch and metric dimensions," tech. rep., ASTM International, 2020.

[120] "Bostik." Accessed: 2024-09-19.

[121] "Transducer Techniques Inc.." Accessed: 2024-09-19.

[122] "Fujifilm." Accessed: 2024-09-19.

[123] K. Lee, G. Tsampras, and C. F. Mayorga, "Reinforced concrete core wall buildings with modified friction-based force-limiting connections: Connection design considerations and 3d response to bidirectional ground motions," *Journal of Structural Engineering*, vol. 151, no. 2, p. 04024203, 2025.

[124] H. Schreier, J.-J. Orteu, and M. A. Sutton, *Image Correlation for Shape, Motion and Deformation Measurements: Basic Concepts,Theory and Applications*. Boston, MA: Springer US, 2009.

[125] "Correlated-solutions." Accessed: 2023-12-05.

[126] "Keyence." Accessed: 2024-09-20.

[127] P. J. Blau, "On the nature of running-in," *Tribology International*, vol. 38, pp. 1007–1012, Nov. 2005.

[128] I. V. Kragelsky, M. N. Dobychin, and V. S. Kombalov, *Friction and wear: calculation methods*. Pergamon Press, 1982.

[129] X. Zhang, L. Zhang, X. Yu, X. Zhu, Y. Tu, and X. Kang, "A novel and quantitative determination method for the running-in process through dimensionless real contact area," *Wear*, vol. 514, p. 204554, 2023.

[130] S. Hsu, R. Munro, M. Shen, and R. Gates, *Boundary Lubricated Wear*, ch. 4, pp. 37–70. John Wiley & Sons, Ltd, 2005.

[131] W. Song, J. Gweon, J. S. Park, J. Kim, J. Kim, and H. Jang, "Role of contact plateaus on velocity-dependent friction of brake friction composite with steel fibres," *Tribology International*, vol. 171, p. 107568, 2022.

[132] S. Wen and P. Huang, *Principles of tribology*. Hoboken, NJ: Wiley, 2017.

[133] S. B. Park, K. H. Cho, S. Jung, and H. Jang, "Tribological properties of brake friction materials with steel fibers," *Metals and Materials International*, vol. 15, pp. 27–32, 2009.

[134] J. W. Kim, B. S. Joo, and H. Jang, "The effect of contact area on velocity weakening of the friction coefficient and friction instability: A case study on brake friction materials," *Tribology International*, vol. 135, pp. 38–45, 2019.

[135] J. H. Dieterich and B. D. Kilgore, "Direct observation of frictional contacts: New insights for state-dependent properties," *Pure and applied geophysics*, vol. 143, pp. 283–302, 1994.

[136] K. Chen, G. Tsampras, S. Cheruvalath, and M. Thundathil, "Experimental characterization of mechanical and tribological properties of composite materials for friction-based force-limiting structural components," *Composites Part B: Engineering*, p. 112472, 2025.

[137] C.-C. Chou, C.-J. Wu, L.-Y. Huang, A. Córdova, H.-Z. Lin, S.-H. Chao, G. Tsampras, C.-M. Uang, S.-H. Chao, and H.-Y. Chung, "Shaking table tests of a three-story re-centering steel braced frame with sliding slab connected to energy dissipation devices," *Earthquake Engineering & Structural Dynamics*, 2025.

[138] G. Tsampras and R. Sause, "Force-based design method for force-limiting deformable connections in earthquake-resistant buildings," *Journal of Structural Engineering*, vol. 148, no. 10, p. 04022150, 2022.

[139] American Institute of Steel Construction, *Specification for Structural Steel Buildings*, 2022.

[140] ANSYS, Inc., *ANSYS Mechanical User's Guide*. ANSYS, Inc., Canonsburg, PA, USA, 2024. Release 2024 R1.

[141] "Autodesk," 2025. Accessed: 2025-04-10.

[142] "Haas," 2025. Accessed: 2025-04-10.

[143] "Gatke," 2025. Accessed: 2025-04-10.

[144] "Onefinity," 2025. Accessed: 2025-04-18.

[145] "Correlated solutions," 2025. Accessed: 2025-04-10.

[146] A. Córdova, C.-C. Chou, C.-J. Wu, G. Tsampras, C.-M. Uang, and S.-H. Chao, "Modeling and response of a three-story steel building with sliding slabs in earthquake motions," *Earthquake Engineering & Structural Dynamics*, vol. 54, no. 3, pp. 1101–1121, 2025.

[147] P. J. Blau, *Friction science and technology: from concepts to applications*. CRC press, 2008.

[148] C.-M. Lin, Y.-W. Chang, C.-C. Chou, S.-J. Jhuang, Z.-k. Lee, C.-L. Wu, S.-H. Chao, J.-Y. Huang, H.-C. Yang, C.-Y. Chang, G. Mosqueda, and C.-C. Hung, "Reconnaissance of the 2022 guanshan and chihshang earthquakes in eastern taiwan," *Earthquake Spectra*, vol. 40, pp. 531–565, 02 2024.

[149] G. Tsampras, *Force-Limiting Floor Diaphragm Connection for Earthquake-Resistant Buildings*. PhD thesis, Lehigh University, 2016.

[150] D. Zhang, R. Fleischman, J. Restrepo, R. Sause, J. Maffei, D. Mar, and G. Monti, "Development of a floor inertial force limiting anchorage system building seismic response," in *Proceedings of the NCEE 2014-10th US National Conference on Earthquake Engineering: Frontiers of Earthquake Engineering*, 2014.

[151] G. Tsampras, R. Sause, R. B. Fleischman, and J. I. Restrepo, "Experimental study of deformable connection consisting of buckling-restrained brace and rubber bearings to connect floor system to lateral force resisting system," *Earthquake Engineering & Structural Dynamics*, vol. 46, no. 8, pp. 1287–1305, 2017.

[152] A. Nema, *Development of low seismic damage structural systems*. PhD thesis, University of California, San Diego, 2018.

[153] Z. Zhang, *Analytical investigation of inertial force-limiting floor anchorage system for seismic resistant building structures*. PhD thesis, The University of Arizona, 2017.

[154] G. Tsampras, R. Sause, R. Fleischman, J. Restrepo, A. Nema, and Z. Zhang, "Practical force-limiting deformable connections in buildings with rocking base mechanism and limited higher-mode responses," in *Proceedings of the 12th national conference on earthquake engineering. Salt Lake City, Utah: EERI*, 2022.

[155] M. Paronesso and D. G. Lignos, "Seismic design and performance of steel concentrically braced frame buildings with dissipative floor connectors," *Earthquake Engineering & Structural Dynamics*, vol. 51, no. 15, pp. 3505–3525, 2022.

[156] M. Paronesso and D. G. Lignos, "Experimental study of sliding friction damper with composite materials for earthquake resistant structures," *Engineering Structures*, vol. 248, p. 113063, 2021.

[157] T. Yang, J. Moehle, Y. Bozorgnia, F. Zareian, and J. Wallace, "Performance assessment of tall concrete core-wall building designed using two alternative approaches," *Earthquake Engineering & Structural Dynamics*, vol. 41, no. 11, pp. 1515–1531, 2012.

[158] M. Sarkisian, E. Long, and W. Hassan, "Performance-based engineering of core wall tall buildings," in *Structures Congress 2013: Bridging Your Passion with Your Profession*, pp. 1094–1108, 2013.

[159] G.-Q. Li, M. Pang, F. Sun, J. Jiang, and D. Hu, "Seismic behavior of coupled shear wall structures with various concrete and steel coupling beams," *The Structural Design of Tall and Special Buildings*, vol. 27, no. 1, p. e1405, 2018.

[160] N. A. Tauberg, K. Kolozvari, and J. W. Wallace, "Ductile reinforced concrete coupled walls: Fema p695 study," *Report Number UCLA SEERL 2019*, 2019.

[161] M. Mavros, M. Panagiotou, I. Koutromanos, R. Alvarez, and J. I. Restrepo, "Seismic analysis of a modern 14-story reinforced concrete core wall building system using the btm-shell methodology," *Earthquake Engineering & Structural Dynamics*, vol. 51, no. 6, pp. 1540–1562, 2022.

[162] B. S. S. Council, "2020 nehrp recommended seismic provisions: Design examples, training materials, and design flow charts," *FEMA*, 2020.

[163] J. R. Brown, M. Li, A. Palermo, S. Pampanin, and F. Sarti, "Experimental testing of a low-damage post-tensioned c-shaped clt core-wall," *Journal of Structural Engineering*, vol. 147, no. 3, p. 04020357, 2021.

[164] M. Bruneau and G. MacRae, "Reconstructing christchurch: A seismic shift in building structural systems," *The Quake Centre, University of Canterbury*, 2017.

[165] S. Agrawal, "Seismic design coefficients for composite plate shear walls-concrete filled (c-psw/cf)," Master's thesis, Purdue University, 2020.

[166] "Speedcore," 2026. Accessed: 2026-04-13.

[167] J. P. Moehle, T. Ghodsi, J. D. Hooper, D. C. Fields, and R. Gedhada, "Seismic design of cast-in-place concrete special structural walls and coupling beams," tech. rep., National Institute of Standards and Technology, 2011.

[168] V. Calugaru and M. Panagiotou, "Response of tall cantilever wall buildings to strong pulse type seismic excitation," *Earthquake engineering & structural dynamics*, vol. 41, no. 9, pp. 1301–1318, 2012.

[169] L. Van Den Einde, J. P. Conte, J. I. Restrepo, R. Bustamante, M. Halvorson, T. C. Hutchinson, C.-T. Lai, K. Lotfizadeh, J. E. Luco, M. L. Morrison, G. Mosqueda, M. Nemeth, O. Ozcelik, S. Restrepo, A. Rodriguez, B. Shing, B. Thoen, and G. Tsampras, "Nheri@ uc san diego 6-dof large high-performance outdoor shake table facility," *Frontiers in Built Environment*, vol. 6, p. 580333, 2021.

[170] P. Weidlinger and M. Ettouney, "Sequential coupling: new structural connection for seismic control," *Journal of Structural Engineering*, vol. 119, no. 1, pp. 181–201, 1993.

[171] P. Weidlinger, "Passive structural control with sequential coupling," *Journal of Structural Engineering*, vol. 122, no. 9, pp. 1072–1080, 1996.

[172] A. Cheraghi and S. M. Zahrai, "Innovative multi-level control with concentric pipes along brace to reduce seismic response of steel frames," *Journal of Constructional Steel Research*, vol. 127, pp. 120–135, 2016.

[173] Z. Huang, W. Huang, C. Zhang, T. Yu, Z. Lin, W. Lie, and F. Zhao, "Design and experiment of an innovative rotational two-level friction damper," *Engineering Structures*, vol. 308, p. 118030, 2024.

[174] C.-H. Lee, J. Kim, D.-H. Kim, J. Ryu, and Y. K. Ju, "Numerical and experimental analysis of combined behavior of shear-type friction damper and non-uniform strip damper for multi-level seismic protection," *Engineering Structures*, vol. 114, pp. 75–92, 2016.

[175] F. Kazemi, N. Asgarkhani, N. Lasowicz, and R. Jankowski, "Development and experimental validation of a novel double-stage yield steel slit damper-buckling restrained brace," *Engineering Structures*, vol. 315, p. 118427, 2024.

[176] P. Pan, W. Li, X. Nie, K. Deng, and J. Sun, "Seismic performance of a reinforced concrete frame equipped with a double-stage yield buckling restrained brace," *The Structural Design of Tall and Special Buildings*, vol. 26, no. 4, p. e1335, 2017.

[177] K. Ke, X. Zhou, S. Hu, Y. Chen, M. S. Alam, Y. Wang, and Z. Zhou, "Development and tests of novel repairable multi-stage yielding steel slit dampers for seismic mitigation," *Journal of Building Engineering*, vol. 86, p. 108809, 2024.

[178] X. Yan, Z. Chen, A. Qi, X. Wang, and S. Shi, "Experimental and theoretical study of a lead extrusion and friction composite damper," *Engineering Structures*, vol. 177, pp. 306–317, 2018.

[179] Y. Liu, X. Chen, and H. Tagawa, "Beam-to-column connection with double-stage yield buckling-restrained steel bar dampers," *Journal of Constructional Steel Research*, vol. 212, p. 108278, 2024.

[180] A. Naeem and J. Kim, "Seismic performance evaluation of a multi-slit damper," *Engineering Structures*, vol. 189, pp. 332–346, 2019.

[181] H. Sha, X. Chong, L. Xie, L. He, Q. Jiang, and J. Gao, "Study on seismic performance of rc frame with uhpc cladding panels and two-level friction damping connections," *Journal of Building Engineering*, vol. 95, p. 110118, 2024.

[182] O. Ranaei and A. A. Aghakouchak, "A new hybrid energy dissipation system with viscoelastic and flexural yielding strips dampers for multi-level vibration control," *archives of civil and mechanical engineering*, vol. 19, no. 2, pp. 584–597, 2019.

[183] C. Xiong, Y. Cao, T. Wang, L. Xie, and D. Wu, "Experimental and numerical studies of a core plate repairable double-stage yield buckling-restrained brace," *Journal of Constructional Steel Research*, vol. 223, p. 109006, 2024.

[184] H. R. Ghorbani and F. R. Rofooei, "A novel double slip loads friction damper to control the seismic response of structures," *Engineering Structures*, vol. 225, p. 111273, 2020.

[185] Y. Yang, J. Xue, Z. Luo, and R. Liu, "Manufacturing, testing and simulation of novel dual-stage energy-dissipation and self-centering friction damper," *Journal of Constructional Steel Research*, vol. 222, p. 108949, 2024.

[186] Y. Wang, Z. Zhou, Q. Xie, and L. Huang, "Theoretical analysis and experimental investigation of hysteretic performance of self-centering variable friction damper braces," *Engineering Structures*, vol. 217, p. 110779, 2020.

[187] Y. Yang, J. Xue, and R. Liu, "Experimental and numerical study on hysteresis behaviour of a novel dual-stage friction damper," *Structures*, vol. 70, p. 107911, 2024.

[188] C.-L. Wang, Y. Qing, J. Wu, J. Wang, and Z. Gu, "Analytical and experimental studies on buckling-restrained brace with gap-supported tendon protection," *Journal of Constructional Steel Research*, vol. 164, p. 105807, 2020.

[189] C. Yang, L. Xie, Q. Liu, A. Li, X. Wang, and Q. Liu, "Experimental and numerical investigations of a novel parallel double-stage crawler-track-shaped shear damper," *Thin-Walled Structures*, vol. 195, p. 111428, 2024.

[190] T. Friis, E. I. Katsanos, M. Saberi, and H. H. H. Koss, "Two-level friction damping and its application for passive multi-functional vibration control of high-rise buildings," *Engineering Structures*, vol. 239, p. 112310, 2021.

[191] C. Yang, H. Wang, L. Xie, A. Li, and X. Wang, "Experimental and theoretical investigations on an asynchronized parallel double-stage viscous fluid damper," *Structural Control and Health Monitoring*, vol. 2024, no. 1, p. 6921518, 2024.

[192] M. Z. Golmoghany and S. M. Zahrai, "Improving seismic behavior using a hybrid control system of friction damper and vertical shear panel in series," in *Structures*, vol. 31, pp. 369–379, Elsevier, 2021.

[193] T. Yu, C. Zhang, Z. Huang, and W. Yuan, "Development and performance evaluation of multi-stage sma damper-restrained flat sliding bearings for deformation mitigation," *Journal of Building Engineering*, vol. 98, p. 111233, 2024.

[194] Q. Jiang, H. Wang, Y. Feng, X. Chong, and L. Hou, "Analytical and experimental studies on a two-level yielding rocking steel frame with buckling-restrained columns (tyrsfb)," *Engineering Structures*, vol. 235, p. 112008, 2021.

[195] C. Bai, J. Xue, Z. Luo, R. Liu, and S. Ding, "Hysteretic behavior and seismic control of a novel dual-stage friction self-centering damper using nitrogen gas springs," *Construction and Building Materials*, vol. 502, p. 144370, 2025.

[196] B. K. Kiani and B. H. Hashemi, "Development of a double-stage yielding damper with vertical shear links," *Engineering Structures*, vol. 246, p. 112959, 2021.

[197] H. Dong, Y. Wang, K. Bi, X. Du, and Q. Han, "Hysteretic behavior of a multifunctional phased self-adaptive rotational friction damper," *Journal of Structural Engineering*, vol. 151, no. 4, p. 04025031, 2025.

[198] B. Shahbazi and E. Moaddab, "A new hybrid friction damper (hfd) for dual-level performance of steel structures," *International Journal of Steel Structures*, vol. 21, no. 4, pp. 1332–1345, 2021.

[199] W. Lie, F. Shi, Y. Zhou, W. Yuan, A. Erbolat, and D. Fang, "Development of a two-stage self-centering brace with dissipating-centering sequence for potential multi-objective seismic design," *Engineering Structures*, vol. 336, p. 120464, 2025.

[200] F.-F. Sun, J.-Q. Yang, M. Wang, and T.-Y. Wu, "An adaptive viscous damping wall for seismic protection: Experimental study and performance-based design," *Journal of Building Engineering*, vol. 44, p. 102645, 2021.

[201] Z. Luo, G. A. MacRae, J. C. C. Golondrino, R. C. Brosnan, and B. A. El-Mashalgi, "Enhancing structural dynamic stability using two-stage friction connections (tfcs)," *Earthquake Engineering & Structural Dynamics*, vol. 54, no. 11, pp. 2748–2764, 2025.

[202] Y. Chen, W. Yu, M. Zhang, and Y. Li, "A novel energy dissipation damper for multi-level earthquakes," *Journal of Constructional Steel Research*, vol. 192, p. 107214, 2022.

[203] H. Pan, H. Wang, T. Wang, and P. Pan, "Development and experimental study of a replaceable double stage coupling beam damper," *Engineering Structures*, vol. 325, p. 119392, 2025.

[204] K. Dai, T. Sun, Y. Liu, T. Li, and A. Camara, "Concept and numerical analysis of a double-stage coupling damper for multilevel seismic protection," *Thin-Walled Structures*, vol. 185, p. 110581, 2023.

[205] M. Sakai, H. Tagawa, X. Chen, M. Uehara, and M. Nishimura, "Gusset plate friction damper with double plate core buckling-restrained brace," *Structures*, vol. 81, p. 110243, 2025.

[206] H. Jiang, L. Xu, X. Xie, and P. Chen, "Seismic behavior of double activation self-centering brace and braced structures," *Journal of Structural Engineering*, vol. 149, no. 7, p. 04023082, 2023.

[207] J. Tian, Z. Wang, and J. Pan, "Investigation on the mechanical behavior of a novel pre-tensioned friction-metal dual-stage energy dissipation brace," *Journal of Building Engineering*, p. 114443, 2025.

[208] K. Ke, Y. Chen, X. Zhou, M. C. Yam, and S. Hu, "Experimental and numerical study of a brace-type hybrid damper with steel slit plates enhanced by friction mechanism," *Thin-Walled Structures*, vol. 182, p. 110249, 2023.

[209] J.-p. Wei, H. Tian, D.-h. Wang, and L.-m. Tian, "Steel frame joints with multistage performance for collaboratively resisting earthquakes," *Soil Dynamics and Earthquake Engineering*, vol. 194, p. 109350, 2025.

[210] F. Li, Y. Du, N. Hong, H. Li, and P. Chi, "Seismic performance of prefabricated replaceable graded-yielding energy-dissipating connectors," *Engineering Structures*, vol. 297, p. 116962, 2023.

[211] Q. Wu, C. Jia, W.-G. Liu, J. Sun, X. Chen, H. Zhu, and D. Wu, "Experimental and numerical study on a novel viscoelastic-friction composite damper," *Structures*, vol. 75, p. 108840, 2025.

[212] Y. Lu, Q. Lv, T. Sun, Y. Liu, and H. Tang, "Experimental and numerical studies on hysteretic behavior of a novel bending-friction coupled damper," *Thin-Walled Structures*, vol. 183, p. 110385, 2023.

[213] C. Zhang, X. Guo, Y. Zhao, and Y. Liu, "Development of an innovative assembled self-centering dual-stage yield buckling-restrained brace for improving seismic resilience," *Engineering Structures*, vol. 329, p. 119804, 2025.

[214] C. Yang, L. Xie, A. Li, and X. Wang, "Development of a double-stage-yield dissipative beam-to-column joint: experimental study and application for structural response control," *Soil Dynamics and Earthquake Engineering*, vol. 171, p. 107997, 2023.

[215] Y. Tan, S. Jin, Q. Liu, and J. Zhou, "Experimental and numerical investigation of a graded yielding metallic damper and its application in simply supported bridges," *Engineering Structures*, vol. 355, p. 122429, 2026.

[216] C.-S. Chang Chien and M.-T. Guo, "Theoretical analysis and experimental validation of multi-level friction damping system," *Earthquake Engineering & Structural Dynamics*, vol. 53, no. 11, pp. 3565–3587, 2024.

[217] Z. Zhou, Y. Zeng, X. Zhou, X. He, and K. Ke, "Performance-based-plastic-design of truss-moment frames incorporating rotary dampers with two-stage energy-dissipation mechanism," *Journal of Constructional Steel Research*, vol. 238, p. 110206, 2026.

[218] H. Dong, Y. Li, K. Bi, Q. Han, and X. Du, "Seismic performance assessment of rc bridge piers with variable hysteresis performance dampers," *Engineering Structures*, vol. 310, p. 118085, 2024.

[219] "Scan pac inc.," 2026. Accessed: 2026-04-23.

[220] F. McKenna and G. L. Fenves, *The OpenSees command language manual*. University of California, Berkeley, 2001.

[221] K. Chen, G. Tsampras, C.-C. Chou, H.-Z. Lin, C.-J. Wu, A. Córdova, C.-M. Uang, and S.-H. Chao, "Low-cost friction-based force-limiting connection with reduced sensitivity to machining tolerances and accelerated repairability," *Earthquake Engineering & Structural Dynamics*, vol. 55, no. 6, pp. 1270–1291, 2026.